NASA/TP—2017–219555

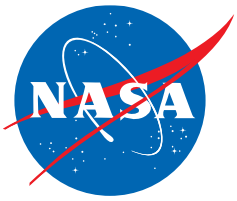

Microwave Thermal Propulsion
Final Report

Kevin L. G. Parkin
Carnegie Mellon University

Thomas Lambot
Carnegie Mellon University

August 2017

NASA STI Program ... in Profile

Since its founding, NASA has been dedicated to the advancement of aeronautics and space science. The NASA scientific and technical information (STI) program plays a key part in helping NASA maintain this important role.

The NASA STI program operates under the auspices of the Agency Chief Information Officer. It collects, organizes, provides for archiving, and disseminates NASA's STI. The NASA STI program provides access to the NTRS Registered and its public interface, the NASA Technical Reports Server, thus providing one of the largest collections of aeronautical and space science STI in the world. Results are published in both non-NASA channels and by NASA in the NASA STI Report Series, which includes the following report types:

- TECHNICAL PUBLICATION. Reports of completed research or a major significant phase of research that present the results of NASA Programs and include extensive data or theoretical analysis. Includes compilations of significant scientific and technical data and information deemed to be of continuing reference value. NASA counter-part of peer-reviewed formal professional papers but has less stringent limitations on manuscript length and extent of graphic presentations.

- TECHNICAL MEMORANDUM. Scientific and technical findings that are preliminary or of specialized interest, e.g., quick release reports, working papers, and bibliographies that contain minimal annotation. Does not contain extensive analysis.

- CONTRACTOR REPORT. Scientific and technical findings by NASA-sponsored contractors and grantees.

- CONFERENCE PUBLICATION. Collected papers from scientific and technical conferences, symposia, seminars, or other meetings sponsored or co-sponsored by NASA.

- SPECIAL PUBLICATION. Scientific, technical, or historical information from NASA programs, projects, and missions, often concerned with subjects having substantial public interest.

- TECHNICAL TRANSLATION. English-language translations of foreign scientific and technical material pertinent to NASA's mission.

Specialized services also include organizing and publishing research results, distributing specialized research announcements and feeds, providing information desk and personal search support, and enabling data exchange services.

For more information about the NASA STI program, see the following:

- Access the NASA STI program home page at http://www.sti.nasa.gov

- E-mail your question to help@sti.nasa.gov

- Phone the NASA STI Information Desk at 757-864-9658

- Write to:
  NASA STI Information Desk
  Mail Stop 148
  NASA Langley Research Center
  Hampton, VA 23681-2199

Microwave Thermal Propulsion
Final Report

Kevin Parkin
Principal Investigator, Carnegie Mellon University

Thomas Lambot
Carnegie Mellon University

Abstract

We have conducted research in microwave thermal propulsion as part of the space exploration access technologies (SEAT) research program, a cooperative agreement (NNX09AF52A) between NASA and Carnegie Mellon University. The SEAT program commenced on the 19th of February 2009 and concluded on the 30th of September 2015. The DARPA/NASA Millimeter-wave Thermal Launch System (MTLS) project subsumed the SEAT program from May 2012 to March 2014 and one of us (Parkin) served as its principal investigator and chief engineer. The MTLS project had no final report of its own, so we have included the MTLS work in this report and incorporate its conclusions here.

In the six years from 2009 until 2015 there has been significant progress in millimeter-wave thermal rocketry (a subset of microwave thermal rocketry), most of which has been made under the auspices of the SEAT and MTLS programs.

This final report is intended for multiple audiences. For researchers, we present techniques that we have developed to simplify and quantify the performance of thermal rockets and their constituent technologies. For program managers, we detail the facilities that we have built and the outcomes of experiments that were conducted using them. We also include incomplete and unfruitful lines of research. For decision-makers, we introduce the millimeter-wave thermal rocket in historical context. Considering the economic significance of space launch, we present a brief but significant cost-benefit analysis, for the first time showing that there is a compelling economic case for replacing conventional rockets with millimeter-wave thermal rockets.

This research was developed with funding from the Defense Advanced Research Projects Agency (DARPA). The views, opinions and/or findings expressed are those of the author(s) and should not be interpreted as reflecting the official views or policies of the Department of Defense or the U.S. Government.

Contents

1 Introduction

The U.S. government is spending $44B on launch-related activities from FY2014 to FY2018 (GAO 2013). This equates to $169M per week. Of this, 25% is being spent on R&D and 75% on building rockets, launching them, and related non-R&D activities. Despite this economically significant expenditure, the U.S. government launches payloads into orbit the same way it did in 1965 – by chemical rockets.

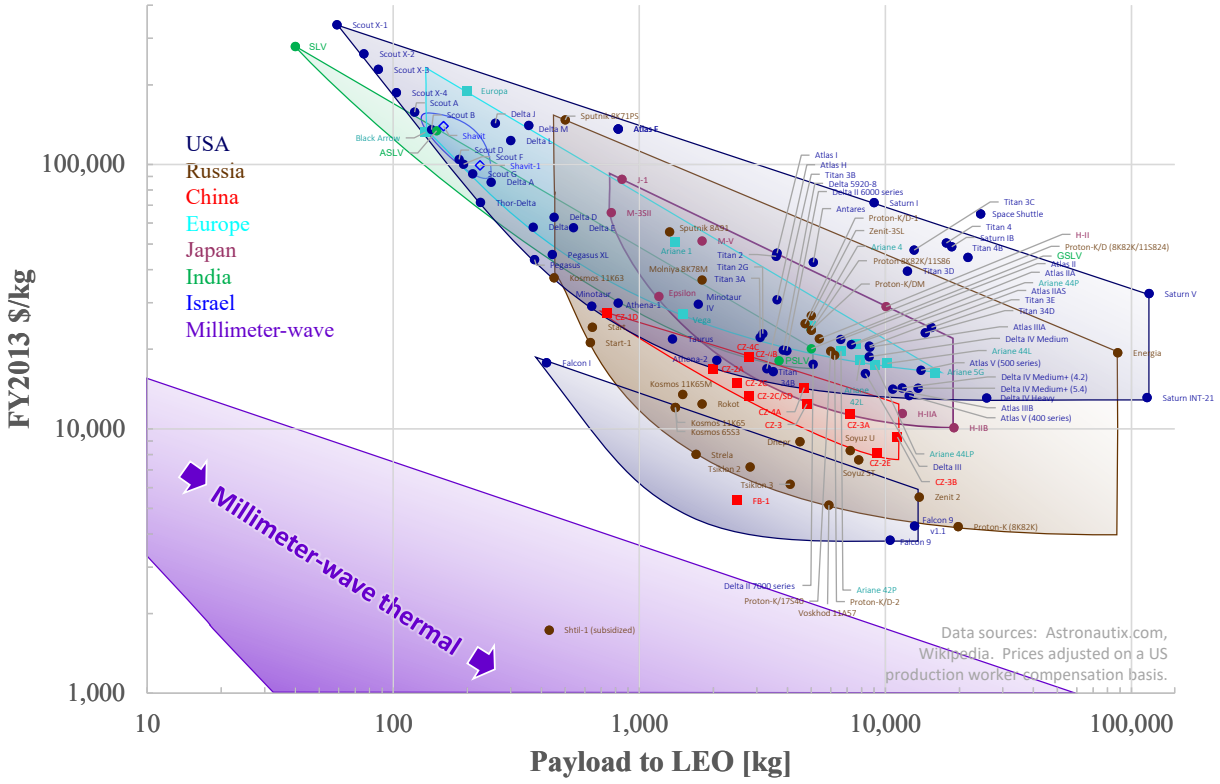

Figure 1 - The price of payload delivery to low Earth orbit (LEO) as a function of rocket payload capacity.

Traditional expendable rockets achieve payload fractions of less than 4.2%. The rocket equation shows how this insufficient payload fraction results from the specific impulse (I_{sp}) of chemical propellants, which long ago reached a practical limit of 460 seconds by reacting hydrogen with oxygen[a]. The LOX/LH_2 reaction releases 16 MJ per kilogram of propellant mixture, whereas the specific energy[b] of low Earth orbit (LEO) is 32 MJ/kg. Conventional rockets reach orbit only because the propellants they expel make them lighter as they go. Additionally, a designer needs to structure the rocket into multiple stages to jettison structural mass as well. Even then, small fractional increases in the structural mass can displace the entire payload mass.

Despite advances in the specific strength of aerospace materials, traditional chemical rockets still need expensive design, construction and testing techniques to make their structures efficient enough to

[a] For H_2/O_2 systems at high pressure. The highest chemical I_{sp} achieved was 523 sec in vacuum using a $Li/H_2/F_2$ tripropellant combination (Arbit, Clapp et al. 1970), but this and other combinations have all proven to be highly impractical, volatile, and economically infeasible for mass production.
[b] Kinetic energy plus gravitational potential energy for a 200 km circular orbit

achieve orbit. These rockets are expensive, unreliable and fragile to build and launch.
The launch cost is reduced by increasing the payload capacity of the rocket, as is evident from Figure 1, but only to a point; prices stop falling as payload capacities exceed 10 metric tons. The figure shows many families of rockets evolving from light to heavy payloads and encompasses data points representing conventional rockets spanning 60 years and hundreds of billions of dollars in evolutionary R&D investment. Data points from each country have the same color, and these points form the boundary of a similar shape in most cases and once prices are corrected on a US production worker compensation basis. We have split the United States into two separate regions in Figure 1 due to multiple outlying data points that naturally form a separate lower region. This lower region contains the SpaceX rockets. SpaceX predicate their prices on lower manufacturing costs and the thesis that reusing the first stage of the rocket will result in cost savings[c]. Figure 1 proves that the price of launch remains above $10,000 per kilogram of payload delivered to LEO for most models of rocket. In contrast, the energy cost of launch[d] is below $100 per kilogram. The ongoing high cost of launch arises for both economic and technical reasons.

On the economic side, market models predict a flat elasticity of demand for space launch (Futron 2003). With modest price reductions only weakly affecting the present market size, a reduction in launch price simply reduces revenue for launch providers. That is, until the payload price is substantially reduced, at which point new markets are enabled[e]. This game-changing price is predicted to be below $1,000 per kilogram (NASA 1994), implying that widespread utilization of space will not happen without at least an order of magnitude cheaper launch costs. At a price of $1,000/kg, the average person needs $70,000 to launch themselves into space[f].

Factors that reduce cost	Pessimist	Nominal	Optimist
Increasing ratio of payload to parasitic dry mass	3	6	12
Moving from 2 propellants to 1	1.5	2	3
Moving from 2-4 stages to 1	1.25	2	4
	6x	**24x**	**144x**

Table 1 - Factors that reduce the cost of a directed energy rocket relative to a conventional chemical rocket.

On the technical side, conventional rockets are a marginal technology in comparison to the alternative of directed energy rockets. A directed energy rocket reduces cost via the factors in Table 1. If each kilogram of dry mass costs a fixed number of dollars to manufacture, for example $1,000/kg, then doubling the ratio of payload to dry mass from 33% to 66% will quarter the overall $/kg of payload to orbit[g].

For directed energy rockets, the higher ratio of payload to parasitic dry mass is fundamentally driven by higher I_{sp} and engine T/W for a given density of propellant. This extra performance enables a single-

[c] Though reuse has not yet been demonstrated as of June 2015
[d] Based on $/kWh of electricity and the amount of energy expended by the rocket.
[e] This is not to say that new markets would spring up overnight even if launch were free, they would likely take years or even decades.
[f] Not including the cost of life support. Other factors like training, specialized clothing and insurance may or may not prove necessary in future routine passenger spaceflight.
[g] Because twice the amount of payload pays for half the amount of parasitic dry mass (dry mass minus the payload mass), neglecting propellant, range and insurance costs.

stage-to-orbit (SSTO) rocket to be built instead of the two to four stages needed for conventional rockets. The unique components needed for stages two, including the inter-stage structure and separation subsystems, all become unnecessary. The workforce corresponding to these components become unnecessary, and the complexity of the overall system is reduced. In addition, the launch range location is no longer constrained by the need to drop stages over the sea, so range costs are reduced and inland launch sites become possible[h].

For directed energy rockets, using one propellant instead of two (used for combustion in conventional rockets[i]) halves the number and of tanks and pumps needed. These tanks and pumps are different models that convey different fluids, so removing them is a simplifying factor in addition to reducing quantity. Again, the workforce corresponding to these components become unnecessary, and the complexity of the overall system is reduced. Other factors depend on context and are not included in the table. For example, with reusable rockets, the ratio of structural margin to parasitic dry mass has a first order effect on recurring launch cost. The complementary effects of full or partial reusability are not included in Table 1.

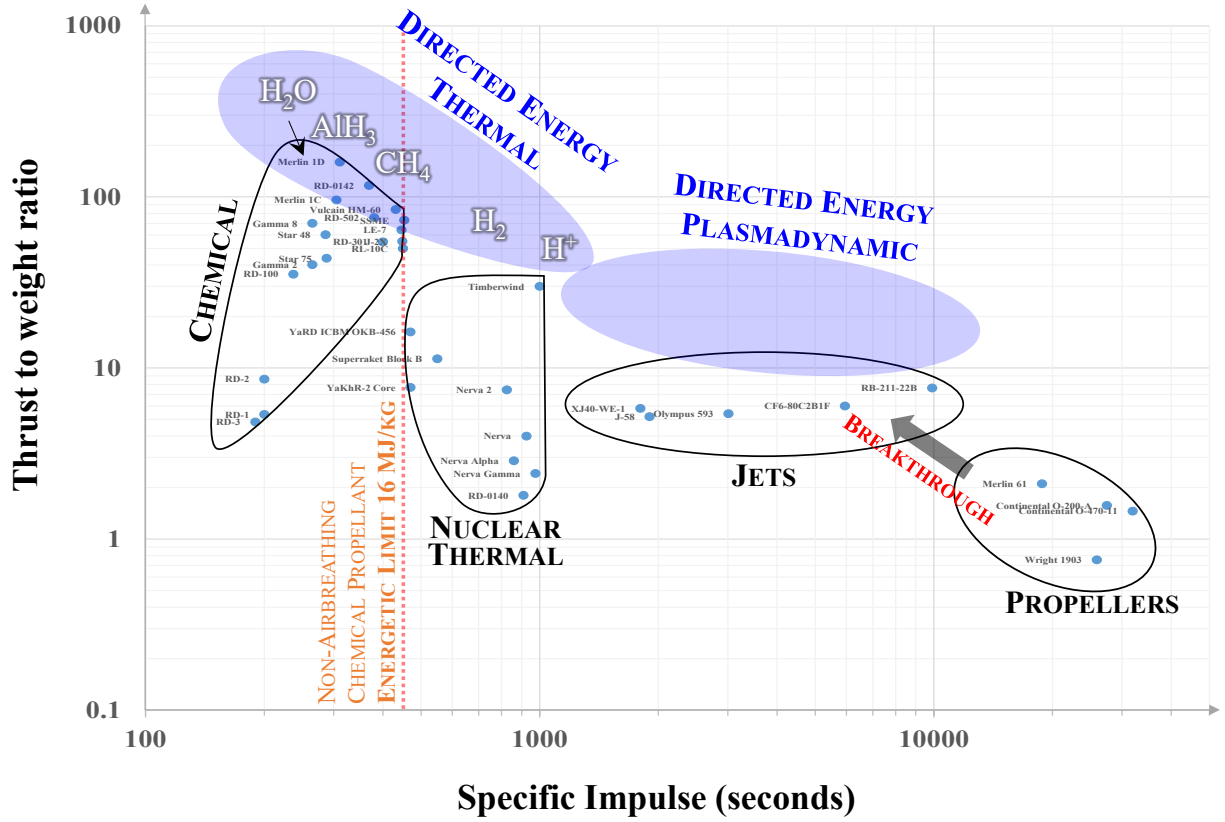

Figure 2 - Forms of propulsion organized by the main metrics of T/W ratio and I_{sp}. Data points are actual engines, grouped by type. Closer inspection of these data points reveals improving performance from early engines through to later ones.

[h] Provided that risk to a person on the ground is within acceptable limits. A rocket that over many years of use proves as reliable as an aircraft might reasonably be allowed to overfly densely populated areas during early ascent.
[i] Conventional monopropellant rockets exist, but specific impulse is prohibitively low for Earth-to-orbit application.

The greater I_{sp} and engine T/W of directed energy thermal rockets is represented by the blue shaded region at the top left of Figure 2. The LOX/LH_2 I_{sp} of 460 seconds represents the practical energy density limit of chemical bonds, the line of data points along it are proof that rocket engines based on chemical energy have reached their theoretical limit. This limit was first reached by the RL-10 engine in 1959 (Sloop 1978). For directed energy thermal rockets, hydrogen only needs to be heated to 1,120 K to exceed the LOX/LH_2 energy density of 16 MJ/kg. Further heating to 2,560 K raises the energy density to 40 MJ/kg.

The newly developed Merlin rocket engine pushes the boundaries of T/W by using denser propellants with lower I_{sp}. This is done because it takes an optimal combination of I_{sp} and T/W to minimize the rocket payload cost. Without the need for combustion, directed energy thermal rockets have more possibilities for molecules to use as propellants. Depending on the optimal combination of T/W and I_{sp} for the application, suitable propellants include hydrogen, methane, or simply water. Using these, directed energy thermal engines outperform conventional chemical rocket engines over the whole range of I_{sp} and T/W.

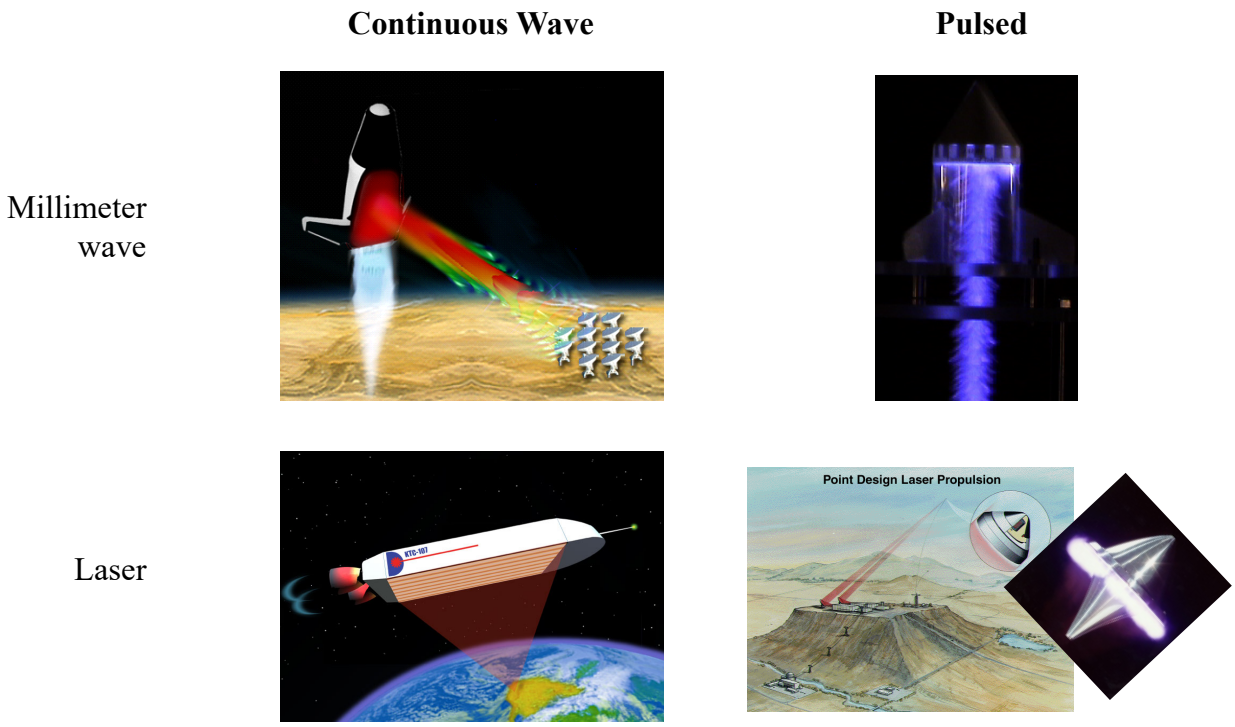

Figure 3 - The four main approaches to directed energy propulsion form a grid. The bottom right approach was proposed in 1972 (Kantrowitz 1972, Minovich 1972), the bottom left in 1992 (Kare 1992), the top left in 2002 (Parkin, Culick et al. 2002), and the top right in 2003 (Oda, Nakagawa et al. 2003).

Konstantin Tsiolkovsky is well known as one of the fathers of rocketry and astronautics. He was the first to derive the rocket equation in 1897. Less known is that Tsiolkovsky himself proposed directed energy rocket launch via a "parallel beam of shortwave electromagnetic rays" in 1924 (Tsiolkovsky 1924). The two-pole magnetron had been invented only three years earlier, and the time average power output at that time was so low that it would take the coherently combined output of millions of such devices to power a microsatellite-class rocket to orbit. In his book, Tsiolkovsky estimates that, due to diffraction, a

ground-based beam director requires an aperture diameter of 12.6 km to produce a beam concentrated enough. He wonders how any receiving material can withstand the intense heat generated the beam, and how it can be directed onto a rocket as it ascends to orbit. He eventually concludes, "This method of imparting velocity raises quite a few difficult problems, the solution of which I shall leave to the future."

In 1959, Willinski proposed for the first time a vehicle wherein "beamed power would be utilized to heat a propulsion fluid, such as hydrogen, ammonia, gasoline, or even water, which would then be expanded through a nozzle to produce thrust" (Willinski 1959). Noting the problems of large apertures and beam diffraction at longer wavelengths, and the opposing problem of atmospheric absorption at wavelengths shorter than 10 cm, his paper dwells predominantly upon a receiving antenna in the form of a large inflated balloon[j]. Due to drag, the vehicle is constrained to operate as an upper stage above the atmosphere. Significantly, Willinski mentions that "the skin of the vehicle itself could possibly be utilized as a surface antenna, thereby allowing operation in the atmosphere."

In 1972, the idea of using a pulsed laser to propel rockets to orbit was proposed separately by Kantrowitz and Minovitch (Kantrowitz 1972, Minovich 1972). The laser had been invented only 12 years earlier, yet it took another 20 years before laser thermal rockets, shown on the bottom left of Figure 3, were proposed (Kare 1992).

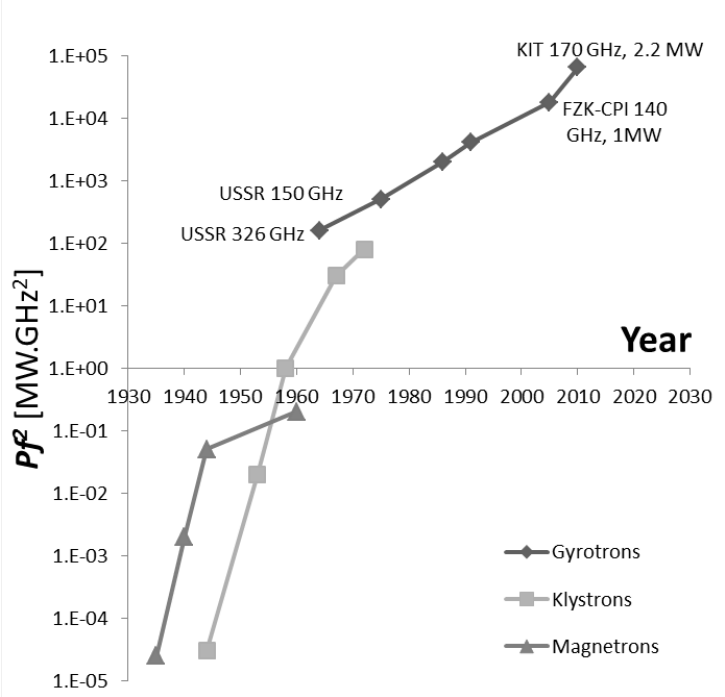

Figure 4 – The rise of high-power microwave sources. Power multiplied by frequency squared is a key figure of merit and is proportional to the brightness of the source in W $m^{-2}sr^{-1}$.

Throughout this time, microwave sources grew in power and frequency, as shown in Figure 4. While microwave and radio sources led Tsiolkovsky and others to estimate aperture sizes exceeding a

[j] clarified in a later paper (Willinski 1966) to focus incoming microwaves to a heat exchanger located at the focus

kilometer[k], millimeter-wavelength sources enable aperture sizes on the order of 100 meters. Millimeter-wave sources were transformed by the advent of the gyrotron oscillator in Russia in the 1970s (Andronov, Fliagin et al. 1978). This era of research boosted the power of gyrotrons from milliwatts to kilowatts (Kupiszewski 1979), and the trend in increasing power output continues to the present day. At this time, a megawatt-class gyrotron can be bought from several manufacturers at a cost of $2-6/Watt. This is one to two orders of magnitude cheaper per Watt than lasers.

Millimeter-waves are attenuated more strongly than L, S, C, X and K-band microwaves in the water-rich lower atmosphere, but conceptual progress was made when Benford & Dickinson pointed out that high-altitude beam director sites greatly reduce the attenuation of millimeter-wavelength sources for Earth-to-orbit power beaming (Benford and Dickinson 1995b).

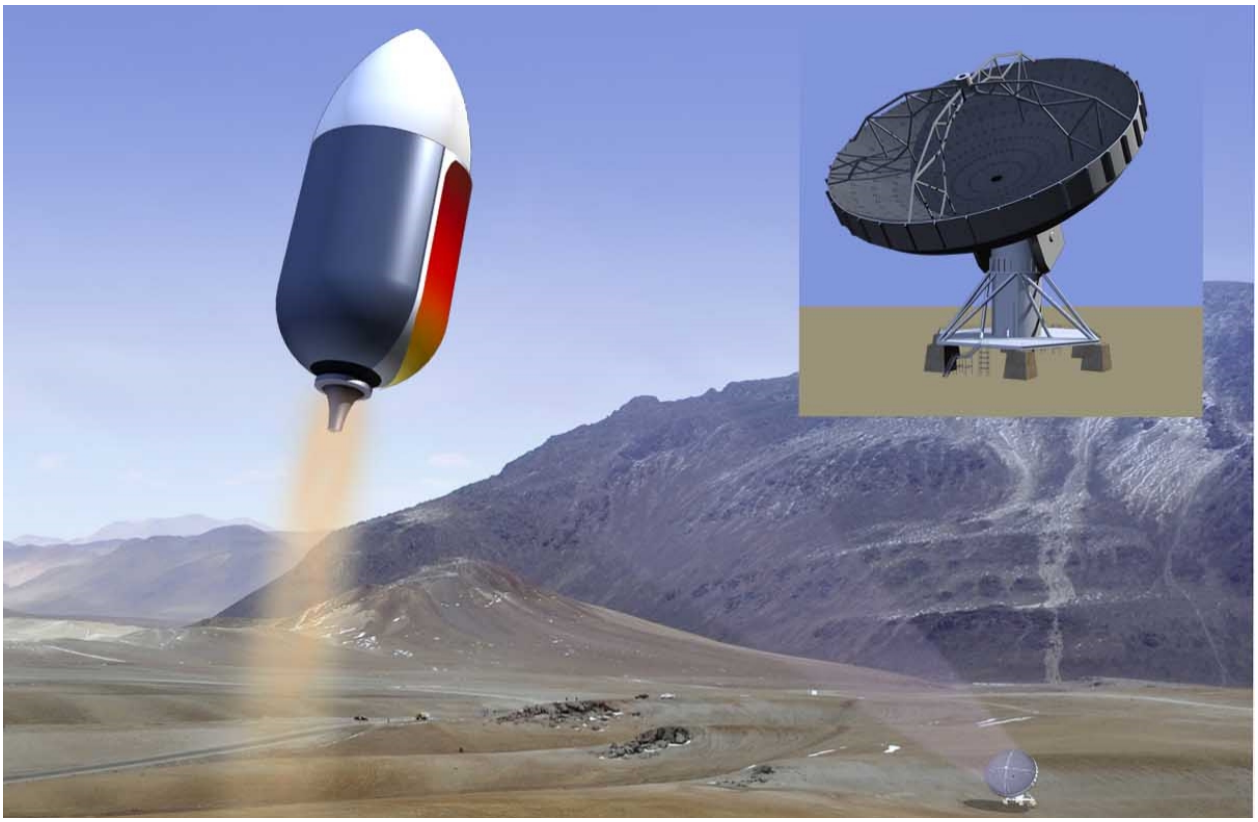

Figure 5 - An implementation of the millimeter-wave thermal concept (not to scale). Picture courtesy of Pat Rawlings. Background scenery: Plateau of Chajnantor. Courtesy ALMA (ESO/NAOJ/NRAO)

In 2002, one of us (Parkin) invented a launch concept that is powered by millimeter-wave sources. Using millimeter-waves reduces aperture sizes and increases plasmadynamic breakdown thresholds, economically favoring a smaller and higher power density vehicle and beam director relative to earlier concepts. The denser vehicle becomes capable of ascending all the way from the ground to orbit using a single stage. A beam-absorbing heat exchanger is chosen as the simplest way to couple energy into the propellant, and one of us (Parkin) named it the microwave thermal rocket by analogy to the heat-

[k] Due to the physics of light diffraction.

exchanger based nuclear thermal rocket (Parkin and Culick 2003, Parkin, DiDomenico et al. 2003). In this work, we favor the more precise name of millimeter-wave thermal rocket.

The current concept, shown in Figure 5, benefits from 12 years of feedback and design evolution. A single foil balloon tank is used to hold the propellant of liquid hydrogen or liquid natural gas. This propellant is then pumped through the heat exchanger so that it reaches the highest possible temperature just prior to being expanded through a spike nozzle to produce thrust. The beam tracks the heat exchanger, which faces the general direction of the beam throughout the ascent to orbit. There is only a single propellant, single tank, single turbopump, and single stage all the way from the ground to orbit.

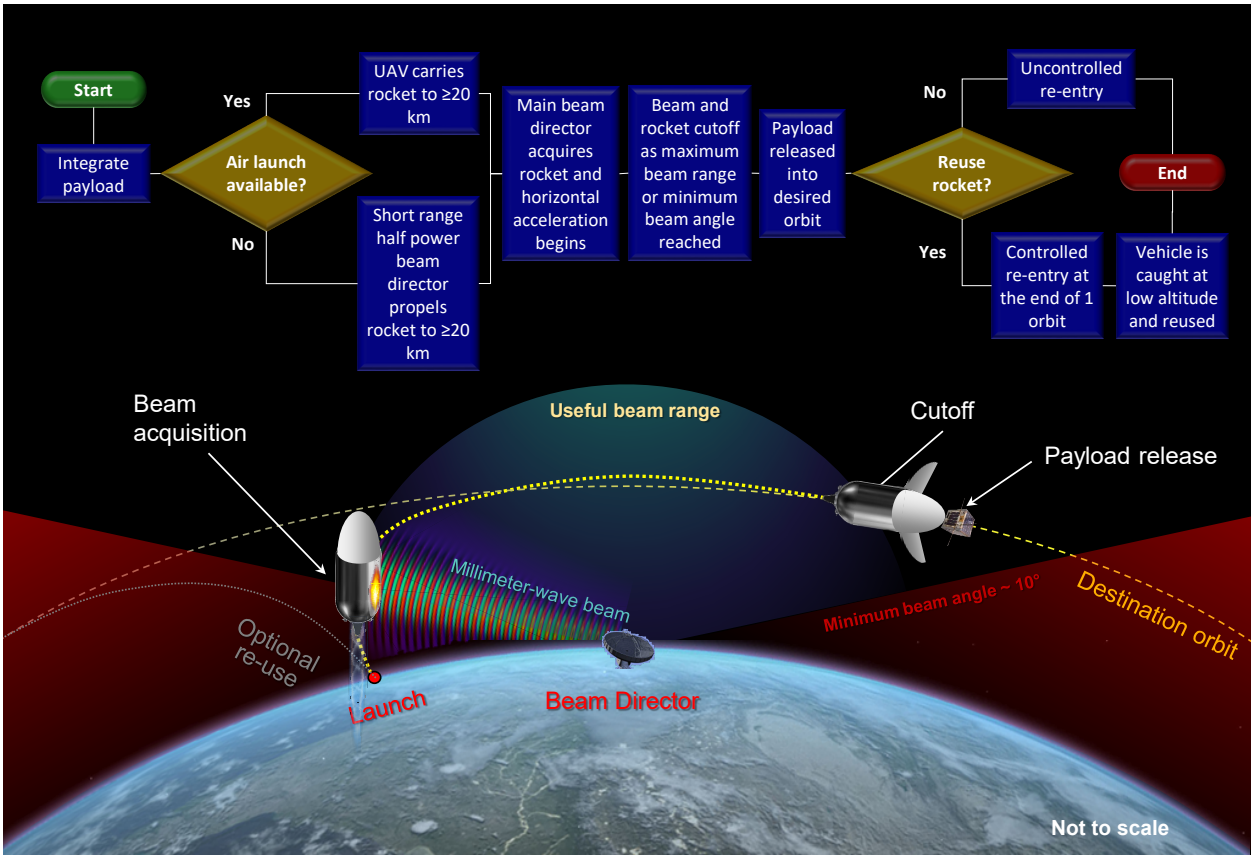

Figure 6 - Concept of operations for the millimeter-wave thermal rocket

The concept of operations for a millimeter-wave rocket is shown in Figure 6. Launch begins from the ground or from an unmanned aerial vehicle (UAV). Launch from the ground is the simplest case, but involves two beam directors; the first boosts the vehicle to >= 20 km altitude, and the second sustains acceleration until the vehicle reaches orbit. UAV-based launch increases the payload capacity of the rocket and enables a single beam director to cover the entire launch trajectory. Once acquired by the beam, the rocket ascends through its ascent trajectory to the desired orbit, and the heat exchanger faces in the general direction of the beam director throughout. The trajectory is optimized such that cutoff occurs before the beam reaches a minimum elevation of 10 degrees, below which propagation deteriorates. The payload is released, and the rocket re-enters after an orbit.

Initial rockets will be expendable, as these are simpler to implement than reusable rockets. In later reusable systems, a rocket configuration such as that shown in Figure 5 might re-enter as a shuttlecock, reusing its carbon plug nozzle as a nosecone and the payload doors as an air brake. If the ballistic coefficient is made low enough, and with the use of hot structures such as a titanium tank, conventional reentry heat shielding is not needed. A correspondingly low terminal velocity of around 30 m/s (70 miles per hour, or half the speed of a carrier landing) in the lower atmosphere makes it possible for UAVs to catch the falling rocket in a net made of silicon carbide fiber, for example, negating the need to carry landing gear all the way to orbit and back.

History shows that rocket families begin small and evolve larger, as is the case for the rocket families that define Figure 1. What is the smallest millimeter-wave thermal rocket that can be built? As rocket mass is reduced, payload fraction decreases until there is no payload and the rocket is barely able to carry itself to orbit. System analysis currently predicts that the millimeter-wave thermal rocket hits this zero-payload point at 30 kg wet mass. Similarly, it predicts that a LH_2 millimeter-wave thermal rocket can launch a 1 kg payload into low Earth orbit (LEO) starting with a wet mass of 50 kg. This corresponds to a SSTO payload fraction of 2% at nearly the smallest scale such a rocket can be built. As the scale is increased, the LH_2 SSTO payload fraction tends toward 15-25%, depending on assumptions and methods used.

The development cost of an initial nanosatellite or microsatellite launch system need not be justified by the demand for small launches; it is justified by reducing prices for heavier payloads as the rockets evolve to higher power. Like conventional rockets, payload cost decreases as payload capacity increases. Developing an initial 1 kg launcher is the cheapest way to retire technical risk, and as such it is a *technology push*.

The cost advantage of millimeter-wave thermal rockets is illustrated by the purple region in Figure 1 and varies between one and three orders of magnitude cheaper than conventional alternatives. History is used as a guide: The purple region is simply the blue region bounding conventional US rockets, but scaled appropriately and anchored on its left to a bottom-up cost estimate for the construction and launch of millimeter-wave thermal rockets with a 50-kg wet mass and 1-kg payload.

The cost advantage is estimated in a different way using the factors in Table 1. These factors are difficult to quantify, except for the ratio of payload to parasitic dry mass, which is informed by point designs and a comparative rocket equation model. Nevertheless, these factors represent the essence of the cost advantage for millimeter-wave thermal rockets. By multiplying the factors in Table 1, a millimeter-wave thermal rocket is predicted to be between 6x and 144x cheaper[l] than a conventional rocket of the same payload capacity.

Because the anticipated cost reduction is large and the feasibility and eventual performance has been characterized a decade ago, the work over the past six years has focused on minimizing the infrastructure cost of an initial system, as opposed to maximizing the performance of an eventual system. This focus on infrastructure cost begs the question: How low must the initial infrastructure cost be for a directed energy rocket to make economic sense?

[l] Depending on methodology, assumptions and scale.

	Baseline	Pessimistic	Nominal	Optimistic	
Maximum payload capacity	20	0.2	10	20	Metric tons to LEO
Market share served by millimeter-wave launch	0%	1%	50%	100%	
Ideal jet power per unit payload mass		3.0	1.0	0.3	MW/kg
Payload cost reduction factor		6	24	144	x
Expenditure on launch (excluding R&D)	125	124	65	1	$M/week
Expenditure on launch (excluding R&D)	130	129	68	1	$B over 20 years
Savings relative to baseline		1	62	129	$B over 20 years
Maximum initial cost (paid for by savings)		**1**	**6**	**22**	**$/Watt**

Table 2 - Spreadsheet to calculate beam director cost thresholds under varying assumptions of technology performance and market share. Input values are shown in green text with black background. Inflation effects are not included. Ideal jet power per unit payload mass is a range taken from values calculated for many propellants and heat exchanger temperatures. Cost reduction factors are from Table 1. Baseline expenditure on launch is from the GAO (GAO 2013).

Initial infrastructure cost is driven by the beam director cost, which itself is comprised of the cost of the millimeter-wave sources plus the cost of aperture, for example the dish shown in Figure 5. Initial infrastructure cost can be expressed in $/Watt[m] and is its most important figure of merit. The $/Watt value at which millimeter-wave launch becomes economically superior to present launch systems is calculated in Table 2 under various assumptions and over a payback time of 20 years[n].

In the baseline case of Table 2, the largest satellite being launched to LEO continues to be 20 tons and the expenditure on launch continues to be $125M/week (excluding R&D). This equates to a $130B expenditure over the 20-year period.

In the pessimistic case, a millimeter-wave rocket with a 200-kg payload capacity to LEO captures 1% of the total revenue for satellite launch. It has a relatively poor jet power per unit payload mass (though not the worst), and a relatively poor cost reduction factor. Consequently, its initial infrastructure needs to cost less than $2/Watt to save money over the period. Current estimates of beam director cost are $1-5/Watt at this scale, and further research is expected to lower this value and its associated uncertainty.

In the optimistic case, a family of millimeter-wave rockets capable of launching up to 20 tons to LEO captures 100% of the revenue for satellite launch, replacing traditional rockets altogether. It has a relatively good jet power per unit payload mass (though not the best) and a relatively good cost reduction factor. Consequently, the initial infrastructure needs to cost less than $22/Watt to save money over the period. Current estimates of beam director cost are $0.1-1/Watt at this scale.

In summary, the conventional rocket industry reached maturity many decades ago and accounts for $169M/week of US government expenditure. Hundreds of billions of dollars have been spent on researching and developing families of rockets and launching them. Directed energy launch was

[m] The Watts used here are Watts of ideal jet power produced by the rocket. One could also use Watts of transmitted power or Watts of 'wallplug' power, but these require additional efficiency factors to be included that vary with rocket size and add additional uncertainty.

[n] Because 20 years is the time horizon used by both the NASA Office of the Chief Technologist and the Air Force Office of the Chief Scientist for their technology roadmaps.

proposed almost 100 years ago by Tsiolkovsky himself, and one by one, the conditions needed for it to become economically superior have fallen into place: Lasers were invented. Gyrotrons were invented. The $/Watt for beam sources fell by orders of magnitude. Detailed proposals were made for pulsed laser rockets (1972), laser thermal rockets (1992), millimeter-wave thermal rockets (2002), and pulsed millimeter-wave rockets (2003). Of these, the laser and millimeter-wave thermal rocket engines outperform chemical engines in T/W and I_{sp}. And of these, millimeter-wave thermal rockets have the lowest initial infrastructure cost as measured in $/Watt. Assuming that the U.S. government is the only customer, simple cost-benefit analysis shows that the $/Watt is already low enough to recommend a changeover from chemical to millimeter-wave thermal rockets.

2 Frequently asked questions

What is the maximum payload size?
There is no maximum scale to the millimeter-wave thermal rocket. If a millimeter-wave rocket can launch a small satellite at 10x lower cost than conventional alternatives, then there is every reason that it will be scaled up to launch all payload classes, through 1 metric ton payloads and even above 100 ton payloads, if needed.

What is the maximum beam director size/power?
Due the physics of beam diffraction, beam directors become smaller as the rocket size (and payload capacity) increases. For these, the limiting factor is power density, or, depending on the way in which millimeter-wave sources are combined to form a single beam (§3.6.5), it can be spectral characteristics that limit the number of millimeter-wave sources per beam director. However, these limits are for a single beam director. Once one beam director has been built, there is no reason a second cannot be built and reuse the same spectrum. Both can then be trained on a single rocket designed for double the power, and due to efficiencies of scale, the rocket payload mass will more than double. Any number of beam directors can be trained on a single rocket because the beam from one beam director has no systematic phase relationship with the beam from any other. This means that their outputs add in the same way that overlapping spots from flashlights do.

What is the minimum beam director size/power?
Due the physics of beam diffraction, beam directors become larger as the rocket size (and payload capacity) decreases. Above a certain aperture size, it minimizes the overall cost to build more millimeter-wave sources and spill more energy than to further increase the beam director size. Curves for cost-minimized beam directors are plotted in §3.6.3, and it turns out that lighter rockets always result in a cheaper beam director.

How much power does it take?
10 MW of 'wall plug' power per kg of payload for the smallest rockets, falling to below 1 MW/kg for the heaviest rockets. This is because the payload fraction and transmission efficiency both improve as the rockets become heavier. The equations needed to make such an estimate are given in §3.3.1.1.

How much of the payload cost is for power?
Power costs $30-100 per kilogram of payload (see Table 4).

How is that much power generated?
The power needed by the thermal rocket engines is comparable with the power developed in

conventional rocket engines of the same thrust, though of course this power is generated on the ground for thermal rockets. Up to 2 GW can be obtained directly from the electrical grid for beam directors that are located near to high-capacity transmission lines, for example in California, and this is enough to launch a rocket with a payload of about 100 kg. This power would cost on the order of 10¢/kWh. For heavier payloads, on-site pulsed power is used. Several of the technologies used or being developed for grid energy storage, such as batteries and flywheels, are suitable for the beam director site. For these technologies, the amortized cost adds < 3¢/kWh to the electricity cost (Viswanathan, Kintner-Meyer et al. 2013). Capital cost is on the order of $1/Watt, whereas the capital cost of a millimeter-wave source (i.e., a gyrotron) including its power supply and supporting equipment is around $5/Watt. Costs will be reduced by further R&D and/or as production quantities increase.

Is plasmadynamic breakdown a problem?
At very high fluxes, the atmosphere breaks down into a plasma, and this type of flux limit was shown to be orders of magnitude greater than that needed for small satellite launchers (Parkin 2006c). It is possible to approach this limit with very heavy payload rockets, but this is not really a limit either, as it is always possible to flatten the rocket and increase the receiving area to keep the beam flux orders of magnitude below the breakdown threshold. Such a flattened rocket is shown in Figure 43.

How is the rocket and payload shielded from the beam?
By metal foil. The thickness of aluminum needed to prevent 99.9% of millimeter waves from penetrating to the other side is only 14 nm, as calculated in §3.5.3.6.1.1. Aluminum kitchen foil is 1000 times thicker and more than suffices for the MTLS project tests documented in §5.2.1. Non-line-of-sight millimeter waves do not affect the rocket payload electronics, LEDs, or cameras. For higher fluxes and longer durations operating in vacuum, we envisage that a roll-bonded metallic heat exchange loop like the roll-bonded evaporators used in home refrigerators will be used to keep metallic surfaces cool.

What if a bird/plane flies into the beam?
Beam directors are located at arid, high-altitude sites in controlled airspace where there are few birds. If a bird flew just above the beam director during operation, the power density it would experience is 1,000 times lower than at the rocket, which is well above the altitudes of birds and planes. The bird would initially experience a growing sensation of heat on its underside, somewhat like opening an oven door, and would flee, it is hoped, in a different direction. The vicinity of the beam is monitored by radar, particularly objects that can intercept it within the duration of an ascent trajectory (3-6 minutes). If something is about to enter the beam, it can dodge, dim, or douse until the obstacle is clear, or it could hand over to a nearby unobstructed beam director. Migrating birds can achieve remarkable altitudes, and the North American flyways are quite well documented. Research on bird radar systems (King 2013) has resulted in commercially available solutions that are capable of the kind of short-range tracking needed, such as the Merlin Avian Radar System offered by DeTect Inc.

What is the best propellant?
A simple comparative model based on the rocket equation (§3.2.1) was developed to estimate performance of a given dense propellant relative to a conventional baseline case (§3.2.3). Using this, a performance scoreboard has been compiled (§3.2.6). Ammonia and methane are at the top and exceed the performance of LH_2. Methane is of greatest interest because it is nontoxic and soot formed by its thermal decomposition can potentially be used as a millimeter-wave absorber to post-heat the

propellant to the melting point of carbon. Water ranks lower in the scoreboard but is still a viable propellant and directly absorbs millimeter-waves.

How hot does the heat exchanger need to be for the concept to be better than existing rockets / have a positive payload?

The dense propellant model (§3.2.1) predicts an economic advantage for ammonia and methane for flow exit temperatures above 1,500 K, for slush hydrogen above 2,000 K, and for water above 2,500 K (§3.2.6). More detailed estimates were made in the original system model (Parkin 2006c), which predicted that for LH_2 and 10 tons wet mass, 0%/10% payload fraction is reached at:

900/1660 K (CC tank, Fig. 2-16), 1400/2200 K (Ti tank, Fig. 2-15), 2000/2900 K (Al tank, Fig. 2-14)

For CH_4 and 10 tons wet mass, 0%/4% payload fraction is reached at (Parkin 2006a):

<1400/1800 K (CC tank, Fig. 3-5), 1400/2100 K (Ti tank, Fig. 3-6), 1600/2700 K (Al tank, Fig. 3-7)

Can sunlight be used to beam energy?

Not to launch rockets. Similar to laser or millimeter-wave beams, longer distances require larger dishes due to the effect of optical diffraction. Let us assume that we want to get most of the beam energy into a 1-meter diameter target at a distance of 350 km. If a laser with a top-hat beam profile is used at a wavelength of 500 nm (500 nm is the wavelength of peak emission of the sun), then 86% of the energy falls inside the target diameter when the diameter of the primary reflector on the ground is,

$$D_t = 2.44\,\lambda R / D_r$$

where $\lambda = 500{\times}10^{-9}$ m, $R = 350{\times}10^{3}$ m, $D_r = 1$ m. This yields a primary reflector diameter of $D_t = 43$ cm. So when a laser is shone onto a suitably shaped reflector that is 43 cm in diameter, reflected light from the whole reflector coherently adds at the position of a 1-meter target that is 350 km away. However, sunlight is very much less coherent as a light source than laser light. Sunlight reflected from one portion of the reflector is not systematically in phase with sunlight from almost anywhere else on the reflector, so it does not coherently add at any distance. That being said, there is some coherence in sunlight, therefore light reflected from one part of the reflector does coherently add with sunlight reflected from a small area around it. This area is known as the coherence area. For sunlight, the coherence area is measured to be $3.7{\times}10^{-3}$ mm^2 (Agarwal, Gbur et al. 2004), which is equivalent to a diameter of 70 microns. We can treat sunlight as we did laser light provided the reflector is smaller than this diameter. A reflector that is larger than this diameter can be thought of as an incoherent array of reflectors that are 70 microns in diameter.

So how far does a sunlight beam from a 70-micron diameter aperture go? Rearranging the same equation as before to yield R and using 70 microns as the diameter of the primary reflector, it is estimated that sunlight propagates for 57 meters before less than 86% of its energy falls within a 1 meter diameter spot. Alternately, using the equation above, the 70-micron beam spreads out over a 350-km distance to become a 6-km spot. 350 km was the altitude of the Znamya 2 Space Mirror, and its spot size (projected onto the Earth) was reported to be 5 km wide. Consequently, sunlight is unsuitable for long distance transmission to a small target like a rocket.

3 Analysis

3.1 Nomenclature

Units are those given in square brackets unless otherwise noted.

a	Acceleration [m/s^2]
A	Area [m^2]
c_v	Specific heat capacity at constant volume [J/kg]
c_p	Specific heat capacity at constant pressure [J/kg]
Δv	Change in velocity (of rocket) [m/s]
e	Internal energy
ε	Area expansion ratio (of nozzle) [-]
f	Fanning friction factor
g	Acceleration due to gravity (equal to 9.81 m/s^2 unless otherwise noted) [m/s^2]
G	Mass flow rate per unit area [kg/(m^2.s]
γ	Ratio of specific heats [-]
Γ	Circumference [m]
h	Specific enthalpy [J/kg]
I_{sp}	Specific impulse [s]
m	Mass [kg]
$\dot{m}$	Mass flow rate [kg/s]
M	Mach number [-]
m_{dry}	Mass of rocket without propellant (includes payload) [kg]
m_{para}	Parasitic dry mass. Equal to mass of rocket without propellant or payload [kg]
m_{wet}	Mass of rocket with propellant (includes payload) [kg]
μ	Bulk viscosity [Pa.s]
Nu	Nusselt number [-]
L/D	Length to diameter ratio [-]
$\mathcal{P}$	Power [W]
P	Pressure [Pa]
Pr	Prandtl number [-]
q	Heat flux [W/m^2]
r	Enthalpy recovery factor [-]
ρ	Density [kg/m^3]
s	Specific entropy [J/kg]
St	Stanton number [-]
t	Thickness (of heat exchanger channel wall) [m]
T	Temperature [K]
$\mathcal{T}$	Thrust [N]
τ	Shaft torque [N.m]
T/W	Thrust to weight ratio [-]
u	Velocity [m/s]
v	Specific volume [m^3/kg]
$\mathcal{W}$	Work done [J]
x	Lengthwise spatial coordinate (along tube) [m]
$\vec{x}$	Position vector [m]

3.1.1 Subscripts

e	Exhaust (of rocket nozzle)
eng	Propulsion subsystem (of rocket)
j	Jet (of rocket nozzle)
oth	Other (parts that do not fall under other rocket subsystems)
pay	Payload (of rocket)
pri	Primary reflector (of beam director)
pro	Propellant (of rocket)
t	Total conditions
$tank$	Tank(s)
w	Wall (of heat exchanger tube)

3.2 Sizing of low-altitude thermal rockets

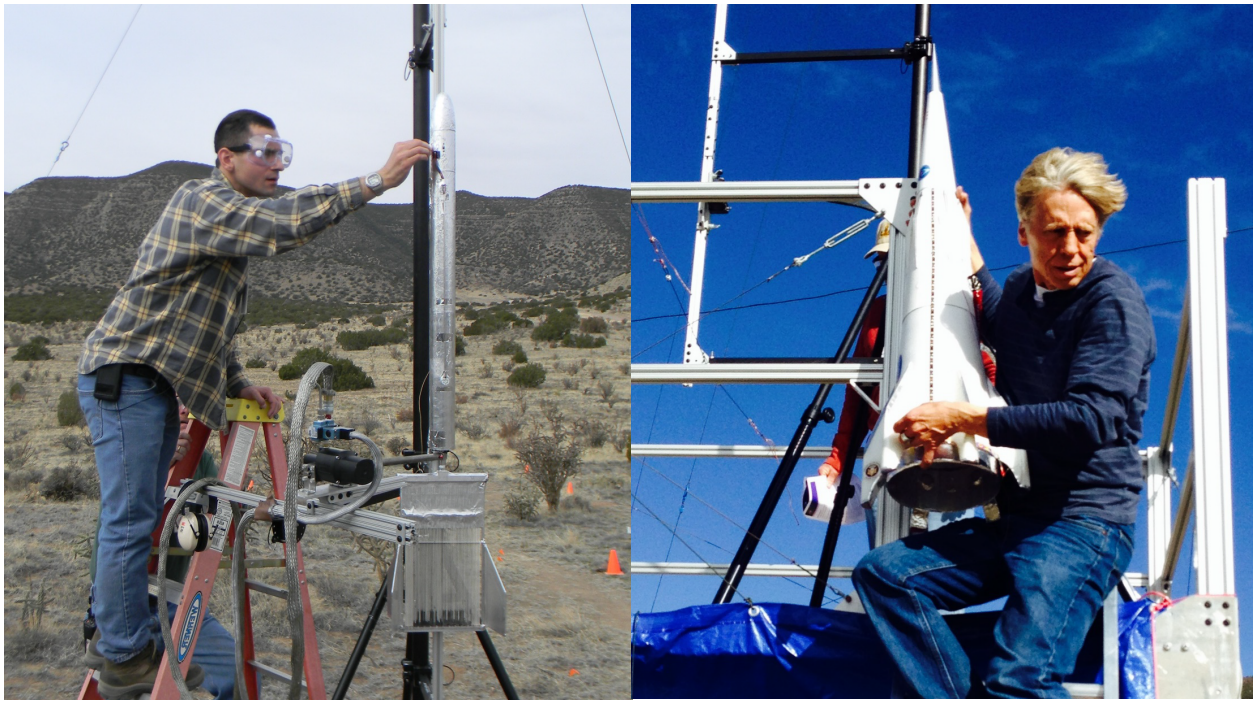

Figure 7 - Examples of low-altitude rockets are these developed for the MTLS project to demonstrate key technologies. Shown on the left is Alex Bruccoleri (Izentis) with a 'side illuminated' millimeter-wave thermal rocket and on the right is Leik Myrabo (Lightcraft Technologies Incorporated) with an 'axial illuminated' millimeter-wave thermal rocket.

Low-altitude thermal rockets, such as those shown in Figure 7, are low-cost, low-mass, low-power rockets whose purpose so far has been to test various technologies associated with thermal rockets more than to achieve particularly high-altitude or large velocity changes. As such, they can be scoped and designed without the rocket equation or trajectory equations.

The design process begins with an initial mass estimate, derived next. Components are then chosen, sized and designed to fit within this mass budget.

It is possible to relate rocket mass to key constraints in a simple way by starting with the equations describing an ideal jet. The jet power P_j in an ideal rocket exhaust is

$$P_j = \frac{1}{2}\dot{m}u_e^2, \qquad [1]$$

where $\dot{m}$ is the mass flow rate and u_e is the velocity of the jet, which is simply given by Earth gravitational acceleration (9.81 m/s^2) multiplied by the specific impulse in units of seconds:

$$u_e = gI_{sp}. \qquad [2]$$

Ignoring pressure effects, thrust T is given by

$$T = \dot{m}u_e. \qquad [3]$$

Equations [2] and [3] can be substituted into [1] and rearranged to yield,

$$T = \frac{2P_j}{gI_{sp}}, \qquad [4]$$

which shows that for a fixed power, thrust is maximized by minimizing the specific impulse.

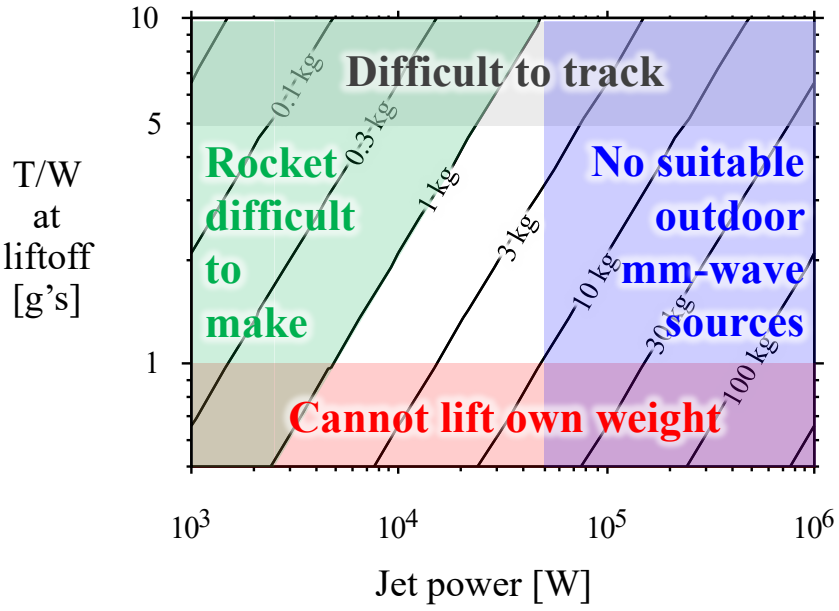

Figure 8 – Bounds on rocket mass given the constraints that: It must be built from model rocket parts where possible, use a 100-kW class beam source, be able to lift of the ground, but not accelerate so fast that it is hard to track with the beam. Contours of mass are plotted for a specific impulse of 100 seconds using equation [5]. An initial guess of 3 kg in this case places the rocket safely inside the white area even if the beam power that is converted to jet power turns out to be considerably less than 50 kW.

In Earth-to-orbit design, it is high I_{sp} that ensures the rocket makes it to orbit, and that it does so with maximal payload performance. For a small technology demonstrator rocket, it is high T that ensures that the rocket can lift off and reach the highest altitude possible using the power, propellant, and components that are available. Equation [4] shows that propellants with a terrible I_{sp} that would never make orbit can be an excellent choice for a low-altitude thermal rocket. The MTLS project used propellants like argon for this purpose.

By dividing equation [4] through by the weight $W = mg$ of the rocket and rearranging for mass yields,

$$m = \frac{2P_j}{(T/W)g^2 I_{sp}}. \qquad [5]$$

This equation is plotted in Figure 8 to show how thrust to weight ratio T/W and available power bound the rocket mass for a given I_{sp}. The I_{sp} used in the figure is 100 seconds, which corresponds to the kind of performance expected from argon at a stagnation temperature 1,100 K being expanded through a nozzle with an expansion ratio of 10.

3.3 Propellant selection for Earth-to-orbit thermal rockets

Performance estimates for the original H_2 millimeter-wave thermal rocket concept (Parkin and Culick 2003) were soon followed by similar performance estimates using methane as a propellant (Parkin 2006a). Dense propellants become relatively attractive when tank and propulsion weights dominate the dry mass or for reusable concepts where the areal density of conventional reentry heat shielding leads to a prohibitive thermal protection system mass if the propellant tank volume is relatively large.

Interest in dense propellants was renewed when scaling arguments made by Bruccoleri (Bruccoleri and Daniel 2009) led to the desire by one of us (Parkin) to make a very clear 'apples to apples' comparison. In August 2010, version 1.0 of a comparative model that is based on the rocket equation was derived by one of us (Parkin) in collaboration with David Murakami of NASA Ames. Using simple assumptions, it captures the leading order scaling of millimeter-wave rocket component masses for various propellants relative to a conventional baseline rocket.

3.3.1 The Simple Comparative Propellant Performance Model (SCPPM) version 1.2

The rocket equation is conventionally written

$$\frac{m_{wet}}{m_{dry}} = e^{\frac{\Delta v}{g I_{sp}}}. \qquad [6]$$

Introducing propellant mass,

$$m_{pro} = m_{wet} - m_{dry}, \qquad [7]$$

the rocket equation can be expressed as

$$\frac{m_{pro}}{m_{dry}} = e^{\frac{\Delta v}{g I_{sp}}} - 1. \qquad [8]$$

Hence, for two rockets of ***equal dry mass***,

$$\frac{m_{wet,2}}{m_{wet,1}} = \frac{e^{\frac{\Delta v}{g I_{sp,2}}}}{e^{\frac{\Delta v}{g I_{sp,1}}}}, \qquad [9]$$

$$\frac{m_{pro,2}}{m_{pro,1}} = \frac{e^{\frac{\Delta v}{g I_{sp,2}}} - 1}{e^{\frac{\Delta v}{g I_{sp,1}}} - 1}. \qquad [10]$$

Equations [9] and [10] can be used to show that *for a given dry mass*, an increase in I_{sp} produces a corresponding decrease in the amount of propellant needed, and hence a decrease in the wet mass of the rocket. However, these equations do not describe the way the rocket cost varies, or the influence of propellant density on cost. To do this, the ratios of payload to propellant mass and payload to parasitic dry mass need to be found, where parasitic dry mass is defined as

$$m_{para} \equiv m_{dry} - m_{pay} = m_{tank} + m_{eng} + m_{oth}. \quad [11]$$

Hence,

$$\frac{m_{pay}}{m_{para}} = \frac{1}{\frac{m_{dry}}{m_{pay}} - 1}. \quad [12]$$

To determine $\frac{m_{dry}}{m_{pay}}$, equation [11] is rearranged to be

$$\frac{m_{pay}}{m_{dry}} = 1 - \frac{m_{tank}}{m_{dry}} - \frac{m_{eng}}{m_{dry}} - \frac{m_{oth}}{m_{dry}}, \quad [13]$$

and the ratios are expanded to reflect scaling relative to a baseline rocket denoted by the subscript 1:

$$\frac{m_{pay,2}}{m_{dry}} = 1 - \frac{m_{tank,2}}{m_{tank,1}}\frac{m_{tank,1}}{m_{dry}} - \frac{m_{eng,2}}{m_{eng,1}}\frac{m_{eng,1}}{m_{dry}} - \frac{m_{oth,2}}{m_{oth,1}}\frac{m_{oth,1}}{m_{dry}}. \quad [14]$$

The ratios $\frac{m_{tank,1}}{m_{dry}}$, $\frac{m_{eng,1}}{m_{dry}}$, $\frac{m_{oth,1}}{m_{dry}}$ are constants of rocket 1, and expressions for the ratios $\frac{m_{tank,2}}{m_{tank,1}}$, $\frac{m_{eng,2}}{m_{eng,1}}$, and $\frac{m_{oth,2}}{m_{oth,1}}$ are derived next.

Starting with tank mass; for any given tank, neglecting inertial forces and gravity, we can conceptually exchange propellant 1 for a propellant 2 of a different density but at the same pressure, so that

$$\frac{m_{tank,2}}{m_{pro,2}} = \eta\frac{\rho_1}{\rho_2}\frac{m_{tank,1}}{m_{pro,1}}, \quad [15]$$

where η is an added structural efficiency factor to account for the inter-tank structure when comparing a monopropellant system to a bipropellant baseline. Substituting in equation [10],

$$\frac{m_{tank,2}}{m_{tank,1}} = \eta\frac{\rho_1}{\rho_2}\frac{e^{\frac{\Delta v}{gI_{sp,2}}} - 1}{e^{\frac{\Delta v}{gI_{sp,1}}} - 1}. \quad [16]$$

The engine is conceptualized to be a duct whose mass scales with the product of wall thickness and diameter, i.e., $m_{eng} \propto Dt$, so that

$$\frac{m_{eng,2}}{m_{eng,1}} = \frac{D_2 t_2}{D_1 t_1}. \quad [17]$$

As a cylindrical pressure vessel, the hoop stress $\sigma = \frac{PD}{2t}$ of the duct is chosen to be the same in both cases, and so is the pressure, giving

$$\frac{D_1}{t_1} = \frac{D_2}{t_2}. \quad [18]$$

Substituting [18] into [17] yields the simple result that the ratio of engine masses is equal to the ratio of duct areas,

$$\frac{m_{eng,2}}{m_{eng,1}} = \frac{D_2^2}{D_1^2} = \frac{A_2}{A_1}. \quad [19]$$

These duct areas can be expressed in terms of the mass flow rate

$$\dot{m} = \rho u A. \quad [20]$$

Making the additional approximation that at any given distance along the duct, the duct velocity u is the same in both cases, yields

$$\frac{m_{eng,2}}{m_{eng,1}} = \frac{A_2}{A_1} = \frac{\dot{m}_2}{\dot{m}_1}\frac{\rho_1}{\rho_2}. \quad [21]$$

To obtain an expression for the ratio of mass flow rates, vehicle acceleration (T/W) on liftoff is chosen to be equal for both vehicles,

$$\frac{T_2}{m_{wet,2}} = \frac{T_1}{m_{wet,1}}. \quad [22]$$

In the ideal case,

$$T = \dot{m} g I_{sp}, \quad [23]$$

so that

$$\frac{\dot{m}_2}{\dot{m}_1} = \frac{I_{sp,1}}{I_{sp,2}}\frac{m_{wet,2}}{m_{wet,1}}, \quad [24]$$

and hence [21] becomes

$$\frac{m_{eng,2}}{m_{eng,1}} = \frac{\rho_1}{\rho_2}\frac{I_{sp,1}}{I_{sp,2}}\frac{m_{wet,2}}{m_{wet,1}} = \frac{\rho_1}{\rho_2}\frac{I_{sp,1}}{I_{sp,2}}\frac{e^{\frac{\Delta v}{g I_{sp,2}}}}{e^{\frac{\Delta v}{g I_{sp,1}}}}. \quad [25]$$

In this simplistic model, other mass m_{oth} is assumed to scale in proportion to dry mass so that

$$\frac{m_{oth,2}}{m_{oth,1}} = 1. \quad [26]$$

Substituting [16], [25] and [26] into [14], and then in turn [14] into [12] yields,

$$\frac{m_{pay,2}}{m_{para,2}} = \frac{1}{\dfrac{1}{1-\eta\dfrac{\rho_1}{\rho_2}\dfrac{e^{\frac{\Delta v}{gI_{sp,2}}}-1}{e^{\frac{\Delta v}{gI_{sp,1}}}-1}\dfrac{m_{tank,1}}{m_{dry}}-\dfrac{\rho_1}{\rho_2}\dfrac{I_{sp,1}}{I_{sp,2}}\dfrac{e^{\frac{\Delta v}{gI_{sp,2}}}}{e^{\frac{\Delta v}{gI_{sp,1}}}}\dfrac{m_{eng,1}}{m_{dry}}-\dfrac{m_{oth,1}}{m_{dry}}}-1}. \quad [27]$$

3.3.1.1 Auxiliary equations

The T/W of the engine is calculated by combining equations [22] and [25] to produce,

$$\frac{(T/W)_2}{(T/W)_1} = \frac{\rho_2}{\rho_1}\frac{I_{sp,2}}{I_{sp,1}}. \quad [28]$$

The energy required per unit payload mass delivered to orbit, E/m_{pay}, can be deduced from the jet power per unit dry mass multiplied by the duration t for which this jet power is maintained:

$$\frac{E}{m_{pay}} = \frac{m_{dry}}{m_{pay}}\frac{P_j}{m_{dry}}t. \quad [29]$$

The duration can be expressed

$$t = \frac{m_{pro}}{\dot{m}}, \quad [30]$$

and equations [1] and [2] substituted to produce

$$\frac{E}{m_{pay}} = \frac{1}{2}g^2 I_{sp}^2 \frac{m_{pro}}{m_{dry}}\frac{m_{dry}}{m_{pay}}. \quad [31]$$

3.3.1.2 LOX/LH$_2$ baseline case

The baseline case for the remainder of this section is chosen to be a LOX/LH$_2$ single stage to orbit rocket with the following characteristics:

ΔV	10 km/s
Average propellant density	361.1 kg/m^2 (corresponds to oxidizer density of 1141 kg/m^2 and fuel density of 70.8 kg/m^2 with O/F ratio of 6)
Specific impulse	450 seconds
Inter-tank structure factor	0.75
η	(this implies that 25% of bipropellant tank mass is inter-tank structure)
$\frac{m_{oth}}{m_{dry}}$	0.14
$\frac{m_{eng}}{m_{dry}}$	0.2

$\frac{m_{pro}}{m_{tank}}$	15 (in combination with other figures in this table, this implies that $\frac{m_{tank}}{m_{dry}} = 0.57$)
Propulsion T/W	80 (for comparison, SSME was 73 using the technology of 40 years ago)
Dry mass cost	$250/kg

Table 3 - Baseline rocket for dense propellant examples and scoreboard

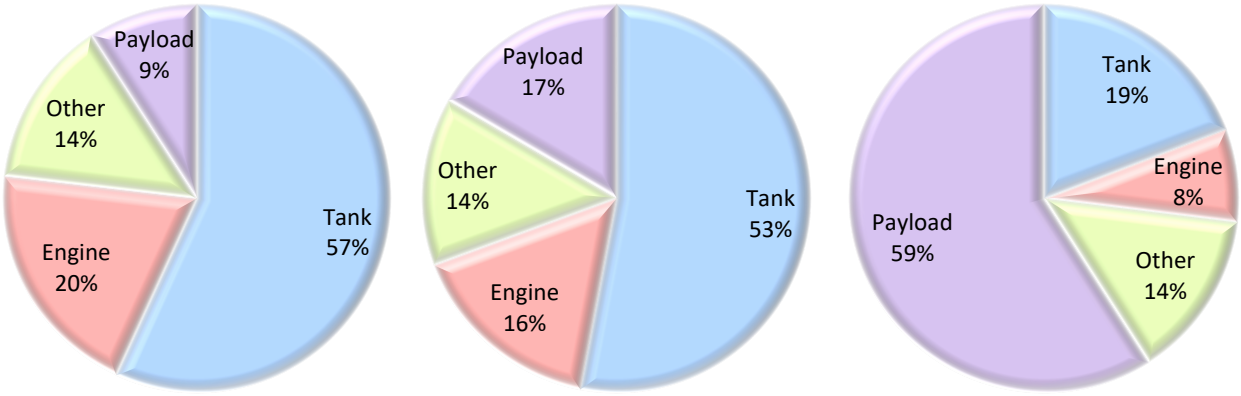

Figure 9 - Dry mass breakdown for LOX/LH_2 baseline rocket (left), LH_2 thermal rocket example (middle), CH_4 thermal rocket example (right)

3.3.1.3 LH_2 example

The ratio of specific impulses is

$$\frac{I_{sp,1}}{I_{sp,2}} = \frac{450\ seconds}{900\ seconds} = 0.5. \quad [32]$$

From [10],

$$\frac{m_{pro,2}}{m_{pro,1}} = 0.24. \quad [33]$$

From [9],

$$\frac{m_{wet,2}}{m_{wet,1}} = 0.32, \quad [34]$$

Hence from [24],

$$\frac{\dot{m}_2}{\dot{m}_1} = 0.16. \quad [35]$$

In other words, for a given dry mass, this LH_2 thermal rocket has a quarter of the propellant mass of the baseline case and hence a third the wet mass. The net effect of this plus the increased specific impulse gives a mass flow rate only 16% of the baseline case.

Nevertheless, LH_2 is not nearly as dense as LOX/LH_2, and this has comparative penalties. The ratio of average densities for a LOX/LH_2 baseline vs LH_2 alone is

$$\frac{\rho_1}{\rho_2} = \frac{361.1\ kg/m^2}{70.8\ kg/m^2} = 5.1. \quad [36]$$

From [16],

$$\frac{m_{tank,2}}{m_{tank,1}} = 0.93. \quad [37]$$

From [25],

$$\frac{m_{eng,2}}{m_{eng,1}} = 0.82. \quad [38]$$

In other words, for a given dry mass, the LH_2 thermal rocket tank mass is only 7% lighter than the baseline case, and would be heavier if not for the extra savings from not having an inter-tank structure. Also, the engine is only 18% lighter than the baseline case, despite having a much lower wet mass to accelerate. This implies that the T/W of the engine is far lower. This ratio can be calculated from equation [28],

$$\frac{(T/W)_2}{(T/W)_1} = 0.39. \quad [39]$$

Given a baseline T/W of 80, consistent with a state-of-the-art LOX/LH_2 engine, this means that the LH_2 thermal engine T/W would be 31. This is on the low side in Figure 2 but still better than the nuclear thermal systems, and high enough for SSTO applications.

From equation [14],

$$\frac{m_{pay,2}}{m_{dry}} = 0.17 \quad [40]$$

The impact of this performance on the relative dry masses of the subsystems are shown in the center of Figure 9. In particular, the payload has risen from 9% of the dry mass in the baseline case to 17% of the dry mass. More detailed system analyses yield a better performance than this, though with these more comprehensive analyses, the direct apples-to-apples relationship with a conventional baseline case is lost.

3.3.1.4 CH_4 example

The ratio of specific impulses is

$$\frac{I_{sp,1}}{I_{sp,2}} = \frac{450\ seconds}{560\ seconds} = 0.8. \quad [41]$$

From [10],

$$\frac{m_{pro,2}}{m_{pro,1}} = 0.60. \quad [42]$$

From [9],

$$\frac{m_{wet,2}}{m_{wet,1}} = 0.64, \quad [43]$$

Hence from [24],

$$\frac{\dot{m}_2}{\dot{m}_1} = 0.51. \quad [44]$$

In other words, for a given dry mass, the CH_4 thermal rocket has 60% of the propellant mass of the baseline case and 64% the wet mass. The net effect of this plus the increased specific impulse gives a mass flow rate only 51% of the baseline case.

CH_4 is denser than LOX/LH_2, as well as having a higher I_{sp}. The ratio of average densities for a LOX/LH_2 baseline vs CH_4 alone is

$$\frac{\rho_1}{\rho_2} = \frac{361.1\ kg/m^2}{480\ kg/m^2} = 0.75. \quad [45]$$

From [16], the combination of higher density, less propellant and having only a single tank makes the tank mass considerably less that the baseline case,

$$\frac{m_{tank,2}}{m_{tank,1}} = 0.34. \quad [46]$$

From [25], the engine is lighter because the rocket is lighter, the propellant is denser and because the propellant has a higher I_{sp},

$$\frac{m_{eng,2}}{m_{eng,1}} = 0.39. \quad [47]$$

From [28], the T/W is higher because the density and I_{sp} are both higher,

$$\frac{(T/W)_2}{(T/W)_1} = 1.65. \quad [48]$$

Given a baseline T/W of 80, consistent with a state-of-the-art LOX/LH_2 engine, this means that the CH_4 thermal engine T/W would be 132. This is close to the Merlin-1D T/W of 150 in Figure 2, yet at 560 seconds the specific impulse is higher than any chemical propellant, whereas the vacuum specific impulse of the Merlin 1-D engine is 340 seconds.

From equation [14],

$$\frac{m_{pay,2}}{m_{dry}} = 0.59 \quad [49]$$

The impact of this performance on the relative dry masses of the subsystems are shown in the right of Figure 9. The payload has risen from 9% of the dry mass in the baseline case to 59% of the dry mass, corresponding to over 14 times more payload per kilogram of parasitic dry mass. This places CH_4 ahead of LH_2 as a priority for more detailed system analyses.

In August 2010 as SCPPM v1.0 was under construction, a paper was published in which the thrust of solid rockets is augmented by beamed microwave heating of micron-sized alumina particles in the exhaust (Gimelshein, Gimelshein et al. 2009, Cornella, Ketsdever et al. 2010). This led one of us (Parkin) to realize that soot particles formed in the decomposition of methane could be used to absorb millimeter waves directly into a channel flow. For methane, granular carbon (soot) forms above about 700 K[o] and can, in principle, heat the surrounding hydrogen flow to 3,823 K, the melting point of carbon. In practice, carbothermic reduction and high-temperature millimeter-wave transparency severely limit the choice of tube materials and maximum temperatures. Aerodynamic windows are one potential way to avoid these limits, as is film cooling of the wall of a single large tube through which the methane or other hydrocarbon propellant flows. It has not been possible to investigate the absorption of soot and other species as part of the present work, but this remains a priority in the future.

3.3.1.5 Scoreboard

The purpose of the scoreboard is to rank new candidates for thermal rocket propellants relative to each other, and allow comparisons of several figures of merit. SCPPM v1.2 is used to compare the relative merits of many dense propellants relative to a baseline case. This scoreboard, shown on the next page in Table 4, will continually change as prices change, SCPPM evolves, and if the baseline case changes.

The propellants are ranked based on the cost reduction factor columns. In particular, the rows are ordered according to the lowest temperature at which the cost reduction factor is >=2.0. This is because any cost reduction lower than this is not of interest, but greater performance at greater temperature is. In cases where the cost reduction factor is the same between two propellants at a given temperature, precedence is given to the propellant with the highest cost reduction factor in the next highest temperature column.

[o] For example, CEA2 predicts methane to decompose to a granular carbon mole fraction of 0.2 when it is heated to 1,000 K at a pressure of 20 bars. The mole fractions for hydrogen and methane are both 0.4 under these conditions.

The CEA2 software (McBride and Gordon 2004) is used to provide estimates of specific impulse for a given total flow temperature just prior to nozzle expansion. Additional assumptions are total pressure of 20 bars just prior to nozzle expansion, a nozzle area expansion ratio of 100, and chemical composition of the flow is frozen at the throat. The relatively low pressure is the result of reduced concern about heat exchanger areal density following recent experiments and system analyses. Hence, a lower mass flow rate per unit area can be tolerated, which results in lower pressures and smaller pumps.

The scoreboard, shown in Table 4, currently ranks solid ammonia as the top propellant based on favorable economics (cost reduction factor column). Propellants that have the highest cost reduction factors also tend to have the lowest temperatures at which they become advantageous relative to the baseline. In the case of solid ammonia and methane, the model predicts that they are economically advantageous even at the relatively low temperature of 1,500 K.

Slush versions of methane, ethane and propane have only modestly lower performance and more conventional techniques of storage, transport and pumping. Slush hydrogen performance is relatively poor, and the model probably under-predicts the payload fraction and propulsion T/W: At 2500 K, the model predicts a payload fraction of 4% and T/W of 30. In comparison, the original system model (Parkin 2006b) predicts 10-22% payload fraction and a T/W of ~150 in Figs. 2-14, 2-15 and 2-16, depending on the tank material chosen. Water is also predicted to be a fair propellant, but only if the heat exchanger can heat it to 2,500 K or more. Note that its relative density is listed as 2.77 in the table because it is 2.77 times denser than the LOX/LH_2 baseline density of 361.1 kg/m^2.

The cost of dry mass still is the dominant cost of rockets using the top-rated propellants. It is 3-5x the energy cost per kg of rocket dry mass. The cost of the propellants themselves is very low, typically 10x lower than the energy cost.

Propellant	Phase	Temperature [K]	Density [kg/m^3]	Relative density	Price [$/kg]	CEA2 vacuum I_{sp} [s]					Engine T/W					Payload/wet mass [%]					Propellant cost/payload mass [$/kg]					Energy cost/payload mass [$/kg]					Parasitic dry mass cost/payload mass [$/kg]					Total cost/payload mass [$/kg]					Cost reduction factor				
						1,500 K	2,000 K	2,500 K	3,000 K	4,000 K	1,500 K	2,000 K	2,500 K	3,000 K	4,000 K	1,500 K	2,000 K	2,500 K	3,000 K	4,000 K	1,500 K	2,000 K	2,500 K	3,000 K	4,000 K	1,500 K	2,000 K	2,500 K	3,000 K	4,000 K	1,500 K	2,000 K	2,500 K	3,000 K	4,000 K	1,500 K	2,000 K	2,500 K	3,000 K	4,000 K	1,500 K	2,000 K	2,500 K	3,000 K	4,000 K
NH_3 (ammonia)	s		817	2.26	0.7	331	376	428	480	588	132	151	171	192	235	1	3	5	7	13	122	26	13	8	5	249	69	45	36	30	1798	402	216	151	99	2169	498	274	195	134	1.2	5.1	9.2	12.9	18.8
CH_4 (methane)	s		522	1.45	0.2	376	433	491	570	662	96	111	126	146	169	1	4	6	10	15	26	5	3	2	1	232	64	44	35	31	1938	422	238	154	114	2196	492	285	191	146	1.1	5.1	8.8	13.2	17.2
C_2H_6 (ethane)	l+s	90	652	1.81	0.2	341	394	448	518	605	109	126	143	165	193	0	3	5	9	13	127	7	3	2	1	1070	74	47	36	31	8855	480	246	155	111	10051	561	296	193	144	0.3	4.5	8.5	13.0	17.5
CH_4 (methane)	l+s		482	1.33	0.2	376	433	491	570	662	89	102	116	134	156	0	3	6	10	14	57	6	3	2	1	506	72	46	36	32	4523	504	267	168	122	5086	582	317	206	155	0.5	4.3	8.0	12.2	16.3
C_3H_8 (propane)	l+s	91.5	727	2.01	0.5	327	379	431	497	583	116	135	153	177	208		2	5	8	12		21	10	5	3		79	48	36	31		497	247	155	109		597	304	196	144		4.2	8.3	12.8	17.5
NH_4BH_4 (ammonium borohydride)	s	250	642	1.78	9.6	360	422	483	637	760	113	133	152	200	239	1	4	7	14	20	985	228	123	54	36	178	56	40	30	29	1352	331	193	104	82	2514	615	357	188	146	1.0	4.1	7.1	13.4	17.2
$NaBH_4$ (sodium borohydride)	s		1070	2.96	2.5	303	338	400	440	569	159	177	210	231	298	0	2	4	6	12	828	143	53	36	17	407	87	45	37	29	2721	487	197	145	87	3956	717	295	219	133	0.6	3.5	8.5	11.5	18.9
NH_3BH_3 (ammonia borane)	s		780	2.16	9.0	329	386	441	588	693	126	147	168	225	265	0	3	5	13	17	2465	294	149	59	40	397	65	43	30	29	2997	377	206	102	81	5859	736	398	192	150	0.4	3.4	6.3	13.1	16.8
N_2H_4 (hydrazine)	l		1005	2.78	2.5	295	337	383	429	524	145	166	188	211	258		1	3	6	10		165	68	41	21		100	53	40	31		590	259	168	104		856	380	249	156		2.9	6.6	10.1	16.1
CH_4 (methane or LNG)	l	NBP	415	1.15	0.2	376	433	491	570	662	77	88	100	116	135		2	5	9	14		8	4	2	1		97	53	39	33		766	341	199	139		871	398	240	174		2.9	6.3	10.5	14.5
C_2H_6 (ethane)	l	NBP	546	1.51	0.2	341	394	448	518	605	91	106	120	139	162		2	4	8	12		9	4	2	1		105	54	39	33		780	325	189	129		894	382	230	163		2.8	6.6	11.0	15.5
NH_3 (ammonia)	l	NBP	619	1.71	0.7	331	376	428	480	588	100	114	130	146	178		2	4	7	12		44	16	10	5		115	56	41	32		834	328	206	123		992	400	257	160		2.5	6.3	9.8	15.7
C_3H_8 (propane)	l	231	581	1.61	0.5	327	379	431	497	583	93	108	123	142	166		1	4	7	11		34	12	6	4		130	58	40	33		981	354	199	132		1145	423	245	169		2.2	6.0	10.3	14.9
$C_{12}H_{24}$ (RP-1)	l		820	2.27	1.0	294	342	391	449	612	118	137	157	180	246		1	3	6	14		90	29	15	6		141	58	41	29		952	320	183	93		1182	407	238	128		2.1	6.2	10.6	19.7
C_4H_{10} (butane)	l		600	1.66	0.6	319	371	422	486	571	94	109	124	143	168		1	4	7	11		49	15	8	5		152	61	41	33		1160	374	205	134		1361	450	254	172		1.9	5.6	9.9	14.7
CH_3OH (methanol)	l	293	792	2.19	0.4	333	337	383	429	524	129	131	149	166	203	1	1	3	5	10	62	45	12	6	3	262	195	66	45	33	1922	1395	384	223	126	2246	1635	462	274	162	1.1	1.5	5.5	9.2	15.6
AlH_3 (aluminum hydride)	s		1486	4.11	3.0	252	288	327	402	462	183	210	238	292	337		1	2	5	8		562	147	54	34		208	70	39	32		1151	319	137	99		1921	537	230	165		1.3	4.7	10.9	15.3
KBH_4 (potassium borohydride)	s		1110	3.07	1.5	248	279	334	369	477	135	152	182	201	259			2	3	8			90	46	16			89	55	33			493	264	116			672	365	166			3.7	6.9	15.2
H_2O	l		1000	2.77	0.0	243	289	332	375	478	119	142	163	184	234			1	3	8			0.08	0.03	0.01			113	57	34			682	286	126			795	343	160			3.2	7.3	15.7
H_2	l+s		85	0.24	1.7	649	769	876	985	1214	27	32	36	41	51		2	8	13	22		62	15	9	4		289	92	66	51		3054	773	446	246		3404	881	520	302		0.7	2.9	4.8	8.3
NaH	s		1390	3.85	4.2	233	285	308	336	380	158	194	210	229	259		0	1	2	4		1532	364	183	96		400	111	66	45		2392	583	306	175		4324	1059	555	315		0.6	2.4	4.5	8.0
Li	s		534	1.48	65.0			490	518	570			128	136	149			6	8	10			883	710	519			43	39	35			233	194	151			1160	943	705			2.2	2.7	3.6
H_2	l	NBP	71	0.20	1.7	649	769	876	985	1214	23	27	30	34	42			4	9	19			31	12	5			187	91	60			1820	717	329			2038	820	394			1.2	3.1	6.4
Li_3AlH_6	s		1130	3.13	100.0		416	456	552	559		230	253	305	310		5	7	12	12		1742	1254	722	697		40	35	29	29		162	126	88	86		1944	1415	839	813		1.3	1.8	3.0	3.1
H_2O_2 (hydrogen peroxide, HTP)	l		1463	4.05	9.9	213	252	289	325	407	153	181	207	233	292			1	2	5			1885	519	171			212	74	38			1186	344	134			3283	936	344			0.8	2.7	7.3
LiH	s		820	2.27	100.0		420	481	541	660		169	193	217	265		5	8	10	16		1984	1171	812	491		47	36	32	29		231	149	114	84		2262	1356	958	604		1.1	1.9	2.6	4.2
B_2H_6 (diborane)	l		482	1.33	92.8	352	413	518	563	692	83	97	122	133	163		2	7	10	16		4019	1076	803	452		99	42	37	31		750	221	173	113		4867	1338	1012	596		0.5	1.9	2.5	4.2
$Be(BH_4)_2$ (beryllium borohydride)	s		609	1.69	244.4	349	415	507	596	737	104	124	151	178	220	0	3	8	12	19	109672	6783	2696	1646	986	730	64	38	32	29	6133	400	177	121	87	116534	7247	2911	1799	1103	0.0	0.3	0.9	1.4	2.3
$LiBH_4$ (lithium borohydride)	s		666	1.84	300.0		470	537	582	747		153	175	190	244		6	10	12	19		4200	2655	2098	1158			41	34	32	29		201	139	118	82		4442	2829	2247	1268		0.6	0.9	1.1	2.0
$Al(BH_4)_3$ (aluminum borohydride)	l		787	2.18	244.4	314	366	453	525	644	121	141	175	203	248		2	6	10	15		11555	3621	2190	1282			85	41	33	29		530	186	126	89		12170	3847	2349	1400		0.2	0.7	1.1	1.8
He	l		145	0.40	5.0	381	440	492	539	623	27	31	35	38	44					3					139				144					1425					1708						1.5
$LiAlH_4$ (LAH)	s		917	2.54	180.0		357	393	484	511		160	177	217	229		2	4	8	9		8289	4535	1990	1680		78	52	35	33		453	260	132	117		8821	4847	2157	1829		0.3	0.5	1.2	1.4
BeH_2	s		650	1.80	745.0	339	412	461	550	671	108	131	147	175	214	0	3	6	10	16	1410922	19876	11407	6175	3672	2907	61	44	34	30	24350	365	222	135	95	1438179	20301	11672	6344	3797	0.0	0.1	0.2	0.4	0.7
SiH_4 (silane)	l	NBP	556	1.54	300.0	262	339	371	409	494	71	92	101	111	135			1	3	7			34940	10495	3815			214	78	42			1742	538	214			36895	11111	4071				0.1	0.2	0.6
MgH_2	s		1450	4.02	630.1	244	335	357	357	435	173	238	254	253	309		2	3	3	7		27157	18990	19180	8642		65	51	52	35		290	211	213	114		27511	19252	19445	8791		0.1	0.1	0.1	0.3
N_2	l		808	2.24	0.5	180	211	238	263	306	71	83	94	104	121																														
CO_2	l		770	2.13		167	196	223	251	312	63	74	84	95	118																														
Ne	l		1207	3.34		170	196	219	240	277	100	116	130	142	164																														
Ar	l		1400	3.88		121	139	156	171	197	83	96	107	117	135																														
I_2 (iodine)	s		4933	13.66		86	107	114	120	131	207	258	275	289	318																														

Table 4 - Scoreboard of dense propellant performance. Estimates are derived from the baseline case in Table 3 using SCPPM 1.2. I_{sp} is estimated using the CEA2 software (McBride and Gordon 2004) with a chamber pressure of 20 bar and nozzle expansion ratio of 100. The chemical composition of the flow is frozen at the nozzle throat, except for I_{sp} values in blue font, where the solution fails without full equilibrium flow, usually when solid particulates in the exhaust fall below software-allowed temperature limits. I_{sp} values in pink font have a reduced expansion ratio to make solution possible, usually as flow constituents fall below temperature limits. Propellant prices are based on bulk internet prices from various sources, values in blue font are estimates based on constituent chemicals. Energy cost is based on $0.1/kWh and 10% 'wall plug' to jet efficiency.

3.3.1.6 Single stage performance variation with ΔV

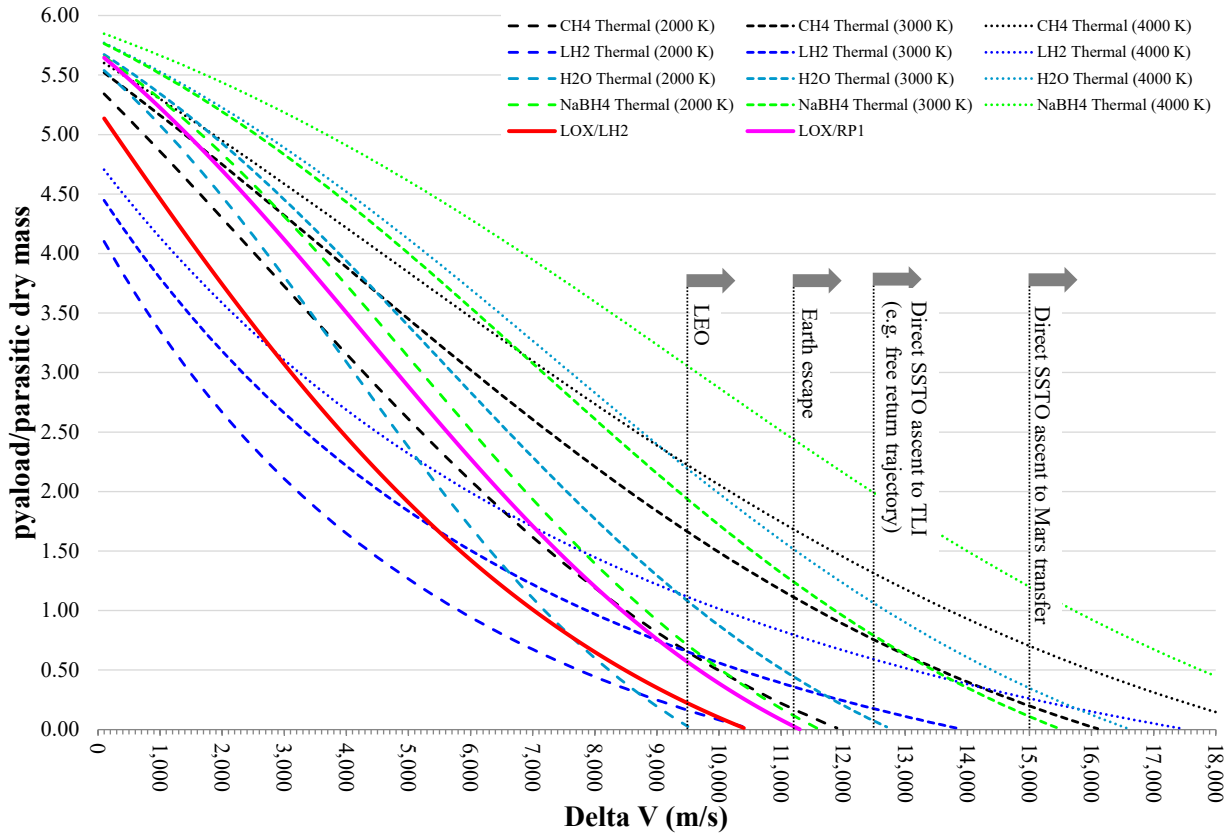

Figure 10 - Ratio of payload mass to parasitic dry mass as a function of ΔV required of the single stage rocket. Parasitic dry mass is defined here as the dry mass minus the payload mass.

SCCPM v1.2 describes how single stage rocket performance varies with mission ΔV, as shown in Figure 10. For low ΔV missions of 3 km/sec, corresponding to a sub-orbital mission with a range of perhaps 2,000 km, a LOX/LH_2 rocket is predicted to have a ratio of payload to parasitic dry mass of 3.1. This is the same as a LH_2 thermal rocket whose propellant is heated to 4,000 K, far above the temperatures anticipated for the first thermal rockets. Water and methane have a greater ratio of payload to parasitic dry mass of 3.7 if they are heated to only 2,000 K. However, a conventional LOX/RP-1 propellant has a ratio of payload to parasitic dry mass of 4.1. This is exceeded by a sodium borohydride propellant, which has a ratio of payload to parasitic dry mass of 4.3, 4.8 and 5.2 if it can be heated to 2,000 K, 3,000 K, or 4000 K respectively. However, once costs are taken into account, the economic performance of sodium borohydride is reduced to nearly the same as methane, as seen in Figure 11 and Figure 12.

For a higher ΔV mission of 11 km/sec, specific impulse has a greater effect on mission performance than propellant density but is still not the decisive factor. SSTO LOX/LH_2 rockets cannot achieve 11 km/sec under the assumptions of the SCCPM v1.2 model, and LOX/RP1 achieves a ratio of payload to parasitic dry mass of only 0.1. In comparison, a methane thermal rocket whose propellant is heated to 2,000 K has double the ratio of payload to parasitic dry mass (0.2), and this increases to 12 times greater (1.2) at 3,000 K. This factor rises to 14 once costs are taken into account in Figure 11.

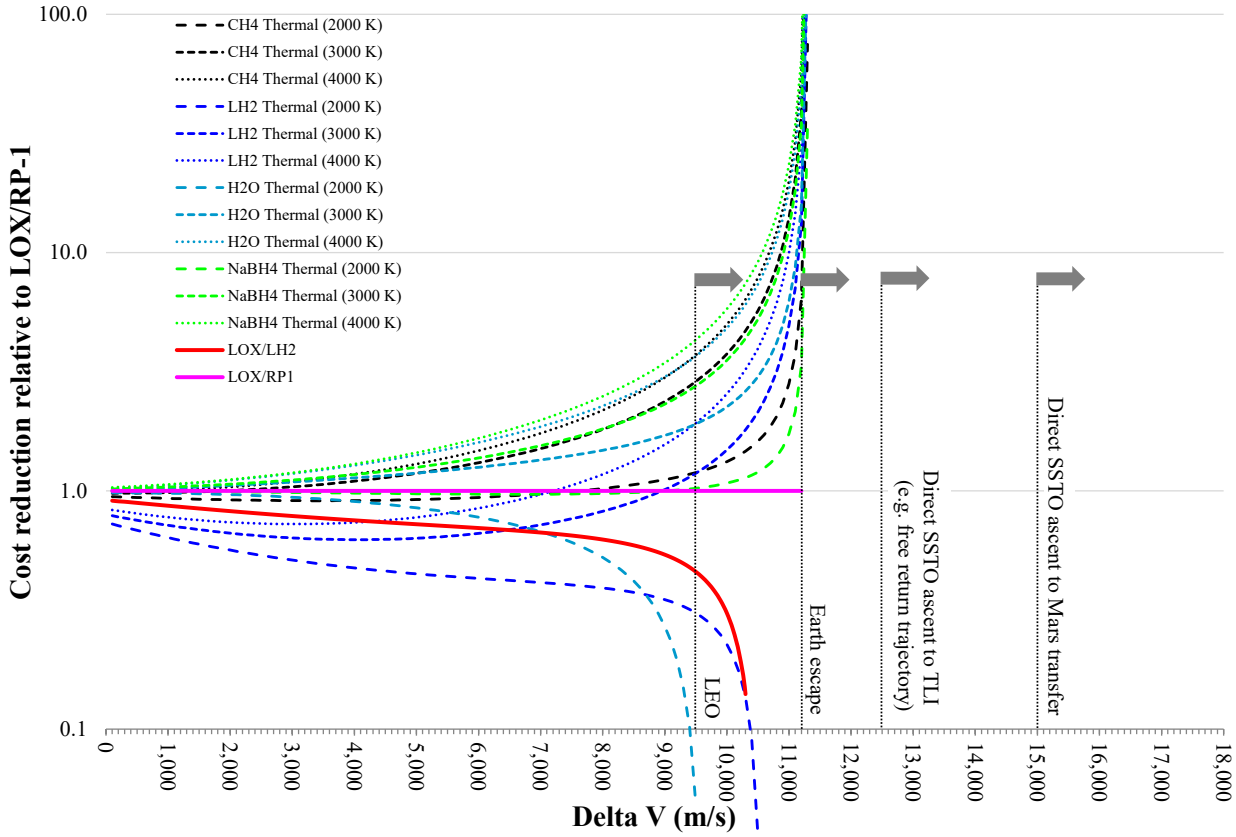

Figure 11 - Ratio of thermal rocket payload cost per unit mass to that of a LOX/RP-1 rocket of the same ΔV, as a function of ΔV required of the single stage rocket.

The cost reduction factors are large for the ΔV of 11 km/sec because LOX/RP1 approaches the limit of its performance, as seen in Figure 11. The exact ΔV at which LOX/RP1 or LOX/LH_2 reaches zero payload is uncertain, as is the cost reduction factor in that range. In addition, the traditional way to extend the ΔV performance of propellants is to add rocket stages. Multistage conventional and thermal rockets are outside the scope of this initial work, but planned for the future, so that performances can be compared. It is difficult to quantify the added cost of rocket staging, and even more so in a concise way. To maintain the apples-to-apples comparison philosophy of SCPPM v1.2, it may be best to compare multistage conventional rockets with thermal rockets having the same number of stages. Any other kind of comparison starts to involve arbitrary factors and might more convincingly be made on the basis of detailed point designs instead.

Figure 11 also shows that despite water being essentially free, this does not make the rocket cheaper unless the water can be heated to 3,000 K or above. At 2,000 K, water underperforms LOX/RP-1, as does LOX/LH_2, which is surprising. Similarly, LH_2 only begins to make sense as a propellant at orbital velocities up to 17.5 km/s. Only methane or sodium borohydride can propel a rocket from the ground to more than 17.5 km/s, but they cannot reach the solar system escape velocity of 42 km/s, at least in a single stage.

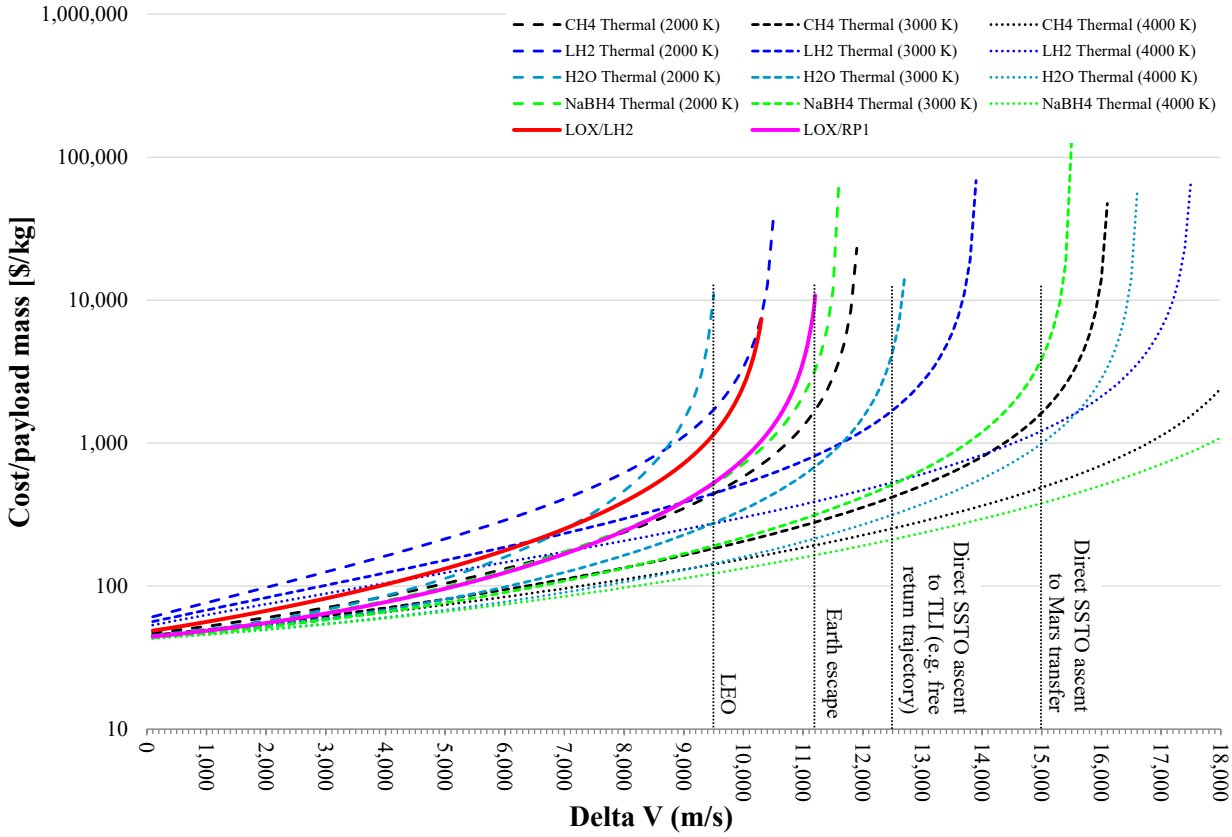

Figure 12 – Rocket cost per unit payload mass as a function of ΔV required of the single stage rocket.

Thermal rockets make possible a five-day trip around the Moon embarking from the ground and returning to the ground, all in the same single stage vehicle, as implied by Figure 12. The cost reduction afforded by thermal propulsion might enable a person to do this for the cost of a house, or if the rocket production volume is large, the cost of a car. If a heat exchanger can be built that heats methane to 3,000 K or above, then single-stage-to-Mars missions also become possible.

The conclusion we draw from varying the ΔV is that the comparative advantage of single stage thermal rockets relative to single stage LOX/LH_2 or LOX/RP1 rockets lies with Earth-to-orbit and long-range suborbital transport, as opposed to short-range suborbital rockets. This is not to say that short-range suborbital rockets would not benefit from switching to thermal propulsion, but the cost reduction factor would not merit the investment unless the quantity of rockets needed was very large. For long-range suborbital missions and the Earth-to-orbit mission, the comparative advantage of thermal propulsion is substantial and increases as the ΔV of the mission increases.

3.4 Earth-to-orbit system model

The purpose of the Earth-to-orbit system model is to numerically represent every relevant aspect of the millimeter-wave thermal launch system and integrate it into a single self-consistent model. This model is used to investigate system-level tradeoffs, perform sensitivity analyses, and to produce performance estimates of higher detail and accuracy than is possible using heuristic methods such as those in §3.3.1.

	Version 1.0	**Version 2.0**	**Version 3.0**
Dates	Jan. 2002-Aug. 2008	Sep. 2008-Mar. 2012	Apr. 2012-present
Used for calculations in publications	(Parkin and Culick 2003, Parkin, DiDomenico et al. 2003, Parkin 2006a, Parkin 2006c, Parkin 2008)	(Parkin, Mikula et al. 2014b, Parkin, Mikula et al. 2014a)	(Lambot, Myrabo et al. 2014a, Lambot, Myrabo et al. 2014b)
Number of variables	O(100) in 2002 O(500) in 2006	O(5,000) in 2010	22,000 in 2015
Architecture	Procedural (4th generation language)	Forward-chaining inference via local propagation (5th generation language)	Forward-chaining inference via local propagation (5th generation language)
Principal language	LabVIEW	MATLAB	C++
Auxiliary software	MATLAB C++ FemLab (now Comsol)	RefProp CEA2	Gnuplot RefProp (uses data files)
Equation of state	Perfect gas	Helmholtz	Helmholtz
Propellants	H_2, CH_4	H_2, He, CH_4, C_3H_8, N_2H_4	H_2, He, N_2, Ar, CO_2, H_2O
Reason(s) discontinued	Superseded by inference engine approach	Prototype only Too slow	

Table 5 – Versions of the Earth-to-orbit system model

To date, three major system models have been written to represent the millimeter-wave thermal rocket, and these are characterized in Table 5. The original system model (Version 1.0) of a decade ago was used to produce the first ascent trajectories for a millimeter-wave thermal rocket and to perform simple local trajectory optimization via a Nelder-Mead simplex method. It was used to integrate heat exchanger channel flows. For a given rocket wet mass, it would automatically vary specific impulse to produce curves of payload fraction, subsystem masses, temperatures and pressures. In essence, these were the first point designs and sensitivity analyses. However, the curves it produced were for a fixed assumed ΔV, and the ascent trajectory model was not recalculated for each data point, nor was the heat exchanger channel flow model integrated with the ascent trajectory. In addition, the perfect gas assumption prevented the heat exchanger channel flow being integrated back to the turbopump.

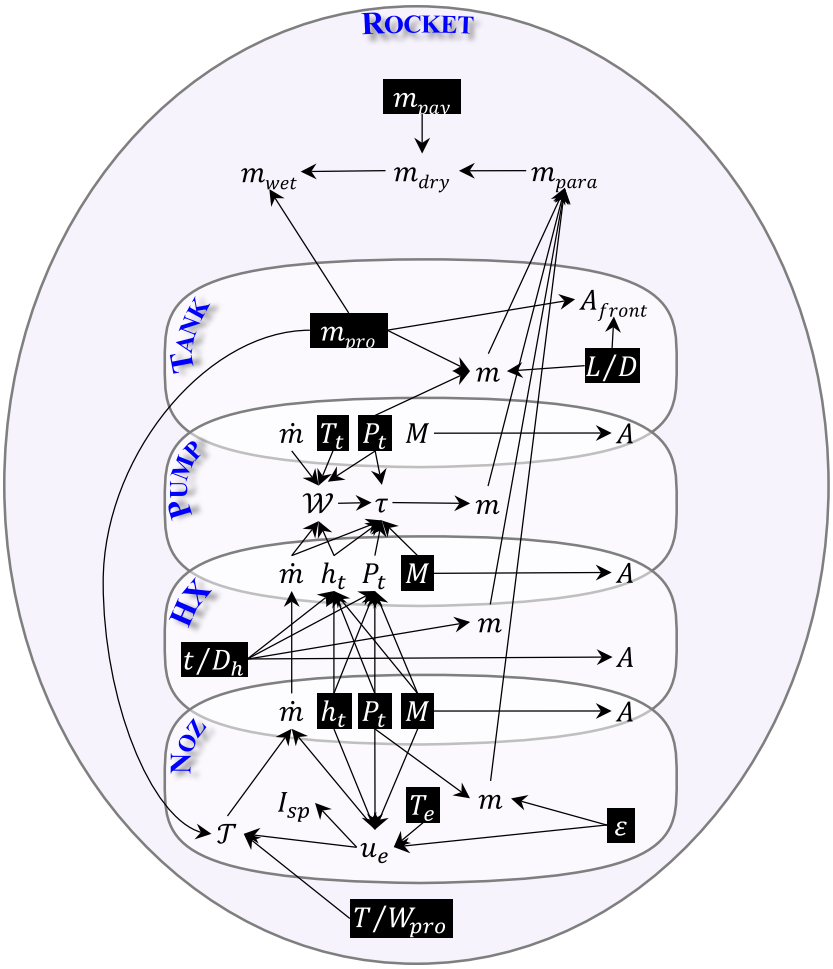

Figure 13 – Euler diagram combined with directed acylic graph showing the top-level propagation of information through the system model. User-defined variables are shown with black backgrounds. Only selected variables and relations are shown.

Version 2.0 of the system model represents the synthesis of artificial intelligence with rocket science, to the best of our knowledge for the first time[p]. A forward-chaining inference engine has been written that, rather than forming the basis of an artificial intelligence system, is instead used to form the basis of a millimeter-wave launch system. The knowledge base of the inference engine is the large number of equations and variables that describe the rocket, beam director and associated ascent trajectories.

As each known value is specified, the inference engine uses its knowledge base to infer everything it can from the new value in combination with everything that was specified or inferred before. In this way, a single specified values cascades into an avalanche of inferred values until every aspect of the launch system is quantified.

Version 1.0 of the system model is written in a 4th generation language based on functional composition, so the user must specify a solution procedure to solve the problem. This is no longer the case for

[p] A similar inference engine has recently been written to assist in the design of synthetic aperture radars (Holzrichter 2012)

version 2.0 of the system model and above, as the solution procedure is implied by the user's choice of independent variables and arises automatically from the inference process.

An example of the solution procedure of the millimeter-wave thermal rocket is shown in Figure 13. The particular combination of input variables implies the direction of the arrows in the diagram. As the system model has evolved over the years, the choice of independent variables has changed. Sometimes an independent variable is changed to eliminate an iteration, thereby reducing computational complexity. At other times, an independent variable is changed because the understanding of which variables are the true constraints that drive the design has changed.

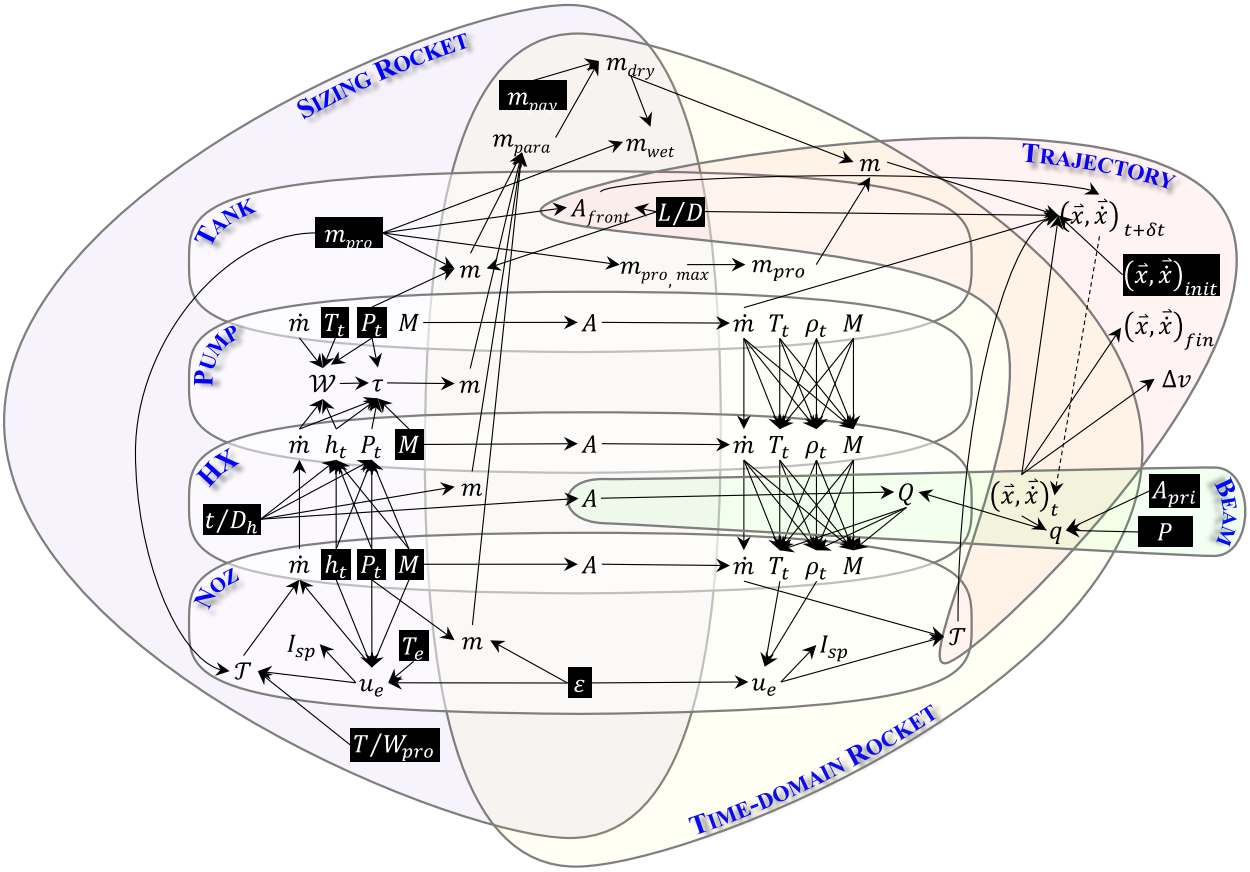

Figure 14 – Euler diagram combined with directed acyclic graph showing the top-level propagation of information through the system model. User-defined variables are shown with black backgrounds. Only selected variables and relations are shown. There are 22,000 variables in the system model as of July 2015.

The automation made possible by the inference engine enables us to drive the same model with different variables at different times without having to rewrite code[q]. In version 3.0 of the system

[q] For complex objects, relations are often missed. Missing relations constitute an incomplete description of the problem and cause numerical inconsistency that can be usually be detected automatically. In gross cases, no numerical inconsistency is detected and the error is deduced by the user when a solution requires more independent variables to be specified than expected. This is debugging; once simple errors are precluded, the remainder of errors are higher-level and often conceptual. Fixing errors becomes fixing one's concept of the problem. There is a great deal of room to automate and support the user in debugging their models in future inference engine versions.

model, shown in Figure 14, the rocket object of Figure 13 is used twice, but in different ways. On the left, an instance of the rocket is created for sizing components. On the right, an instance is created for simulating the time-dependent response of the flow path as the tank empties and the beam intensity varies over the heat exchanger as the rocket travels downrange.

The variables joining the two objects are the invariants, shown in the overlapping region. Inside these rocket objects, when flow path subsystems overlap, this represents an interface between them. For example, the overlap of the tank and pump subsystem represents the outlet of the tank and the inlet of the pump. Returning to the 'sizing rocket' object on the left, propellant properties specified in the flow path infer some invariants, the materials and geometry of the flow path, from the tank through to the nozzle. These invariants are then used to infer the propellant properties for the flow path of the time-dependent rocket on the right. Thus, the same object is used twice and joined to itself, but each side has a different solution procedure.

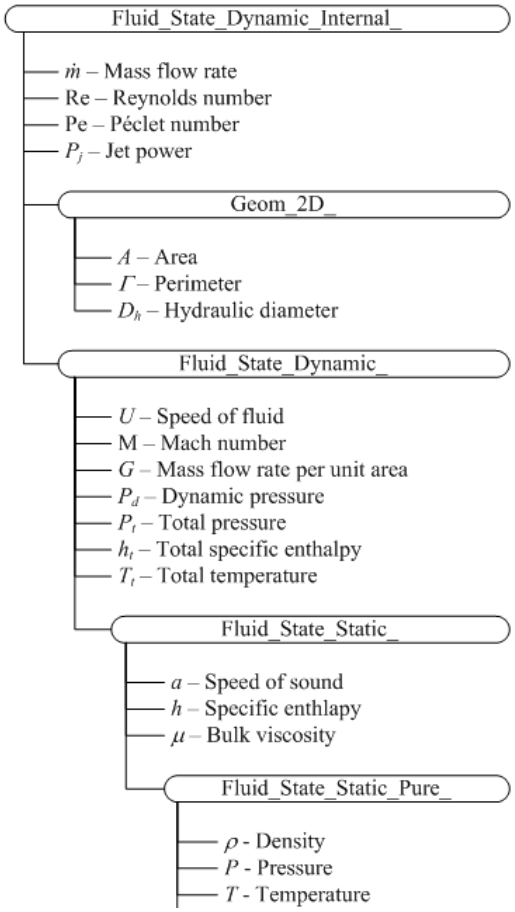

Figure 15 – An object representing the state of a quasi-1D fluid flowing through an internal duct. The object is built from a heiracrchy of sub-objects. This example is from the Version 2.0 ontology.

In the inference engine, the joined variables within the composite object become one and the same variable in memory. By specifying which variables are the same, small models are joined together to form larger more complex ones. Indeed, an ontology of models spanning everything from mathematics to geometry, to thermodynamics and fluid flow has been written. These are the building blocks from which the rocket, trajectory, and beam director models are constructed.

An example from basic fluid mechanics is given in Figure 15. The problem to be solved is that the quasi-1D flow of fluid through an internal duct needs to be represented and solved given a valid combination of input variables. The object that does this is built from a number of sub-objects in the same way that a function in a fourth-generation language might be built from a number of function calls to sub-objects or libraries. The difference is that there are no function calls to write. As described already, the equations that relate the objects are given, and any variables that are the same are joined. The rest is left to the inference engine.

For a simple fluid, it takes two thermodynamic variables to uniquely determine the state of the fluid at rest; a further speed-like variable to uniquely determine a dynamic state; and a further spatial scale to uniquely determine an internal dynamic state. For the variables shown in Figure 15 there are:

- 9 different ways to imply a static state (Fluid_State_Static_), assuming the fluid is one for which $a(T)$, $h(T)$, $\mu(T)$:
  ((T | a | h | μ) & (P | ρ)) | (P & ρ)
- 63 different ways to imply a dynamic state (Fluid_State_Dynamic_):
  (Fluid_State_Static_) & (U | M | G | P_d | P_t | h_t | T_t)
- 756 different ways to imply a dynamic internal state (Fluid_State_Dynamic_Internal_), assuming geometry for which $A(D_h)$, $\Gamma(D_h)$:
  (Fluid_State_Dynamic_) & (A | Γ | D_h) & ($\dot{m}$ | Re | Pe | P_j)

The ontology extends down into the representation of thermodynamic state for a simple compressible substance. This is not shown in the diagram due to space, but there are an additional 11,104,365,420 possible ways (PW Bridgman, 1914) to imply the state of this fluid as it flows through a duct. As the descriptions of the fluid become more complex, the state is implied via different thermodynamic potentials or derivatives that are defined within the simple compressible substance object. For example, when additional phases are introduced, the Gibbs potential is needed. Or when integrating from one state of a fluid to another, for example along an isentropic path, the thermodynamic base object comes into play.

It should be added that there are situations where closed-form equations do not exist and they are needed. For example, the Helmholtz equation of state is an explicit function of temperature and density, but what if temperature and pressure are specified instead? The engine would not have the equations it needs to propagate this information back to a value for density. To solve this, we currently declare implicit relationships and the inference engine automatically deduces an iterative solution. In this case, the engine would vary density such that the pressure is correct. Writing a subroutine to do this and checking it would previously take an hour or more. It is now accomplished automatically in a fraction of a second, even recursively.

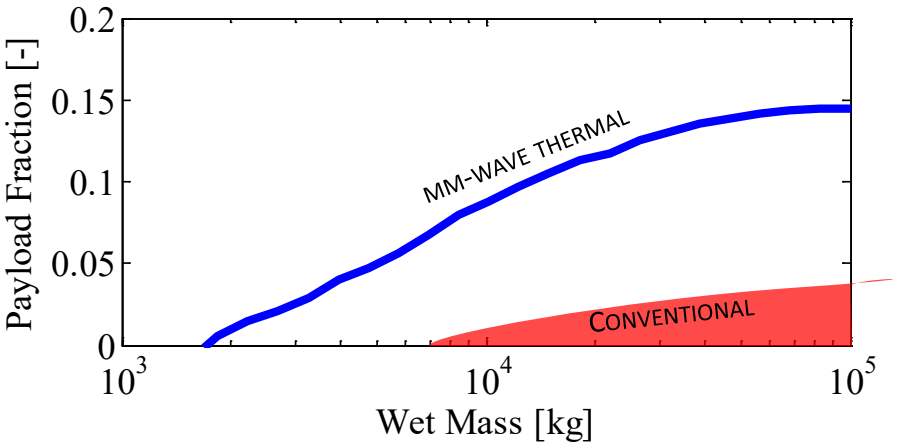

Figure 16 - Source: 11/2011 an early parametric scoping analysis using version 2.0 of the inference engine (Parkin). Payload fraction vs. wet mass for a millimeter-wave thermal rocket using a LH_2 propellant. Later point designs based on updated scaling laws and assumptions extended the zero payload point down to about 30 kg wet mass.

Returning to the full system model shown in Figure 14, version 2.0 of the inference engine uses a different combination of independent variables to infer the family of rockets shown as a curve in Figure 16. It is a goal of version 3.0 of the inference engine to produce a new version of this curve with the wet mass scale extending down to 1 kg. Figure 16 was generated in 2011 to show that such a plot was now possible and that as scale decreases, rocket mass tends to zero at a particular wet mass. It was not intended as a final result, and the full set of values from which it was generated were not recorded. In particular, the curve does not extend down to the 50-kg wet mass envisaged by later point designs. This is because the values used were evidently conservative (the payload fraction tends to only 15% as wet mass increases) and the design rules behind it may not have contained the detail needed to correctly represent the choices that would be made for a small rocket. For example, the tank subsystem model may have hit the minimum gauge for carbon composite tanks. In the current behavior, the system model switches to metallic tanks as the rocket gets smaller and these become lighter than carbon composite tanks at minimum gauge.

Although it looks simple, Figure 16 it is very hard to produce correctly. For each data point within it, an ascent trajectory to a given altitude is calculated and optimized, and a different rocket design is converged and optimized. For each run of the trajectory optimization loop, a different beam director design is produced. For each step of the trajectory integration, the beam profile on the heat exchanger is recalculated and the flow path through the rocket is recalculated. The design rules by which the rocket and beam director are constructed must be valid over the whole range of input variables that are encountered not only in the wet mass range of 1-100 metric tons, but at the extreme ends of bisection loops and other numerical root-finding methods. The results for every component must be well-behaved over their entire design range and the entire operating range for a new Figure 16 to be correctly generated.

The inference engine in Version 2.0 of the system model produced Figure 16 over the course of a few days on a mid-range desktop PC circa 2011. Part of the slow speed is due to the computational complexity of the problem, caused by the number of nested iterative solutions. The inference engine minimizes computational complexity in two ways. First, when deducing an algorithm to be iteratively

solved, the inference engine omits all calculations that do not depend in the variable whose value changes. This means that constant values are not needlessly recalculated on every iteration. Second, the inference engine uses iterative solutions only when there is no closed-form alternative. In Version 3.0 of the system model, the inference engine explicitly calculates the computational complexity of each function and chooses the path of minimum computation. However, it was found that the most important factor slowing Version 2.0 of the system model was memory operations due to the architecture of MATLAB. While the language was excellent for prototyping and debugging, a faster language was needed.

Version 3.0 of the system model is built on a new inference engine written in C++. Because of the effort involved and the available resources, it has not been possible to add new features and bug fixes to Version 2.0 of the system model while also developing Version 3.0. Hence, development of Version 2.0 was discontinued in March 2012. This leads to the present situation in which Version 3.0 is not yet finished and Version 2.0 is obsolete.

The endpoint of inference engine development has always been that it can automatically generate families of millimeter-wave thermal rockets as a function of payload mass. Because of the priority attached to this goal, we defer a more comprehensive description of the inference engine until it is complete.

3.4.1 Point designs

	2012 Parkin 50 kg point design (§3.4.1.1)	COMPASS TSTO (George and Beach 2012)	COMPASS SSTO (George and Beach 2012)	Conservative (Parkin and Webster 2012)	Less conservative (Parkin and Webster 2012)	2000 K HX, carbon tanks (Parkin 2006a)	Original point design (Parkin and Culick 2003)	Saturn V AS-506	GT RASCAL Study (Young and Olds 2005)	Pegasus	Scout G
Stages	1†	2	1	1†	1†	1	1	3	2†	3†	4
Propellant	LH_2	LH_2	LH_2	LH_2	LH_2	CH_4	LH_2				
E=Expendable R=Reusable	E†	E	E	E†	E†	E	E	E	E†	E†	E
Wet Mass (tons)	0.05†	2.2	4.7	5.3†	2.6†	10	1.0	2,938	7.8†	19†	21
Dry Mass (tons)	0.013	0.74	1.1	1.4	0.89	0.85	0.28	277	1.3	2.8	2.9
Native EDMM (%)	22	30.5	30.5	23	23	0	0	0	12	0	0
Adjusted EDMM for comparison (%)	30 15 0	30 15 0	30 15 0	30 15 0	30 15 0	30 15 0	30 15 0	30 15 0	30 15 0	30 15 0	30 15 0
LEO Payload (kg)	1.0* 3.0* 4.9*	49* 159* 270*	50* 213* 375*	130* 341* 553*	166* 299* 431*	395* 523* 650	16* 58* 100	36,983* 78,592* 120,200	-119* 72* 263*	-467* -46* 375	-654* -222* 210
Payload fraction (%)	2.0†* 5.9†* 9.8†*	2.3* 7.4* 12.5*	1.1* 4.5* 7.9*	2.5†* 6.5†* 10.5†*	6.4†* 11.5†* 16.5†*	4.0* 5.2* 6.5	1.6* 5.8* 10.0	1.3* 2.7* 4.1	- 0.9†* 3.4†*	- - 2.0†	- - 1.0
Parasitic Mass/Payload	12.0†* 3.4†* 1.7†*	14.2* 3.6* 1.7*	20.6* 4.1* 1.9*	9.8†* 3.1†* 1.5†*	4.3†* 2.0†* 1.1†*	1.2* 0.6* 0.3	16.5* 3.8* 1.8	6.5* 2.5* 1.3	- 16.7†* 3.8†*	- - 6.5†	- - 12.7

† Not counting air-breathing first stage.

* Derived from native EDMM by re-categorizing margin from parasitic dry mass to payload or vice versa. Dry mass, which is the sum of payload mass and parasitic dry mass, is unchanged.

Table 6 - Comparison of point designs

A summary of notable millimeter-wave point designs is presented in Table 6. These include the original point design published in 2003 and several since. A meaningful comparison of these designs involves weighing the amount of margin carried with each. The margin greatly affects the figures of merit. The most important figure of merit is the ratio of parasitic mass to payload mass, from a cost point of view.

To provide a common basis on which to compare margins, we define an Effective Dry Mass Margin (EDMM). The EDMM is the amount of dry mass that would be counted as payload, but is instead counted as dry mass to allow for growth in subsystem masses and residual propellant(s). EDMM is also expressed as a percentage of the dry mass, which includes the mass of the payload and the margins.

The AIAA S-120-2006 standard (AIAA 2006) is used by the COMPASS Studies (George and Beach 2012) and defines a more nuanced framework of three different types of mass margin. It also recommends programmatic go/no-go criteria. Some of the values in Table 6 are color coded by EDMM and correspond to the color codes in the AIAA standard at the time of preliminary design review. Green (>21% EDMM) means that mass risks are minimal and no remedial action is required. Yellow (13-21% EDMM) means that there is medium mass risk and a risk handling plan should be prepared. Red (<13% EDMM) means that there is high mass risk and an immediate audit, reduction effort and mitigation process should begin.

The COMPASS designs achieve positive payloads despite a 30% EDMM, a feat that conventional rockets of a similar size are not capable of. RASCAL, Pegasus and Scout are shown as cases in point. As a consequence of carrying this margin, the COMPASS team converged on an SSTO wet mass that was higher than wanted. This drove them to reduce the wet mass by adding a solid rocket second stage.

Methane propellant is shown to have a substantially higher ratio of parasitic mass to payload than hydrogen in Table 6. This is similar to the advantage that is predicted by SCPPM version 1.2 and shown in Figure 9. Because two different types of model predict a comparative advantage, methane is a high-priority propellant for future point designs and experimental tests.

No significant point designs have been generated since 2012 because, as already discussed, Version 3.0 of the system model is not yet finished and Version 2.0 is obsolete.

3.4.1.1 50 kg wet mass

Wet mass	50 kg
EDMM	22%
ΔV	9.7 km/s
LH2 initial tank state	1.5 bar, 16 K
Tank L/D ratio	2
Nose fineness ratio	2
Tank overall factor of safety	1.25*2.0 = 2.5
Nozzle factor of safety	2.0
Maximum T/W_0	5.4
Overhead for structural mounts	10% of propulsion subsystem mass
Stagnation pressure at nozzle	10 bar
Nozzle expansion ratio	100
HX channel	Roughness = 0.002, Wall thickness = $D_h/20$
HX channel outlet	Re = 15,000, M = 0.7, static T = 1,750 K

Table 7 - Inputs for the 50-kg wet mass point design

Masses	
Tank	1.5 kg (0.62 m diameter, 42 μm thick 15-3 Ti)
Turbopump	1.9 kg

Heat exchanger	2.0 kg (622 alumina channels, D_h = 1.9 mm, peak wall T = 1,900 K, inlet P = 45 bar, avg. intensity at surface = 6 MW/m^2)
Nozzle	0.1 kg (I_{sp} = 724 sec, length = 28 cm, Nb-alloy)
Nosecone	0.63 kg
Payload adapter	0.25 kg
Reaction control system	8.5 g (this is low and the rule-of-thumb that produced it will be revised in the next system model)
Structural mounts	0.4 kg
Avionics	1.0 kg
Dry mass margin	2.9 kg
Payload	2.0 kg
Propellant	37 kg

Figures of merit	
Payload fraction	4.0 %
Payload	2.0 kg
Vacuum I_{sp}	721 sec
Propulsion T/W	67
Absorbed power	10 MW
Areal density of heat exchanger	1.4 kg/m^2
Thrust	2.6 kN
Mass flow rate	0.37 kg/sec of H_2

Table 8 – Outputs for the 50 kg wet mass point design. This point design was generated using Version 2.0 of the system model in July 2012.

At the outset of the MTLS project in 2012, DARPA requested that we work towards the smallest possible millimeter-wave thermal rocket that can place a payload into LEO. It was a happy coincidence that in 2010 one of us (Parkin) discovered that smaller rockets always produce cheaper beam directors provided that the energy spillage is chosen to minimize the cost. Prior to this, an assumption of fixed energy spillage led to an optimal scale of rocket often in the hundreds or thousands of kilograms, as explained in §3.6.3Cost using optimal spillage.

Other developments contribute to producing a smaller rocket than Figure 16 predicts is possible. First, the advent of smartphones and the PhoneSat mission (Marshall and Beukelaers 2011) makes it apparent that older rules of thumb over-predict the avionics mass. This is also evident from the <10 kg avionics of the 1990s era kinetic kill vehicles (Wilkening 2003), which use 100 gram, 100 Newton divert thrusters developed by Marquardt (Ruttle and Fitzsimmons 1993). Similarly, the F2M2 missile developed by China Lake Naval Air Weapons Station is the world's smallest, weighing just 2.5 kg (5.5 lbm). Much of this mass is the warhead and solid rocket motor, and the remaining avionics contains a camera and processor capable of guiding the missile to a designated target. Consequently, an avionics mass of 1 kg, as shown in Table 8 for the 50-kg rocket, is regarded as feasible.

The payload adapter mass shown in Table 8 is 250 grams in order to hold and launch a 2-kg satellite. In comparison, the RUAG PAS 175 system has a total mass of 350 grams and is designed to hold and launch satellites in the 10-60 kg range.

It is the assumption of large fixed masses for subsystems like these that caused earlier system models to predict that zero payload is reached at a wet mass of nearly two tons, as shown in Figure 16. Updates with smaller components and scaling laws that extend down into a lower mass range result in the 50-kg point design of Table 8. Experimentation with Version 2.0 of the system model at the time the point design was generated showed that zero payload is reached at 30 kg wet mass (or alternately if the ΔV is increased past 11 km/s). Further reduction of fixed masses is expected to lower the zero-payload wet mass further.

3.5 Flow path

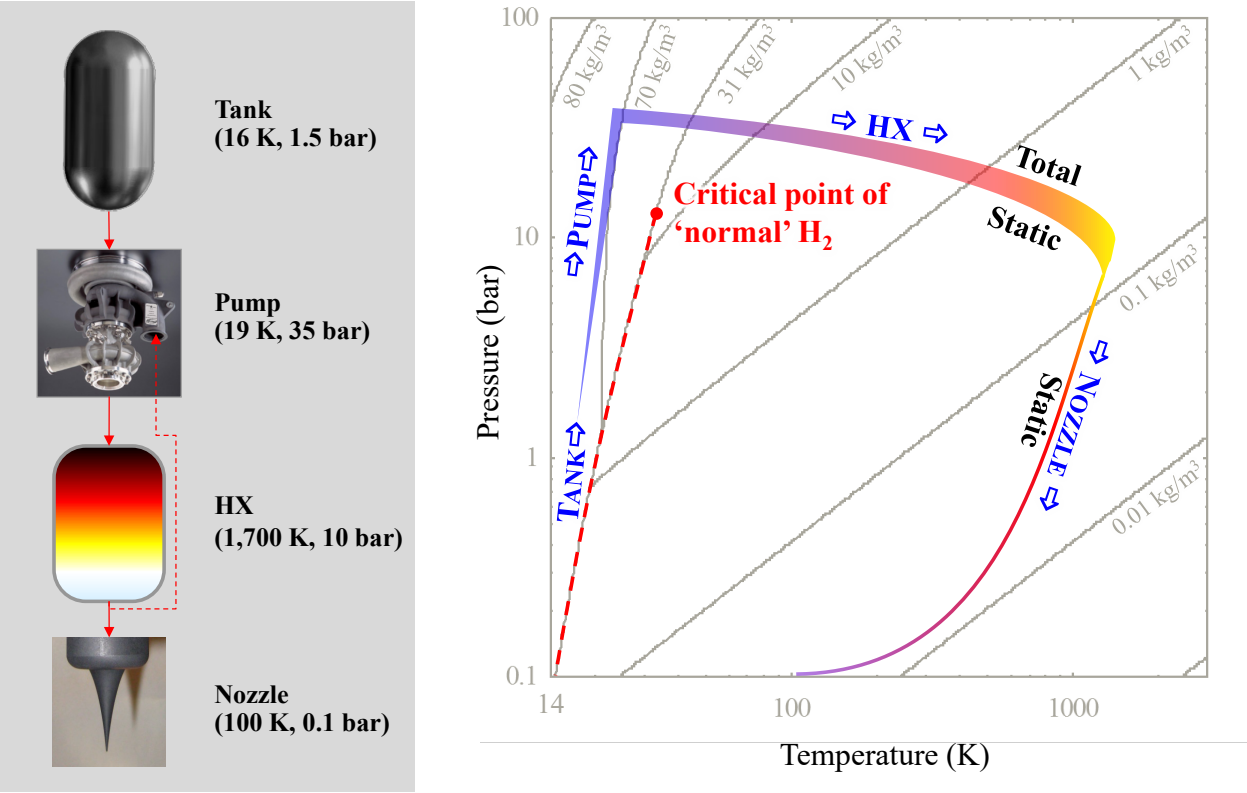

Figure 17 - Overview of the LH_2 thermal flow path and transcription onto the LH_2 phase diagram. The LH_2 phase diagram is generated using a multiphase fluid object within Version 3.0 of the system model.

3.5.1 Helmholtz equations of state for propellants

In simulating the flow path of the rocket, propellant calculations for the tank, pump and inlet end of the heat exchanger involve compressibility effects and careful navigation around the critical point, as shown in the LH_2 phase diagram on the right of Figure 17.

Version 1.0 of the system model considered only a perfect gas and used additional information calculated outside the model to size the tank and pump. It also needed to assume a heat exchanger inlet temperature well above the critical temperature of the propellant in order to produce a valid channel flow prediction, both because of the propellant model and also because the channel flow model assumed a perfect gas.

In subsequent versions of the system model we have implemented a Helmholtz equation of state based on the approach, source code and data files implemented by National Institute of Standards and Technology Reference Fluid Thermodynamic and Transport Properties Database, abbreviated as NIST REFPROP (Lemmon, Huber et al. 2002).

To the best of our knowledge, this is the first time that a program to predict fluid properties has been ported into an inference engine. The first advantage to doing so is that the inference engine can verify the thermodynamic self-consistency of a state from the temperature and density through to the various compress abilities and thermodynamic partial derivatives. It does this by taking every inferred value and comparing it with the result from every function that can produce that value. Each of these functions takes different inputs, and the more functions that are deduced by (currently by the user) and given to the inference engine, the more cross-checks there are. The second advantage is that, as previously mentioned, the inference engine minimizes computational complexity during iteration by omitting redundant steps. The further the problem is decomposed into its atoms, the greater the savings possible. The speed of execution of the equation of state has a leading order effect on the speed of solution for the entire flow path.

3.5.1.1 Static and total states

The inference engine integrates between states by asserting that $ds = 0$ (for an isentropic transformation) and $dv = 1$, or similar, depending on which variable is used to imply the other state. For example, if the user specifies $\{T, v, T_t\}$, then the inference engine uses $ds = 0$ and $dv = 1$ (with variable step size) to deduce dT and integrate forward to the desired value of T_t. The RK45 algorithm is currently used. We can specify $\{h, P, U\}$ or $\{T, P, M\}$ or many other possible combinations to imply the static and total states.

Combinations that imply integrating the other way need a little more care. For example, $\{h_t, P_t, G\}$ has both a supersonic and a subsonic solution. In this case, the description of the static state is incomplete because it does not specify the branch. The description is completed by adding a Boolean variable to indicate whether the solution is supersonic or subsonic. Using this additional branch index to remove the non-uniqueness, the integrator finishes at the desired branch.

3.5.1.2 Multiple phases

In the multiphase representation of a fluid described by the Helmholtz equation of state, there is extra logic used to deduce the phase of the fluid. The multiphase fluid object developed in Version 3.0 of the system model is used to plot the LH_2 phase diagram in Figure 17 and is used in the next section to deduce the maximum speed at which LH_2 can be withdrawn from the tank without boiling.

3.5.2 Tank

The tank is usually the heaviest single structure in a LH_2 thermal rocket, so the way materials and margins change with scale is of first order importance to the payload performance of the system. The ratio of propellant to tank mass changes as a function of scale due to the minimum gauge (thickness) of carbon composite tanks relative to titanium.

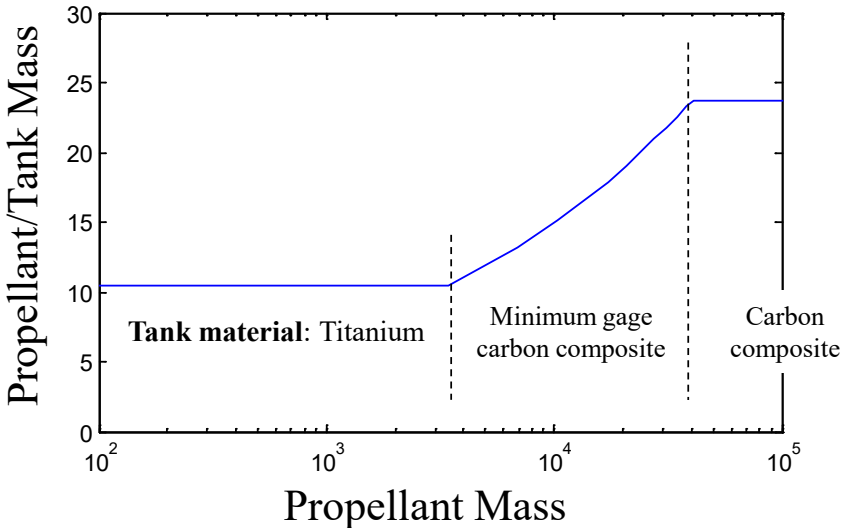

Figure 18 – Structural performance of tanks as a function of enclosed propellant mass

Since Version 2.0 of the system model, the tank subsystem has been capable of automatically selecting the tank material that minimizes the mass, as shown in Figure 18. Between titanium and carbon composite tanks, there is a region where a carbon composite tank is lighter than a titanium tank, even though it is at minimum gauge and thicker than required. The inference engine uses design rules like this to be able to plot performance of rockets over a wide range of possible masses without intervention from the user. This type of autonomous material selection is undesirable at other times, and the user can directly specify the tank material instead.

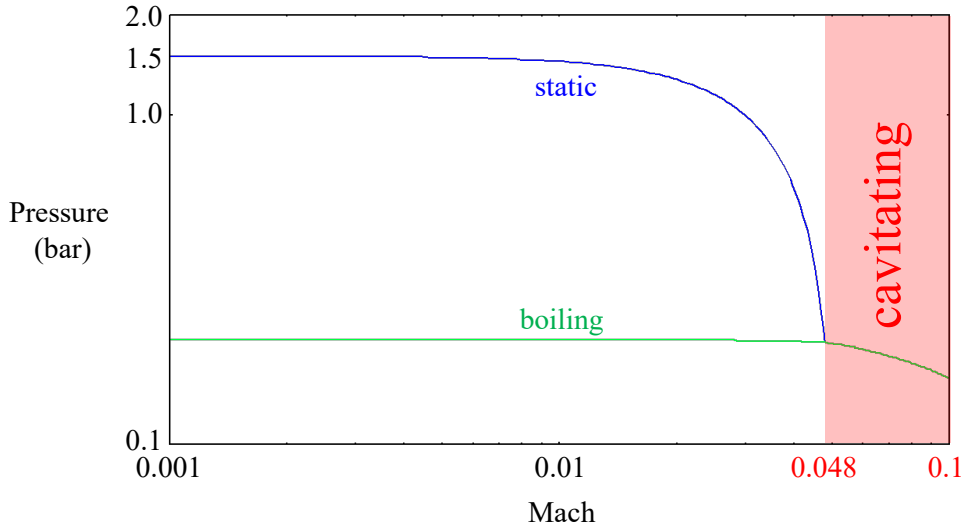

Figure 19 – Maximum speed of LH_2 propellant withdrawal from a cryogenic tank in order to avoid boiling (generated using Version 3.0 of the system model)

In withdrawing a LH_2 propellant from the tank, there is a speed above which static pressure falls below boiling pressure, and the propellant boils. For a total pressure of 1.5 bar and total temperature of 16 K in the tank, this limit is found to be Mach 0.048, as shown in Figure 19. This corresponds to a velocity of 58.8 m/sec, a mass flow rate per unit area of 4,430 kg/s/m^2, and a static temperature of 15.96 K. This

has implications for pump design, as the pump will cavitate in boiling flow, and even at higher static pressure, local variations of pressure on the depression sides of pump blades can also result in cavitation.

3.5.3 Heat exchanger

3.5.3.1 Quasi-1D channel flow model

The comparative advantage of a quasi-1D channel flow model based on Nusselt number correlations is that the solutions is very fast, making it suitable for computationally complex tasks like exploring the design space to arrive at an optimal heat exchanger design. This is especially important when the heating pattern across the array of channels varies in space and/or time. One of us (Parkin 2006c) showed that the quasi-1D solutions compare closely with the results of a 2D Navier-Stokes solver despite wall heating violating some of the assumptions of the Nusselt number correlations used. More complex codes can be used to verify solutions, and, if the results can be adequately parameterized, they can be compiled into their own correlations and used with the quasi-1D solution procedure presented here.

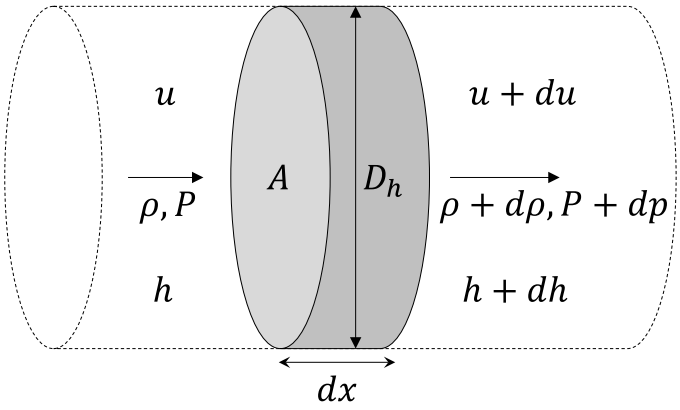

Figure 20 - Control volume for constant area channel flow

Beginning with a steady state control volume analysis, the mass, momentum, and energy conservation equations of the flow are derived. The control volume, shown in Figure 20, is drawn about an element *dx* of the channel flow.

3.5.3.1.1 Continuity

For a steady flow in the absence of sources or sinks, the continuity equation is

$$\oint \rho \mathbf{u} \cdot d\mathbf{S} = 0. \qquad [50]$$

By integrating, this becomes

$$\rho u A = (\rho + d\rho)(u + du)A. \qquad [51]$$

Neglecting higher order terms, this reduces to

$$d(\rho u) = 0. \quad [52]$$

Hence

$$\rho u = G, \quad [53]$$

where G is the mass flow rate per unit area, a constant along the channel.

3.5.3.1.2 Momentum

For a steady flow the momentum equation is

$$\oint \rho \mathbf{u}\mathbf{u} \cdot d\mathbf{S} = -\mathbf{i} \cdot \oint P\mathbf{n}dS + \mathbf{i} \cdot \oint \mathbf{n} \cdot [\boldsymbol{\tau}]dS\,. \quad [54]$$

By integrating this becomes

$$[(\rho + d\rho)(u + du)^2 - \rho u^2]A = -[(P + dP)A - PA] - \tau \Gamma dx. \quad [55]$$

Using continuity, the definition of hydraulic diameter $D_h \equiv \frac{4A}{\Gamma}$, and the definition of Fanning friction factor $f = \frac{2\tau}{\rho u^2}$, the above simplifies to

$$d(P + \rho u^2) = -\frac{2f}{D_h}\rho u^2 dx. \quad [56]$$

3.5.3.1.3 Energy

For a steady flow the energy equation is

$$\oint \rho(h + u^2/2)\mathbf{u} \cdot d\mathbf{S} \;=\; -\oint \mathbf{q} \cdot d\mathbf{S} + \oint \mathbf{n} \cdot [\boldsymbol{\tau}] \cdot \mathbf{u}dS. \quad [57]$$

Neglecting viscous dissipation and using the abbreviation $h_t = h + u^2/2$, the equation integrates to

$$GA(h_t + dh_t) - GAh_t \;=\; q\Gamma dx, \quad [58]$$

and further simplification yields

$$\mathrm{d}\left(h + \frac{u^2}{2}\right) = \frac{4q}{GD_h}dx. \quad [59]$$

3.5.3.1.4 Transformation to equations explicit in specific volume and temperature (for use with Helmholtz form of equation of state)

The Helmholtz form of the equation of state (Jacobsen, Penoncello et al. 1997) is explicit in specific volume and temperature. Hence, for computational efficiency the channel flow equations also need to be explicit in specific volume and temperature. To accomplish this, equations [56] and [59] are rewritten using $v \equiv \frac{1}{\rho}, x' \equiv \frac{x}{D_h}, \tilde{f} \equiv -2fvG^2$, and $\tilde{q} \equiv \frac{4q}{G}$. In addition, equation [53] is used to eliminate u in favor of v and the invariant G:

$$dP = \tilde{f}dx' - G^2dv, \quad [60]$$
$$dh = \tilde{q}dx' - G^2vdv. \quad [61]$$

$dP(v,T)$ and $dh(v,T)$ are now expressed in terms of v and T by using thermodynamic partial derivatives,

$$dP = \left(\frac{\partial P}{\partial T}\right)_v dT + \left(\frac{\partial P}{\partial v}\right)_T dv, \quad [62]$$
$$dh = \left(\frac{\partial h}{\partial T}\right)_v dT + \left(\frac{\partial h}{\partial v}\right)_T dv. \quad [63]$$

Equating [62] and [63] with [60] and [61] respectively eliminates dP and dh,

$$\left(\frac{\partial P}{\partial T}\right)_v dT + \left[\left(\frac{\partial P}{\partial v}\right)_T + G^2\right] dv = \tilde{f}dx' \quad [64]$$
$$\left(\frac{\partial h}{\partial T}\right)_v dT + \left[\left(\frac{\partial h}{\partial v}\right)_T + G^2v\right] dv = \tilde{q}dx'. \quad [65]$$

Eliminating dT between [64] and [65] produces

$$dv = \frac{\left(\frac{\partial h}{\partial P}\right)_v \tilde{f} - \tilde{q}}{\left[\left(\frac{\partial P}{\partial v}\right)_T + G^2\right]\left(\frac{\partial h}{\partial P}\right)_v - \left[\left(\frac{\partial h}{\partial v}\right)_T + G^2v\right]} dx'. \quad [66]$$

The partial derivatives in this equation can be expressed explicitly as functions of v, T, and the specific heat capacities $c_p(v,T), c_v(v,T)$. To obtain an expression for $\left(\frac{\partial h}{\partial P}\right)_v$, we can start with the definition of specific enthalpy

$$h \equiv e + Pv. \quad [67]$$

Taking derivatives and using chain rule,

$$dh = de + Pdv + vdP. \quad [68]$$

Choosing v to be constant, equation [68] can be expressed in Jacobian notation as

$$\partial(h,v) = \partial(e,v) + v\partial(P,v). \quad [69]$$

Using the definitions

$$c_v \equiv \left(\frac{\partial e}{\partial T}\right)_v = \frac{\partial(e,v)}{\partial(T,v)}, \quad [70]$$

$$\alpha \equiv \frac{1}{v}\left(\frac{\partial v}{\partial T}\right)_P = \frac{1}{v}\frac{\partial(v,P)}{\partial(T,P)}, \quad [71]$$

$$\beta_T \equiv -\frac{1}{v}\left(\frac{\partial v}{\partial P}\right)_T = -\frac{1}{v}\frac{\partial(v,T)}{\partial(P,T)}, \quad [72]$$

equation [69] can be reduced to

$$\left(\frac{\partial h}{\partial P}\right)_v = \frac{\partial(h,v)}{\partial(P,v)} = \frac{c_v\beta_T}{\alpha} + v. \quad [73]$$

To obtain an expression for $\left(\frac{\partial h}{\partial v}\right)_T$, we can start by expressing $dh(T,P)$ in terms of partial derivatives;

$$dh = \frac{\partial(h,P)}{\partial(T,P)}dT + \frac{\partial(h,T)}{\partial(P,T)}dP. \quad [74]$$

At constant specific volume this becomes

$$\partial(h,v) = \frac{\partial(h,P)}{\partial(T,P)}\partial(T,v) + \frac{\partial(h,T)}{\partial(P,T)}\partial(P,v). \quad [75]$$

Using the definition

$$c_p \equiv \left(\frac{\partial h}{\partial T}\right)_P = \frac{\partial(h,P)}{\partial(T,P)} \quad [76]$$

and the definitions [70]-[72], equation [75] reduces to

$$\left(\frac{\partial h}{\partial v}\right)_T = \frac{\partial(h,T)}{\partial(v,T)} = \frac{c_p - c_v}{\alpha v} - \frac{1}{\beta_T}. \quad [77]$$

To obtain an expression for $\left(\frac{\partial P}{\partial v}\right)_T$, equation [72] is rearranged;

$$\left(\frac{\partial P}{\partial v}\right)_T = \frac{\partial(P,T)}{\partial(v,T)} = -\frac{1}{v\beta_T}. \quad [78]$$

At last, equations [73], [77], and [78] are substituted into equation [66]. After some canceling, this yields

$$dv = \frac{(c_v\beta_T + \alpha v)\tilde{f} - \alpha\tilde{q}}{c_v\beta_T G^2 - \frac{c_p}{v}}dx'. \quad [79]$$

An expression for dT is obtained by rearranging equation [62],

$$dT = \frac{dP - \left(\frac{\partial P}{\partial v}\right)_T dv}{\left(\frac{\partial P}{\partial T}\right)_v}. \quad [80]$$

An expression for $\left(\frac{\partial P}{\partial T}\right)_v$ is obtained by dividing equation [71] by equation [72],

$$\left(\frac{\partial P}{\partial T}\right)_v = \frac{\partial(P,v)}{\partial(T,v)} = -\frac{\alpha}{\beta_T}. \quad [81]$$

Substituting equations [78] and [81] into equation [80] yields the desired expression for dT,

$$dT = -\frac{1}{\alpha}\left(\beta_T dP + \frac{dv}{v}\right). \quad [82]$$

In summary, the quasi-1D channel flow ODE integration procedure is as follows: For an initial $\{T, v, G, x_0'\}$ and prescribed functions for fanning friction factor $f(x', T, v, G)$ and useful heat $q(x', T, v, G)$, equation [79] is used to calculate dv, followed by equation [60] to calculate dP, followed by equation [82] to calculate dT. Using the values of dx', dT and dv, the integrator yields new values of $\{T, v, x\}$ from which $\{f, q, c_p, c_v, \alpha, \beta_T\}$ are calculated. The cycle repeats until a desired termination condition is reached, for example sonic flow, a particular tube length, or a particular total enthalpy.

When considering other losses such as heat radiating from the outer wall of the heat exchanger into free space, evaluating $q(x', T, v, G)$ requires an iterative thermal circuit calculation and is not an explicitly prescribed function of the incident beam profile. Similarly, radiatively participating fluids complicate the thermal circuit.

The temperature, density and other properties of the fluid described by this quasi-1D channel flow model represent only bulk properties of the fluid is it moves along the channel. This model does not describe the properties of the fluid across the channel. In particular, this model says nothing about the temperature of the fluid at the wall of the channel. If a high enough value of q is imposed, then the wall temperature needed to impose such a flux may be higher than the thermal limits of the tube material. We describe how to calculate this next.

3.5.3.1.5 Auxiliary equations

As propellant passes through the heat exchanger, it changes in temperature from cryogenic (e.g., 30 K for hydrogen) up to 2,500 K, invalidating the ideal gas approximation and the assumption of constant specific heat capacity across the channel, among other transport properties. Consequently, heat transfer is expressed in terms of enthalpy instead of temperature. The useful heat flux q absorbed from the channel wall is expressed as,

$$q = G\ \mathrm{St}\left[(h_w - h_t) + (1 - r)\frac{u^2}{2}\right]. \quad [83]$$

where St is the Stanton number, G is the mass flow rate per unit channel cross-sectional area, $h_w - h_t$ is the difference in specific enthalpy between fluid touching the wall and the bulk flow if adiabatically

brought to rest. The enthalpy recovery factor r corrects for boundary layer effects. For a rough tube, the Stanton number is approximated as a function of tube roughness and Reynolds number only (Kakaç, Shah et al. 1987). Roughness can be used to vary the heat transfer performance. This comes at the cost of increased friction, which increases pressure losses.

3.5.3.2 Design tradeoffs

The design objectives of the heat exchanger are threefold. First, the heat exchanger should raise the temperature of the propellant as close as possible to the thermal limit of its materials. Second, it should undergo minimal pressure loss as it does so. Third, it should do this using minimal mass.

The first objective maximizes specific impulse, the second objective minimizes pump mass and power, and there is a system-level tradeoff between these two objectives. The third objective involves varying the heat exchanger size and flux to trade specific impulse against heat exchanger mass (as opposed to pump mass).

Equation [59] can be integrated over the length of a heat exchanger tube to produce,

$$\Delta h_t = \frac{4L\langle q\rangle}{GD_h}, \qquad [84]$$

where average wall flux ⟨q⟩ over the surface of the tube is defined by,

$$\langle \mathrm{q}\rangle \equiv \frac{1}{L}\int q\, dx. \qquad [85]$$

Choosing a rise in specific enthalpy of $\Delta h_t = 30$ MJ/kg is equivalent to heating hydrogen by around 2,000 K, corresponding to an ideal vacuum I_{sp} of about 750 seconds. Equation [84] illustrates a key tradeoff between tube length L, average wall flux ⟨q⟩, mass flow rate per unit area G, and hydraulic diameter D_h. For example, if the wall flux is doubled, then the same Δh_t is maintained by halving the tube length, doubling the tube diameter (there is a greater depth of fluid to absorb each unit of incident flux), doubling the mass flow rate per unit area (e.g., by increasing the pressure), or some combination of thereof. It is the combination of these factors that allows the flux-absorbing capabilities of the heat exchanger to be tailored over many orders of magnitude.

In addition to choosing $\Delta h_t = 30$ MJ/kg as above, we will choose an average wall flux ⟨q⟩ of 7.5 MW/m^2, yielding

$$\frac{4\langle q\rangle}{\Delta h_t} = \frac{GD_h}{L} = 1\ \mathrm{kg/s/}m^2. \qquad [86]$$

Notice that Reynolds number can be expressed as

$$\mathrm{Re} = \frac{GD_h}{\mu} = \frac{1}{\mu}\frac{4L\langle q\rangle}{\Delta h_t}. \qquad [87]$$

G and D_h are invariant along this tube, but for hydrogen the bulk viscosity μ varies between about 2×10^{-6} kg/m/s at cryogenic inlet temperature and 3×10^{-5} kg/m/s at 2,000 K outlet temperature. For a 10 cm long tube as might be used in a sub-scale demonstration, this means that the Reynolds number is 50,000 at the inlet but only 3,300 at the outlet. The inlet is comfortably turbulent, but the outlet is in the transitional regime in which heat transfer is relatively poor and unstable. This regime is traditionally avoided in heat exchanger design.

As described by equation [87], the Reynolds number can be controlled by changing the length, flux or specific enthalpy rise. We will raise the Reynolds number by a factor of 10 by increasing the length of the tube to 1 meter. Equation [86] then becomes,

$$GD_h = 1 \text{ kg/s/m}. \qquad [88]$$

Increasing the length of the tube has the downside of increasing the pressure drop along it. More seriously, the flow can become sonic prior to the planned tube length, in which case the inlet conditions would adjust such that the sonic point moves to the end of the tube. The hydraulic diameter D_h can be varied to control these two effects.

A larger D_h reduces the ratio of tube length to diameter (a key similarity variable) and also G via equation [88], hence pressure gradient is reduced and the Mach number at the outlet of the tube is reduced. However, the heat transfer performance described by equation [83] is also reduced, hence the temperature difference between the wall and the bulk flow must increase in order to attain a given flux. To prevent the tube from unacceptable softening as the thermal limit is exceeded, the specific enthalpy rise is reduced. Herein lies the key tradeoff between specific impulse performance and pressure drop.

A related tradeoff exists between the flux and the heat exchanger mass: A higher flux enables a lighter heat exchanger, but this has higher thermal gradients and therefore lowers specific impulse for a given material thermal limit. A larger heat exchanger enables a smaller beam director and lowers flux, therefore raising specific impulse (for a given material thermal limit). The determining factor for the optimum of this tradeoff is the areal density of the heat exchanger.

3.5.3.3 Crash development for the MTLS project

The MTLS project imposes the following constraints on a millimeter-wave heat exchanger:

1. Absorption at 95 GHz or 110 GHz
2. 10-100 kW incident flux
3. Peak temperature of > 1,500 K in air at an internal pressure of > 5 bar
4. < 1 kg mass based on Figure 8
5. Interface to feed system and nozzle
6. >5 seconds operation

3.5.3.3.1 Heat exchanger tube selection

We use ceramic tubes for the core element of beam absorption for three reasons: First, due to the high temperatures needed, which would make metals too soft. Second, due to their successful use in

previous studies (Parkin 2006c, Bruccoleri, Parkin et al. 2007). Third, because many of them are transparent to millimeter-waves, whereas metal heat exchangers reflect millimeter-waves very efficiently. It was thought easier to start with a substance which is transparent and can later be modified for absorption. The ceramic path includes the possibilities of susceptor absorption, volume absorption into the heat exchanger structure, and absorption directly into the propellant itself, which is of interest for water and hydrocarbon propellants such as methane.

The tubes are made of 99.98% alumina (Aluminum Oxide, Al_2O_3) and mullite ($3Al_2O_3\ 2SiO_2$) of different grades from the manufacturers Coorstek and Omega. Alumina can withstand temperatures higher than 2,000 K without melting, but has the disadvantage of being brittle, complex to machine, and relatively poor in its resistance to thermal shock. Purity and porosity are important factors as they influence thermal and electromagnetic properties of the ceramic (Auerkari 1996, Penn, Alford et al. 1997). Mullite has a lower melting point due to its silicate content, but offers easier handling due to higher flexibility, and somewhat better machining properties. Various diameters and wall thicknesses are used for testing, ranging from 1.32 to 1.98 mm outer diameter for a length of 30 cm.

3.5.3.3.2 The inlet manifold

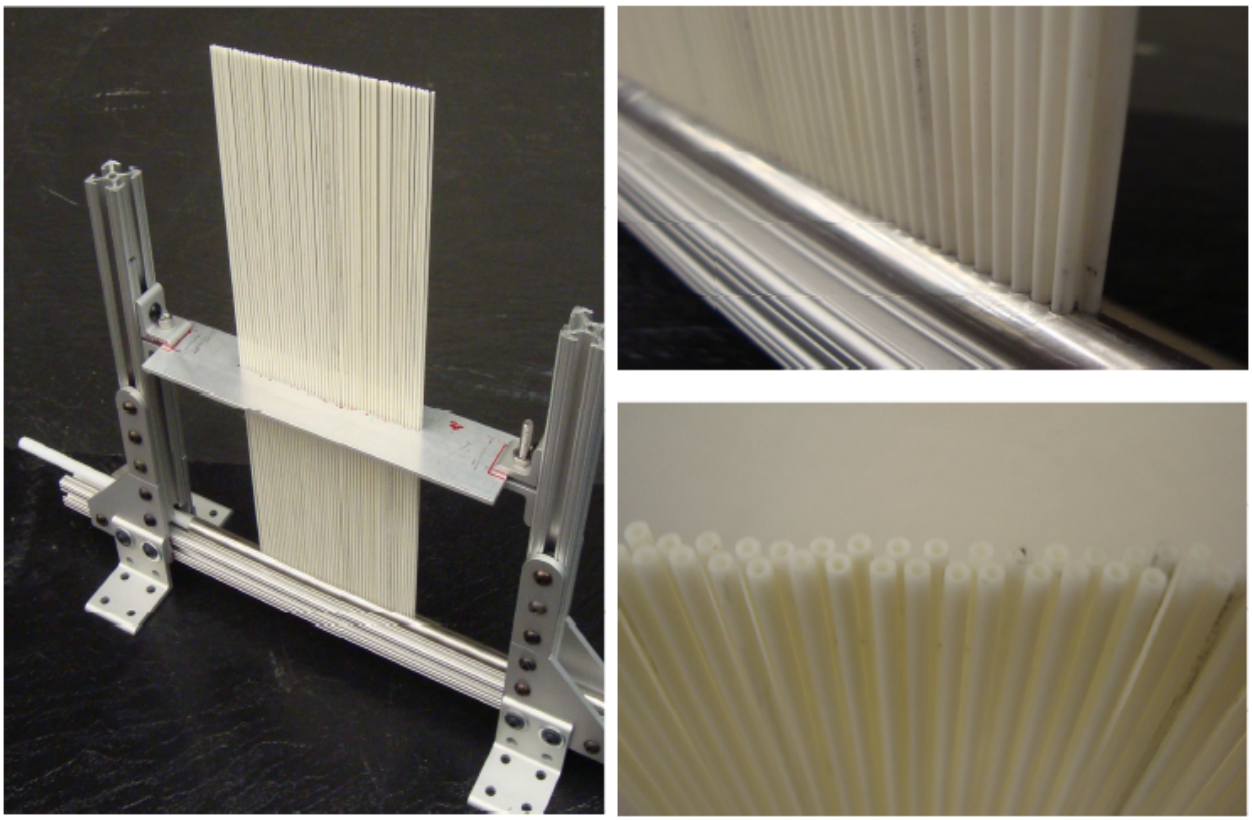

Figure 21 – The planar alumina heat exchanger circa November 2012. The tubes are not yet joined to the inlet pipe. A hole pattern is used here with a row spacing of 0.75xOD and a column spacing of 1xOD. This relatively tight spacing leads to high tube breakage during assembly. For this reason, the final heat exchanger uses a row spacing of 1xOD and a column spacing of 2xOD. This row spacing has leaves few gaps between tubes as viewed from normal incidence up to an angle of 30 degrees off-normal.

For the baseline heat exchanger design, tubes of small diameters are disposed in an array giving a planar shape to the heat exchanger, as shown in Figure 21. The tubes are connected to an inlet from which the propellant gas is supplied, and an outlet where the hot gas is collected and expanded through the nozzle to produce thrust. Because the inlet supports an array of holes drilled side-to-side, the tubes are staggered into two rows and aligned in a way such that there are minimal losses in the inter-tube space for an incoming beam at normal incidence. Assuming a beam diameter of 20 cm, 100 tubes are needed to compose one heat exchanger.

Due to a variation in the straightness the tubes and the way they sit in the holes, a jig (in the form of a perforated plate, seen on the left of Figure 21) is used to enforce the tube pattern along the length of the heat exchanger. This plate still allows the tubes to expand in the longitudinal direction.

The key structural problem is how to attach the ceramic tubes in a gas-tight way to both the inlet and outlet manifold. The tubes expand when heated, potentially in a non-uniform way, and the outlet end reaches > 1,500 K for the few seconds in which the rocket is operating. Because of the technical difficulty and schedule risk of this problem, several different solutions were tried in parallel.

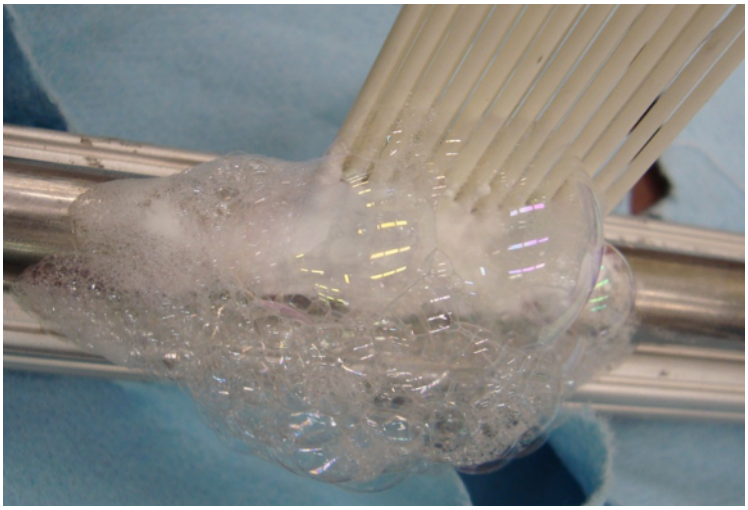

Figure 22 – Leak testing of a metal to ceramic paste joint of alumina to stainless steel at a pressure of 2 bar. Soapy water reveals a porous joint that is unable to hold pressure.

Multiple glues and epoxies were tested but failed to attach to the alumina surface to a metal inlet pipe. One that came the closest was the Cootronics Resbond 940 HT ceramic to metal paste, which requires curing at 100 °C for 20 minutes. However, the resulting joint was porous and therefore leaked, as shown in Figure 22.

Another solution tried was a brazing approach. Research revealed that a Ticusil® (Ag-26.7Cu-4.5Ti) brazing mixture could be used to bond alumina to steel (Wiese 2001), and it was expected that this would produce the strongest most temperature resistant bond possible to a steel inlet. This approach was tried by Michael Gusman at NASA Ames and involved the refurbishment of a retort furnace. The tubes were placed in countersunk holes machined in the inlet to offer somewhat flat contact between the bottom of the alumina tube and the stainless steel pipe. These holes would retain braze paste and removable fiber used inside the tube to prevent clogging. The primary hole had a dimension of OD+100 microns to allow the brazing mixture to flow inside the gap. The procedure used was as follows:

All joining surfaces are cleaned before the brazing run using the following procedure:

1. Ultrasonically cleaned in de-ionized water for 10 minutes
2. Rinsed in running de-ionized water for 1 minute
3. Ultrasonic rinse in de-ionized water for 5 minutes
4. Rinsed in running de-ionized water for 1 minute
5. Ultrasonic final rinse in 100% ethanol
6. Parts placed in a clean drying oven at 80°C, under a watch glass overnight.

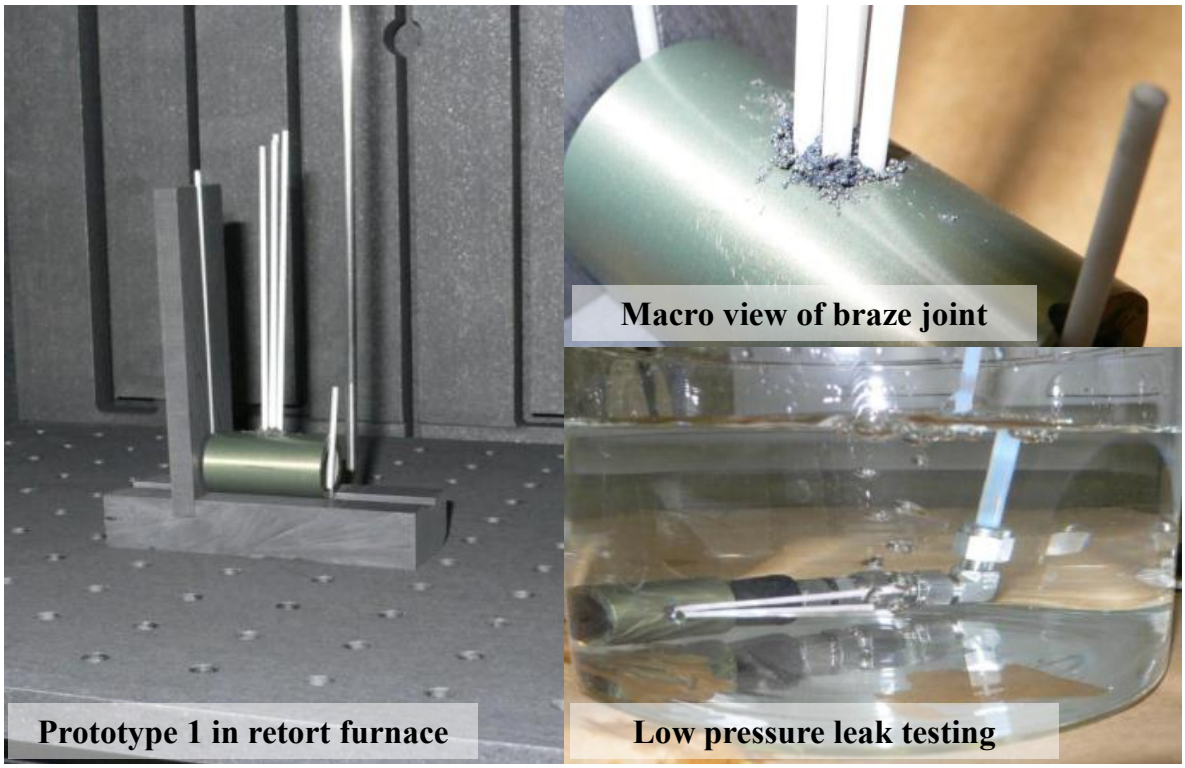

Figure 23 – Brazing alumina tubes to a steel inlet pipe. Images from Michael Gusman, NASA Ames.

The furnace, shown in Figure 23, is:

1. Pumped down to a vacuum of ~10^-4 Torr (no gas sweep)
2. Heated at 5 K/min to 760 °C
3. Held at 760 °C for 10 minutes
4. Heated 5 K/min to 860 °C
5. Held at 860 °C for 15 minutes
6. Cooled 5 K/min to 500 °C

The outcome, shown in Figure 23, is that a functional braze joint is produced, but further process refinement is needed. The first prototype leaks severely at pressures as low as 2 bar. A suspected cause for this leakage is the tricky geometry of the assembly, where the surface of contact between the metal and the ceramic cannot be maintained on an important planar surface, leading to poor joint quality. Work began on a second prototype; however, this work was superseded by a superior technique.

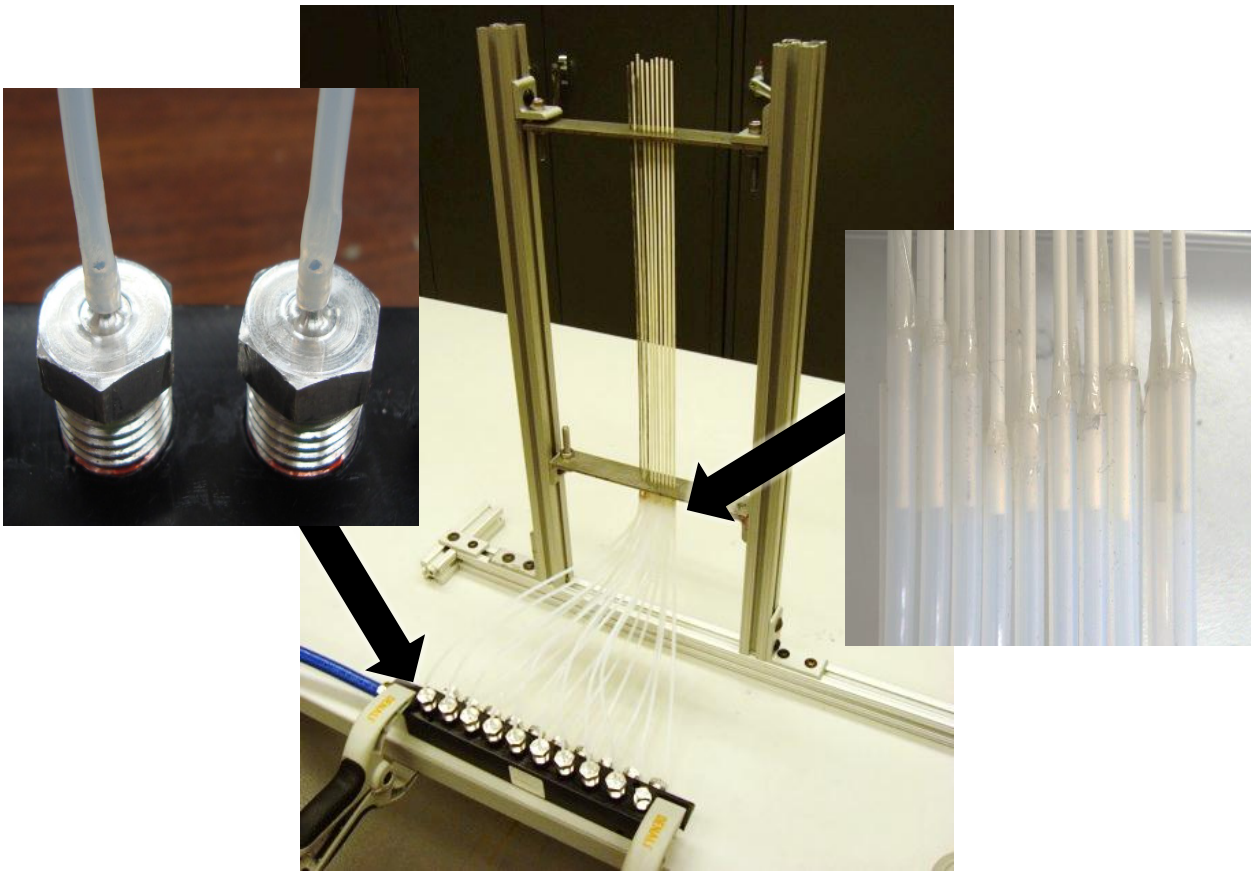

Figure 24 - Alumina channels fitted in PTFE flexible tubes connected to manifold through barbed fittings. Flexible tubes allow tube to expend and make assembly easier.

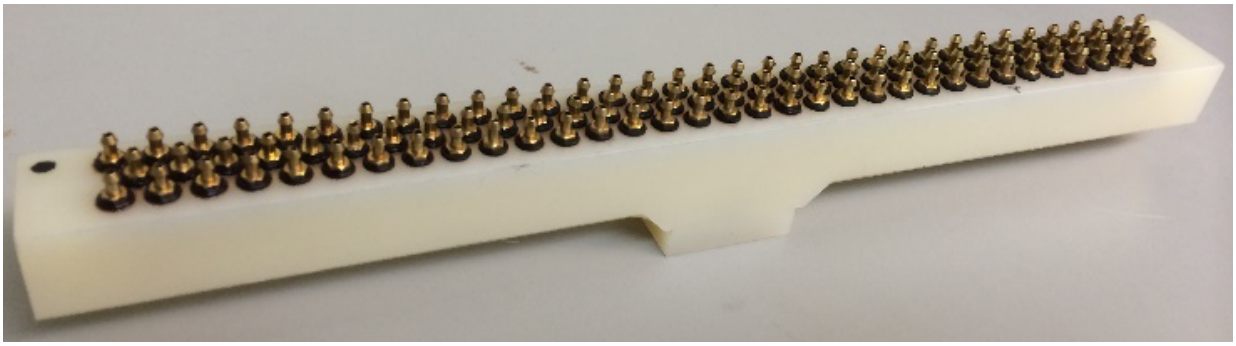

Figure 25 – The compliant inlet after further experimentation and refinement. Bottom: Nylon manifold with brass barbed fittings. Top: Soft flexible polyurethane tubes are clamped to ceramic tubes.

After further experimentation and refinement, the eventual solution uses a nylon manifold connected to the ceramic tubes by soft flexible PFA or polyurethane tubing, as shown in Figure 25. As the ceramic tubes can expand and twist when heated, a floating design on the inlet side gives a degree of freedom to the assembly, allowing them to move, preventing breakage, and greatly simplifying the assembly of the heat exchanger. The choice of nylon for the inlet was motivated by its light weight and relative robustness. Brass barbed fittings sealed with Viton O-rings are used to connect the soft tubing to the inlet while its other end is clamped on the ceramic tube.

3.5.3.3.3 The outlet manifold

The heat exchanger outlet manifold joins the heat exchanger tubes to the inlet end of the nozzle. It must do so in a gas-tight way. Also, the manifold is joined to the hottest end of the heat exchanger tubes, which need to operate at the highest temperatures possible to maximize the exhaust velocity. All this is to be achieved using the minimum possible mass.

Figure 26 – An experimental graphite flange outlet with compressed Grafoil gasket.

Isomorphic graphite was our initial choice of material for the outlet manifold, as shown in Figure 26. It is cheap, machinable, compliant, and has lower creep than metals and ceramics like alumina, mullite and silicon carbide at temperatures greater than 2,000 K. It also has high specific strength at elevated temperatures up to 3,000 K. Pyrolytic grades and graphene operate at even higher temperatures. By starting with graphite, we began on a technical path that can lead to very high-temperature thrusters whose full operating temperature can be realized once the rocket is nearly in the vacuum of space.

The current alumina and mullite heat exchanger tubes are constrained by the temperatures at which they soften and by carbothermic reduction. For alumina tubes at atmospheric pressure, carbothermic reduction occurs wherever carbon is in contact with alumina at >2,250 K, resulting in molten aluminum and carbon monoxide gas. As the pressure drops to 0.01 bar, this temperature falls to 1,850 K

(Halmann, Steinfeld et al. 2014). Inside the tubes, there is a pressure of several bars at least, so it is the outsides of the tubes, where they are in contact with carbon, that the risk is thought to be greatest. Oxide tubes such as zirconia and thoria also suffer from the carbothermic reduction temperature constraint. If needed, tubes can be placed within tubes to thermally isolate the hottest pieces from the structural carbon manifold.

For the manifold configuration shown in Figure 26, the outlet is composed of two parts: A top flange with undersized holes with respect to the tubes OD, and a bottom flange with the same design as its metallic counterpart. Here, the ceramic tubes are mechanically press-fitted in the undersized holes with RTV. This method works well with Alumina but gives poor results with mullite, where the hole's size leads either to poor seal quality or broken tubes in the press-fitting process.

Another version of the manifold of Figure 26 used an overwrap of carbon fiber instead of the steel screws shown. This was found to be impractical for initial testing purposes. Graphite screws were also considered and ceramic screws were briefly tried but proved unsuitable as a direct replacement. To shrink-fit the tubes into the manifold, calculations showed that the tolerances on the tubes and holes needed to be an order of magnitude tighter, requiring post-processing of the tubes. It was eventually realized that the better solution is to use threaded ceramic tubes.

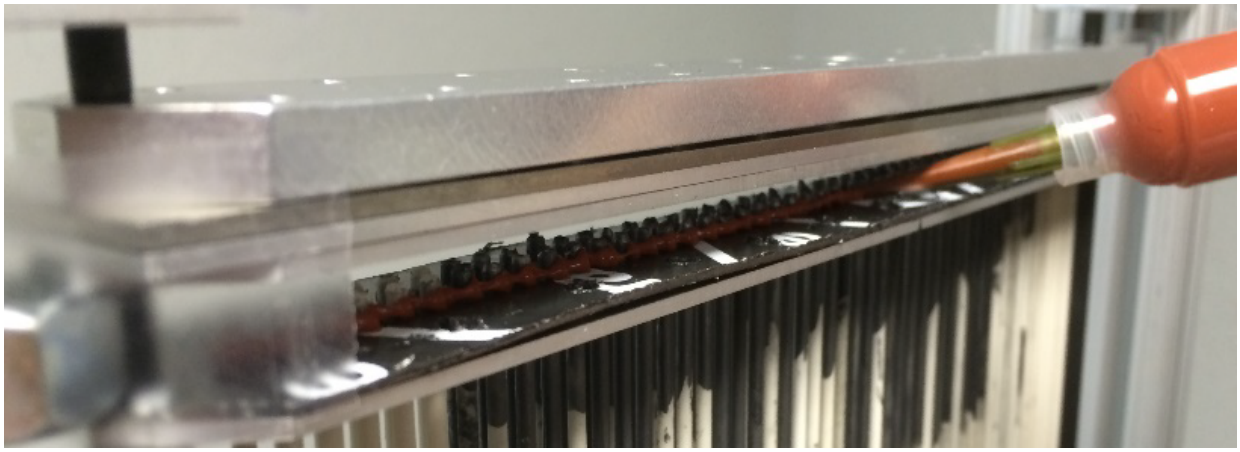

Figure 27 – Metallic manifold for short tests

Because of time and labor constraints, it was eventually decided to use a metallic manifold made of Aluminum and Titanium, which is shown in Figure 27. Although not it would not survive thermal steady state, it proved more than sufficient for the short test times of the MTLS project. The final design uses a system of flanges to form a chamber within which the hot gas is collected before nozzle expansion. A high-temperature flexible graphite (*Grafoil*) gasket is used in combination with RTV to ensure the sealing of the flanges, which are held together by titanium fasteners.

The configuration uses three parts: Two thin plates with high-tolerance holes corresponding to a close fit for the outer diameter of the ceramic tubes, and a bottom flange with a chamber and nozzle machined into it. A pre-perforated Grafoil gasket with undersized holes is placed between the two thin parts and the tubes are then inserted through. After injecting RTV at the junction of the tubes, the assembly is carefully tightened. The flexible gasket deforms and crushes against the tubes while the RTV fills the imperfections in the seal.

3.5.3.3.4 Tube coating

Figure 28 – Top: One of us (Lambot) in the process of coating tubes. Bottom: Excess Aquadag is expelled from air-dried tubes in early experiments. Vaccum oven-dried tubes were used later.

As discussed in the introduction, ceramic tubes were chosen because they can be microwave transparent, and it was later planned to find a way to make them absorb millimeter waves. Ways of doing this were examined by one of us in earlier work (Parkin 2006c). Through the experimentation described in §5.1.2.1, it was found that millimeter waves can be absorbed by using a susceptor layer on the inside of an alumina or mullite tube. This susceptor layer is a layer of graphite, and it is deposited by using a product called Aquadag (Acheson 1907), which, among other uses, is used to produce conductive graphite coatings on cathode ray tubes. We present some of the theory behind this susceptor arrangement in §3.5.3.6.

Different methodologies are used to coat the ceramic tubes. For each tube, the interior is cleaned by squirting acetone through it before applying the Aquadag E mixture. In the first method tried, a ceramic tube end is connected to a plastic syringe while the other end is immersed in the Aquadag mixture. The mixture is drawn into the syringe and pumped out again a couple of times. Excess coating is then forced out of the tube by repeating the above procedure with air. The tubes are left to dry in an upward position in air at ambient temperature, as shown at the top of Figure 28.

In preparing later batches of tubes, the drying step is replaced by a three-hour cure in a vacuum oven at 230 ^{o}C to solve the issue of the slow drying in air. Residual wet Aquadag in the tubes resulted in anomalous test results in early tests at General Atomics. The bottom of Figure 28 shows this residual being blown out of the tubes prior to first use in these early tests.

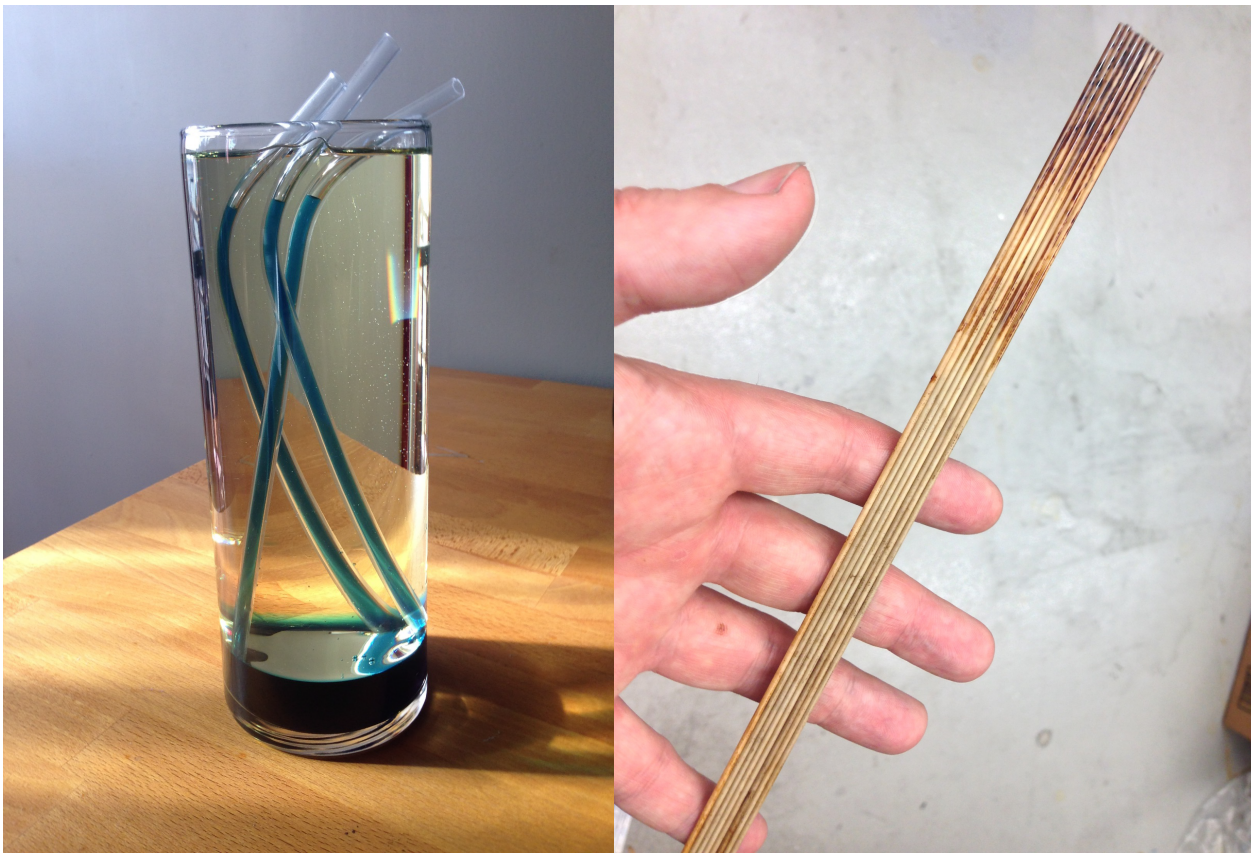

Figure 29 – Method of coating the inside of hundreds of tubes simultaneously using Canola oil

The syringe tube coating method, while giving somewhat repeatable coating quality, has the disadvantage of taking up to a minute of time to prepare each tube. About 100 tubes are needed to build one full size heat exchanger, so to reduce the manual labor involved we devised a method of coating the insides of hundreds of tubes with Aquadag simultaneously. It was also hoped that this method would improve the uniformity of coating. Our coating principle is illustrated using blue dye with large transparent drinking straws on the left side of Figure 29. The blue dyed water represents the Aquadag. Aquadag is poured into the container first, and the tubes are then placed inside. Next, Canola oil is carefully added down the side of the container so as not to disturb the reservoir at the bottom. As more oil is added, its weight forces Aquadag up into all the tubes simultaneously. Eventually, the oil level reaches the top of the container. The small gap at the top of the tubes is a consequence of the density difference between canola oil and water. At the end of the procedure, the oil is removed (e.g., by suction) and the tubes are removed and dried using a vacuum oven.

When tried with actual heat exchanger tubes and Aquadag, it proved difficult to encourage the Aquadag to fill some of the tubes, and additional agitation or suction was needed. For other tubes, Aquadag wicked a short distance up the outside. Upon removal of the tubes from the container, some oil got into the ends of the tubes. In the vacuum oven, residual oil did not evaporate as had been hoped, but instead at least one component broke down into a brown residue that stuck the tubes together as seen on the right of Figure 29.

The deciding factor in abandoning the oil approach was that the tubes had lower absorption performance than those prepared by the syringe method. We attributed this at the time to the very slow flow of Aquadag as it fills the tube over the course of 5 minutes, as opposed to the forced turbulent flow generated by the syringe method[r].

Consequently, the currently preferred method uses a manifold and a hand pump to coat multiple tubes at once. The tubes are fitted in flexible tubing connected to a manifold while the other end of the tube is immerged in the Aquadag mixture. This technique uses the same approach as the original method, pumping the coating a couple of time and blowing it out afterwards. The drying step stays unchanged.

3.5.3.3.5 Tube coating quality control

Non-uniform absorption is caused by a non-uniform Aquadag coating. It results in heat exchangers with hots spots and cold spots, as well as tubes that are broken due to thermal stresses. Depending on the coating method, there can be a zone of very strong absorption next to a zone where the beam is barely absorbed.

[r] James F. Gilchrist of Lehigh University has suggested that we try using a technique in which a bubble pushes the Aquadag coating onto the tube wall. We would like to try this technique in future work. It conflicts with our earlier hypothesis that a slow flow of Aquadag is insufficient to deposit a high-quality graphite coating.

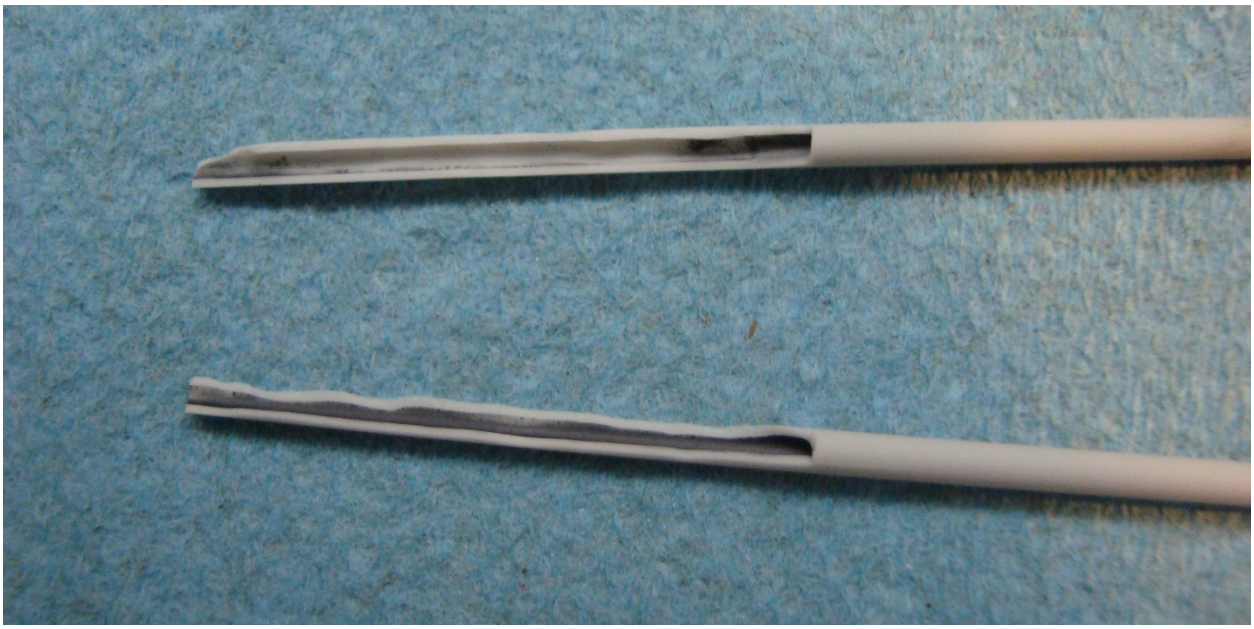

Figure 30 – A heat exchanger tube whose axial fracture is suspected to be caused by an excessive thermal gradient. The excessive gradient could be generated from the region of missing Aquadag coating on the upper piece of tube.

An example of non-uniform coating is seen in a tube that fractured in Figure 30. The graphite coating is almost completely absent in one region. At high fluxes, rapid heating of alumina and mullite tubes leads to thermal shock, a strong gradient of temperature that causes the tube to bend and sometimes break.

The quality of coating is evaluated by two means:

1. The sheet resistance of the tube is measured and compared to theory in §3.5.3.6. A multimeter with probes at either end of the tube is used to measure the resistance of the coating in Ohms. The number of squares the coating would make if laid out flat is calculated by dividing the tube length by the perimeter. The ratio of resistance in Ohms to the number of squares yields the sheet resistance in Ohms per square. For a batch of tubes, one of the tubes is broken into many parts and the sheet resistance measured in each of them to deduce the uniformity of the coating.
2. A carefully aligned red pointer laser is used to illuminate the tube from one end and propagates along the inside of the tube through the air gap. In a dark room, imperfections in the coating are visible from the outside of the tube as glowing red cracks and regions. Experience has shown that darker areas in which the coating is thicker absorb the millimeter-wave beam better than the more transparent areas.

Visual inspection after splitting tubes open reveals that the current method of coating gives unsatisfactory uniformity. Thermal infrared images during operation show an unsatisfactory variation in the tube temperatures. The methods of quality control described above do not provide an effective way to screen out tubes with imperfections. That being said, these methods were developed as part of a crash program and performed well enough for initial results to be obtained. It is recommended that future work in this direction take a more methodical scientific approach. In addition, it is recommended that tubes be tried in which the graphite is mixed in with the bulk alumina or mullite.

3.5.3.3.6 Assembly

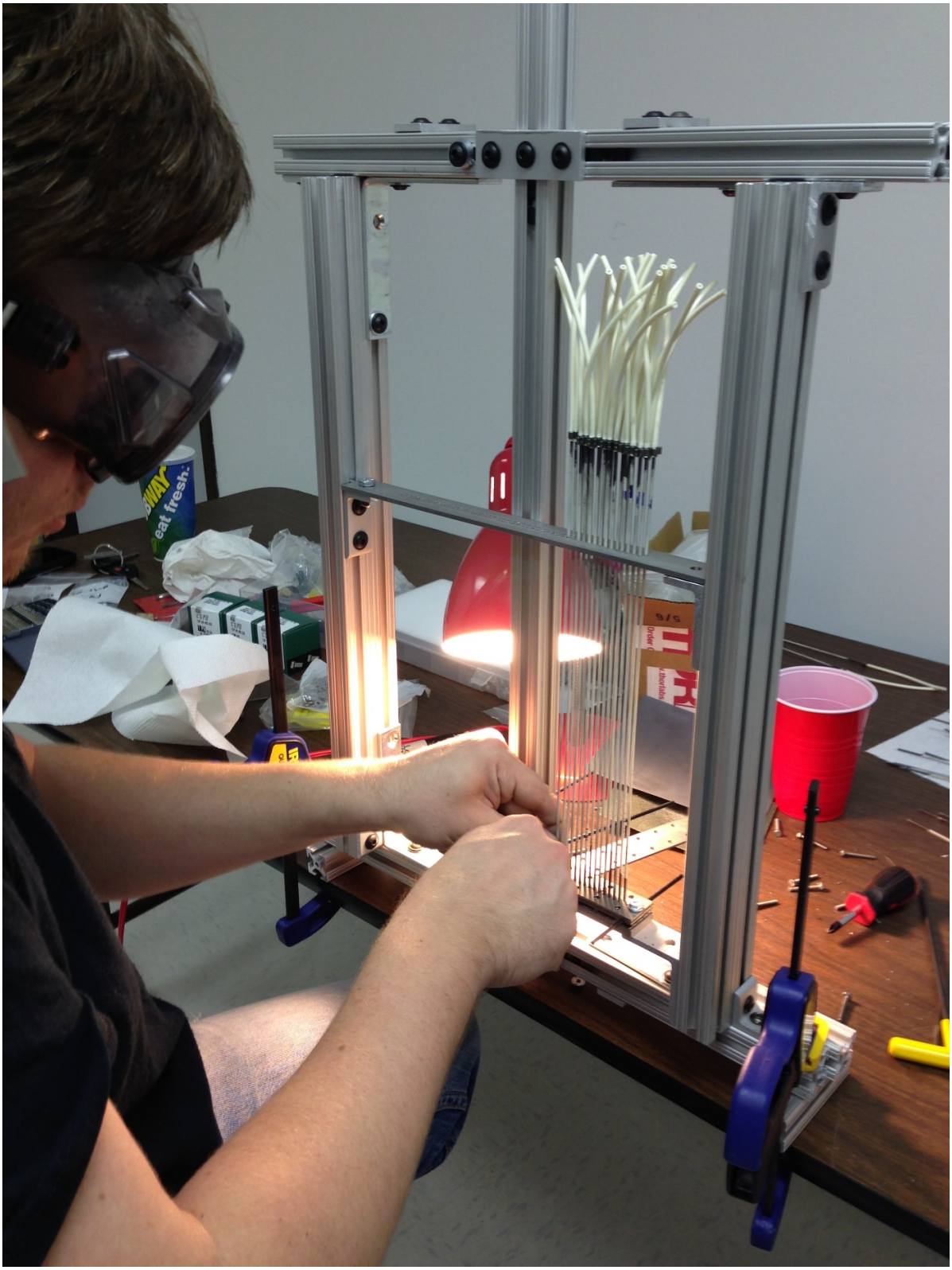

Figure 31 – The heat exchanger is field-assembled or repaired during testing campaigns.

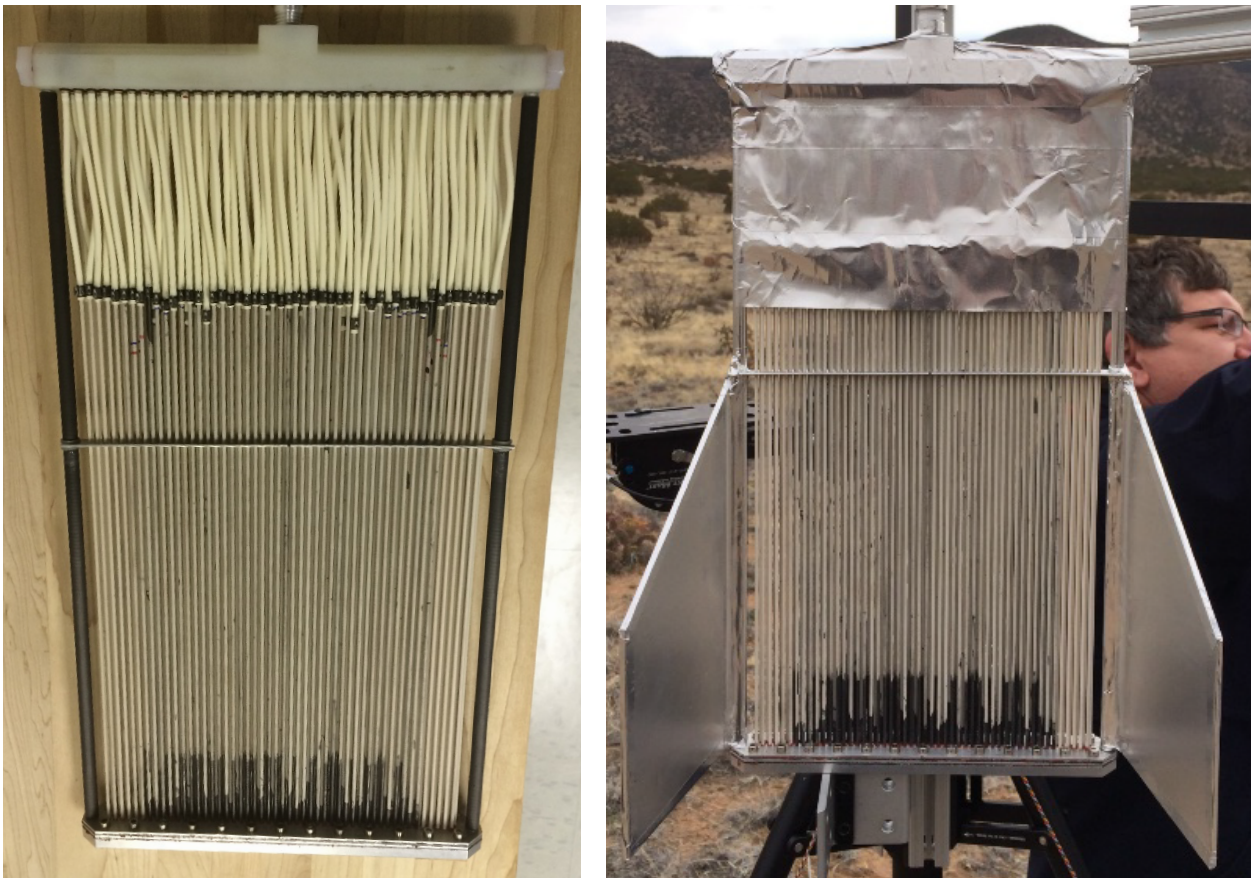

Figure 32 – Left: Final heat exchanger assembly before inegration with rocket. Right: Final heat exchanger assembly after integration with rocket.

Figure 31 shows the various heat exchanger tubes being assembled into a heat exchanger. Carbon fiber struts with threaded inserts fasten into the inlet and outlet manifolds, as shown on the left of Figure 32. Two epoxied Garolite rings hold the alignment jig in place between them. Finally, aluminum kitchen foil covers the soft inlet tubes to prevent them from melting in the millimeter-wave beam during launch, as shown on the right of Figure 32.

3.5.3.3.7 Future work

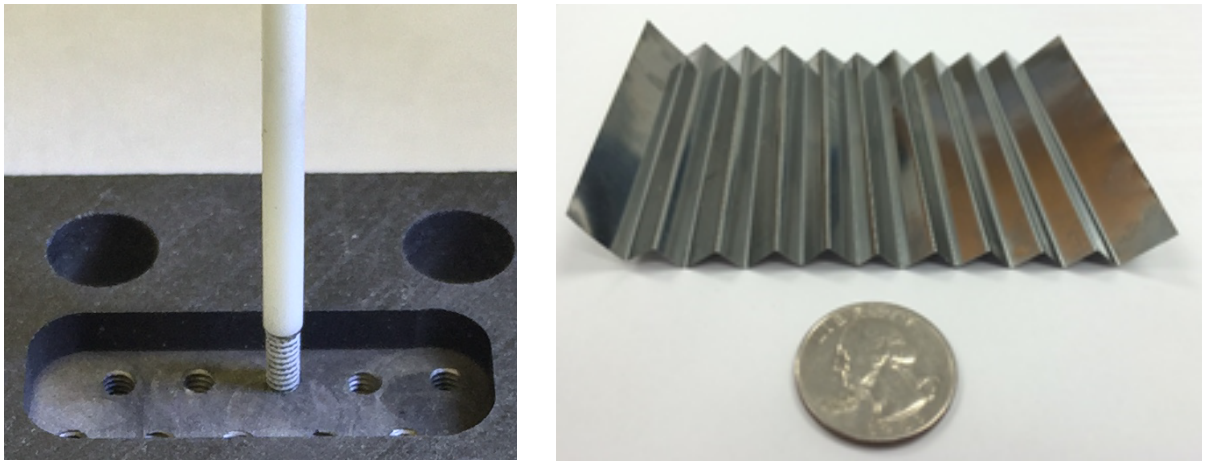

Figure 33 – Future approaches. Left: A threaded alumina tube screws into a threaded graphite outlet manifold, making assembly and replacement are very much quicker and easier. Right: A molybdenum foil back-reflector cuts down the number of tubes needed by a factor of 2-3, eliminating the need for double-row inlet and outlet manifolds, and adding to the rigidity of the entire heat exchanger assembly.

In future work, we recommend threading the ceramic tubes and directly screwing them into the outlet manifold. High-temperature graphite thread sealant can seal them in place. The left side of Figure 33 shows a prototype of this configuration that we built using tubes custom-threaded to 0-80UNF by Coorstek. This prototype proved to be quick to assemble and gas-tight, at the expense of a longer lead-time and an order of magnitude increase in cost per tube. This avoids a disadvantage of the outlet configurations shown in Figure 26 and Figure 27, which is the inability to repair the engine in the case of a broken tube. In the earlier approaches, tube replacement involves taking the whole assembly apart in the metallic case, or risking cracks and breakage in the graphite case.

We also recommend trying a high-temperature foil back-reflector as shown on the right of Figure 33 for future heat exchangers. The back reflector concentrates the incident flux on fewer tubes, substantially reducing the areal cost and areal density of the heat exchanger. It also adds transmits forces around the heat exchanger tubes, especially axially, and adds to the rigidity of the assembly, which would reduce the damage from a repeat of the impact seen in Figure 133.

Finally, we recommend that future work addresses the key problem of poor absorption uniformity (as reported in §5.1.2). James F. Gilchrist of Lehigh University has suggested to us that we use a bubble to push the Aquadag coating onto the inner wall of a tube at low Péclet number (Frank, Anderson et al. 2003). It is also possible to mix graphite, carbon nanotubes, graphene, titanium dioxide, and other additives directly with the alumina or mullite paste from which the tubes are extruded in order to modify their electrical resistivity for the purpose of volume absorption. Both these approaches should be tried in future work.

3.5.3.4 Non-uniform illumination

What happens when the heat exchanger is not uniformly illuminated? In a heat exchanger comprised of similar tubes of uniform length and diameter, the total enthalpy of the flow varies between tubes. Alternately, it is possible to vary the diameter of each tube such that all tubes produce equal total enthalpy at their exits. This happens because the tube diameter controls the ratio of flux to mass flow rate per unit surface area.

Propellant	CO_2
Total pressure at outlet	5 bar
Static pressure at nozzle outlet	1 bar (for perfectly matched expansion)
Total temperature at inlet	300 K
Total temperature at outlet of pilot tube	1,700 K
Transmitted power	50 kW
Hydraulic inner diameter of pilot (central) tube	0.79 mm
wall thickness / inside hydraulic diameter	0.5
Heat exchanger width	30 cm
Heat exchanger length	60 cm
Tube roughness	0 microns
Tube material	Al_2O_3

Table 9 – Input values for fixed and variable diameter heat exchanger calculations under non-uniform illumination

Making a heat exchanger with tubes of equal diameter is cheaper and quicker than making a heat exchanger with many tubes of differing diameters. For the MTLS project, we asked ourselves whether it was necessary to vary the tube diameter, or a fixed tube diameter would suffice. To answer this question, we modelled the heat exchanger as an array of alumina tubes containing quasi-1D channel flows and illuminated by a Gaussian beam centered upon it. We used the input values given in Table 9 to model heat exchangers with fixed diameter tubes and variable diameter tubes.

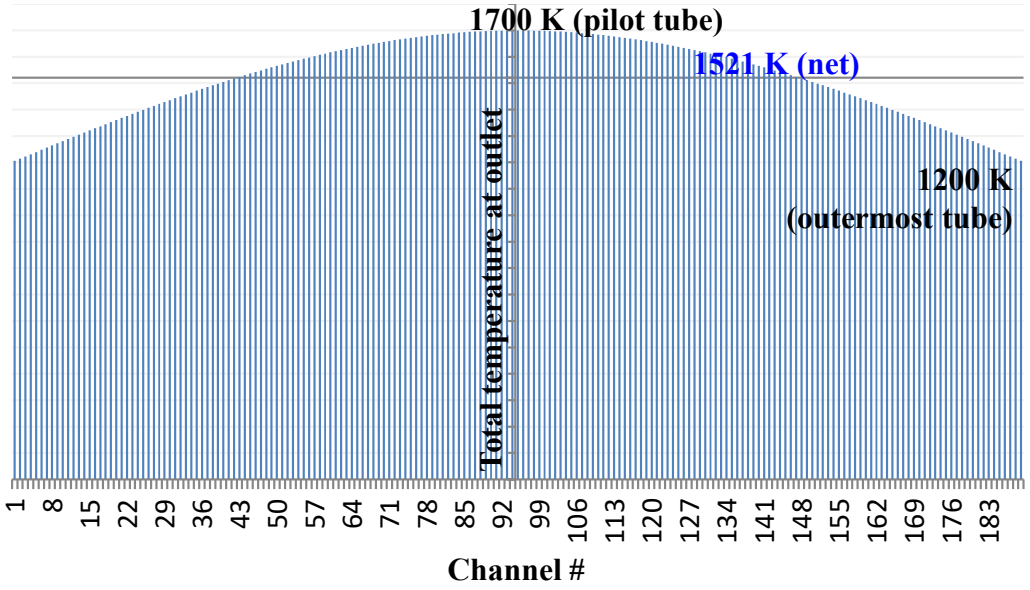

Figure 34 – Non-uniformly illuminating tubes of uniform diameter leads to varying tube outlet temperatures

For both fixed and variable tube diameter heat exchangers, the solution procedure for the pilot (central) tube is the same. The central tube we call the pilot tube because it is the tube in the most intense part of the beam with the maximum overall power. Given the other boundary conditions in Table 9, it turns out that if the pilot tube does not prematurely reach the sonic before the prescribed tube length, then neither do the other tubes, which receive less power.

Other assumptions used for the simulations are that the tubes perfectly absorb the flux that is incident upon them, and that there is no re-radiation of heat or other coupling between the tubes, except for the fluid conditions at the inlet and outlet manifolds.

	Uniform tube diameter	**Variable tube diameter**
Absorbed power	33 kW (34% beam spillage)	33 kW (34% beam spillage)
Total pressure at inlet	10.2 bar	10.2 bar
Wall flux of pilot tube	135 kW/m^2	135 kW/m^2
Power absorbed by pilot tube	200 Watts	200 Watts
Inlet Mach number of pilot tube	0.05	0.05
Outlet Mach number of pilot tube	0.27	0.27
Thrust	18.6 N	20.5 N
$\langle T_t \rangle$ over all tubes at outlet	1,521 K	1,700 K (an input in this case)
Specific impulse	97 sec	91 sec
Nozzle area expansion ratio	1.5	1.5
Mass flow rate	20 grams/sec	23 grams/sec
Number of tubes	233	191
Mass of tubes	570 grams	670 grams
Areal density	3.2 kg/m^2	3.7 kg/m^2

Table 10 – Results from Version 2.0 of the system model for heat exchanger performance in the cases of uniform tube diameter and variable tube diameter (such that the total temperature at the outlet is equal to the pilot tube). Results that should be the same in both cases are shaded with a gray background.

Every tube has the same total pressure at the inlet and outlet because manifolds join them. For the pilot tube, we use a root-finding algorithm to vary the Mach number at its outlet such that the inlet matches the prescribed temperature of 300 K given in Table 9. Integrating backwards from the outlet implies a total pressure of 10.2 bar at the inlet, as shown in Table 10.

For a heat exchanger comprised of equal diameter tubes, we use a root-finding algorithm to vary the inlet Mach number of each tube such that the total pressure at the outlet matches the value in Table 9. Non-uniform illumination causes the variation in outlet temperatures seen in Figure 34. The pilot tube outlets at 1,700 K and the outermost tube outlets at 1,200 K. Surprisingly, the net outlet total temperature is 1,521 K because less mass flows through the colder tubes. Consequently, we chose a fixed tube diameter for the MTLS heat exchanger. For a small orbital system, it is likely that the beam will be much larger than the rocket in order to reduce beam director cost, thus illuminating the heat exchanger nearly uniformly.

For a heat exchanger comprised of varying diameter tubes, we use the procedure for uniform tube diameter in combination with an outer root-finding loop that varies each tube diameter such that the tube outlets at 1,700 K. We show the resulting diameters vertically on the left of this page, side-by-side with (and to relative scale with) the uniform diameter tube heat exchanger.

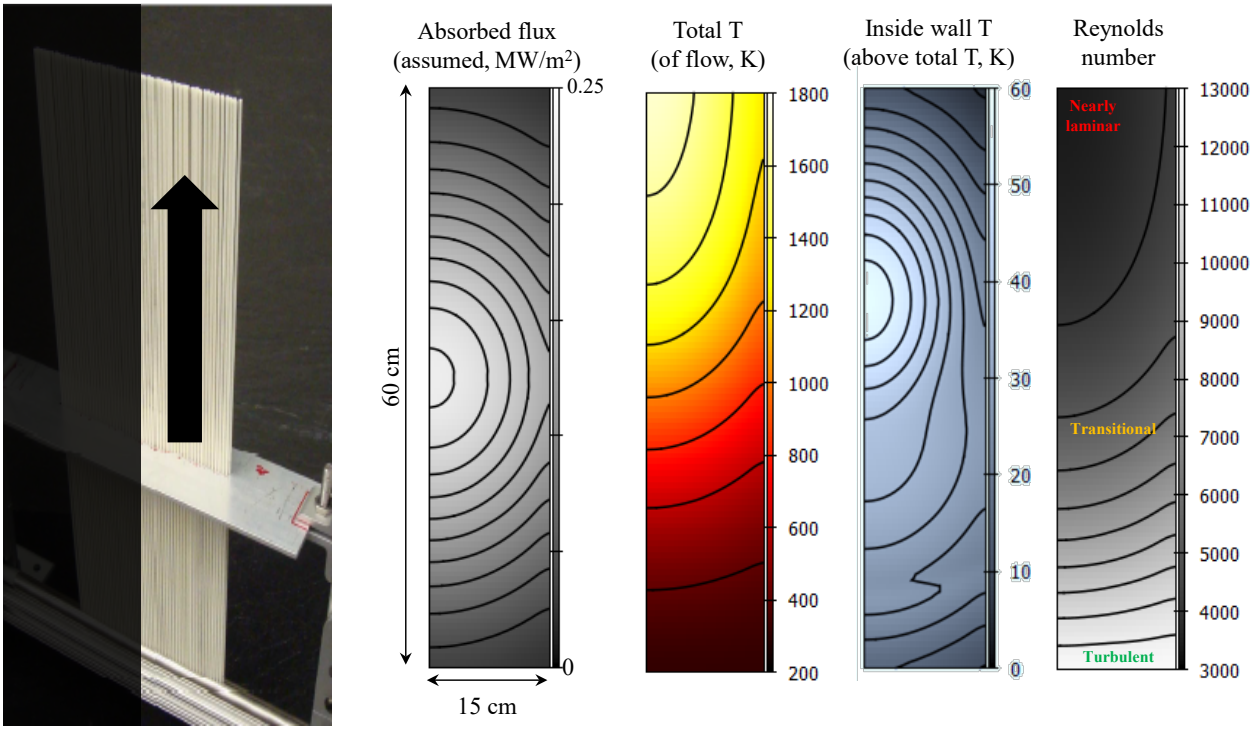

Figure 35 – Simulated right half heat of exchanger for uniform channel diameters. Values shown correspond to the case described in Table 9 and Table 10. Note that that scales are shown immediately to the right of each contour map. In the case of the Reynolds number, ignoring the scale gives the incorrect impression that turbulent flow occurs at a Reynolds number of 3,000 as opposed to 13,000.

It is also possible to produce maps of heat exchanger quantities of interest, as shown in Figure 35. A particular design concern was that the power level and size of the heat exchanger needed for the MTLS project tended to produce channel flows that spanned the transitional flow regime in which heat transfer can be particularly poor and hard to predict.

Since the calculations described above were carried out (in 2013), we have discovered an error in the calculation of Fanning friction factor. We have corrected this error in Version 3.0 of the system model, but as previously discussed, this version of the model is not yet ready and so this calculation cannot yet be re-run. Nevertheless, we present Figure 34, Table 10, and Figure 35 here to illustrate the qualitative effects of non-uniform illumination and to show how to model these effects.

3.5.3.5 Materials

3.5.3.5.1 Alumina

In the case of alumina, some of the best measurements of real and imaginary dielectric constants as a function of temperature and material grade were taken by ORNL in the 1980s during a search for suitable gyrotron window materials (Ho 1984). Other early room-temperature datasets were compiled for millimeter-wave radar applications and millimeter-wave optics in the context of telescopes (Lamb 1996). Many of these properties are collated by Goldsmith (Goldsmith, Electrical et al. 1998).

The temperature-dependent complex permittivity of alumina has been published (Katz 1992) based on measurements of Sumitomo grade AKP-50 alumina at 90-100 GHz. It is this data that is used in the absorption model presented in §3.5.3.3. In this case, we express the relative complex permittivity ε^* as,

$$\varepsilon^* = \varepsilon' - i\varepsilon''. \quad [89]$$

The real part of the relative complex permittivity, more conventional known as the relative dielectric constant ε', is approximated to Katz's data by a polynomial function of temperature,

$$\varepsilon' = 1.97\times10^{-3}T + 8.76. \quad [90]$$

The loss tangent $\tan\delta$ implies the imaginary part of the relative complex permittivity via,

$$\varepsilon'' = \varepsilon' \tan\delta, \quad [91]$$

where $\tan\delta$ is approximated to Katz's data by a polynomial function of temperature,

$$\tan\delta = 4.087\times10^{-13}T^3 - 1.799\times10^{-13}T^2 - 2.318\times10^{-13}T + 1.018\times10^{-13}. \quad [92]$$

When plotted, the loss tangent is relatively flat until about 1,000 K, followed by a sharp increase above that temperature. For both equations [90] and [92], temperature T is measured in Kelvin and the approximations are valid in the range 300-2,000 K.

3.5.3.5.2 Mullite and mullite-type ceramics

Ordinary mullite consists of 60% Al_2O_3 by moles and 40% SiO_2. Previously published emissivity values for mullite (Goodson 1997) are inconsistent with other publications and undoubtedly vary with temperature, wavelength and sample. Mullite melts at 2,110 K, and this melting point slowly decreases as the silica content is increased (Duval, Risbud et al. 2008).

A mullite-type ceramic with the trade name of Omegatite 200 consists of 55.40% Al_2O_3, 42% SiO2, 0.80% Fe_2O_3, 0.70% K_2O, 0.50% TiO_2, 0.50% Na_2O, 0.10% Ca, and 0.04% MgO. Because it is close in composition to pure mullite, we assume here that the melting point is also 2,110 K. Based on an experiment reported in §5.1.2.2.3 in which two tubes of this material melt, we estimate its high-temperature total hemispherical emissivity in the long-wave infrared (LWIR) range of the FLIR camera to be 0.65.

3.5.3.6 Absorption

As part of the MTLS project, it was necessary to build a millimeter-wave absorbent heat exchanger for the first time. Of the several millimeter-wave absorption mechanisms available (Parkin 2006c), it is susceptor absorption (absorption by a thin conducting layer) that was the first to work well enough in practice to be used as the basis for a thruster.

In §5.1.2.1 we describe the first experiments where a susceptor successfully absorbs millimeter-waves within the heat exchanger. The best performing susceptor tried so far is a graphite layer coated onto the inside of a mullite thermocouple tube. The coating is applied to the inside of a tube in the form of

Aquadag E (Acheson 1907), a commercial form of colloidal graphite suspended in water with added ammonia to improve surface adhesion. Changing the mixture ratio of Aquadag to distilled water controls the sheet resistance of the graphite layer.

To maximize absorption, we can control tube wall thickness, tube diameter, and graphite sheet resistance. Given this, what are the best values to choose? This question motivates the following theoretical work.

3.5.3.6.1 Simple planar susceptor model

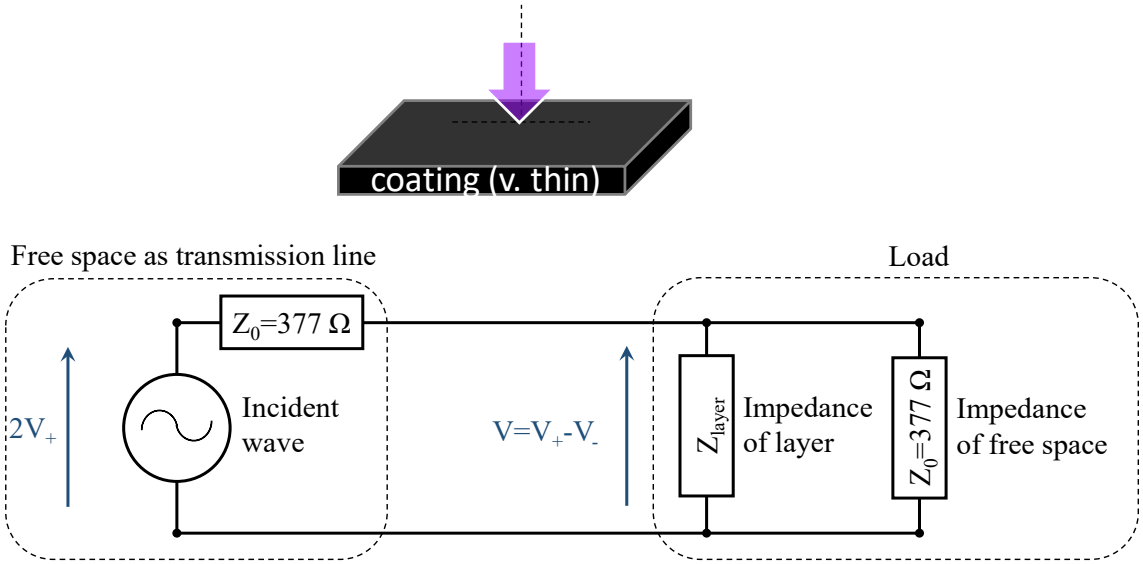

Figure 36 – Top: Planar susceptor layer under normal illumination. Bottom: Thévenin equivalent circuit of the arrangement.

An initial description of susceptor absorption can be made by considering the arrangement shown in Figure 36. At the top of the figure, a wave is normally incident on the susceptor layer. A portion of this wave is reflected, a portion absorbed, and a portion transmitted into free space, and this can be represented as a transmission line. This transmission line can in turn be represented as the Thévenin equivalent circuit shown at the bottom of the figure. The incoming electromagnetic wave is an AC voltage source in series with free space, the susceptor layer is a resistor, and the free space behind the susceptor layer is another resistor in parallel. These last two resistors together form the circuit load.

We define the voltage incident on the load to be V_+. If the coating were to be taken away, there would be no resistor representing it and no reflected wave, so the circuit would consist of two resistors each of 377 Ω, and thus having equal voltage across them. Since one of these resistors is our load, which we have defined to have an incident voltage V_+, it follows that our Thévenin equivalent source voltage is $2V_+$.

The effective impedance Z_e of the load (2 resistors in parallel) can be written,

$$Z_e = \frac{1}{\frac{1}{Z_{layer}} + \frac{1}{Z_0}}. \qquad [93]$$

By equating the current I corresponding to voltages $2V_+$ and V respectively,

$$I = \frac{2V_+}{Z_0 + Z_e} = \frac{V}{Z_e}, \quad [94]$$

and rearranging for voltage V across the load,

$$\frac{V}{V_+} = \frac{2}{\frac{Z_0}{Z_e} + 1}. \quad [95]$$

Defining the ratio r of layer impedance to free space impedance,

$$r \equiv \frac{Z_{layer}}{Z_0}, \quad [96]$$

Equation [95] reduces to,

$$\frac{V}{V_+} = \frac{1}{\frac{1}{2r} + 1}. \quad [97]$$

Since

$$V \equiv V_+ - V_-, \quad [98]$$

equation [97] can be arranged into an expression for voltage reflection ratio Γ,

$$\Gamma \equiv \frac{V_-}{V_+} = \frac{1}{1 + 2r}. \quad [99]$$

The incident, reflected, transmitted and absorbed powers can be transcribed directly from the equivalent circuit in Figure 36,

$$\mathrm{P}_+ = \frac{V_+^2}{Z_0}, \quad [100]$$

$$\mathrm{P}_- = \frac{V_-^2}{Z_0}, \quad [101]$$

$$\mathrm{P}_T = \frac{V^2}{Z_0}, \quad [102]$$

$$\mathrm{P}_A = \frac{V^2}{Z_{layer}}. \quad [103]$$

Hence, simple expressions for the reflectance R, transmittance T and absorptance A can be found by dividing equations [101]-[103] by equation [100]:

$$R = \Gamma^2 = \frac{1}{(1+2r)^2}, \quad [104]$$

$$T = \frac{4r^2}{(1+2r)^2}, \quad [105]$$

$$A = \frac{4r}{(1+2r)^2} \quad [106]$$

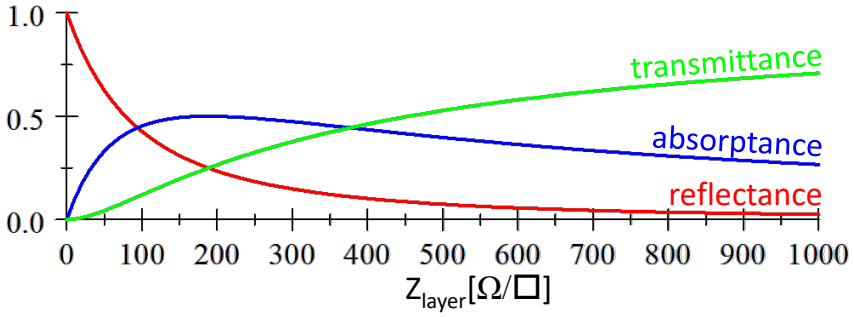

Figure 37 – Reflectance, transmittance and absorptance of a thin conducting layer as a function of sheet resistance. The higher the sheet resistance, the more like a dielectric insulator the layer behaves, corresponding to higher transmittance. The lower the sheet resistance, the more metallic the layer behaves, corresponding to higher reflectance.

Equations [104]-[106] are plotted in Figure 37. As sheet resistance tends to zero, the layer becomes a reflector and no energy is transmitted or absorbed. As sheet resistance tends to infinity, the layer becomes transparent, and no energy is reflected or absorbed. Between those extremes, there is an optimum sheet resistance at which absorptance is maximized. Differentiating equation [106] shows that a theoretical maximum of 50% absorption occurs at $r = 1/2$. Inspection of equations [104]-[106] shows that their sum equals unity, as expected from energy conservation,

$$\mathrm{R} + \mathrm{T} + \mathrm{A} = 1. \quad [107]$$

The simple planar susceptor model predicts a maximum of 50% absorptance at a sheet resistance of 189 Ω/□. To improve on this absorptance and to model the local effect of the tube wall, another layer must be added in front of this coating. The mathematical description and performance of this layered approach is given in §3.5.3.6.2.

3.5.3.6.1.1 Shielding thickness

Simple metal foil can shield from millimeter-waves, but how thick does it need to be? For a conductive film of thickness t, transmission line theory (Liu and Tan 2013) yields the following expression for AC sheet impedance Z_{layer},

$$\mathrm{Z}_{layer} = \frac{\rho}{\delta}\frac{1}{1-e^{-t/\delta}}. \quad [108]$$

Skin depth δ is a function of electromagnetic wave frequency f, bulk resistivity ρ, and permeability μ,

$$\delta = \sqrt{\frac{\rho}{\pi f \mu}}. \qquad [109]$$

In the DC limit as $f \to 0$,

$$\mathrm{Z}_{layer,DC} = \lim_{t/\delta \to 0}\left(\mathrm{Z}_{layer}\right) \to \frac{\rho}{t}. \qquad [110]$$

This corresponds to $t \ll \delta$. When $t \gg \delta$, the sheet impedance becomes independent of the thickness,

$$\lim_{t/\delta \to \infty}\left(\mathrm{Z}_{layer}\right) = \mathrm{Z}_{layer,DC}\,\frac{t}{\delta} \to \frac{\rho}{\delta}. \qquad [111]$$

Notice that this expression is similar to the last. It is equivalent to a DC current being passed through a thickness equal to the skin depth. Equation [111] is substituted into equation [108] to yield,

$$\frac{\lim_{t/\delta \to \infty}\left(\mathrm{Z}_{layer}\right)}{\mathrm{Z}_{layer}} = 1 - e^{-t/\delta}. \qquad [112]$$

This is rearranged to form the useful expression,

$$t/\delta = -\ln\left(1 - \frac{\lim_{t/\delta \to \infty}\left(\mathrm{Z}_{layer}\right)}{\mathrm{Z}_{layer}}\right). \qquad [113]$$

Combining equations [96], [105], [108] and [109] yields the following relation between transmittance and thickness:

$$t = -\delta \ln\left[1 - \frac{2\rho}{\delta Z_0}\left(\frac{1}{\sqrt{T}} - 1\right)\right] \qquad [114]$$

Putting in numbers: The impedance of free space $Z_0 = 377\ \Omega/\square$. For aluminum, $\rho = 26.5\ n\Omega \cdot m$ and $\mu = \mu_0 = 4\pi\times10^{-7}\ \mathrm{H/m}$. Choosing $T = 0.0001$ (0.01% transmittance) and $f = 95\ \mathrm{GHz}$, equation [114] predicts a foil thickness of just 14 nm! The skin depth is 266 nm, so this is just 5% of the skin depth.

3.5.3.6.1.2 Optimal absorber thickness

Differentiating equation [106] shows that a theoretical maximum of 50% absorption occurs at $r = 1/2$. Equation [113] shows that this corresponds to a thickness of just 0.14 nm, or 0.05% of the skin depth for aluminum. This is 100 times thinner than the reflector calculated in the previous section and is about three times smaller than the lattice spacing of the aluminum crystal structure. That is to say, a single monolayer of aluminum atoms would conduct too well to form an optimal absorber.

Of greater interest for absorption is carbon. Using a bulk resistivity of $100\ \mu\Omega\cdot\mathrm{m}$ and a relative permeability of 1 for graphite, Equation [113] predicts maximum absorption at a thickness of 0.5

microns, or 3% of the skin depth. In comparison, the thickness of a pencil line is estimated to be around 20 nm, so this is 25 times thicker. For Aquadag graphite layers, the loose flake structure gives an even higher bulk resistivity. These Aquadag layers are characterized directly in terms of sheet resistance as a function of preparation method, thickness and bulk resistivity are uncertain and not typically used, measured or calculated.

3.5.3.6.2 Planar stratified layer model

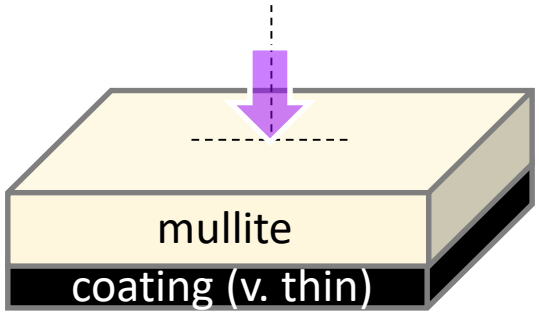

Figure 38 – A thin susceptor layer as in Figure 36 but this time with a mullite layer on top.

The planar stratified layer model describes electromagnetic properties in layered structures, such as that shown in Figure 38. We state without proof the following equations for the reflectance, transmittance and absorptance of a layered structure,

$$R = \left(\frac{\eta_0 B - C}{\eta_0 B + C}\right)\left(\frac{\eta_0 B - C}{\eta_0 B + C}\right)^*, \quad [115]$$

$$T = \frac{4\eta_0 \,\mathrm{Re}(\eta_m)}{(\eta_0 B + C)(\eta_0 B + C)^*}, \quad [116]$$

$$A = \frac{4\eta_0 \,\mathrm{Re}(BC^* - \eta_m)}{(\eta_0 B + C)(\eta_0 B + C)^*}. \quad [117]$$

Where,

$$\begin{bmatrix} B \\ C \end{bmatrix} = \left\{\prod_{r=1}^{q} M_r\right\}\begin{bmatrix} 1 \\ \eta_m \end{bmatrix}, \quad [118]$$

$$Y = C/B, \quad [119]$$

$$M_r = \begin{bmatrix} \cos\delta_r & (i\sin\delta_r)/\eta_r \\ i\eta_r \sin\delta_r & \cos\delta_r \end{bmatrix}. \quad [120]$$

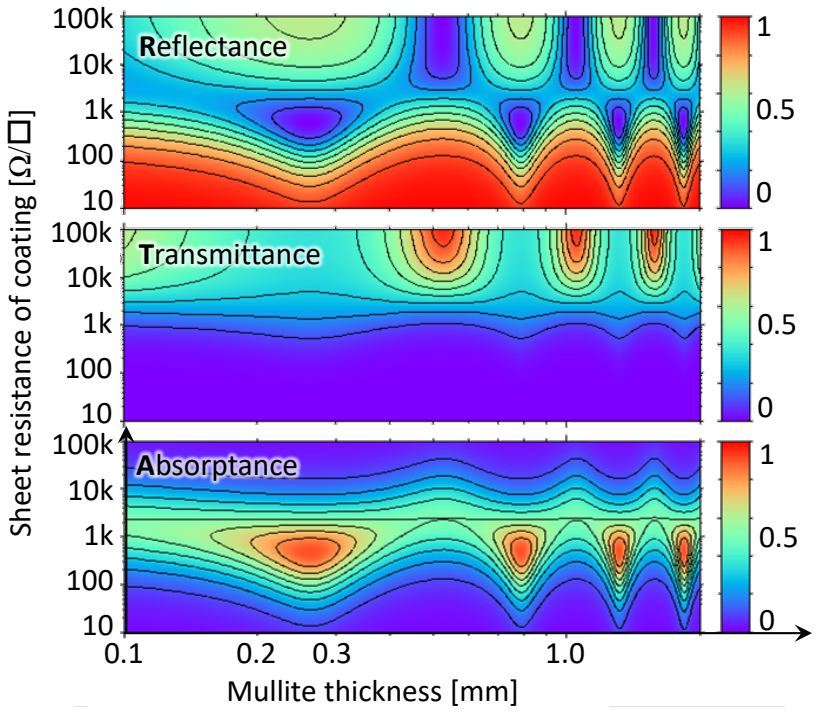

Figure 39 - Up to 90% absorption around 0.2-0.3 mm (1/4 wavelength thick and multiples thereof) and 100-1,000 Ω/□.

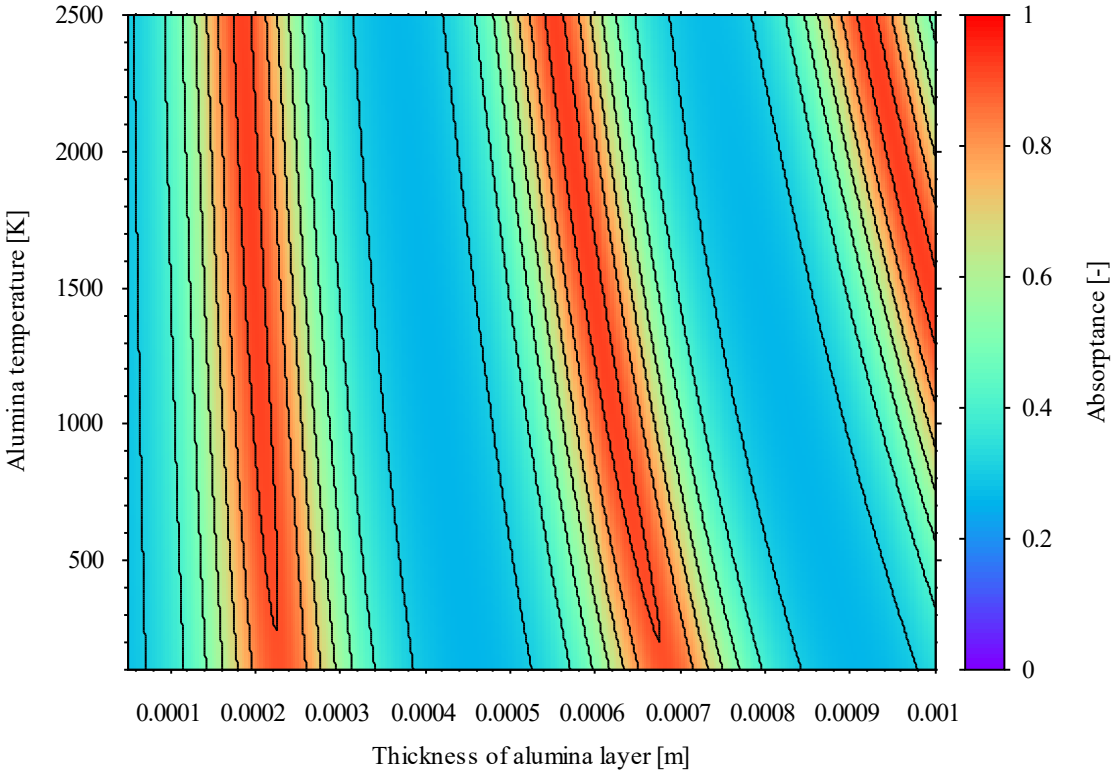

Figure 40 - Absorptance in an alumina slab as thickness and temperature are varied. Additional assumptions: 110 GHz illumination at normal incidence.

3.5.3.6.3 2D finite element periodic tubular absorption model

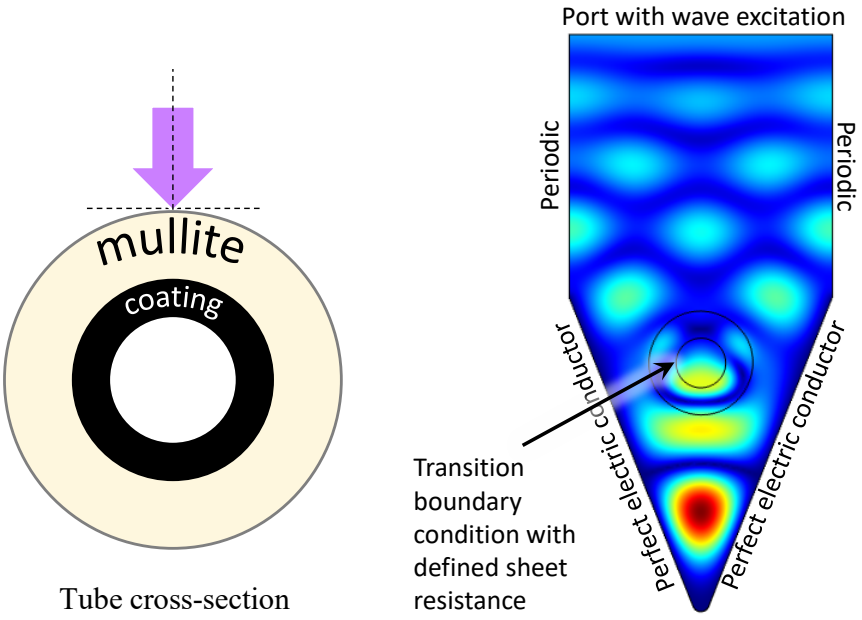

Figure 41 – 2D finite element model of heat exchanger tube in an array with foil back-reflector

The planar stratified layer model fails to take into account the curvature of the heat exchanger tubes, which is important because the tube diameter is on the order of the incident wavelength. Consequently, we are constructing a finite element model using the COMSOL software to see whether or not the predictions of the stratified layer model can be used as an approximation. This finite element model is shown on the right of Figure 41 and includes the V-shaped foil back-reflector and concentrator of Figure 33. Furthermore, it uses periodic boundary conditions so that coupling effects within arrays of heat exchanger tubes are also captured.

Although Figure 41 shows preliminary results from a calculation of the norm of electric field within the structure, major efforts remain and must now be left to future work. This future work is to verify the correct and intended operation of the boundary conditions, to map out the performance of the heat exchanger structure as a function of tube dimensions and reflector dimensions, and to investigate the degradation of performance due to misalignments and manufacturing tolerances.

3.5.3.7 Areal Density

The areal density of the heat exchanger, measured in kg/m^2, is a key figure of merit. It affects the thrust to weight ratio of the propulsion subsystem and other design decisions for the rocket. It is a figure that has been debated, used and questioned during preliminary subsystem mass estimates.

By the end of the MTLS project in May 2014, a heat exchanger areal density of 5 kg/m^2 had been achieved. This figure includes the mass of the frame and inlet and outlet manifolds. It is expected that this areal density can be decreased by a factor of two to four by using a foil back-reflector, which decreases the number of ceramic tubes, and by refinement of the inlet and outlet manifolds. Further reductions are possible by increasing the concentration ratio of the back reflector, and by making the

tube walls thinner. The tube walls themselves are thicker than needed to contain the operating pressures. On the other hand, our experience with thinner tubes is that they are harder to extrude at length, easier to break, harder to assemble into a heat exchanger, and they are also harder to thread.

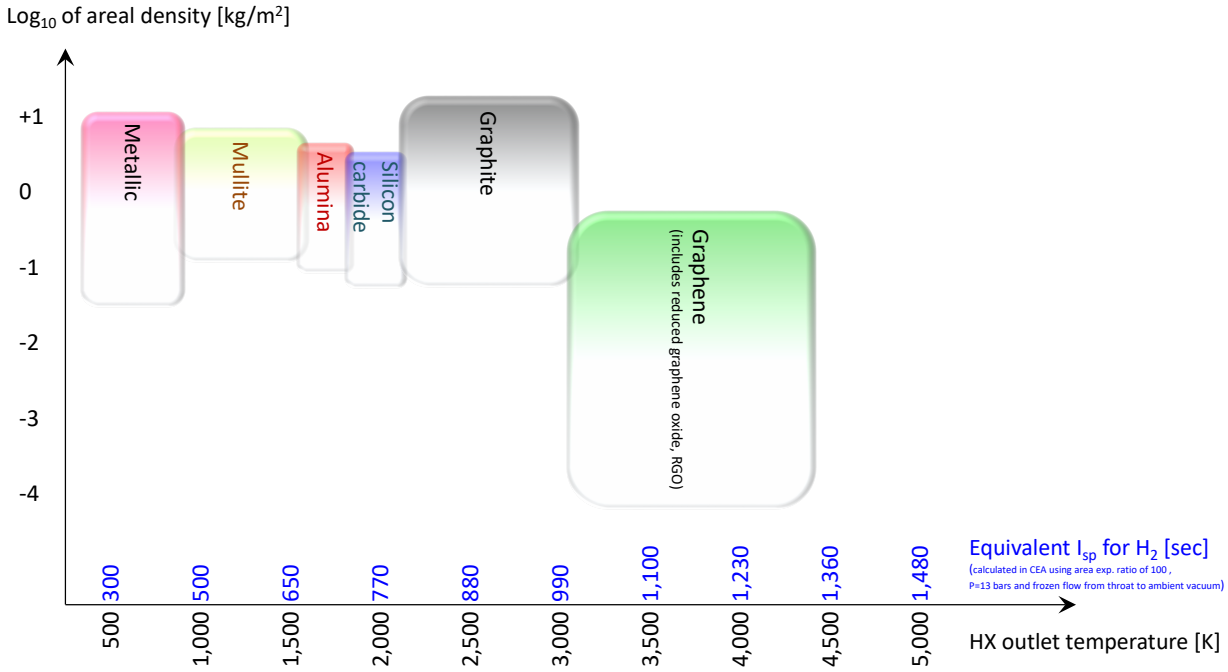

Figure 42 - Roadmap for heat exchanger materials

The 50 kg wet mass point design has an areal density of 1.4 kg/m^2 and a peak wall temperature of 1,900 K. Simple evolution of the existing mullite heat exchanger will likely achieve the areal density target, but the temperature target will likely require a switch to a different material or an added post-heating stage made of a different material. Figure 42 shows a likely progression of selected heat exchanger tube materials and the approximate temperature range and areal density range that is best suited to each.

Metallic heat exchangers can be very lightweight and easy to build, for example using the roll-bonding technique. We have developed mullite and alumina heat exchangers for the MTLS project. Silicon carbide was one of the earliest materials identified for the millimeter-wave absorbent heat exchanger (Parkin, DiDomenico et al. 2003) due to its combination of high maximum temperature, low areal density, and tunable resistivity. However, silicon carbide is also much more expensive than alumina and mullite and its resistivity is not typically controlled for structural (non-electronic) applications. Carbon in the form of pyrolytic graphite or graphene is the ultimate heat exchanger material in terms of both peak temperature and areal density.

For propellants such as methane that are thought to be direct absorbers of millimeter-waves, and for ionized propellants, it is possible to use various techniques to keep the wall much cooler than the bulk flow while still heating that flow. For example, heat exchanger tubes can be nested, with the inner tube holding the hottest flow and the outer tube holding much colder flow. The inner tube can be porous, so that colder flow at higher pressure forms a cool film against the tube wall. For now, we assume that these techniques are not used.

3.5.3.8 Segmentation

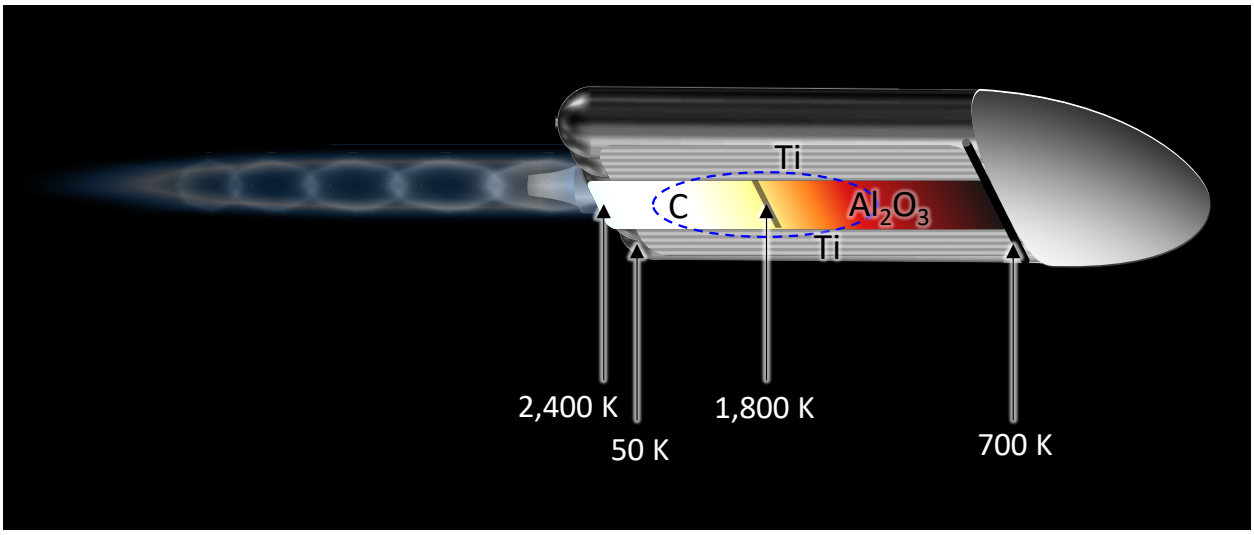

Figure 43 – A high-performance variant of the millimeter-wave thermal rocket. The tank is segmented to provide greater beam interception area, which in turn reduces the size of the beam director. The heat exchanger is segmented to maximize propellant temperature while minimizing cost and mass.

In the previous section we mention metallic, ceramic and carbon heat exchangers. For each of these types, there is a characteristic cost range, ease of use, maximum flux, and maximum temperature. In Figure 43, we show how the comparative advantage of several of these can be combined.

The comparative advantage of roll-bonded metallic heat exchangers is their low cost and low areal density, so they are ideal for large area coverage over less intense areas of the beam outside the blue dashed line in Figure 43. Aluminum is typically used for such roll-bonded heat exchangers, but high temperatures require steel or titanium. The figure shows titanium because our experiments affirm that a thin titanium dioxide coating is an effective millimeter-wave absorber. In this metallic segment of the heat exchanger, an LH_2 propellant, for example, would enter at 50 K and be heated to a maximum of 700 K before reaching a manifold that interfaces with the narrower alumina heat exchanger.

The comparative advantage of a heat exchanger based on extruded alumina tubes is the higher temperature capability than metallic heat exchangers. It is anticipated that even with foil back-reflectors, extruded alumina heat exchangers will have a greater areal cost and areal density than metallic heat exchangers. In Figure 43, propellant enters the heat exchanger at 700 K and passes into the region of greatest flux, reaching a peak temperature of 1,800 K as it enters the next manifold.

The comparative advantage of a carbon heat exchanger is that it has a higher temperature capability than an alumina heat exchanger and potentially a much lower areal density, but for greater areal cost. Vapor deposited pyrolytic graphite tubes are possible, as are woven composites, and the ultimate would be multilayer graphene tubes if a method of making these can be found. To survive very high temperatures, absorption may need to be via surface patterning techniques instead of a silicon carbide layer. In Figure 43, propellant enters the heat exchanger at 1,800 K and reaches a peak temperature of 2,400 K as it enters a final manifold leading to the nozzle. We envision that the entire flow path from a temperature of 1,800 K upwards is carbon.

3.6 Beam director

3.6.1 Goubau beam

Goubau beams (Goubau and Schwering 1968, Goubau 1970) are commonly cited in the field of wireless power transmission because they model near-optimal energy transfer between finite apertures. A true Gaussian beam profile transforms to another Gaussian beam profile in the far field. Therefore, it would require infinite apertures on both ends. A top-hat beam profile transmits uniform intensity from a finite aperture, but transforms to a sinc function beam profile of infinite extent in the far field. One can choose to spill part of the far field of the sinc or Gaussian function, but this requires larger aperture sizes than a Goubau beam does to achieve the same energy efficiency.

A single parameter τ parametrizes the energy transfer efficiency at a wavelength λ between finite transmitting aperture of area A_t and a finite receiving aperture of area A_r separated by a distance Z,

$$\tau \equiv 2\pi \frac{\lambda Z}{\sqrt{A_t A_r}}. \qquad [121]$$

This expression implies that if the diameter of the transmitting aperture is halved, then the diameter of the receiving aperture must be doubled in order to achieve a given energy transfer efficiency $\eta(\tau)$. Instead of doubling the diameter of the receiving aperture, we can instead halve the distance between the transmitter and receiver.

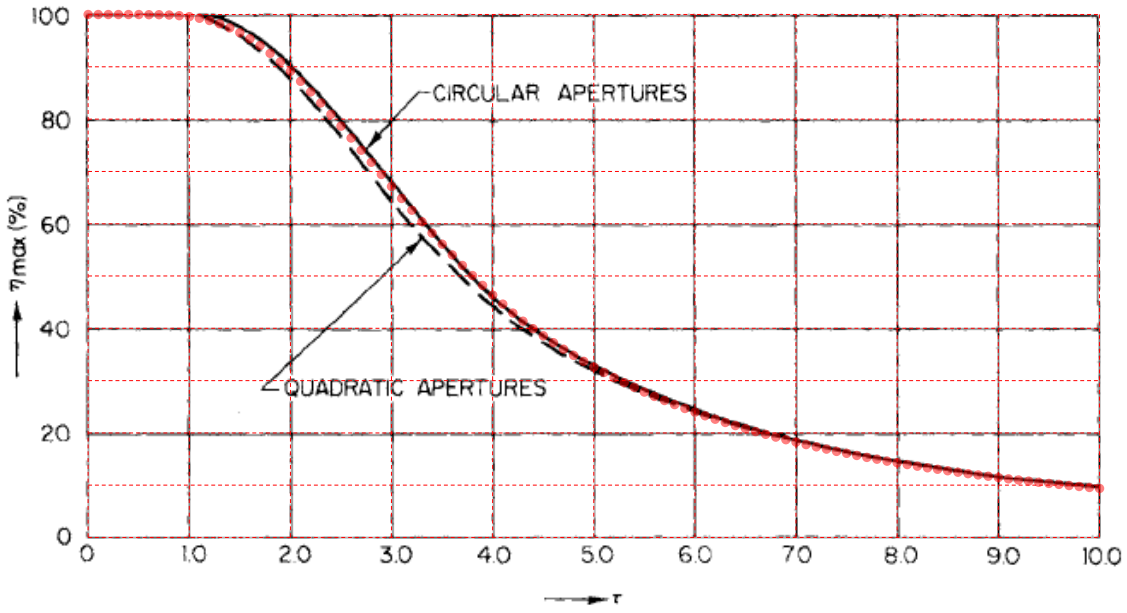

Figure 44 – Equation [122] is plotted in red dots over the original graph of Goubau beam transfer efficiency $\eta(\tau)$ (Goubau and Schwering 1968)

In Goubau's paper, the expression for $\eta(\tau)$ is shown graphically, but he does not make a compact closed-form approximation for it. We show this graph in Figure 44. Many subsequent papers show this original graph and refer to it when estimating transfer efficiency. We have used Goubau's solution procedure to produce the following compact closed-form approximation of $\eta(\tau)$:

$$\eta(\tau) = \begin{cases} \frac{1}{4} e^{-2a^2} \left(a^4 + \sqrt{a^8 - 4a^4 e^{a^2} + 4e^{2a^2} - 8e^{a^2} + 4} \right)^2 & \text{if } a > 1.2174805119418 \\ \left(\frac{a^2}{2} - \frac{a^6}{32} + \frac{7a^{10}}{4608} \right)^2 & \text{otherwise} \end{cases} \quad [122]$$

where

$$a = \sqrt{\frac{2\pi}{\tau}}. \quad [123]$$

This adheres to the published curve for both small and large limits as shown in Figure 44.

The downside in using a Goubau beam is that it can be difficult to produce the amplitude and phase distribution needed at the transmit aperture. It can be shown that a minimum of two reflections are needed to produce any given amplitude and phase distribution.

3.6.2 Cost using fixed spillage

What is the minimum initial cost of the beam director? To answer this question involves a tradeoff of the cost of aperture (primary reflector or equivalent thereof) against the cost of millimeter-waves (gyrotrons and supporting equipment). A smaller aperture costs less but spills more of the beam, and more gyrotrons to compensate for the added spillage may cost more than the extra aperture would. The optimum depends on the relative cost of aperture vs. millimeter-wave sources. As a rule of thumb, matching aperture cost to millimeter-wave source cost minimizes the combined cost.

Energy loss inputs	
Gaussian beam spillage	14%
Atmospheric absorption	10%
Dish scattering / absorption	10%
HX reflection / re-radiation	20%

Geometric inputs	
Beam wavelength	1.76 mm (170 GHz, λ/20 = 88 microns)
Gnd/target aperture shape	Rectangular
(HX length) / (tank length)	1
(HX width) / (tank width)	2
Tank L/D ratio	4 (elliptical end caps)
Maximum beam tilt angle	40° along-track, 10° cross-track
Maximum target range	120 km (at cutoff)

Vehicle inputs	
Specific impulse	800 seconds (LH_2)
Peak acceleration	20 g's (just before cutoff)

Tank ullage	10%
Tank propellant density	68.9 kg/m^3 (LH_2, 22 K)

Table 11 – Inputs to Version 2.0 of the system model

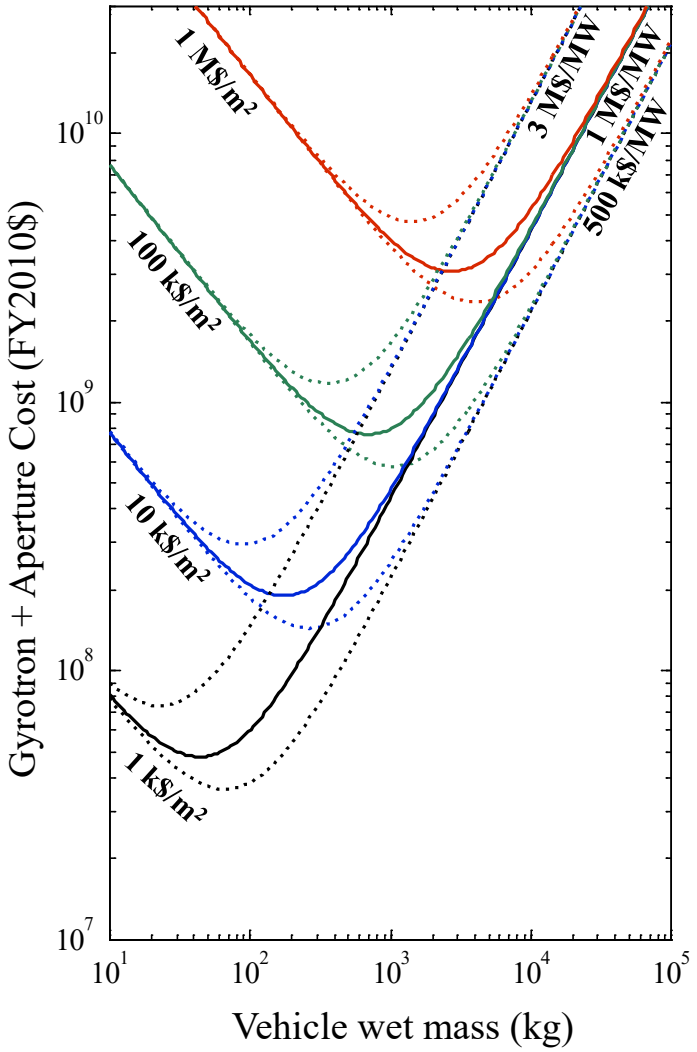

Figure 45 – A family of gyrotron + dish cost curves obtained from Version 2.0 of the system model using the inputs given in Table 11. Technology assumptions about dish cost are made on the left, and gyrotron production economics are made on the upper right. The curve connecting the two represents both assumptions.

If the beam director cost is amortized over the launches, then the equipment must last an average of 5,500 hours to contribute $100/kg to the payload cost. This assumes a rocket with a 10% payload fraction and 180-second pulse length per launch to orbit. This equipment lifetime is well within the capabilities of vacuum tube and radio telescope technology.

3.6.3 Cost using optimal spillage

In 2010, one of us (Parkin) tried varying the beam spillage such that the beam director cost is minimized. When this is done, it turns out that beam director cost always decreases for a smaller rocket, as we will show.

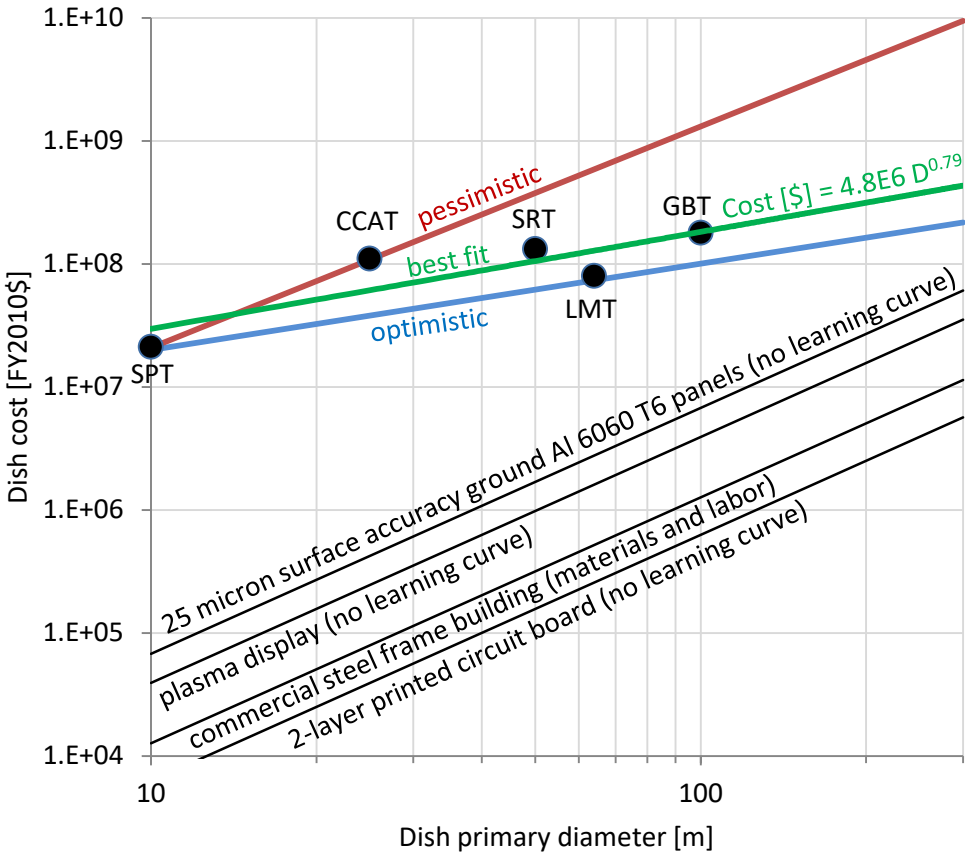

Figure 46 - Each data point represents the construction cost of an active surface millimeter-wave telescope. The best fit curve to the data is a power law where dish cost varies with diameter to the power of 0.79. Historical dish costs are inflation-adjusted on a production worker compensation basis.

To minimize beam director cost using numerical methods, it helps to have smooth functions for the millimeter-wave source cost and the aperture cost. To provide a smooth function for the aperture cost, a best-fit power-law is deduced by plotting the cost of several active surface millimeter-wave telescopes vs. their primary diameter. This plot is shown in Figure 46 alongside some more pessimistic and more optimistic line fits. At the bottom of the figure, there are costs associated with other technological approaches to providing the primary aperture. These approaches are discussed in a later section.

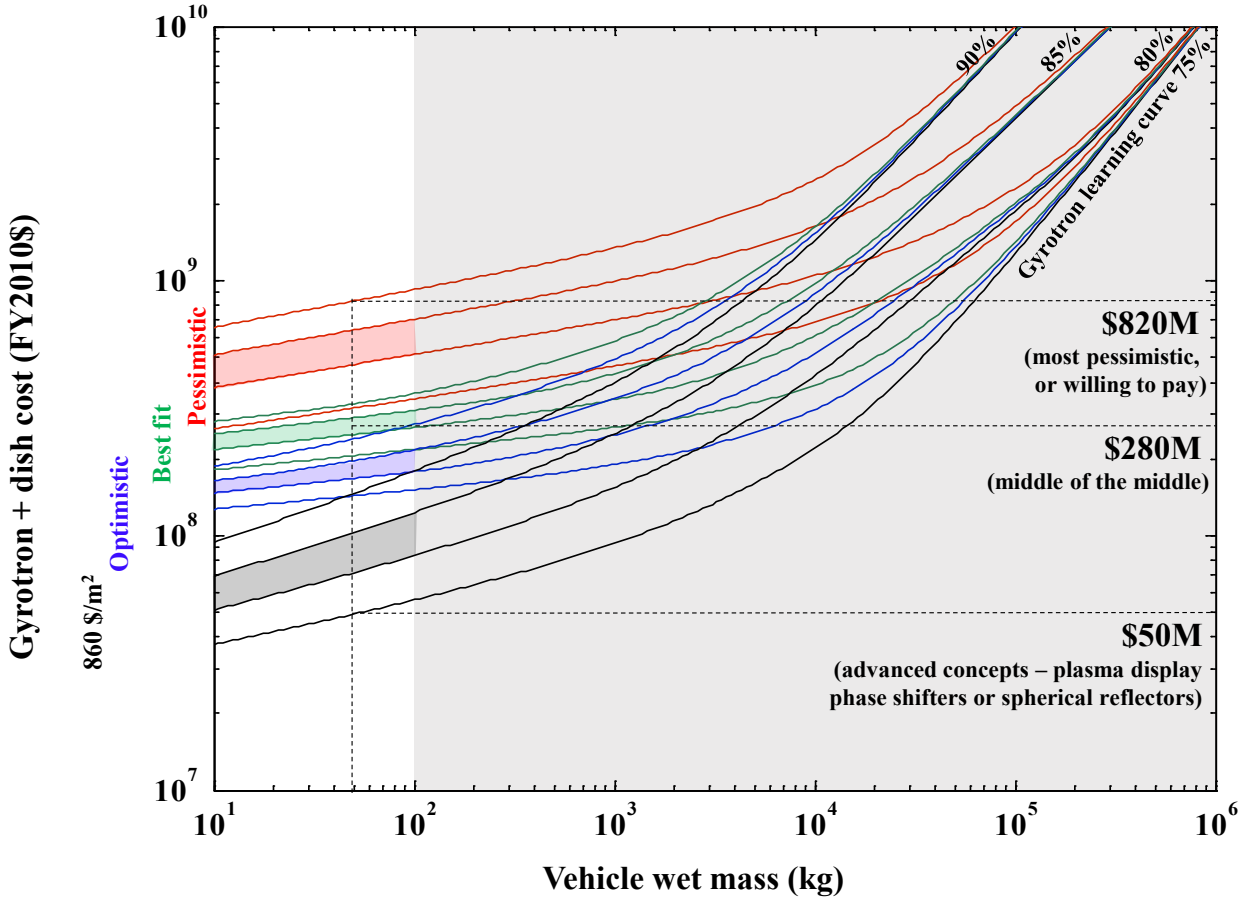

Figure 47 – By varying beam energy spillage fraction, curves of cost-minimized gyrotron + dish cost are obtained. Technology assumptions about dish cost can be made on the left, and gyrotron production economics can be made on the upper right. The curve connecting the two represents both assumptions.

The algorithm to minimize the beam director cost proceeds as follows. For a given target diameter and received power:

1. The primary reflector diameter of the telescope is guessed
2. The spillage from beam truncation at the primary and spillage around the target are calculated based on the model of Goubau. This is rolled into the overall transmission efficiency estimate.
3. The transmission efficiency is used to calculate the number of gyrotrons needed.
4. A Wright learning curve (Wright 1936, Boren and Campbell 1970) is used to estimate total gyrotron cost. Unless otherwise indicated, a gyrotron refers to a 'turnkey' gyrotron subsystem including the gyrotron itself plus magnet, power supply and cooling.
5. The number of telescopes is chosen such that for a given beam director spectrum allocation, the individual gyrotron bandwidth is not lower than a specified minimum. This minimum determines the tolerances of the gyrotron cavity temperature and power supply voltage.
6. The cost of each telescope is determined using the diameter from step 1 and the active surface telescope cost model.
7. The cost of the gyrotrons is added to the cost of the telescope(s) to produce an estimate of the beam director cost.

8. The beam director cost is minimized by varying the reflector diameter in step 1 and repeating steps 2-7 until this is so.

The algorithm above is repeated for different assumptions of gyrotron production learning curve and for the pessimistic, best fit, and optimistic line fits of Figure 46 in order to produce Figure 47. Figure 47 was generated in 2010 and enabled us to consider very small rockets and payloads for the first time. It paved the way for the 1 kg payload rocket that DARPA would request of the MTLS project. At this scale (50 kg wet mass rocket), the beam spillage can be 80% or more as the beam is oversized for the rocket. The benefit of the oversized beam is that the pointing tolerances are much reduced and the beam is essentially uniform over the heat exchanger.

3.6.4 Parametric tradespace map

Design range between beam director and rocket (this is not the maximum range)	100 km
Beam director center frequency	170 GHz
Beam director spectrum allocation	10 GHz
Minimum individual gyrotron bandwidth	10 MHz
Efficiency of energy conversion from wall-plug to heat exchanger, excluding beam spillage at beam director and heat exchanger	36% (includes losses in the gyrotron, feed system including beam combiner, primary surface scattering, atmospheric absorption, and heat exchanger reflection and re-radiation)
Cost of first gyrotron including power supply, cooling and other auxiliary equipment	$6/W (based on KSTAR value of $5.6/W and JET value of $6.0/W)
Gyrotron single unit power output	2.0 MW (based on the FZK coaxial design under development for ITER (Rzesnicki, Piosczyk et al. 2010))
Gyrotron + supporting equipment learning curve	82.5% based on advice of J. Benford
Gyrotron + supporting equipment cost floor	$90K
Maximum primary reflector diameter for a single telescope (a beam director can be comprised of many telescopes, and a rocket can be powered by many beam directors)	100 meters
Electricity cost	3.4 cents/kWh (consistent with off-peak nuclear-powered night launch)
Beam director pulse length per launch	300 seconds
Equipment lifetime	20,000 hours (most equipment will last much longer, except for the gyrotron cathodes, which need to be replaced every 10,000-15,000 hours at a cost of roughly half the initial cost of the gyrotron tube excluding supporting equipment)

Table 12 – Inputs used by Version 2.0 of the system model to produce Figure 48.

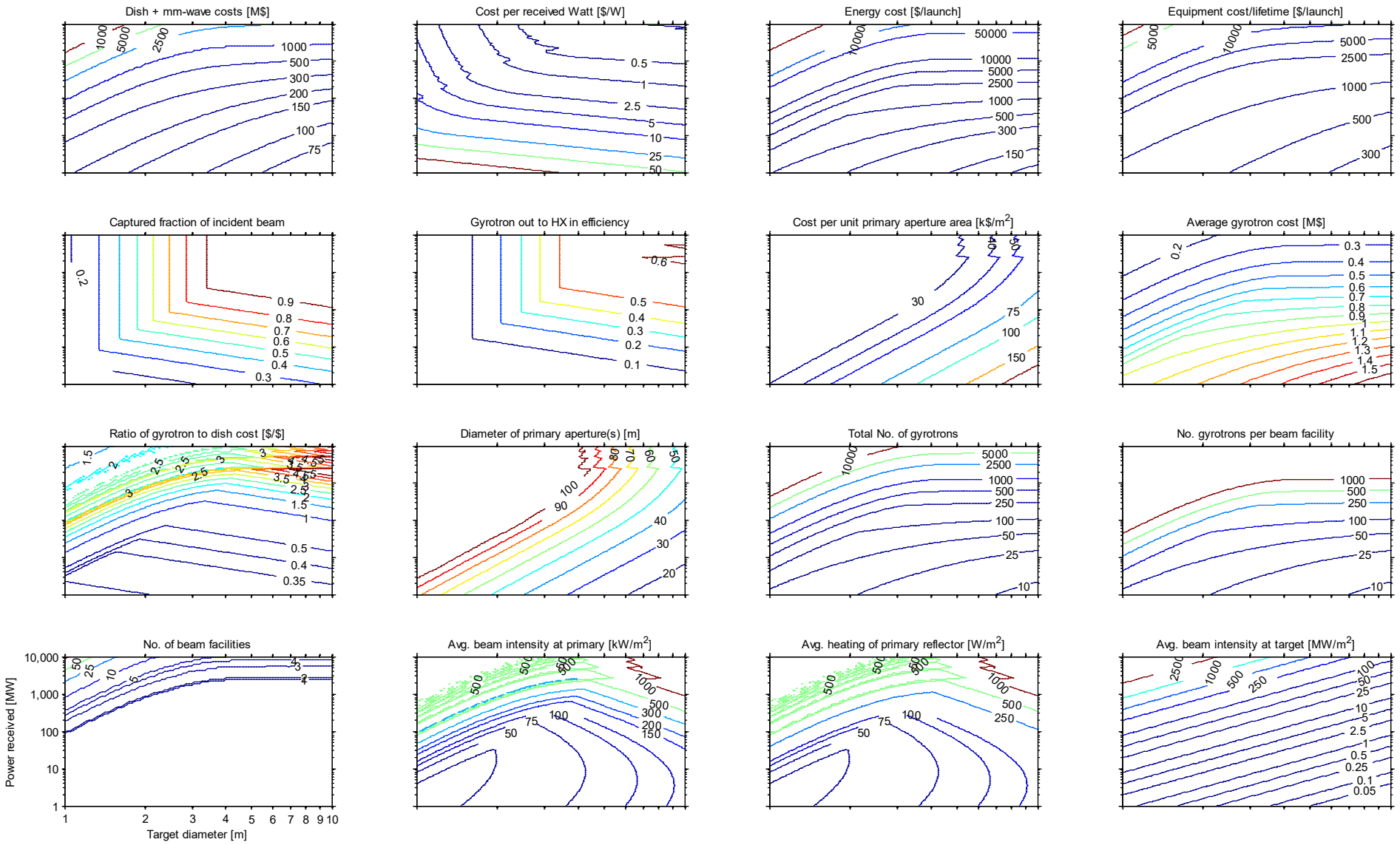

Figure 48 – Beam director performance maps generated by Version 2.0 of the system model. Version 3.0 corrects a bug in which the optimum dish configuration is not necessarily chosen; however, this version is not yet ready to generate new performance maps. The axes in each plot are identical to those in the plot in the bottom left-hand corner.

3.6.5 Beam Combining

There are several ways of combining the power output of millimeter-wave sources, including:

- Master Oscillator Power Amplifier (MOPA) beam combining
- Phase-locked oscillators
- Temporal beam combining
- Spectral beam combining

The first and second approaches require the millimeter-wave sources to have a systematic phase relationship between them (mutual coherence). MOPA beam combining is achieved by a single oscillator producing a wave that is amplified by many amplifiers in parallel. This approach is technically conservative but not as financially attractive as combining the output of many oscillators because amplifiers are more expensive per watt of output.

The high cost of amplifiers makes phase-locking oscillators together look more attractive. The phase locking of two oscillators can be achieved by leaking some of the signal from oscillator A into oscillator B and vice versa, with the conditions described by Adler's relation (Benford, Swegle et al. 2007). Unfortunately, gyrotron oscillators are highly overmoded structures many wavelengths across resonating far from their fundamental frequency, so phase locking of high-power megawatt-class gyrotrons is very difficult to achieve in a stable way and has yet to be experimentally demonstrated. Conceptual progress has recently been made in simulating the phase-locked regime (Bakunin, Denisov et al. 2014, Ginzburg, Sergeev et al. 2015, Starodubova, Usacheva et al. 2015).

Temporal beam combining is best suited to sources that are optimized for pulsed operation. Since the available gyrotrons are continuous wave, it is not considered here or elsewhere.

Spectral beam combining (SBC) is the reverse of splitting white light into a rainbow using a prism, diffraction grating, or hologram. This technique is used in the telecommunications industry and in high-power lasers, and has been used to combine the outputs from hundreds of lasers simultaneously (Drachenberg 2011). Using a reflective metal grating, the Gaussian beams from many gyrotron oscillators of slightly different frequency and incident angle can be combined into a single Gaussian output beam (which can subsequently be directed to the rocket via a telescope).

The maximum number of gyrotron beams that can be combined using SBC depends on their bandwidth. The smaller the bandwidth, the better. The bandwidth of the commercially-available CPI VGT8115 gyrotron (110 GHz, 1.3 MW) is less than the 5 MHz resolution of CPI's measurement equipment. The instantaneous linewidth of low-power gyrotrons is 200 kHz, but for megawatt-class gyrotrons, electrical noise in the power supply shakes the center frequency over a MHz range, especially during startup. If a 5 MHz bandwidth is assumed, then a 5 GHz band can in principle contain the combined output of at least 1,000 gyrotrons. In practice, the ratio of gyrotron bandwidth to spectral separation affects the beam combining efficiency, as does spectral stability. Until a model is derived that relates gyrotron spectral properties to combining efficiency, we recommend that only up to 100 gyrotrons should be assumed to combine per beam director. This is not to say that two or more beam directors cannot be built side-by-side to provide more power. Each of these beam directors reuses the same spectrum.

At 170 GHz, diffraction grating grooves are on a scale of millimeters and can be made using a simple CNC micromill. The grating need not be a single piece, but can be milled in sections then mounted to a water-cooled backing structure. Because it is possible to achieve high tolerances and 99.9% reflectance using aluminum, the beam combining losses are expected to be only a percent or two of the incident energy. Belousov et al. (*Quasi-optical Multiplexer Based on Reflection Diffraction Grating*, 1991) measure less than 1% energy loss in combining a 70 GHz and 79 GHz beam. This kind of performance should be demonstrated with many simultaneous frequencies, and this can be demonstrated at low power using IMPATT diodes or the 95 GHz and 110 GHz Gunn oscillators discussed in §4.1. Using a fixed plus a tunable source, the combining efficiency of any number of sources within the frequency range can be deduced using the principle of superposition. Note that the size of the diffraction grating can become physically large if the sources are close in frequency.

3.6.6 Approaches to building the primary aperture

There are many possible optical approaches to building the primary aperture of a millimeter-wave beam director. For each of these, there are technologies particular to that approach. In an ideal world, one of these approaches would possess all the following characteristics:

- Modular
- Scalable
- Low initial cost
- Low maintenance cost
- Low technical risk
- Low lead time
- Long service life

Thus far, there is no approach that is clearly superior. Consequently, we do not downselect to a particular approach. Instead, we present here our thinking on a range of possible approaches.

3.6.6.1 Parabolic reflector(s)

A beam director based on an active surface parabolic reflector is described by one of us (Parkin) in other publications (Parkin 2006c, George and Beach 2012, Parkin and Webster 2012).

A beam director based on a phased array of parabolic reflectors is described by Benford (Myrabo and Benford 1994, Benford and Dickinson 1995a) and by one of us (Parkin) in other publications (Kare and Parkin 2005, Parkin 2006c). In these earlier phased arrays, the millimeter-wave sources are phase-locked oscillators or a MOPA arrangement to combine their power across the array.

It is also possible to use millimeter-wave sources that are spectrally beam combined in combination with a phased array. To do this, all sources are centrally combined and then spilt into sub-beams, one to each parabolic reflector. This combining and splitting can be accomplished within waveguides or by using free-space diffractive optics.

3.6.6.2 Spherical reflector(s)

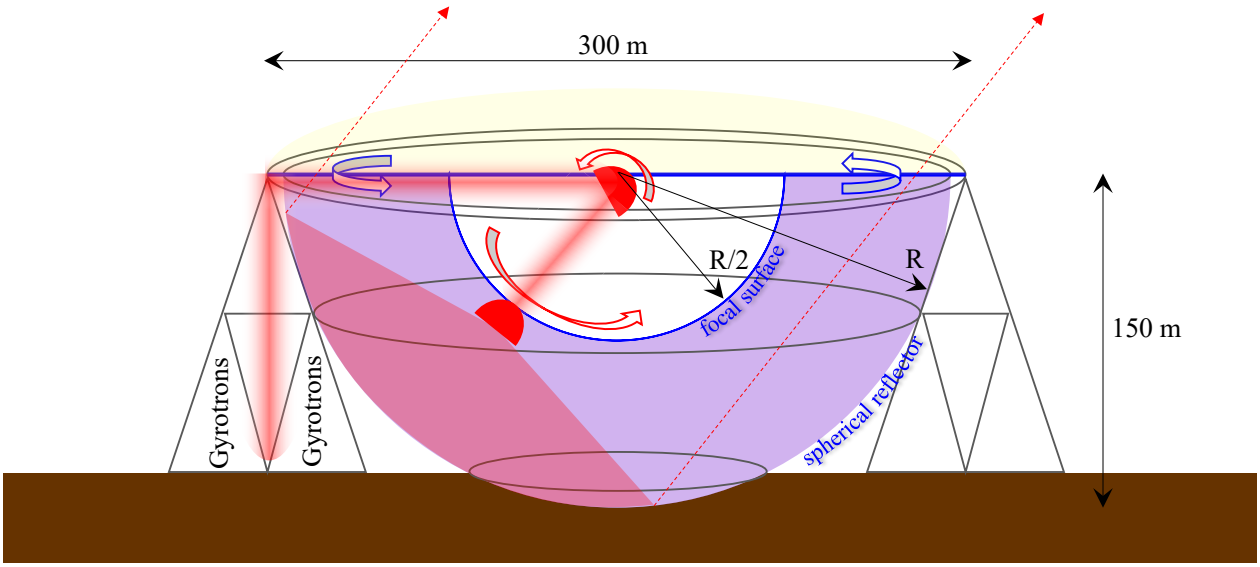

Figure 49 – A millimeter-wave beam director based on a fixed spherical reflector

A spherical primary reflector does not move and can be fixed rigid to the ground. In comparison, a parabolic primary reflector must be actuated. To steer the beam from spherical primary reflector, a secondary reflector is moved across the focal surface, which occurs at half the radius of the spherical reflector.

Spherical reflectors have the following four comparative advantages:

1. **Steel is cheap and actuators are expensive, so rigidity is better than active surface control**. If the beam points toward zenith and the reflector illuminates the spherical cap up to its height, then by simple geometry the effective diameter of the reflector is 86.6% of the spherical reflector diameter. The aperture efficiency of the Arecibo spherical reflector telescope is 67.5% (Burrows and Ricardi 1967). Because the surface area is proportional to the square of the diameter, the effective diameter of the reflector is 82% of the spherical reflector diameter, which is very close to the 86.6% limit. For off-zenith pointing, there can be additional spillage that we ignore in this ideal case. Choosing a spherical reflector diameter of 300 meters, we deduce an effective diameter of 246 meters. For an active surface parabolic reflector, extrapolating the best-fit curve of Figure 46 to a 246 meter reflector yields a cost estimate of \$372M (\$7,800/m^2). How much does a spherical reflector cost? A typical commercial steel frame building costs \$75-110/m^2 in materials and \$55-90/m^2 in labor, so we average and combine these to estimate a rough cost of \$12M (\$165/m^2) for the steel superstructure. In addition, the reflector itself is assumed to be identical aluminum hexagonal hydroformed panels costing a total of \$35M (\$250/m^2). This totals \$47M for the steel superstructure plus the aluminum reflector. \$325M remains from which to build the secondary and tertiary reflectors, feed system, and optional radome, before the expense exceeds that of the active surface parabolic reflector. In addition, the largest active surface parabolic reflector is 110 meters in diameter, so the spherical reflector is a more conservative technological approach.
2. **Fixed spherical reflectors can be built hundreds of meters in diameter.** Parabolic reflectors must transmit forces through their mount points, maintain surface accuracy as they slew and

under thermal loads, so this limits their size as described by the Von Hoerner diagram (von Hoerner 1975). Arecibo is 305 meters in diameter and supports its segments from a suspended steel rope. Despite this, it has an RMS surface accuracy of 5 ± 0.6 mm as measured shortly after a long-needed tune-up in 2001 (Goldsmith 2001). For a spherical reflector that is supported by a rigid steel structure instead of steel cables, every panel can be supported and stiffened by the steel framework. The objective is to eliminate as many actuators as possible (these are otherwise used to maintain the surface accuracy of the overall dish). Thermal deformation will likely be the largest source of surface error and is dealt with by operating at night and using heaters within the structure. When the beam is on, the heaters are turned off to keep the structure in thermal steady state.

3. **Spherical reflectors have no frequency dispersion**. The focal length of a parabolic primary reflector is a function of the frequency used (Goldsmith, Electrical et al. 1998). This is not the case with a spherical primary reflector. This becomes more of an issue if a large number of gyrotrons are spectrally combined, taking a large bandwidth.
4. **Spherical aberration is corrected by secondary and tertiary reflectors that are much smaller than the primary**. This is the case for the Arecibo (Altschuler 2002), Hobby-Eberly, and SALT telescopes.

If a radome is used, it can be suspended by the pressure of the enclosed atmosphere. Also, the enclosed atmosphere can be made water-free to reduce absorption losses. This is also helpful when the feed system is a quasi-optical transmission line as opposed to a waveguide feed system. Finally, a small amount of construction cost could be saved by digging a hole under the center of the reflector as opposed to building the sides of the reflector higher. This is a simple engineering tradeoff.

3.6.6.3 Geometric phase shifting

It is possible to abstract the idea of the beam director as simply a phase transformation that redirects wavefronts that are diverging from a feed system into wavefronts that are converging onto a target. If one considers two sequential phase transformations separated by some distance, then both the amplitude and phase may, in principle, be arbitrarily controlled.

A simple way of doing this is to imagine that a parabolic dish is collapsed down into a Fresnel reflector (Minin and Minin 2004) into order to provide an equivalent phase transformation. If this Fresnel reflector is subdivided into a grid, for example, then an equivalent grid of actuators that move up and down can be used to approximate its shape. If the free space wavelength is 1.76 mm (for 170 GHz), then half of this (880 microns) is the amount of travel needed on each actuator to provide 360 degrees of phase shift (because the wave is reflected so travels the displacement twice).

Ideally, each actuator would be a half wavelength or less in diameter, and their surfaces would be good conductors that are in electrical contact with each other. There are many technologies that could be used to provide such a physical phase shifter and there are many requirements in common with the field of haptic displays. These technologies include miniature solenoid arrays, pneumatic actuators (Moy, Wagner et al. 2000, Vidal-Verdú and Navas-González 2003), shape memory alloy actuator arrays (Velazquez, Pissaloux et al. 2005), mems arrays, piezoelectric arrays, and artificial muscles (Prahlad, Pelrine et al. 2005). The main problem with these existing approaches is their high areal cost.

3.6.6.4 Passive reflectarray

At the scale of a wavelength, an equivalent circuit can replace a reflector surface. By arraying these equivalent circuits, the electrical equivalent of the whole reflector surface is produced. Given an understanding of how the unit cell equivalent circuits are varied, reflectors of arbitrary geometry (usually flat) can be synthesized but behave as if they are parabolic reflectors, for example. The reflectarray antenna was first conceived in the 1960s (Berry, Malech et al. 1963) and printable microstrip reflectarrays were developed in the late 1980s and early 1990s.

Reflectarrays can now be etched onto two-layer printed circuit board (Huang and Encinar 2008), making them potentially very cheap. At \$100/m^2, a 200-meter diameter flat printed circuit reflectarray would cost only \$3M. However, a flat passive reflectarray still needs to be mechanically pointed, and there is an extra bandwidth constraint caused by differential spatial phase delay (Huang and Encinar 2008).

3.6.6.5 Active reflectarray

In an active reflectarray, the effective shape of the aperture is varied by varying the electrical characteristics of the reflectarray by including active components, such as diodes, liquid crystals or photo-conductive elements (Hum and Perruisseau-Carrier 2014). The energy efficiency of these approaches is usually <50%.

Metamaterial Huygens' surfaces (Pfeiffer and Grbic 2013, Yu and Capasso 2014) achieve nearly 100% beam redirection efficiency by manipulating both the electric and magnetic field components.

3.6.7 High-power single sources

Using a single high-power millimeter-wave source negates the need for spectral beam combining or phase locking. A single high-power beam can be split into many beams in vacuum and ported into the atmosphere via many windows, for example diamond windows or even low-cost sapphire windows. Since all such beams originate from a single source, they will have the same exact frequency and be in phase.

3.6.8 Efficiency estimates

	Individual efficiency			Wallplug to Jet cumulative			Gyrotron to Jet cumulative		
	Low	Med	High	Low	Med	High	Low	Med	High
Power supply	85%	92%	98%	85%	92%	98%			
Gyrotron	45%	54%	62%	38%	49%	61%			
Dish feed system	75%	86%	97%	29%	42%	59%	75%	86%	97%
Surface accuracy	95%	98%	100%	27%	41%	59%	71%	84%	97%
Diffraction	76%	86%	95%	21%	35%	56%	54%	72%	92%
Atmospheric transmission	75%	86%	97%	16%	30%	54%	41%	62%	89%
Absorption into propellant	80%	89%	98%	**12%**	**27%**	**53%**	**32%**	**55%**	**88%**

Table 13 – Efficiency estimates for a 170 GHz beam director

3.7 Ascent trajectories

There are two different types of ascent trajectory, shown in Figure 50. Ascent to a transfer orbit makes the beam director cheaper, at the expense of an extra 50-100 m/s ΔV later to circularize the orbit.

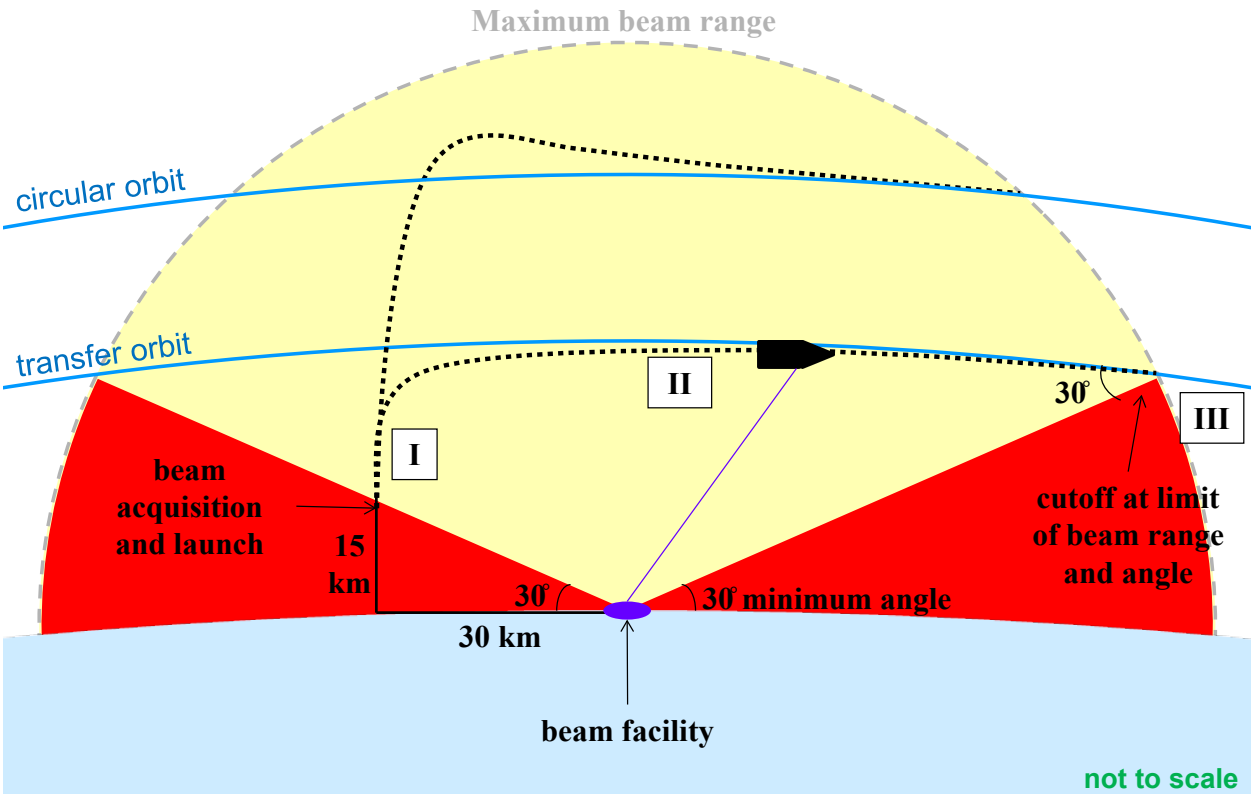

Figure 50 – The two types of millimeter-wave rocket ascent trajectory

3.7.1 Generated by system model version 2.0. Single Beam Director, Air Launch Case

The trajectories from version 2.0 of the system model were generated several years ago to illustrate progress on the ascent trajectory model and were not intended as final results. They are presented here because they illustrate the two types of trajectory described in the introduction to this section, and because version 3.0 of the system model is not yet able to generate equivalents. It was the imperfections in these trajectories and the slowness with which they were generated that motivated the use of C++ instead of MATLAB for version 3.0 of the system model. In particular, it became clear that the computational complexity that would be added by co-optimizing the vehicle, trajectory and beam director would render version 2.0 of the system model unusable in any reasonable length of time.

Version 2.0 was used to experiment with ascent trajectories in a qualitative sense and at a time when there was interest in confining the launch concept to a single beam director in order to minimize initial infrastructure costs. Through the minimum elevation angle, the single beam director constraint implies that the rocket is air launched from the highest possible altitude and at a slightly retrograde angle. The retrograde angle spends a little bit of trajectory efficiency to provide a better combination of distance and power for horizontal acceleration later in the trajectory.

The two trajectories presented next were the first to integrate a beam director model, so contours of available power are shown on the ascent trajectory plot. By integrating the beam director model, the received power was recalculated at every step of the trajectory integration and every watt of available power could be used. In contrast, version 1.0 of the system model had assumed a fixed available power for the beam director, which meant that the beam director was considerably oversized as a result.

The input parameters shown in Table 14 are common to the following pair of trajectories. Unfortunately, not all the parameters were recorded that would be needed to reproduce the trajectories.

Initial mass of the rocket	1,646 kg
Destination circular orbit altitude	284 km
Standard gravitational parameter μ	3.9863e+014 m^3/s^2 (for Earth)
Radius of central body	6,378 km (for Earth)
Initial velocity	0 m/s
Total pressure at ideal nozzle inlet	50 bar
Average ratio of specific heats for nozzle exhaust	1.35
Density of propellant in tank	76.3 kg/m3
Vacuum specific impulse	850 seconds

Table 14 – Input parameters used for ascent trajectories in this section

3.7.1.1 Earth to slightly elliptical

Ultimately, the ascent trajectory is where all the top-level performance tradeoffs are made between the beam director and the rocket. Trajectory optimization involves working with a varying beam transmission efficiency, shown by the gray contours in Figure 51. Each line represents a 10% decrease relative to transmitted power. Ascending to a transfer trajectory greatly reduces the size of beam director needed relative to ascending to a circular orbit. The penalty paid is an added ΔV of 50-500 m/s needed to circularize the trajectory. As shown in Table 15, the periapsis of this trajectory is such that this circularization must happen during the first orbit.

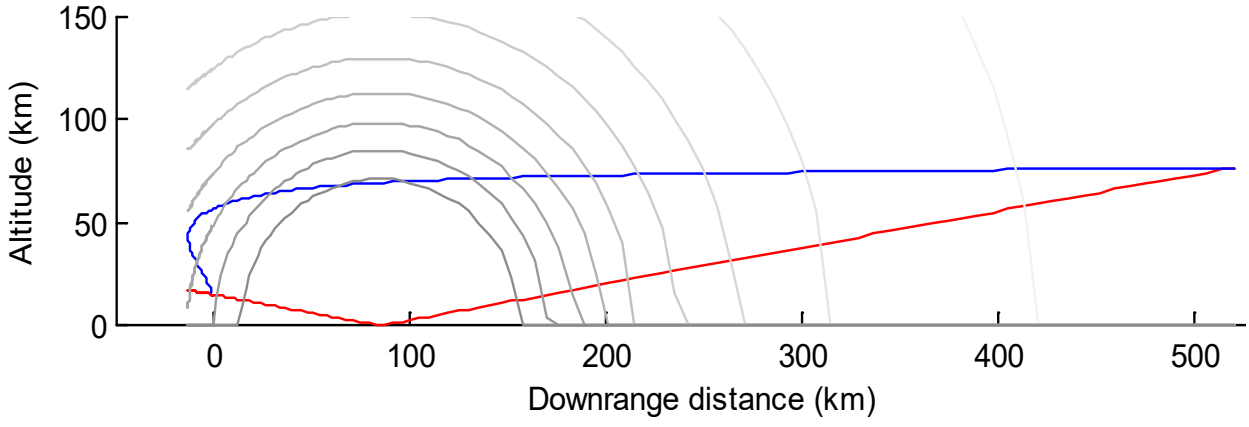

Figure 51 - An example ascent trajectory to a transfer orbit which is very close to the destination circular orbit.

Inputs (additional to those in Table 14)	
Length:	12.2 m
Diameter:	2.1 m
Initial altitude	15 km
Minimum beam elevation above horizon	10 degrees
Optimized variables	
Vehicle T/W at launch	6.8 g's
Altitude at which gravity turn becomes horizontal thrust	34 km
Initial angle	-5.9 degrees from zenith
Outputs	
Final mass of the rocket	432 kg
Frontal area	3.5 m^2
Apoapsis altitude at cutoff	619 km
Periapsis altitude at cutoff	-400 km
Altitude at cutoff	68.4 km
ΔV needed by payload to circularize orbit after cutoff	490 m/s
Cutoff time	168 seconds after launch

Table 15 - Inputs and outputs associated with the ascent trajectory shown in Figure 51

3.7.1.2 Earth to circular

The millimeter-wave thermal launch system can ascend directly to a desired circular orbit, as shown in Figure 52 by the blue line. As before, each contour represents a 10% decrease in transmitted power.

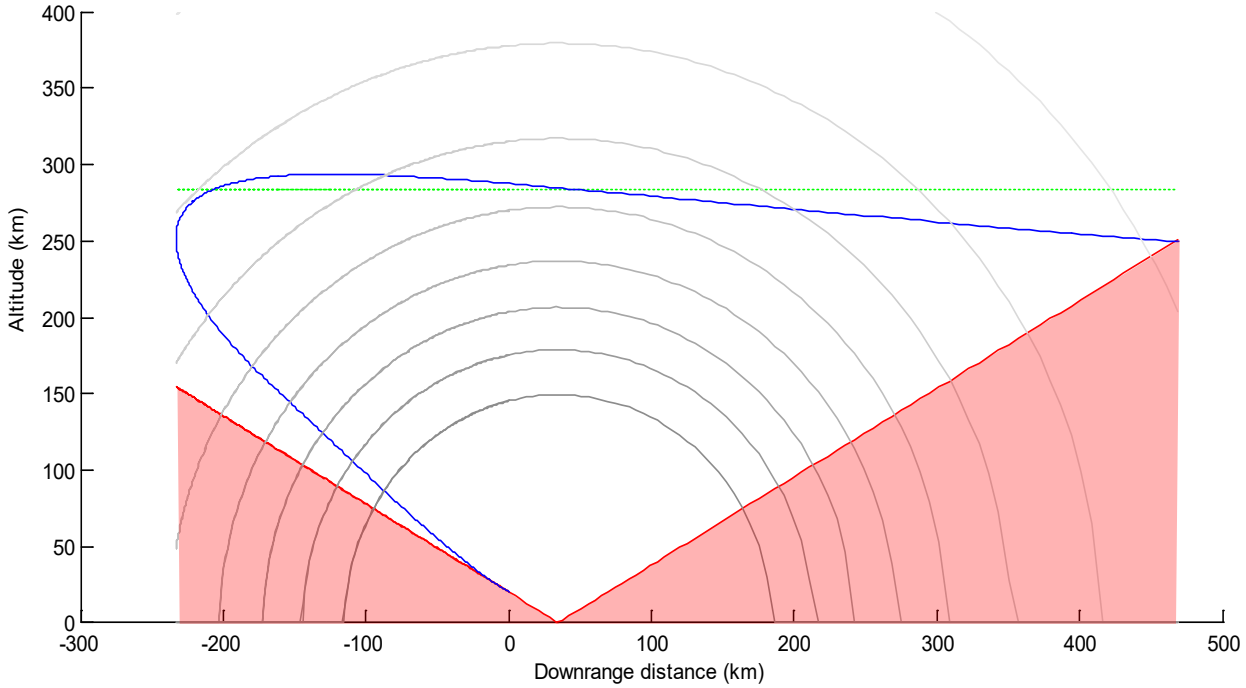

Figure 52 - An example ascent trajectory to a desired final circular orbit

Inputs (additional to those in Table 14)	
Length:	5.1 m
Diameter:	2.5 m
Initial altitude	20 km
Minimum beam elevation above horizon	30 degrees
Optimized variables	
Vehicle T/W at launch	1.7 g's
Altitude at which gravity turn becomes horizontal thrust	155 km
Outputs	
Final mass of the rocket	294 kg
Frontal area	4.9 m^2
Apoapsis altitude at cutoff	273 km (249 km circular was target; difference is 26 m/s)
Periapsis altitude at cutoff	166 km (249 km circular was target; difference is 26 m/s)
Altitude at cutoff	249 km
Cutoff time	522 seconds after launch

Table 16 - Inputs and outputs associated with the ascent trajectory shown in Figure 52

As is seen in Figure 52 and Table 16, the simplistic optimization scheme used is not able to exactly match the target altitude. The Δv difference between the orbit at cutoff and a 249-km circular orbit is only 26 m/s, so it is not far off.

3.7.1.3 Reverse time method

The reverse time method has been developed to ensure that the ascent trajectory reaches the exact target orbit by integrating backwards from the desired endpoint. Without constraints on the throttle values, the solution can become unphysical when integrating backwards in time. To provide the constraints on these throttle values, a forward trajectory is integrated from the desired start point and used as a constraint on the throttle profile of the backward trajectory. Any mismatch of assumptions between the two trajectories is converged via iteration.

This method works well in test cases and is being developed to automatically produce families of trajectories in Version 3.0 of the system model.

3.7.2 Ascent to primary beam acquisition point

High attenuation for horizontal beam propagation limits the minimum beam elevation to about 15 degrees for beam directors that are not within a few kilometers of the launch point. Consequently, there are three main options for the initial (mostly vertical) phase of the ascent trajectory, described next.

3.7.2.1 Ascent via millimeter-wave thermal rocket

A millimeter-wave rocket can use two beam directors to ascend all the way from the ground to orbit. The first beam director is a short-range "boost" beam director to power the rocket from the ground to the point it is acquired by the second "sustain" beam director that powers it through to the end of the ascent trajectory. More beam directors may be used for a longer ascent trajectory; however, initial systems would logically start with two. Programmatically, the boost beam director would be the subscale demonstration of the sustain beam director.

3.7.2.2 Ascent via UAV

A high-altitude UAV can carry the rocket from the ground to a beam acquisition point at ~20 km altitude. The UAV would use air-breathing turbofan propulsion like that used on the U-2 high-altitude aircraft. The cost per flight hour is on the order of $10,000 for a Boeing 747 airliner, so the UAV is expected to be far lower. The drawback is that the ascent will take on the order of an hour. If the propellant is cryogenic such as LH_2, then a helium-pressurized shroud would be used to preclude oxygen ice buildup on the tank, and boil off from the tank would be countered with extra propellant held or manufactured on board the UAV.

3.7.2.3 Ascent via microwave rocket (with millimeter-wave thermal rocket as payload)

The microwave rocket (MR) is our preferred alternative to the UAV and is being developed by the Komurasaki research group at the University of Tokyo (Oda, Nakagawa et al. 2003, Oda 2008, Shibata 2008, Shiraishi 2009, Shimada 2010, Yamaguchi 2010, Fukunari 2012, Saito 2013, Kurita 2014).

The MR is a pulsejet that is comprised of a tube that is open on one end and within which microwave-supported detonations occur many times per second. It is axially illuminated from the ground, meaning that the beam is vertical or nearly so at all times. The propulsion scheme is analogous to an air-breathing pulse detonation engine and can propel its payload (the thermal rocket) from the ground to an altitude of 34 km with a residual vertical velocity of 1 km/second and takes just 80 seconds to do so, thereby mostly removing the problem of propellant boiloff and tank ice formation associated with using a UAV (Kakinuma, Fukunari et al. 2015). The MR stage itself is very simple, requiring no turbomachinery and costing only an estimated $8,000 to lift a 50-kg thermal rocket stage. Its frequency of operation is 170 GHz, the same as the millimeter-wave thermal rocket.

3.8 Beam conjunction

A beam conjunction analysis was initiated by one of us (Parkin) in collaboration with James Mason of NASA Ames Research Center to answer the recurring question "Will the beam interfere with satellites in orbit?" The analysis was carried out by James Mason using the Satellite Tool Kit software, and the results, summarized next, were delivered in October of 2010 (Mason 2010). We conclude that beam conjunction is rare, not catastrophic when it does happen, and easily avoidable.

Launches are simulated every four minutes for eight consecutive days. Each intersection between the microwave beam and background satellites is recorded. Beam divergence is estimated by assuming a conical beam with a half angle calculated to coincide with the width of the (120 km) focused millimeter-wave beam at GEO (36,000 km). An additional 30% is added to the width of the beam as a margin, to account for the shortened focus during the vertical ascent. The intensity is estimated by assuming 30 MW/m^2 average intensity at the focus to be spread normally across the diverging beam, with no atmospheric losses.

3.8.1 Launch into 36-degree inclination from China Lake, CA

- On average there are 5.25 intersections per day, each for 0.2 seconds
- Histogram showing the distribution of intersection maximum intensity during the 8 days – note that most have I_{max} less than 100 W/m^2 (i.e. 8% of solar const.)
- Histogram of clear launch windows – periods that have no intersections. Over the 8 days there are 29 periods with more than one hour of clearance.

3.8.2 Launch into 98-degree SSO from China Lake, CA

- On average there are 12.75 intersections per day, each for 0.03 seconds.
- Histogram of clear launch windows – periods that have no intersections. Over the 8 days there are 41 periods with more than one hour of clearance
- Histogram showing the distribution of intersection maximum intensity during the 8 days – note that most have I_{max} less than 200 W/m^2 (i.e. 15% of solar const.)

3.9 Beam director site location

Submillimeter-wavelength astronomy has highlighted the existence of high-altitude locations with particularly low atmospheric water content, opening new transmission windows from 35 to 300 GHz and sometimes beyond. The atmospheric scale height of water vapor is only 1 to 2 km, allowing mountain ranges to create 'rain shadow' regions with comparatively good millimeter-wave propagation.

Figure 53 - A temperature inversion over the Kazakh city of Almaty traps water vapor and other aerosols beneath the altitude of the upper mountain slopes. Picture credit: Igors Jefimovs, released under CC BY 3.0

In addition, some locations form low-altitude temperature inversions that lock in water vapor and other aerosols beneath them, leaving the sky above clear. Figure 53 shows a particularly vivid example of this over the city of Almaty in Kazakhstan. Similar inversions form over Denver, Colorado and Salt Lake City, Utah. The altitudes of the temperature inversions tend to descend at night, and winds die down at this time too, making this a comparatively attractive time to launch directed energy rockets.

Satellite data can be used to map suitable locations for beam directors worldwide. As seen in Figure 54, the Himalayas hold back water vapor, making Tibet an ideal location for directed energy launch in China. The Alps are suitable for Europe, and the Andes suitable for South America, with the Chilean Atacama Desert particularly prolific for submillimeter-wave astronomy. This resolution is insufficient to see particular mountains in Ecuador and Kenya that have both good propagation conditions and are close to the equator; these mountains are visible in the larger dataset. Also not easily visible are the islands of Hawaii, which are known to have excellent propagation characteristics.

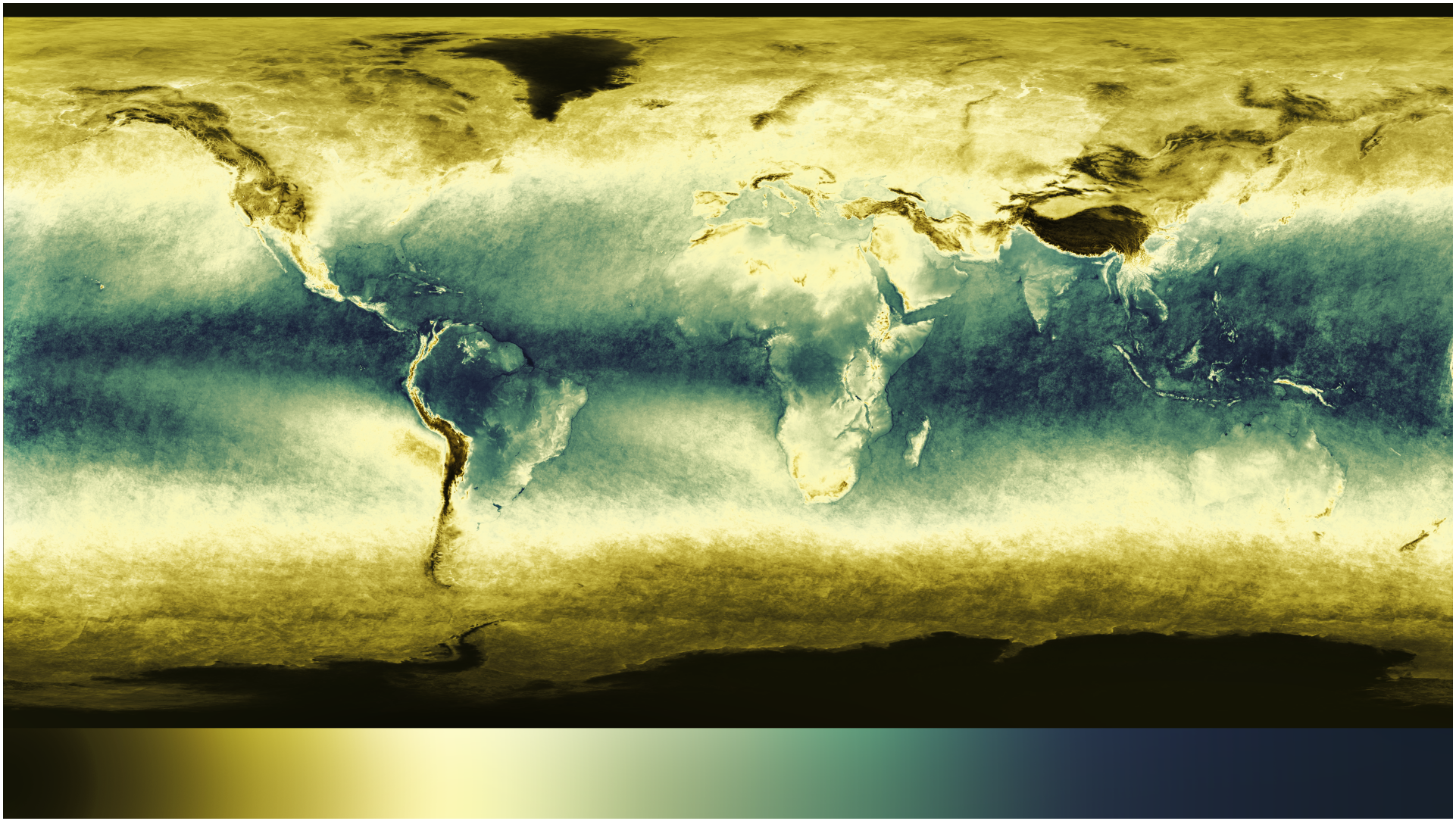

Figure 54 - Satellite data indicating the locations worldwide where atmospheric water vapor content is lowest, and therefore millimeter-wave propagation is most efficient. Using the color scale at the bottom of the image, low water vapor is indicated by black/brown end of the scale and high water vapor by the dark blue end of the scale. Because of the diversity of locations and their small scale in some cases, we present this image in its native 8000x4500 pixel resolution and encourage viewers of the original PDF file to zoom in. This level of detail reveals individual mountains with low water vapor, for example Mauna Kea and Mauna Loa on the Big Island of Hawaii, or Mount Kenya in Africa. Source: ENVISAT MERIS 2003 1-year average, courtesy ESA.

For the continental United States (CONUS), Figure 54 shows that the mountainous southwest of the country has a comparative advantage in transmission efficiency to the southeast, with the humid Florida weather proving prohibitive for millimeter-wave propagation. Ongoing site surveys and millimeter-wavelength projects, such as the CARMA array in eastern California, are revealing many suitable locations for a beam director on the United States mainland.

3.9.1 Launch from Alaska

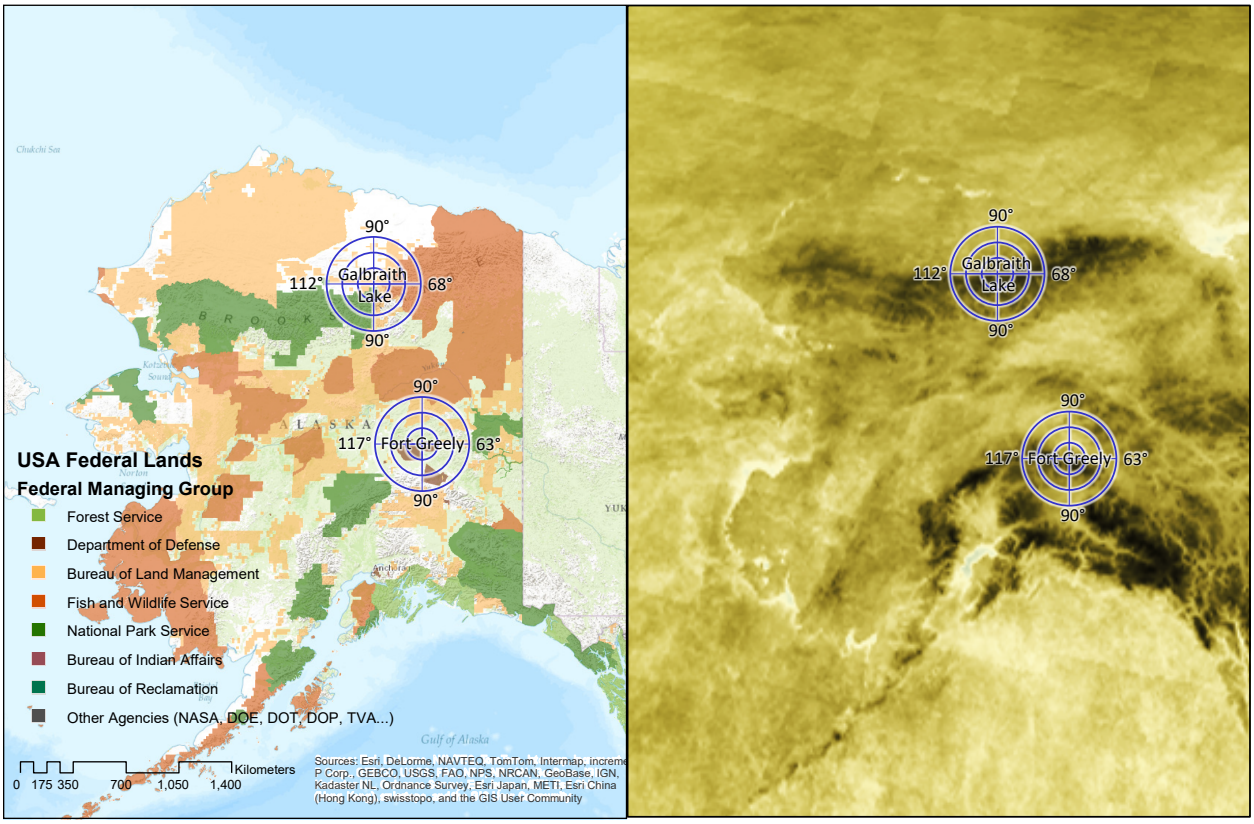

Figure 55 – Notional beam director sites in Alaska at Galbraith Lake and Fort Greely. Each concentric ring represents 100 km. Assuming that the beam director is located close to the center of the ascent trajectory, the outer ring gives the approximate extent of an ascent trajectory from the ground to a 300-km circular orbit, as shown in Figure 52.

Alaska is a good candidate for a millimeter-wave rocket launch site because 78% (523 of 669) of satellites in LEO are in near-polar orbits between the 63°-117° inclinations accessible from this region. Proposed LEO constellations, some of them consisting of thousands of satellites, may greatly boost this fraction, but their business cases await low-cost launch.

Alaska combines low population density with suitable Federal lands at high altitudes where millimeter-wave attenuation is low. We use the TerraGo software to create the map of US government land in Alaska shown on the left of Figure 55, and we illustrate notional launch sites at Fort Greely and Galbraith Lake. On the right of the figure, we show the corresponding part of Figure 54 to allow various locations to be correlated with areas of high millimeter-wave propagation quality.

3.9.2 Launch from southwest continental United States

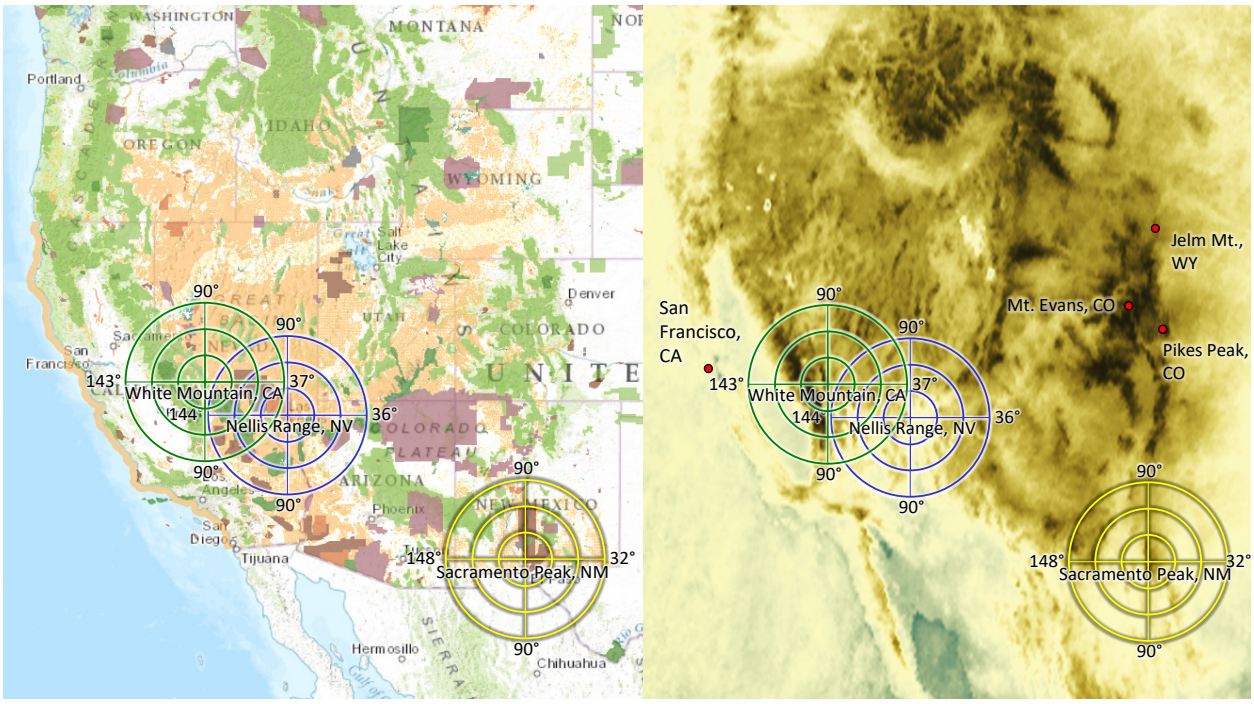

Figure 56 - Map of federal lands using same color key as Figure 55 and overlaid with notional beam director sites at China Lake Naval Air Weapon Station and White Mountain in California and adjacent to Nellis Air Force Base Range in Nevada. Concentric rings are spaced at intervals of 100 km.

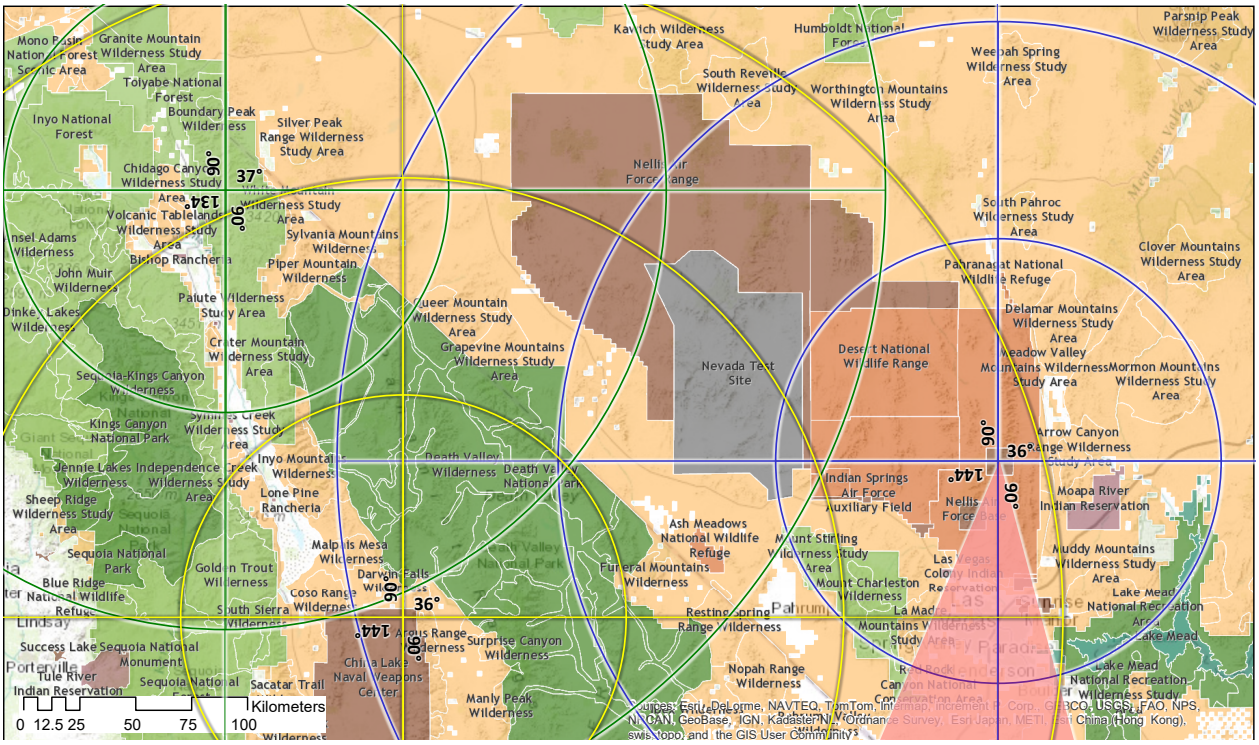

Figure 57 - Map of federal lands using same color key as Figure 55 and overlaid with notional beam director sites at China Lake Naval Air Weapon Station and White Mountain in California and adjacent to Nellis Air Force Base Range in Nevada. Concentric rings are spaced at intervals of 100 km.

The southwest continental United States is a good candidate for millimeter-wave rocket launch sites because 98% (654 of 669) of satellites in LEO and 61% (768 of 1263) of all satellites are in orbits between the 32°-148° inclinations accessible from this region. The southwest United States has a low population density due to lack of water, the most sunny days per year of any part of the continental United States, and a great deal of federal land on which to build, test and operate millimeter-wave launch systems and associated beam directors.

An envisioned complex of three overlapping beam director sites based in California and Nevada is shown Figure 57. Using these three sites, it is possible to launch a thermal rocket in any orbital inclination between 37 and 143 degrees without overflying significant population densities. Additionally, the probability of unsuitable weather obscuring all three beam directors is lower than at a single one.

As rockets overfly more populated areas, their reliability will need to increase to aircraft-like levels for the probability of injury or death for a person on the ground to stay within mandated limits. Conventional rockets are too heavy and unreliable, but we see no reason why this must be the case for millimeter-wave rockets. Indeed, for the 50-kg rocket point design, we estimate the probability of injury in people/hour/km^2 per continuous stream of millimeter-wave rocket launches over the southwest United States to be >4 times lower than the probability of injury per UAV flying over New Jersey. Nevertheless, the direction overflying Las Vegas has been assumed to be unusable for early launches and is blocked out in red in Figure 57 from the notional beam director site at Nellis AFB Range. In practice, the rocket does not need to fly directly overhead of the beam director; it can do so at an offset to avoid areas of higher population density.

4 Facilities

4.1 Reflectometer test facility (incomplete)

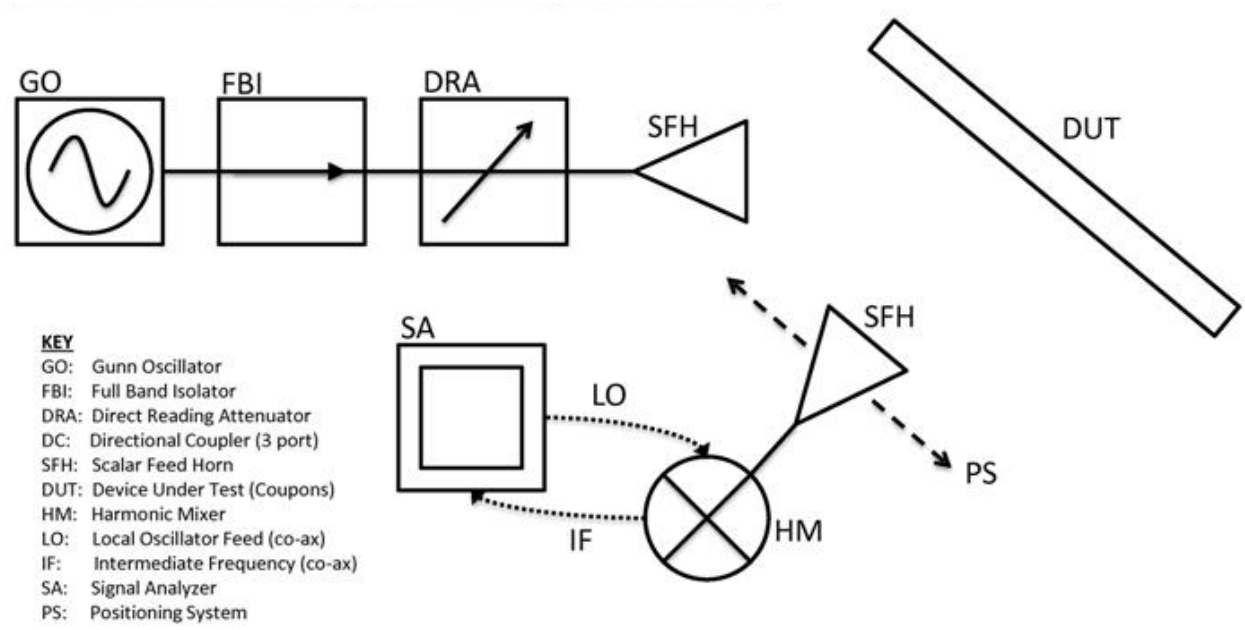

Figure 58 - Basic reflectometer setup for inclined angles of incidence

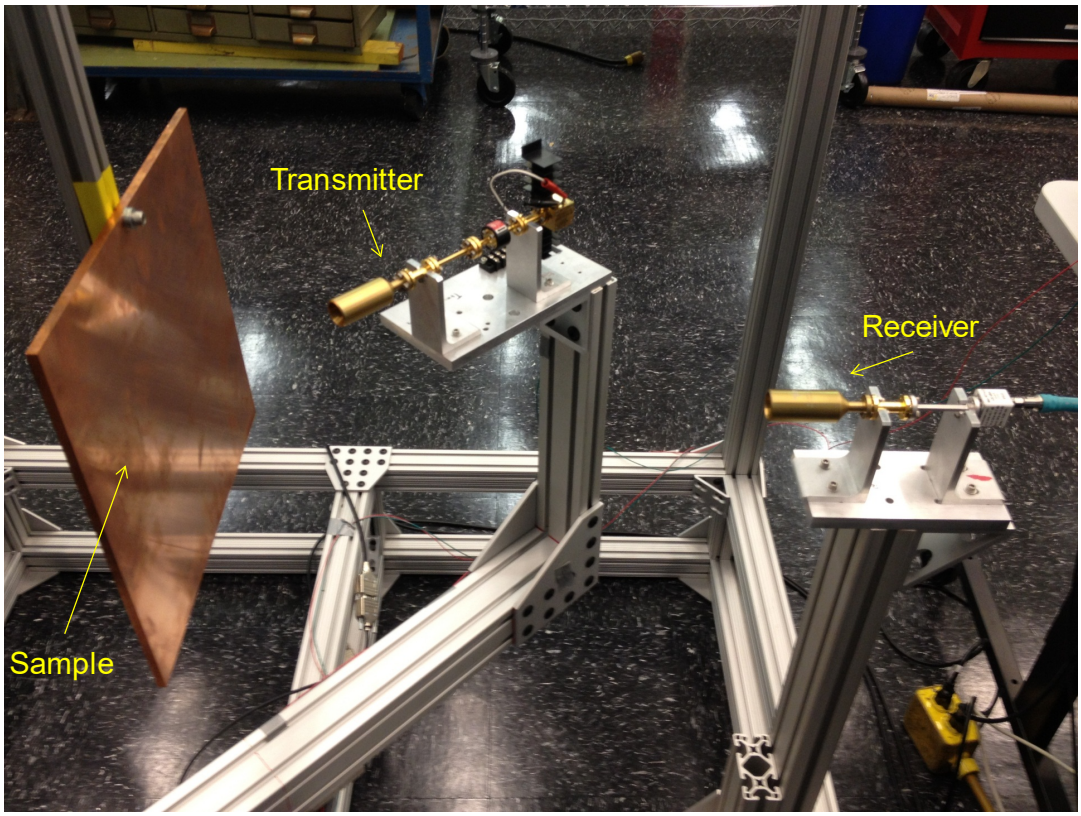

Figure 59 – Implementation of the millimeter-wave reflectometer

Measurements of millimeter-wave material properties are need from room temperature to 2,000 K and above. The objective of the reflectometer is to characterize the millimeter-wave absorption of various heat exchanger materials and the heat exchangers themselves by measuring reflected energy vs. angle of beam incidence. A secondary objective is to obtain these data sets as a function of temperature from room temperature up to the operating heat exchanger temperature of 2,000 K.

The basic reflectometer setup in shown in Figure 58. The key equipment used are Quinstar Gunn oscillators at 95 GHz (16 dBm) and 110 GHz (13 dBm). A MS2830A-044 Anritsu Spectrum Analyzer is used to measure the reflected signals.

Test coupon materials intended for characterization by the reflectometer include Cu, Al, Si, SiC, SiO_2, C allotropes, BN, B_4C, Al_2O_3, YSZ, and TiB_2.

Fibers intended for characterization by the reflectometer include Quartzel, K1100, SCS-6, YF-100, ZOF-100, CeW-30, Nextel, Tyranno, and Hi-Nicalon-S.

Coatings intended for characterization by the reflectometer include SiC:V, Y_2O_3, ThO_2, HfO_2, SiO_2, BeO, CaO, MgO, and Al_2O_3.

Work on the reflectometer facility began shortly before the DARPA-NASA MTLS project. At the commencement of the MTLS project, we prioritized heat exchanger development, rocket development and system modeling above the reflectometer test facility. Consequently, the testing and calibration of the reflectometer test facility is not yet complete.

4.2 10 kW floodlight static test facility

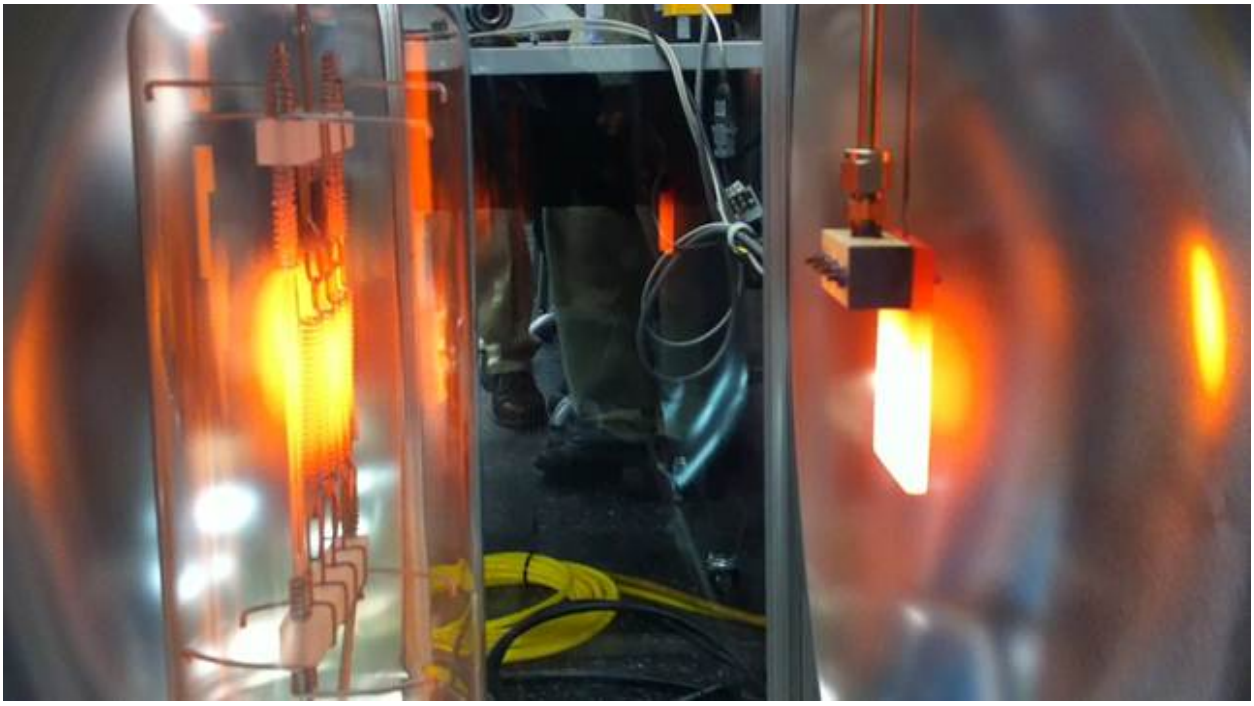

Figure 60 - Left: 20 kW tungsten filament about 5 seconds after power-off. Right: Graphite heat exchanger target (no flow). Target is size of credit card. White hot color indicates surface temperature ~ 2000 K. Inlet manifold from above. Small tube to right is thermocouple.

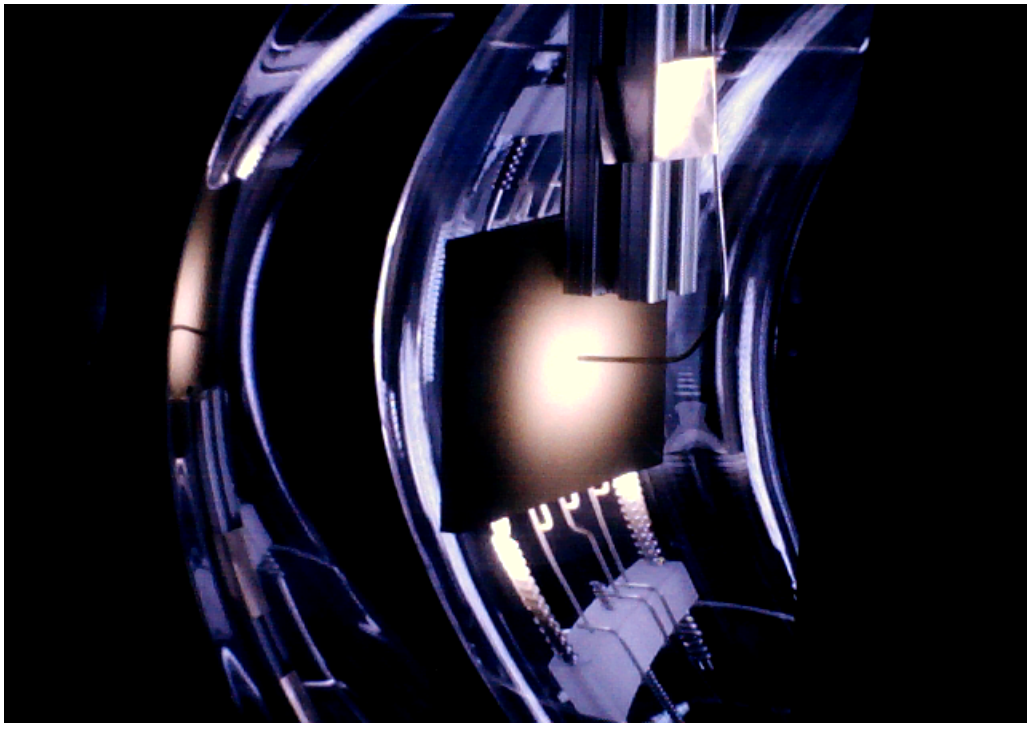

Figure 61 - CCD Image of calorimetry test (graphite target). The distorted image of the 20-kW tungsten filament is seen in the left parabolic mirror behind the target.

The objective of the 10-kW floodlight static test facility shown in Figure 60 is to provide a low-cost way to test initial multichannel heat exchanger concepts, measure their surface temperature distribution, achieve peak wall temperatures exceeding 2000 K, verify heat transfer models, and characterize oxidation damage.

The facility was built in 2008 and first used in 2009. It consists of a 20-kW floodlight bulb (Ushio 1002288) and two parabolic mirrors. Once the basic operation had been proven, the original low-quality parabolic mirrors were replaced with much higher quality protected gold mirrors, making the image of the test target visible in the mirror shown in Figure 61.

The floodlight facility yields peak fluxes of up to 2.5 MW/m^2. In comparison, the National Solar Thermal Test Facility is capable of producing peak fluxes of up to 12 MW/m^2 (United States. FedBizOpps: Federal business opportunities. Washington 2014).

Figure 62 – A demonstration of the 10-kW floodlight test facility to visiting dignitaries from China Lake NAWS

The facility is very bright, so welding googles are used when it is in operation, as seen in Figure 62. The 10 kW-class graphite plate heat exchanger described in §5.1.1 was tested in this facility.

4.3 10 kW floodlight launch test facility (not implemented)

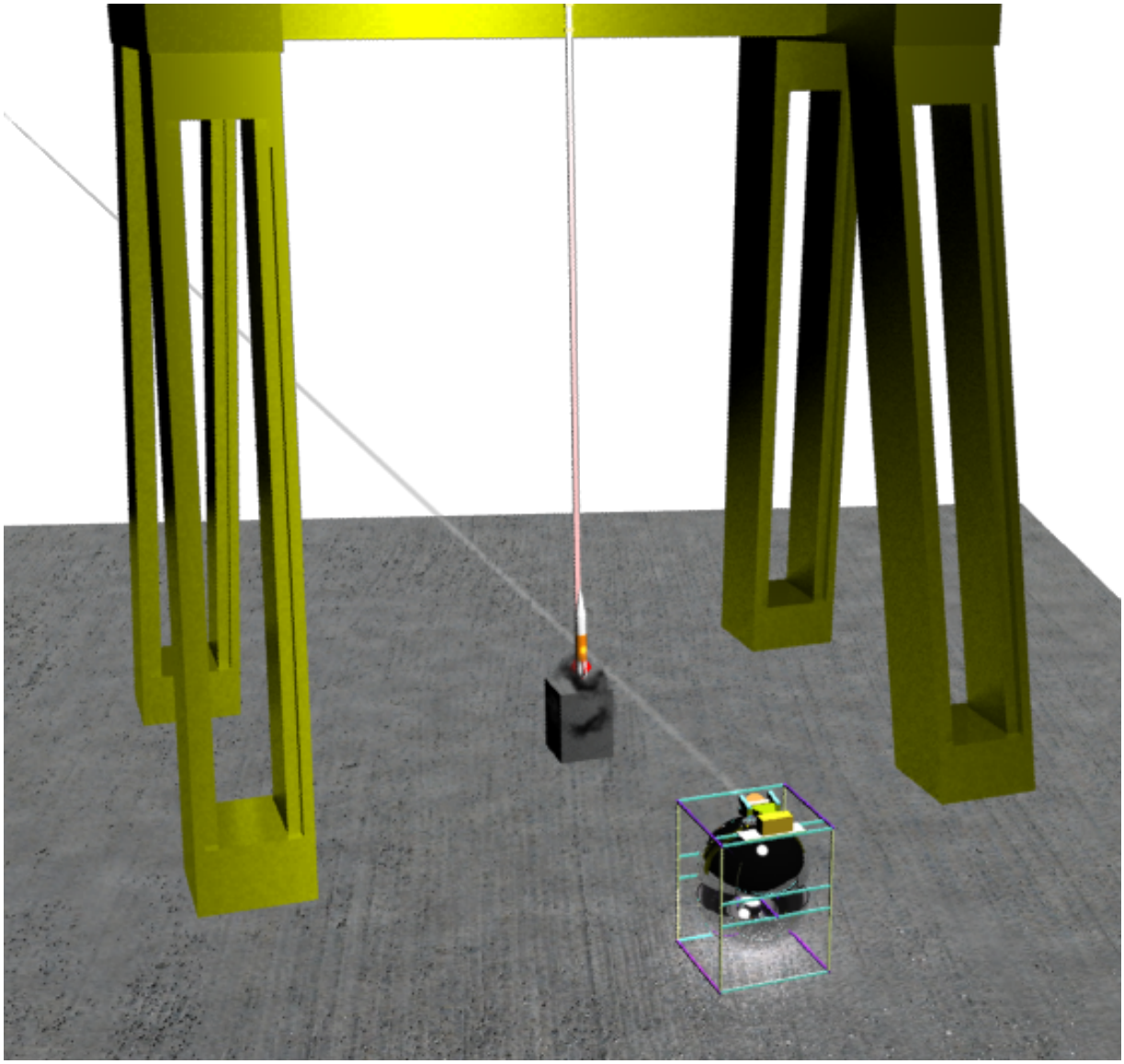

Figure 63 - Experimental arrangement for a 10-kW thermal rocket launch test facility at NASA Ames. The beam director is evolved from the 10-kW floodlight static test arrangement, and the rocket is constrained to a ribbon. The rendering is by Jacob Gold.

The floodlight launch facility shown in Figure 63 was developed as a concept starting in 2008. Its objective was to enable an initial thermal rocket and heat exchanger to be developed and tested at the smallest possible scale, and to test beam tracking techniques, all for later use with a gyrotron source. The system was to be located at NASA Ames.

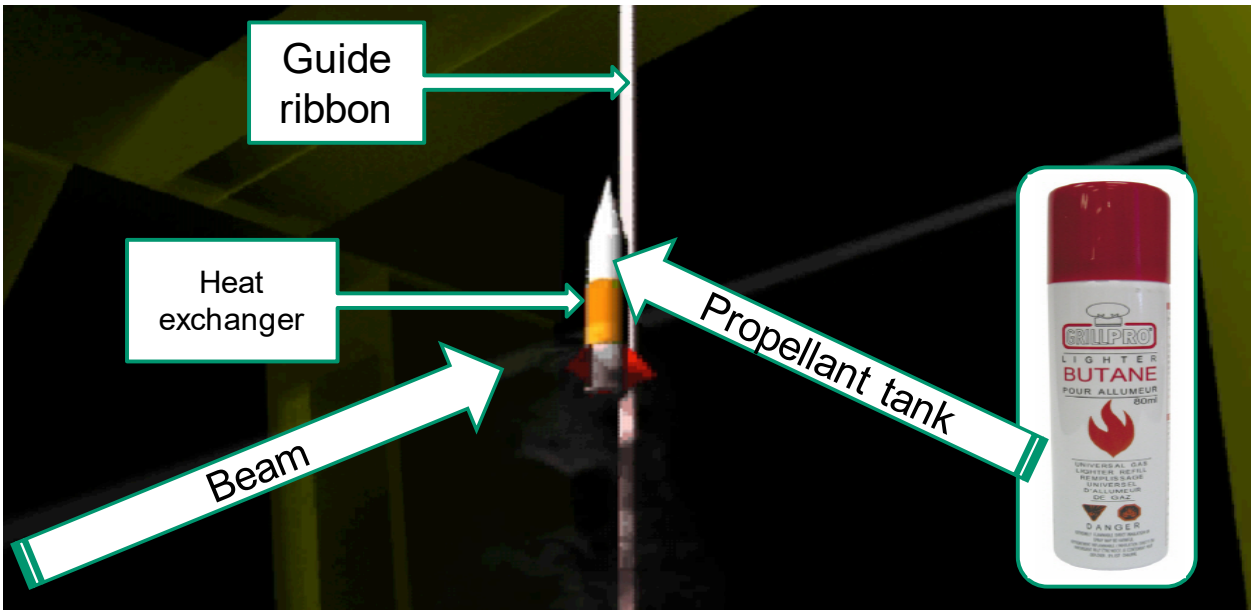

Figure 64 - Simple thermal rocket consisting of butane bottle, passive valve and heat exchanger

The rocket, shown in Figure 64, was to consist of a pressurized gas bottle (tank) connected to a beam-absorbing heat exchanger. Butane was envisaged as the propellant because inside the tank it exists as a mixture of liquid and gas in equilibrium. This equilibrium regulates the discharge pressure and mass flow rate of butane to be constant throughout the trajectory, provided that the tank temperature remains constant and that discharge is slow enough that thermal equilibrium can be maintained.

Thus, the thermal balance of the butane tank was key. The beam would initially heat the tank and heat exchanger until the pressure reached the 'cracking pressure' of the valve. Butane would then discharge through the heat exchanger, be heated to as high a temperature as possible (ideally more than 1000 K), and then expanded via a nozzle to produce thrust. The rocket could carry extra weight to ensure that the acceleration and height traveled were within the capabilities of the tracking and imaging systems.

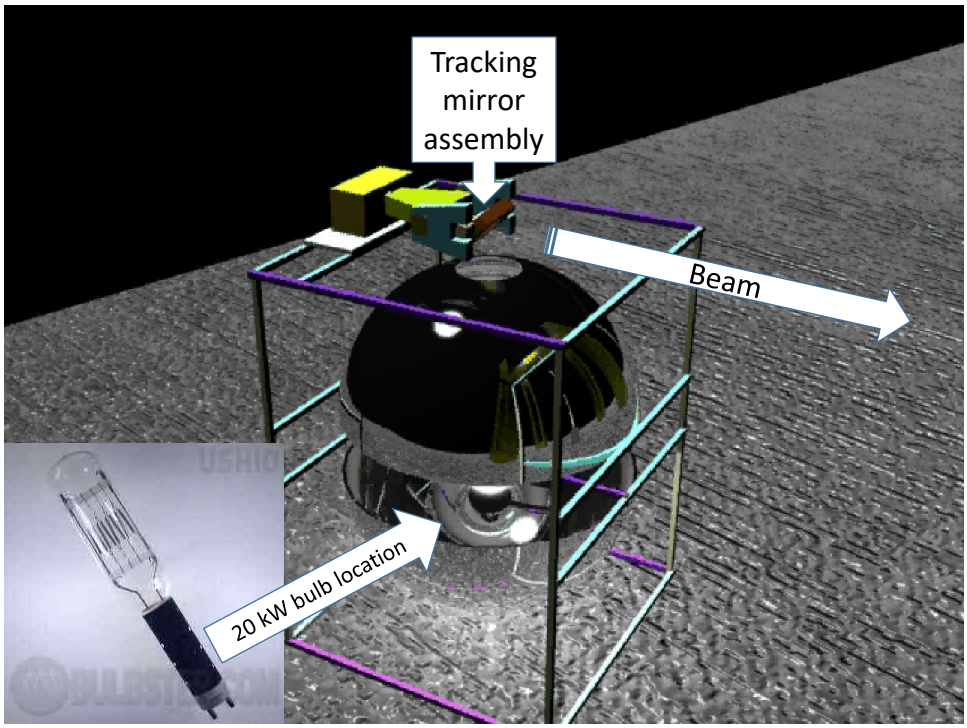

Figure 65 - Tracking mirror assembly for the 10-kW floodlight launch test facility. The rendering is by Jacob Gold.

The tracking mirror assembly, shown in Figure 65, was based on the 10-kW floodlight static test facility described earlier. The beam was to be generated using the 20-kW searchlight bulb (available commercially at a cost of $1,000) and focused down into a narrow beam by a system of mirrors. The tracking system would have steered the beam using actuators to follow the movement of the heat exchanger.

Experimental diagnostics were to include two imaging infrared cameras at different wavelengths to deduce the time evolution of the heat exchanger temperature as the craft ascended. This knowledge was and is key for evolving design codes, which build upon design codes and expertise developed in the prior experiments. The cameras were to be mounted to the tracking mirror assembly so that movement of the heat exchanger in camera view would provide a steering signal. In this way, the heat exchanger would be tracked by the beam, and the infra-red diagnostics would be recorded in a stationary frame.

In practice, it became apparent that the finite extent of the bulb filament would limit the effective range of the beam. An effort began to quantify this, and to examine arrays of carbon arc lamps due to their more ideal point-like source characteristics. The comparative advantage of the tungsten lamps was that they required no power conversion – the model was driven directly by 208 volts AC. On the other hand, carbon arc lamps require a power supply to initiate and maintain the arc which greatly multiplies the cost.

The path forward was an economic tradeoff involving the rocket and beam director. Before this work began in earnest, it was superseded by the MTLS project, which was to use gyrotron oscillators of at least 100 kW.

4.4 100 kW hot jet static test facility

The objectives of the 100-kW hot jet static test facility are to simulate a 100-kW gyrotron beam at very low cost, to understand heat exchanger dynamics, and to optimize heat transfer prior to gyrotron testing.

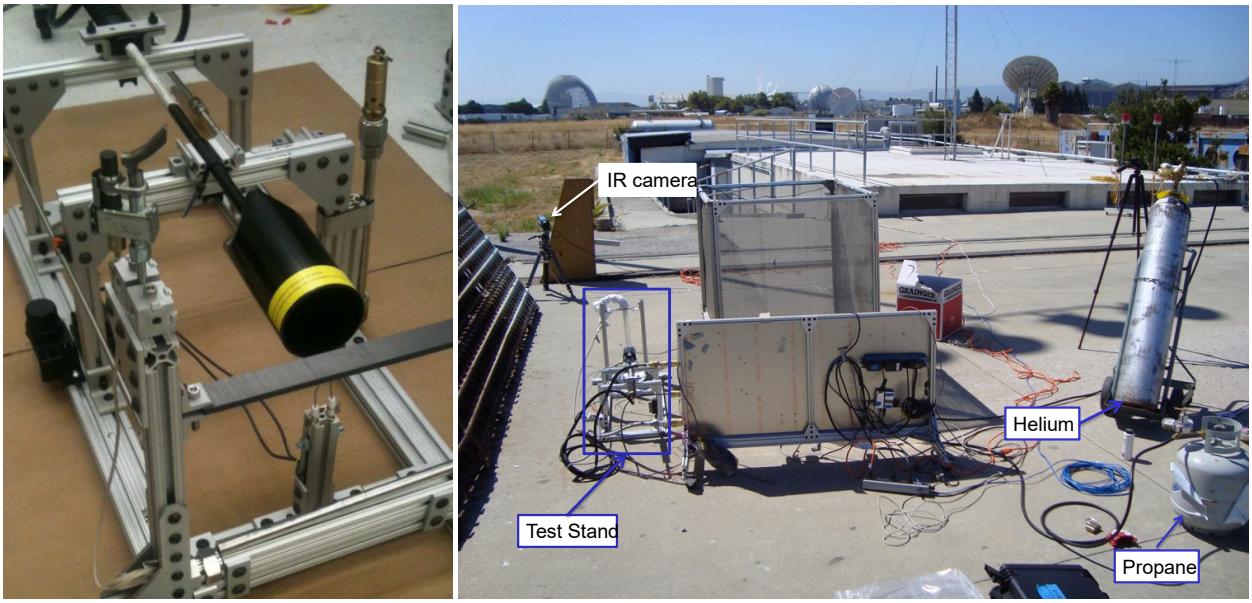

Figure 66 – Left: A low-cost commercial 100 kW propane torch (weed burner) is integrated into an automated test stand to comply with NASA safety requirements. Right: The automated test stand is operated from a remote bunker to comply with NASA safety requirements.

To do this, an instrumented test stand has been developed at NASA Ames Research Center using a low-cost commercial 100 kW propane torch, shown on the left of Figure 66, which provides a Gaussian-type distribution of heat flux similar to a gyrotron output. A long wave infrared camera is used for surface temperature diagnostics during testing, along with thermocouples. A mass flow controller is used for controlling and measuring the mass flow and monitoring the propellant inlet temperature.

For some experiments, the exhaust of the tubes is collected in a stagnant reservoir with a small outlet orifice in order to estimate the peak stagnation temperature of the propellant.

The adiabatic flame temperature of propane in air is 2,200 K, representing the theoretical maximum temperature that our non-premixed propane torch can produce. In practice, the propane feed pressure is reduced such that the heat exchanger tubes reach a maximum temperature of around 1,500 K in order to avoid local deformation of the tubes over experimental runs lasting 20 minutes or more.

Due to the San Francisco Bay winds ramping up during the day, experiments are carried out in the early morning to ensure accuracy and repeatability.

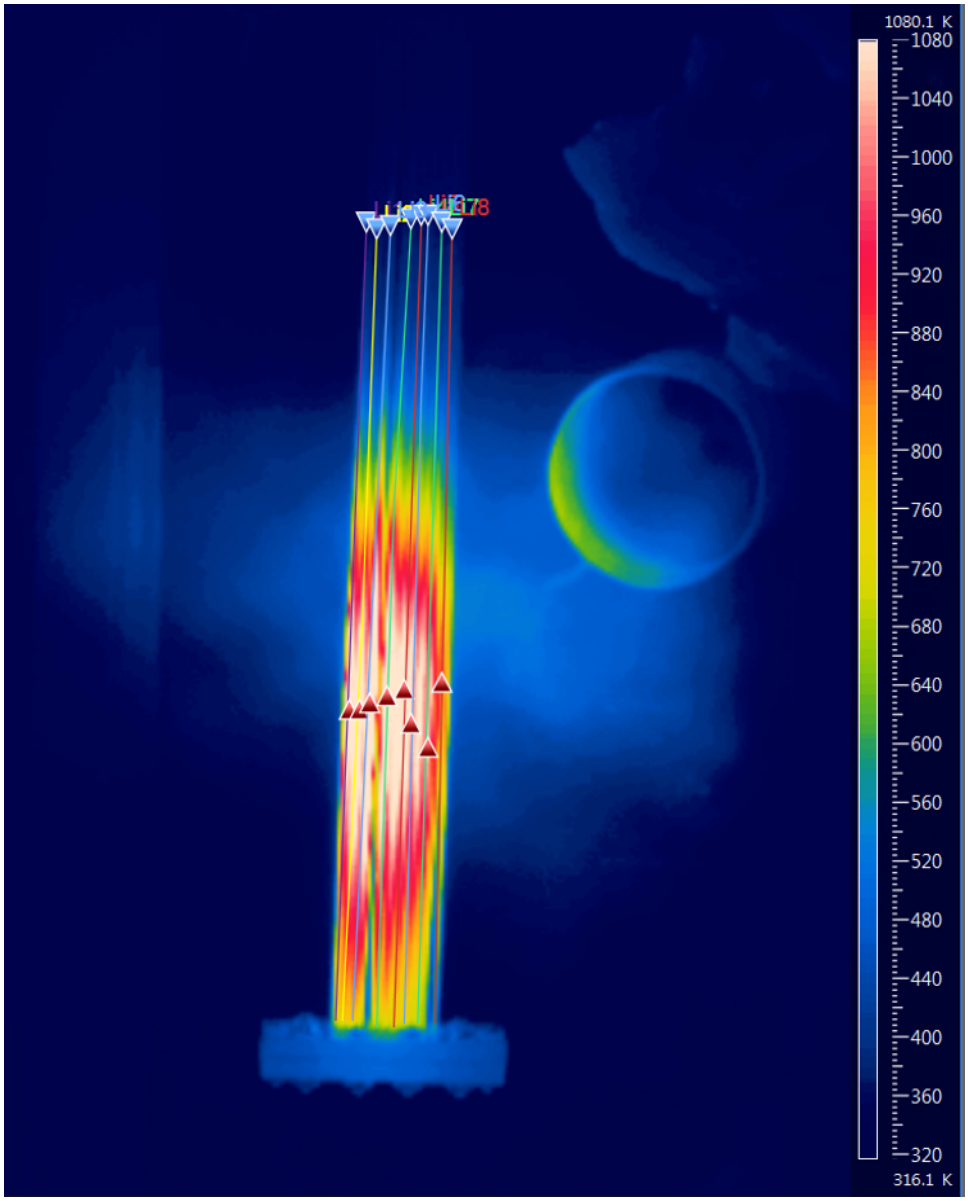

Figure 67 - Test of an early graphite outlet concept for a heat exchanger comprised of 18 alumina tubes. The test demonstrated that the tube to outlet joins and manifold assembly could support repeated thermal and pressure cycles.

4.5 1 MW, 110 GHz static test facility

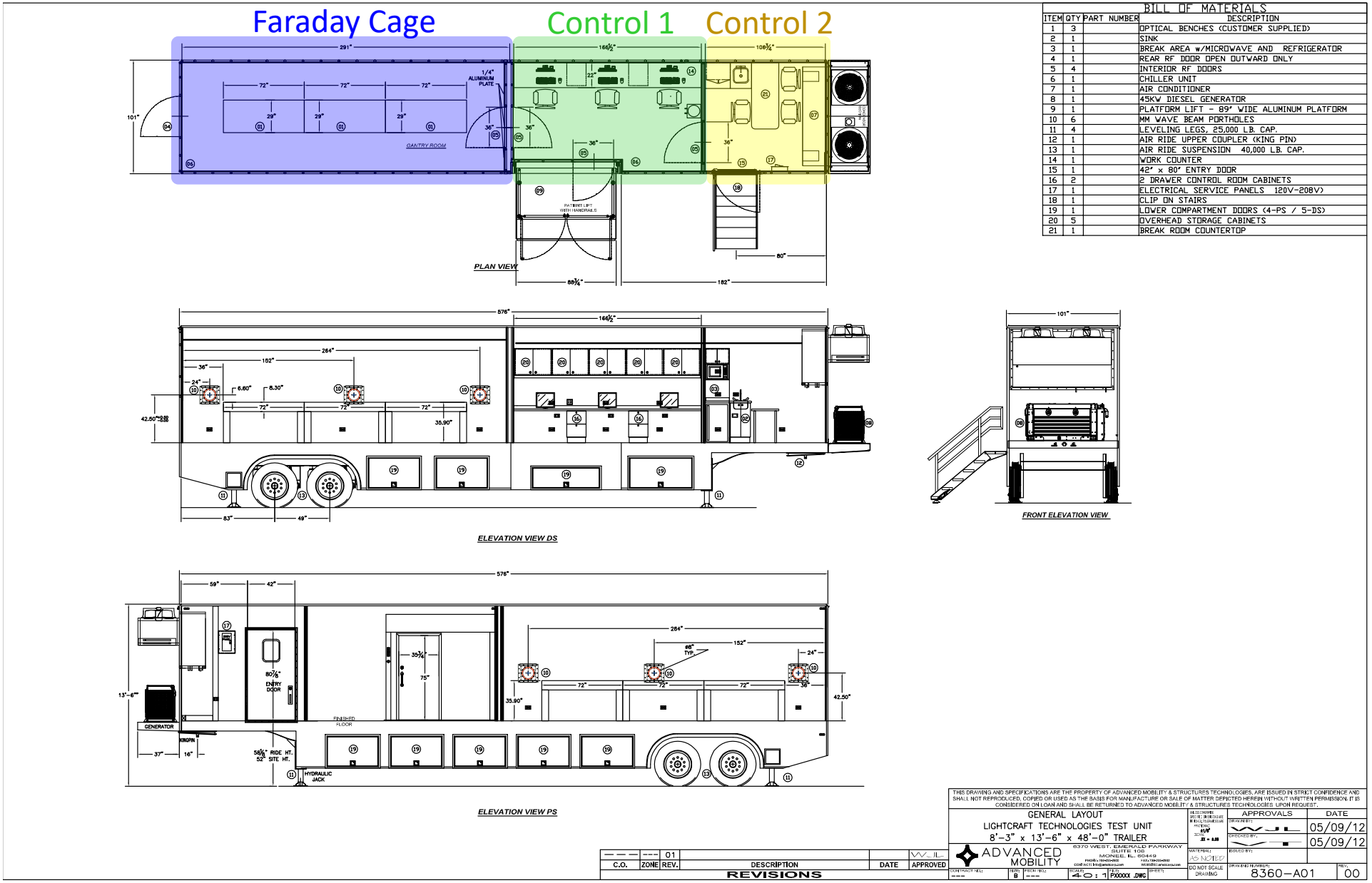

Figure 68 - Mobile Test Unit (MTU) plan.

Figure 69 – Mobile Test Unit (MTU) designed by Leik Myrabo/LTI and Advanced Mobility Specialty Vehicles of Monee, IL, who built the test unit. Myrabo realized that MRI trailers have steel shielding and could be repurposed at low cost to form a Faraday cage and control room for millimeter-wave tests.

The mobile test unit (MTU) is a laboratory for heat exchanger testing that is relocatable to any one of several possible sites that house suitable millimeter-wave sources for testing propulsion systems. When located at the DOE/General Atomics DIII-D fusion reactor in San Diego, it constitutes a 1 MW, 110 GHz static test facility with a maximum beam duration of 3 seconds.

The MTU is housed within a repurposed 48' MRI trailer, the plan of which is shown in Figure 68 and the realization of which is shown in Figure 69. The test area is a Faraday Cage and has three waveguide ports on each side for a beam input. Control 1 is a primary control room, which connects to instrumentation in the Faraday Cage via fiber optic cables running through a special feedthrough port. Control 2 is a secondary control room, intended for separate launch control, or can be used for other control functions where team crosstalk during critical operations is unwanted. Late in the final design, we modified control room 2 to place the table against the wall as opposed to the configuration shown here. Computers and instrumentation in all areas of the MTU are capable of being tied in and integrated via the fiber optic networks.

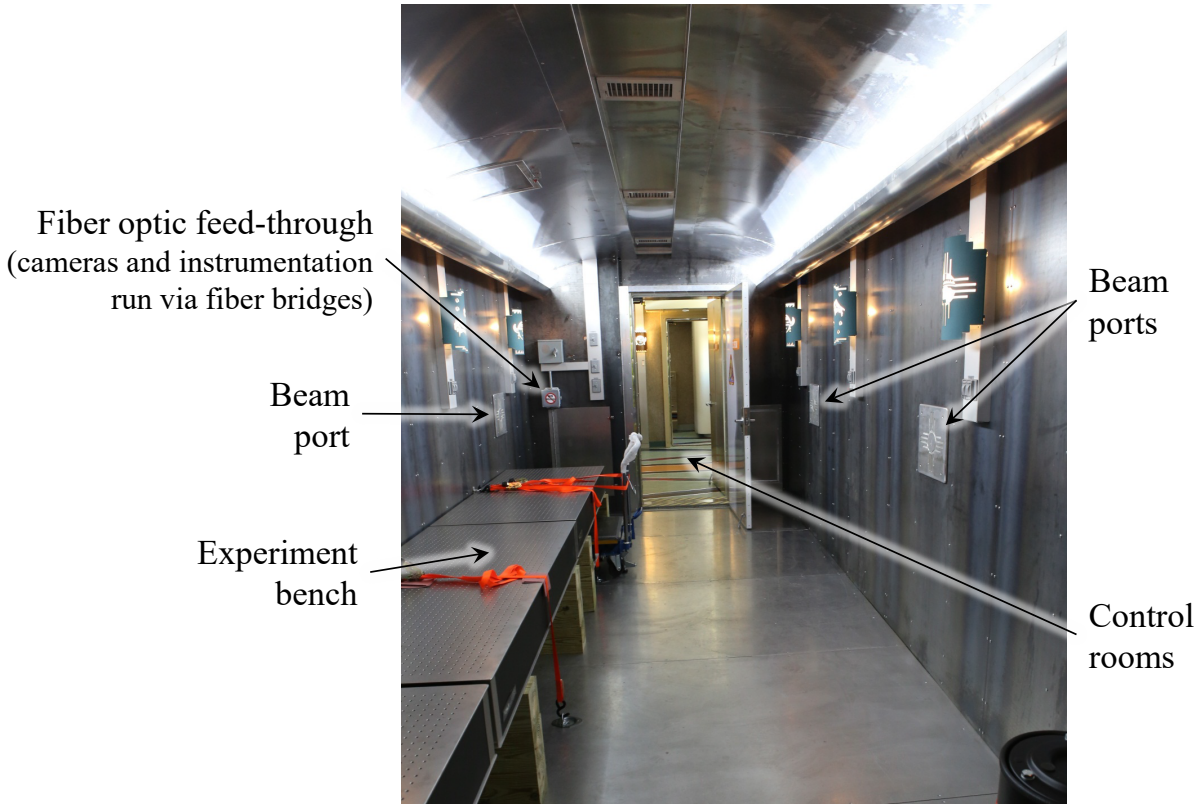

Figure 70 – The experimental test section of the MTU prior to flame-spraying the steel walls, floor and ceiling with a TiO_2 coating to absorb stray millimeter-waves. This coating was suggested by Dr. John Lohr of General Atomics based on prior experience.

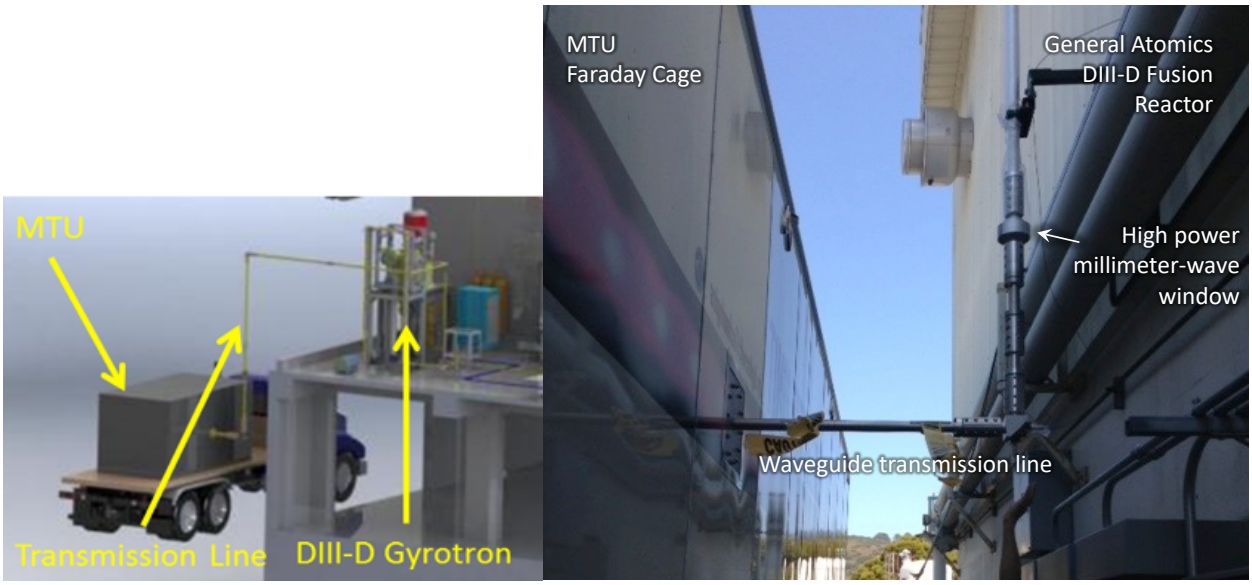

Figure 71 – The gyrotron subsystem of the DOE/General Atomics DIII-D fusion reactor is interfaced with the MTU Faraday cage via a waveguide transmission line. Left: Initial concept. Right: Realized solution.

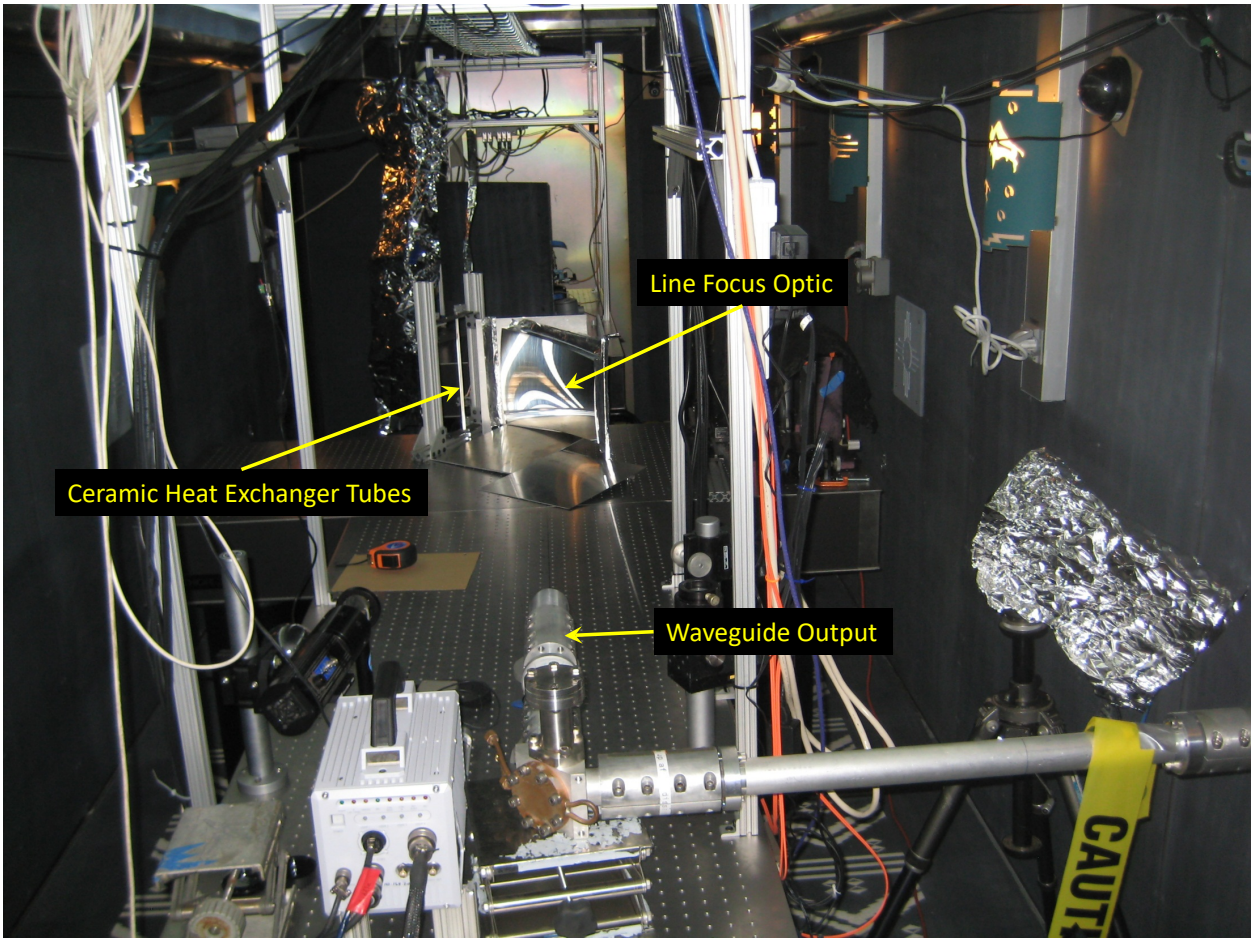

Figure 72 – A typical experimental arrangement in the MTU.

Figure 73 – The MTU control room 1 in use with one of us (Parkin) shown preparing the test sample for an upcoming experiment. The Faraday cage test area is visible through the open doorway, and the image is taken from control room 2 through its open doorway.

Instrument	Specification	Manufacturer, model and serial
High-speed camera	100,000 fps 1024x1024 pixels monochrome	Photron FASTCAM SA1.1
Thermal camera	640x480 pixels @ 50 fps 640x120 pixels @ 200 fps LWIR Max. temperature 2,300 K	FLIR A655sc Unless otherwise specified, images taken using this camera are through a FOL41 lens at 50 frames per second and assume a target emissivity of 0.95
High-definition camera	2048x2048 pixels @ 180 fps color	Basler ACE 2040-180kc Unless otherwise specified, images taken using this camera are through a Fujinon HF35SA-1 lens.

Table 17 – Key instrumentation

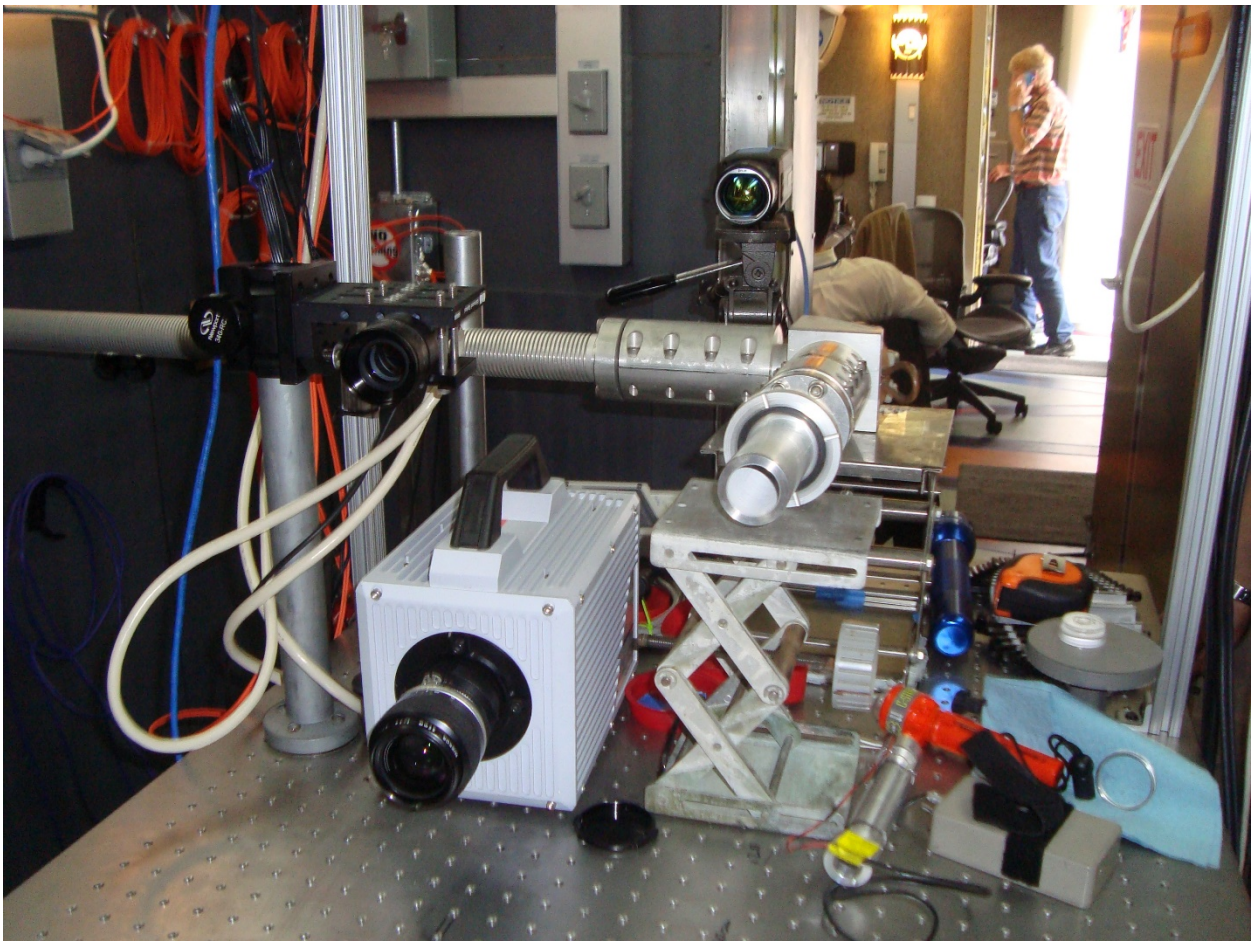

Figure 74 - Instrumentation of Table 17 as deployed for data acquisition. Source file: 2013-08-13 00.49.02.jpg

4.6 100 kW, 95 GHz circular motion test facility (not implemented)

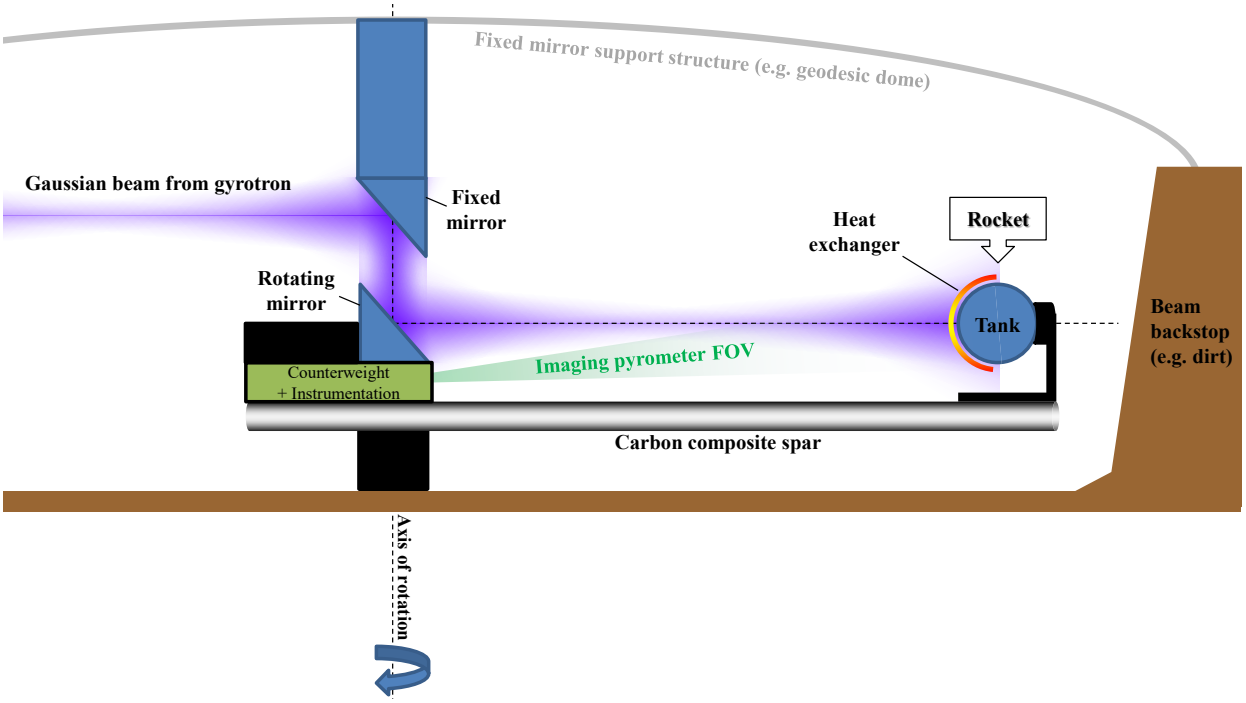

Figure 75 – Concept for the circular motion test facility

The circular motion test facility shown in Figure 75 was envisioned as a step between static testing and launch testing. Relative to static testing, circular motion enables body forces to be exerted on the tank and heat exchanger in order to identify dynamic instabilities that may occur between the tank and heat exchanger while accelerating. Relative to launch testing, the circular motion arrangement provides an axis of rotation through which a beam can be kept on the rocket without the need to build an active tracking and beam pointing system or vary the system focal length. It also makes it easy to keep the heat exchanger stationary in the frame of imaging diagnostics. Other benefits include:

- T/W<1 is possible (it is also possible for horizontal or inclined, not vertical launch)
- The beam is not pointed skyward

For the MTLS project, it was ultimately decided to move directly from static testing to launch testing, in part because the DARPA wanted us to attack the problem of building a beam director and cooperative targeting system, and in part because there is only an indirect correspondence between the type of body forces generated in the circular motion system and the type that would be generated by linear motion during an actual launch. Other drawbacks include:

- Additional mass of spar reduces acceleration
- Direction of body forces is different to vertical ascent (though tank could be oriented perpendicular to heat exchanger and exhaust to compensate)
- Propellant drainage from tank may be impacted (gas phase may not be where outlet is)
- Instrumentation may need to be wireless

4.7 100 kW, 95 GHz launch test facility

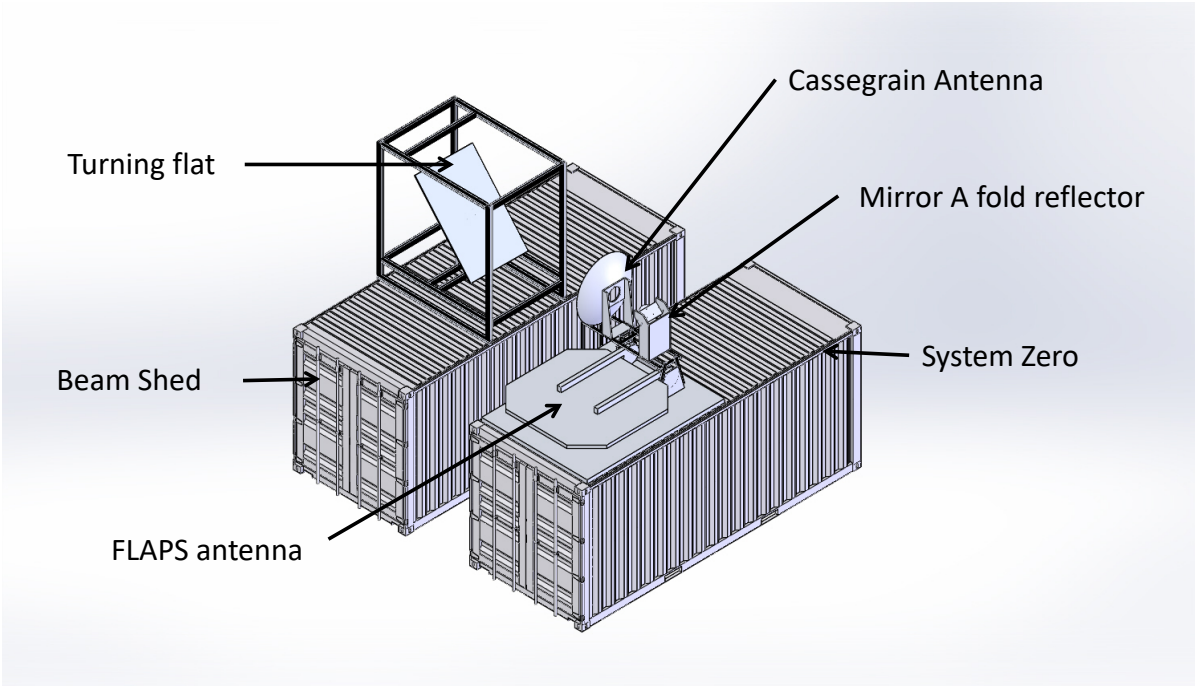

Figure 76 – Concept of how the existing containers are retrofitted to include beam steering and focusing optics.

An existing 100 kW, 95 GHz source located at Kirtland Air Force Base, New Mexico, is the basis around which a launch test facility has been built.

	Side-illuminated	Axial-illuminated
Elevation	0° to 45° (0° to 90° desired)	0° +/- 10°
Range	150 to 250 meters (75 to 500 m desired), focus waist to +/-5 m along range axis	75-105 m w/ 180cm BD 44-74 m w/ 120cm BD 13-43 m w/ 60cm BD
Peak angular velocity	45°/s (El) (90°/s desired)	4.5 to 45°/s
Worst case angular acceleration	45°/s^2 (El) worst-case (90°/s^2 desired)	4.5 to 45°/s^2
Closed loop pointing accuracy	0.003° (Az) and 0.006° (El) (0.001°desired, both axes, but accuracy on Az most important)	0.003° to 0.03°
Beam waist diameter	0.4 m or best effort	0.2-0.4 m

Table 18 – Original requirements for the beam director. Due to the time and cost constraints of the MTLS project, these were all negotiable and the final system was not held to them.

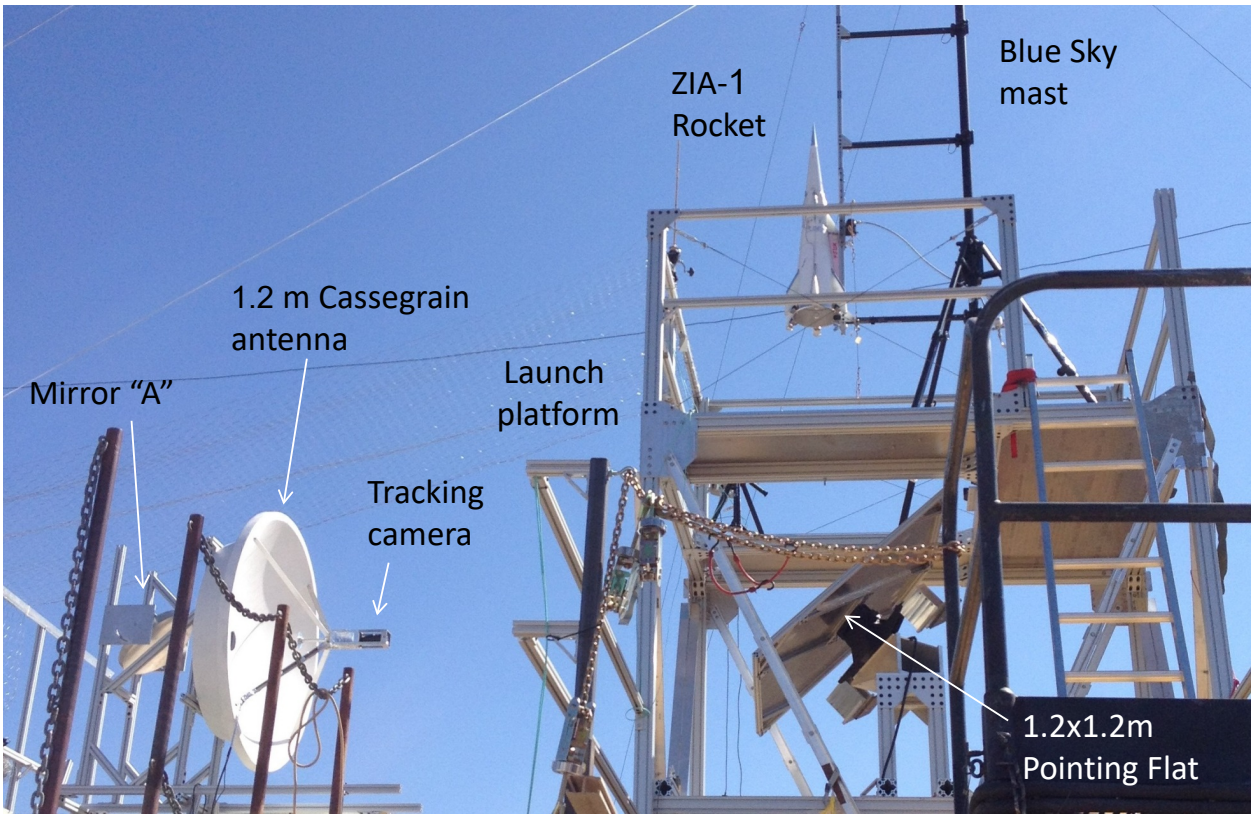

Figure 77 – Layout of the beam director and launch platform for axial-illuminated rockets of Myrabo/LTI.

Figure 78 – Layout of the beam director and launch area for side-illuminated rockets

For the side-illuminated layout, shown in Figure 78, the millimeter-wave beam is reflected by the Cassegrain antenna and onto to the pointing flat, which redirects it toward the target on or above the launch rail. The pan-tilt unit (PTU) used to steer the pointing flat is visible on the bottom right of Figure 77.

The PTU used is a FLIR PTU-D300-EX model (specifically, a D300E-UD-SS-000-SS), chosen because it had the highest payload capacity within the stringent cost and schedule constraints of the MTLS project. Unfortunately, the pointing flat turned out to be too heavy for this unit. In the video of actual rocket tests, the PTU lags the command to move upward by approximately 150 milliseconds. In addition, it halts intermittently when commanded to tilt either up or down. Consequently, the beam director is

unable to track the side-illuminated rockets as they launch and instead oscillates about the rocket's position. In short, there is a lack of control authority. In future work, we recommend that the PTU be upgraded to a heavier payload model, that the turning flat be lightened, and that adequate time is given to write the control system and thoroughly test it prior to attempting millimeter-wave rocket launches.

Figure 79 – The beam characterization procedure featuring Julie Mikula (MTLS project manager) on the right.

The beam produced by the beam director is characterized by thermally imaging a carbon-loaded Teflon board, shown in Figure 79, at different distances.

4.7.1 Cooperative tracking subsystem

The key distinction between a cooperative target and an uncooperative target is that a cooperative target can emit a beacon and/or feedback signal to assist with steering the beam.

Co-operative tracking

- High brightness green LEDs (527 nm)
- Clustered toward top and bottom of rocket
- Tracking camera uses 527 nm filter with 20 nm bandwidth.
  - Optical path bounces off the turning flat and is co-aligned with the beam
- Software processes ~24 fps to produce steering signal for pan-tilt unit of turning flat

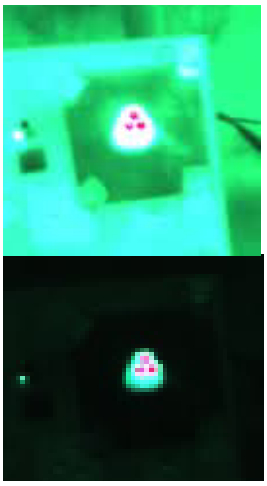

Top left: A scene taken through the green filter. The LEDs saturate the CMOS sensor of a Basler ACE acA2040-180kc camera (not the tracking camera used). Bottom left: The same scene taken at minimum exposure time of 24 µs. The sensor is still saturated and background clutter reduced to essentially none.

527 nm LEDs in bright daylight (without filter)

5 Experiments

5.1 Heat exchanger

5.1.1 10 kW-class (incomplete)

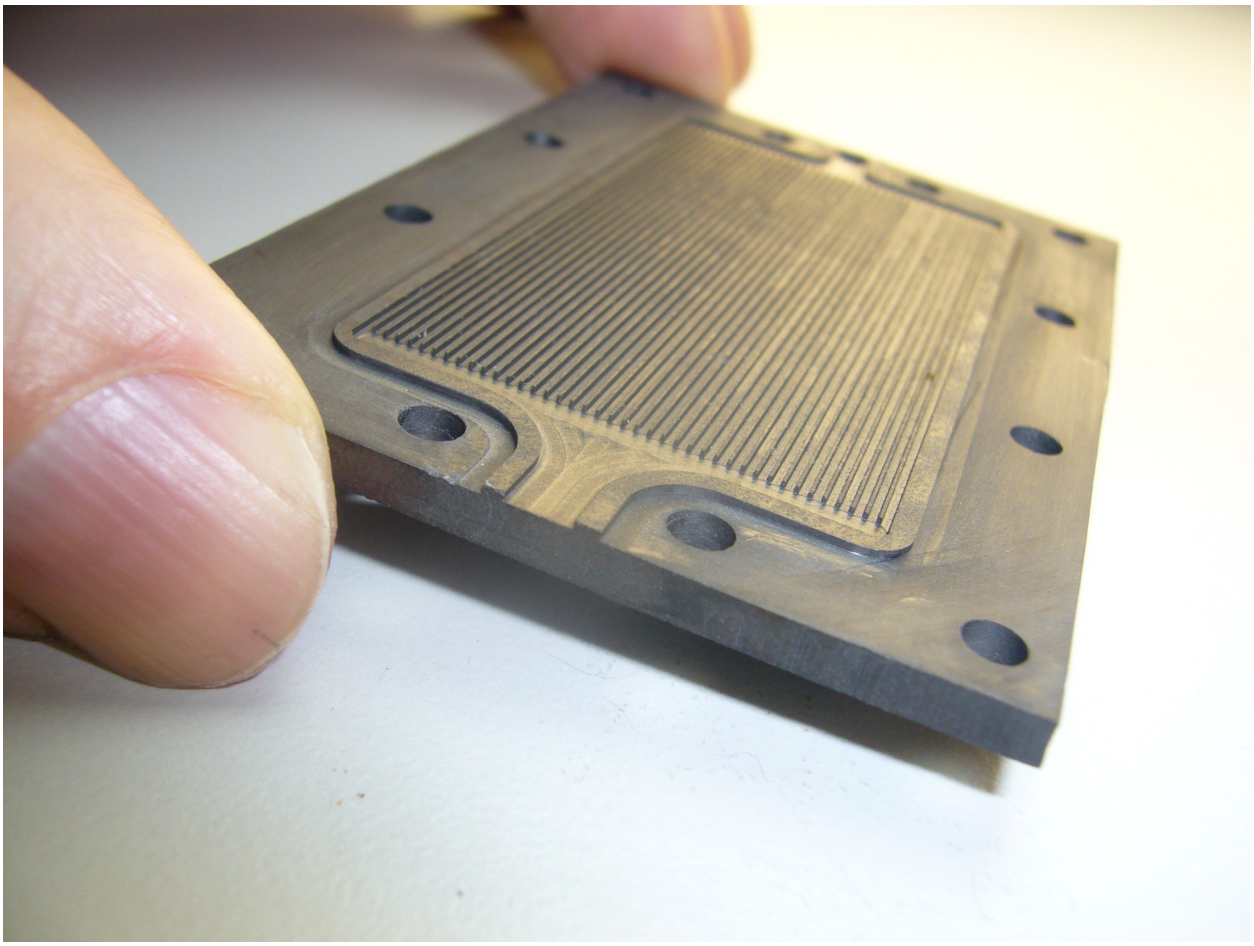

Figure 80 - Graphite multichannel heat exchanger produced by David Murakami in 2011

5.1.2 100 kW-class

The design of the 100 kW-class heat exchanger is detailed in §3.5.3. In this section, we explain that at the outset, only theoretical knowledge existed to describe how a millimeter-wave beam might be absorbed into a heat exchanger. Consequently, we decided that the best approach would be to build a heat exchanger from a millimeter-wave transparent ceramic material and then to use theory and experimentation to find a way to make it absorb millimeter-waves. This was as opposed to starting with a millimeter-wave reflective material such as a metal and trying to find a millimeter-wave absorbent coating with good adhesion or develop an absorbent metasurface.

The goals of the 100 kW-class heat exchanger experiments were therefore:

1. Find a way to make the heat exchanger absorb millimeter-waves and maximize the absorption efficiency
2. Investigate the various types of surface and volume plasmadynamic breakdown that limit the intensity of the incident beam
3. Achieve high-temperature heat exchanger operation at > 1,500 K
4. Achieve high-flux heat exchanger operation[s]

Our label	Manufacturer and part number	Material	Inner diameter	Outer diameter	Wall thickness	Length
A	CoorsTek 65651	Alumina 99.8%	0.794 mm (1/32”)	1.588 mm (1/16”)	0.40 mm (1/64”)	350 mm
B	CoorsTek 33459 (custom-made)	Alumina 99.8%	0.914 mm (0.036”)	1.321 mm (0.052”)	0.20 mm	>152 mm (>6”)
C	CoorsTek 66618	Mullite	1.19 mm (3/64”)	1.98 mm (5/64”)	0.40 mm (1/64”)	304.8 mm (12”)
D	Omega ORM-132116-12	80% Mullite, 20% Glass	0.794 mm (1/32”)	1.588 mm (1/16”)	0.40 mm (1/64”)	304.8 mm (12”)

Table 19 – Summary of ceramic tubes used in the experiments

Our label	Product	Mixture ratio (product : water)
1	Aquadag E (colloidal graphite)	1 : 1
2	Aquadag E (colloidal graphite)	1 : 2
3	Oxititan (titanium dioxide nanopowder)	1 : 5.5

Table 20 – Summary of coating mixtures used in the experiments

To meet goal 1 (find a way to make the heat exchanger absorb millimeter-waves and maximize the absorption efficiency a series of coatings are investigated), coated and uncoated tubes of mullite and

[s] Left unquantified at the time so as not to distract from the other goals. The 50-kg point design of §3.4.1.1 assumes an average flux of 6 MW/m^2. If this turns out to be difficult to achieve, the flux limit is mitigated by increasing the area of the heat exchanger and lowering the areal density of the heat exchanger.

alumina are used. These are given in Table 19. Each tube is left bare or coated with one of the coatings given in Table 20.

Position	Jig-A	Jig-B	Jig-C	Jig-D	Jig-E	Flow-1	Flow-2	Flow-3	Flow-4
7	A.2.O	D							C.1.I
6	A.2.O			A.1.I		C.1.I	C.1.I	C.1.I	
5	A.2.O	C.1.I			C.1.I				C.1.I
4	A.1.O			B.1.I		C.1.I	C.1.I	C.1.I	
3	A.1.O	C.1.I	C.1.I		D.1.I				D.1.I
2	A.1.O	B		B.1.I		D.1.I	D.1.I	D.1.I	
1	A.3.O	C	C.1.I		D.1.I				D.1.I
0	A.3.O	B		B		D.1.I	D.1.I	D.1.I	
-1	A.3.O	A.1.I	A.1.I		B.1.I				A.1.I
-2	A.1.I			D.1.I		B.1.I	B.1.I	B.1.I	
-3	A.1.I	A.1.I	A.1.I		B.1.I				A.1.I
-4	A.1.I			D.1.I		B.1.I	B.1.I	B.1.I	
-5	A.2.I	D			C.1.I				B.1.I
-6	A.2.I			C.1.I		A.1.I	A.1.I	A.1.I	
-7	A.2.I								B.1.I

Table 21 – Summary of tube combinations used by experiment. The left column is the position of the tube in the metal frame (jig); the top is the label used for the jig configuration in experimental test lists given later. The notation used is Tube.Mixture.I/O: The tube labels from Table 19 denote the tube. The mixture labels from Table 20 denote the mixture. The I/O denotes whether the mixture is applied to the inside or the outside of the tube. A tube label given without mixture information implies that the tube was left uncoated as an experimental control.

Figure 81 – One of us (Lambot) preparing the Flow-3 jig for experiments. The tube positions of Table 21 are marked in black ink on either side of the jig, with higher numbers being physically at the top.

Each tube is placed in one of 14 possible positions vertically in a spacer, held together by an aluminum frame at a given distance from the waveguide's horn. This jig is shown in Figure 81. To try many approaches quickly, a tournament is carried out in which each configuration, listed in Table 21, is used to test many tube and mixture combinations in parallel. The most promising qualify for later tests. The various jigs are exposed a beam at 110 GHz for short durations ranging from 20 to 3000 milliseconds. These durations are limited by the heating of the waveguide quartz window and an administrative limit on the pulse lengths produced by the gyrotrons.

5.1.2.1 5/20/2013 - 5/31/2013 test campaign at 1 MW, 110 GHz static test facility

5.1.2.1.1 Monday 5/20/2013. Beam Characterization

		Experimental parameters								Outcome					
Time	Run #	Position [cm]	Gyrotron voltage [kV]	Requested duration [ms]	Duty cycle [%]	Line focus used?	Peak flux at target [MW/m^2]	Fastcam rate [kFPS]	FLIR range [1/2/3]	Flow?	Full Pulse?	Actual duration [ms]	Fault?	Pop sound?	See FastCam data?	See HDCam data?	FLIR max temp [K]	Comments
Installed model XXa: 10cm parabolic reflector axi-symmetric for breakdown threshold experiments																		
17:20	1	70	68	0.1	100	N	44											For later reference:
	2	70	68	3.2	100	N	44											FLIR range 1 = 233-433 K
	3	70	68	3.2	100	N	44											FLIR range 2 = 373-973 K
	4	70	68	4	100	N	44											FLIR range 3 = 473-2273 K
	5	70	70	5	100	N	55											
	6	70	72	5	100	N	66											
	7	70	74	5	100	N	77						Y					
17:40	8	70	73	5	100	N	72						Y					

Table 22 – Tests conducted on Monday 5/20/2013

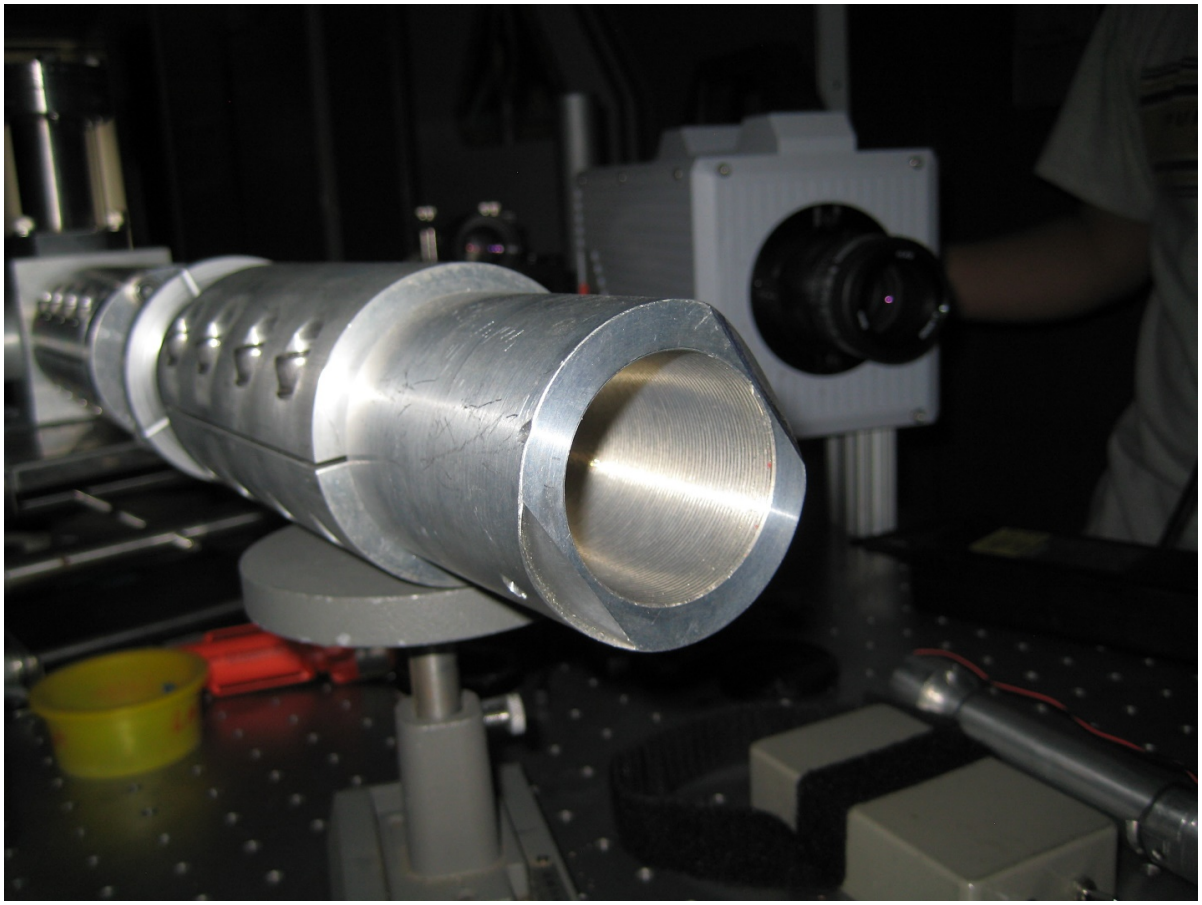

Figure 82 – The beam launcher. Source file: IMG2841.jpg

The beam is first characterized using by shooting very short pulses at a paper target while recording the thermal image on a LWIR camera. For these short times, conduction of heat along the paper or from the face of the paper into the air is negligible. This procedure is repeated at several distances from the beam launcher, shown in Figure 82, to quantify the flux. After some distance, the beam starts to reflect off the table and interferes with itself to form the beam profile as seen on the bottom right image. This phenomenon increases in intensity as distance from the waveguide end is further increased.

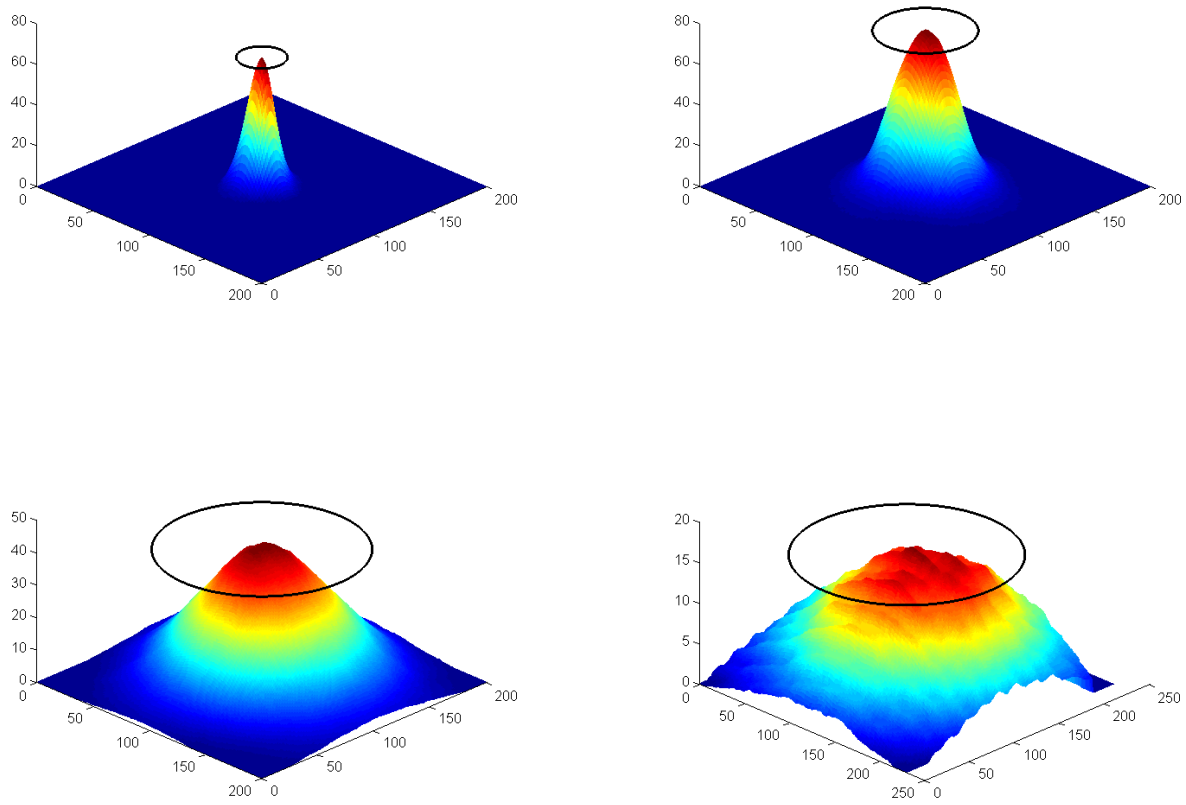

Figure 83 – Fits of Gaussian beam radii to measured beam profiles at different ranges from the beam launcher. The black circle shows the e^{-1} diameter which we refer to as the "beam diameter" hereafter. The data plotted is actually the temperature rise induced in a paper target by a short pulse of the beam, and measured by LWIR camera.

From each of these frames, a Gaussian beam is fitted, as seen in Figure 83. These radii are plotted vs. distance and a linear fit to the data yields an expression for beam radius as a function of distance from the beam launcher,

$$D[cm] = 0.1405 * Distance[cm] - 0.1392. \quad [124]$$

The Gaussian beam intensity is then related to this beam diameter using,

$$I_{peak}\left[\frac{W}{cm^2}\right] = \frac{8P_0[W]}{\pi(D[cm])^2}, \quad [125]$$

where P_0 is the power output from the waveguide.

5.1.2.1.2 Tuesday 5/21/2013. Inducing breakdown

Experimental parameters										Outcome					
Time	Run #	Position [cm]	Gyrotron voltage [kV]	Requested duration [ms]	Duty cycle [%]	Line focus used?	Peak flux at target [MW/m^2]	Fastcam rate [kFPS]	FLIR range [1/2/3]	Flow?	Full Pulse?	Actual duration [ms]	Fault?	Pop sound?	See FastCam data?	See HDCam data?	FLIR max temp [K]	Comments
Installed model XXb: 10cm parabolic target with pin in the middle for breakdown threshold experiments																		
16:30	1	70	63	3.2	100	N	17						N					
	2	70	63	3.5	100	N	17						Y					
	3	70	63	3.3	100	N	17						N					
	4	70	63	3.4	100	N	17						N					
	5	70	63	3.5	100	N	17						N					
	6	70	63	3.6	100	N	17						N					
	7	70	63	3.7	100	N	17						N					
16:45	8	70	63	3.8	100	N	17						N					
	9	70	64	3.3	100	N	23						N					
	10	70	65	3.3	100	N	28						Y					
	11	70	65	3.3	100	N	28						Y					
	12	70	65	3.3	100	N	28						N					
	13	70	65	3.3	100	N	28						N					
17:00	14	70	66	3.3	100	N	33						Y					
	15	70	66	3.3	100	N	33						Y					
	16	70	66	3.3	100	N	33						N					
	17	70	66	3.3	100	N	33						N					
	18	70	66	3.3	100	N	33						N					
	19	70	67	3.3	100	N	39						Y					
	20	70	67	3.3	100	N	39						Y					
	21	70	67	3.3	100	N	39						Y					
	22	70	67	3.3	100	N	39						Y					
	23	70	67	3.3	100	N	39						Y					
17:45	24	70	67	3.3	100	N	39						Y					

Table 23 - Tests conducted on Tuesday 5/21/2013

The experimental objective for the early tests was to induce the various types of plasmadynamic breakdown that might impose incident flux limits on the heat exchanger. Tuesday was primarily occupied by setup and calibration activities. Later in the day, there was a little time left for informal attempts at inducing breakdown using the LTI 11 cm axisymmetric parabolic optic. To lower the breakdown threshold, a pin was added at the focus. Breakdown was reliably and repeatably achieved using 3.3 ms pulses. This could be considered a successful demonstration of a pulsed-plasma air-breathing millimeter-wave engine; however, the video subsystem was not yet ready to take data.

5.1.2.1.3 Wednesday 5/22/2013. Flat plate absorption.

Experimental parameters										Outcome				
Time	Run #	Position [cm]	Gyrotron voltage [kV]	Requested duration [ms]	Duty cycle [%]	Line focus used?	Peak flux at target [MW/m^2]	Fastcam rate [kFPS]	FLIR range [1/2/3]	Flow?	Full Pulse?	Actual duration [ms]	Fault?	Pop sound?	See FastCam data?	See HDCam data?	FLIR max temp [K]	Comments
Continued with model XXb: 10cm parabolic target with pin in the middle for breakdown threshold experiments																		
?	1		63	3.3	100									N				
10:19	2		65	3.3	100									Y	N			FastCAM: C001H001S0001.avi
10:44	3		65	3.3	100									Y	N			FastCAM: C001H001S0002.avi
11:18	4	70	65	3.3	100	N	28	30						Y	Y			FastCAM: C001H001S0003.avi
11:24	5	70	65	3.3	100	N	28	90						Y	Y			FastCAM: C001H001S0004.avi
11:30	6	70	65	3.3	100	N	28	54						Y	Y			FastCAM: C001H001S0005.avi
11:39	7	70	65	3.3	100	N	28	125						Y	Y			FastCAM: C001H001S0006.avi
11:40	8		64	3.3	100									N	N			
Installed 6”x6” TiO2 coated 1/8” aluminum plate with coating thickness of 0.013”-0.015” at angle of ~45 deg from horizontal																		
12:25	9	30	64	3.3	100	N	128							N				
12:27	10	30	67	3.3	100	N	220							N				
12:28	11	30	70	3.3	100	N	313							N				
12:31	12	30	73	3.3	100	N	406							N				
12:32	13	30	75	3.3	100	N	468							N				
12:37	14	30	78	3.3	100	N	561							N				
12:40	15	30	79	3.3	100	N	592						Y	Y	N			
12:46	16	30	77	3.3	100	N	530							N	N			
12:50	17	30	78	3.3	100	N	561							N	N			
Installed 6”x6” TiO2 coated 1/8” aluminum plates, with coating thickness of 0.007” – 0.010” – set at angles of ~50 deg from horizontal																		
14:25	18	30	78	3.5	100	N	561							N	N			
14:30	19	30	77	5	100	N	530						N	Y				
14:40	20	30	77	5	100	N	530	30					N	Y	N			
14:45	21	30	77	5	100	N	530	5					N	Y	N			
14:50	22	30	77	5	100	N	530						N	N				
14:55	23	30	77	6	100	N	530							N	N			LM: Conditioning of surface
14:59	24	30	77	6	100	N	530							N	N			LM: Conditioning of surface
15:50	25	30	78	6	100	N	561	30					Y	Y	N			
15:52	26	30	77	6	100	N	530	5					Y	Y	N			From Yuri Gorolev's FLIR camera videos, the
15:53	27	30	76	6	100	N	499	5					Y	Y	N			0.013-0.015” thick TiO2 coating provided far
15:55	28	30	76	5	100	N	499	5					N	N	N			superior absorption than the 0.007-0.010.”
Installed alumina plate (127mm x 127 mm x 0.125” thick) set at ~60deg from horizontal																		
16:30	29	90	76	5	100	N	53	30						N	N			
16:35	30	90	76	7	100	N	53							N				
16:36	31	90	76	10	100	N	53							N				Flir movie from Yuri Gorolev
16:37	32	90	76	7	100	N	53							N				Flir movie from Yuri Gorolev
16:45	33	90	76	15	100	N	53							N				Flir movie from Yuri Gorolev
16:46	34	90	76	20	100	N	53						Y	Y				

Table 24 - Tests conducted on Wednesday 5/22/2013

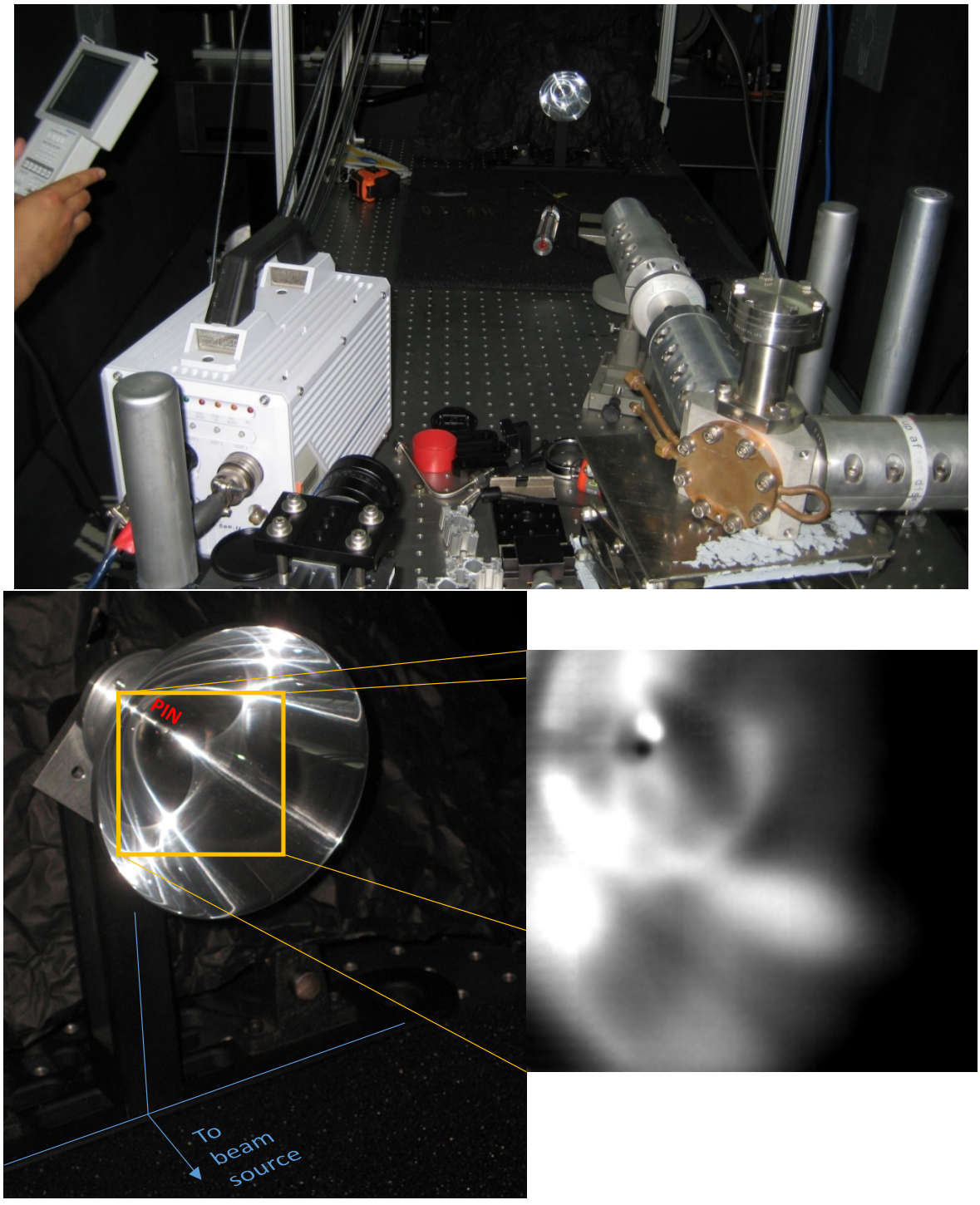

Figure 84 – Model XXb, an 11-cm diameter axisymmetric parabolic reflector with 'igniter' pin at focus led by Myrabo/LTI. Top: Experimental layout showing the relative positions of the parabolic reflector, waveguide and FastCAM (white box). Bottom left: Image taken just prior to run #1 Table 11. The image contains reflections and poor image contrast on the black mount and surroundings, so the pin and direction to the beam source are indicated. The orange square indicates the approximate field of view for FastCAM images during runs 2-7. Bottom right: Image taken from run #7, during which a plasma had formed and decayed after the beam turned off, leaving a remnant plasmoid attached to the pin (small bright white area adjacent to small black area). This plasmoid subsequently detaches from the pin and splits as it rises.

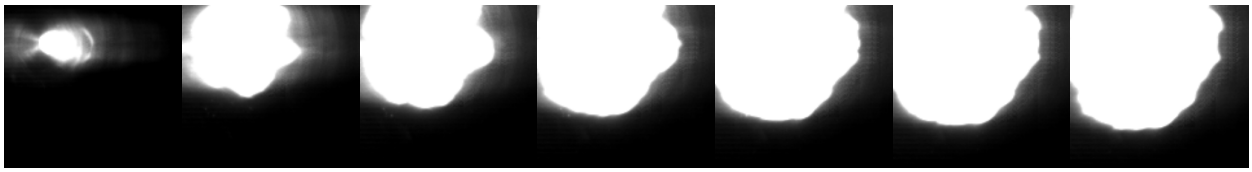

Figure 85 - Plasmadynamic breakdown initiated from a pin at the focus of a parabolic mirror during run #7 shown in Table 11. Starting on the left from the frame where breakdown is first seen, each subsequent frame is taken at 8 microsecond intervals.

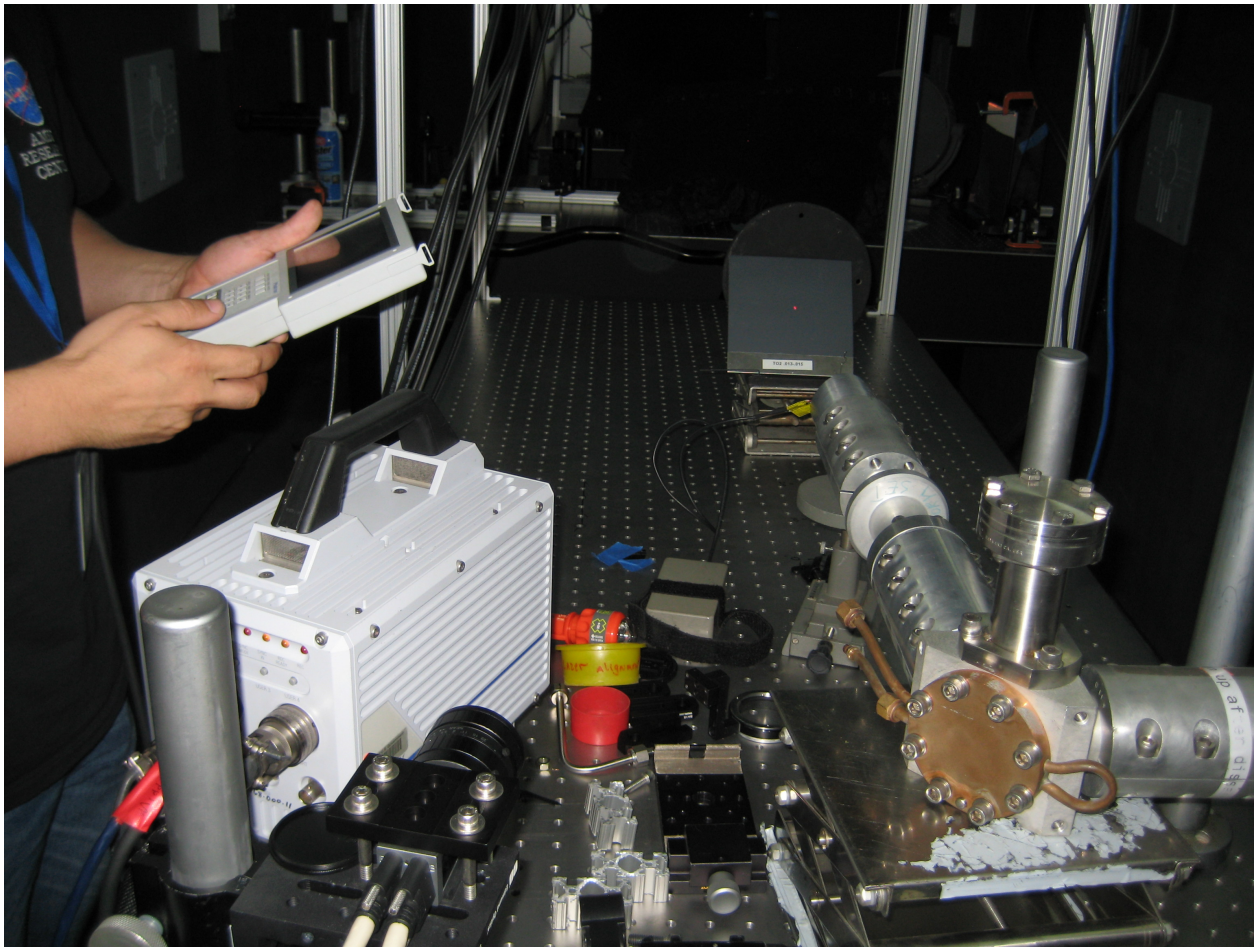

Figure 86 – Coupon tests are performed for absorption by differing thicknesses of TiO_2. Based on a succession LWIR still camera frames taken by Yuri Gorolev of General Atomics, the 330-380 micron thick TiO_2 coating provides superior absorption to the 180-250 micron thick coating.

Figure 85 shows plasmadynamic breakdown initiated from the pin at the focus of the optic. This breakdown is an electron avalanche process that is fed by the energy of the incoming beam and is in some ways analogous to a flame. The analogy extends to the gasdynamics of millimeter-wave supported detonation, which is the basis of an air-breathing propulsion scheme that was invented in 2003 (Oda, Nakagawa et al. 2003) and is being developed by the Komurasaki research group at the University of Tokyo (Oda 2008, Shibata 2008, Shiraishi 2009, Shimada 2010, Yamaguchi 2010, Fukunari 2012, Saito 2013, Kurita 2014). The Japanese experiments use 170 GHz, 1 MW peak power and a flat or

conical reflector. The LTI experiment shown in Figure 85 is the first using a parabolic dish at 110 GHz and 100 kW peak power.

In the next series of tests, shown in Figure 86, the objective was to investigate the absorption properties of titanium dioxide coatings similar to those that coat the interior walls of the test room itself. The test specimens were flat plate coupons at range of 30 cm: 6"x6" TiO_2 coated 1/8" aluminum plates, with coating thicknesses of (0.013"-0.015") and (0.007" – 0.010") – set at angles of ~45 and ~50 degrees from horizontal. From the LWIR camera videos**,** the 0.013-0.015" thick TiO_2 coating provided superior absorption to the 0.007-0.010" coating.

Breakdown occurred at 460 kW and 3.3ms; 425 kW and 6 ms, 390kW and 5 ms (and 6 ms), as well as 360 kW and 6 ms; these pulse durations were the requested pulse durations, not the cutoff, which is driven by when the breakdown actually occurred.

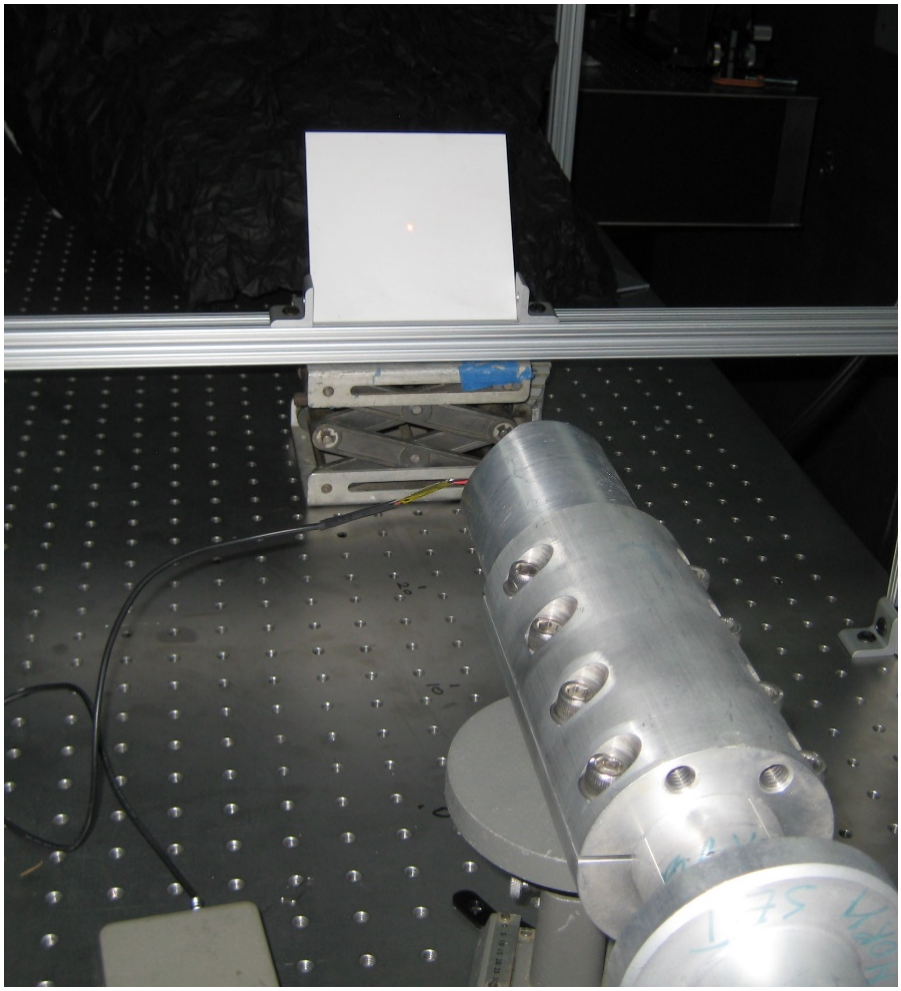

Figure 87 - Alumina plate (127mm x 127 mm x 0.125" thick) at range of 90 cm, set at 60 degrees from horizontal

The next test specimen was an alumina plate (127mm x 127 mm x 0.125" thick) at range of 90 cm, as shown in Figure 87. It was tested at 360 kW with pulse durations ranging from 5 to 15 ms without window light (breakdown) faults. A fault was triggered at 360 kW and 20 ms (requested).

5.1.2.1.4 Thursday 5/23/2013. Flat plate absorption and first tests using a line focus optic provided by Myrabo/LTI.

		Experimental parameters									Outcome				
Time	Run #	Position [cm]	Gyrotron voltage [kV]	Requested duration [ms]	Duty cycle [%]	Line focus used?	Peak flux at target [MW/m^2]	Fastcam rate [kFPS]	FLIR range [1/2/3]	Flow?	Full Pulse?	Actual duration [ms]	Fault?	Pop sound?	See FastCam data?	See HDCam data?	FLIR max temp [K]	Comments
Tests continued with alumina plate, except now coated with graded thicknesses, copper on the left and graphite on the right																		
11:20	1	90	76	5	100	N	53							N				
11:25	2	90	86	7	100	N	86							N				
11:30	3	90	76	6	100	N	53	10					Y	Y				
11:35	4	90	72	5	100	N	40	90					Y	Y				
11:40	5	90	68	5	100	N	27	90										
11:42	6	90	68	7	100	N	27	30						N	Y			LM: flash on copper
11:46	7	90	68	10	100	N	27	10					N					
11:50	8	90	68	15	100	N	27	10					N					
11:53	9	90	68	20	100	N	27	10					N					
11:57	10	90	68	40	100	N	27	10					N					
11:59	11	90	68	80	100	N	27	10					N					
12:05	12	90	68	160	100	N	27	30					Y					
12:13	13	90	64	250	100	N	14	30					N					
12:20	14	90	64	360	100	N	14	30					Y					
TiO2 coated aluminum 6”x6” specimen at angle of 60-deg																		
14:46	15	90	64	5	100	N	14											no flir
14:47	16	90	64	10	100	N	14											no flir
14:48	17	90	64	20	100	N	14											no flir
14:50	18	90	64	20	100	N	14											flir camera
14:55	19	90	64	30	100	N	14						Y					
14:59	20	90	64	11	100	N	14						Y					
Angle adjusted to ~50 degrees																		
15:30	21	90	64	20	100	N	14											flir
15:32	22	90	64	30	100	N	14						Y					flir
1/16” OD alumina tube (single tube this time) using the 25cm off-axis 2D parabolic mirror (rear surface at 190 cm)																		
18:40	23	190	64	5	100	Y	120						Y					flir
18:44	24	190	64	5	100	Y	120	500					N					
18:45	25	190	64	7	100	Y	120	500					N					
18:47	26	190	64	10	100	Y	120						N					
18:49	27	190	64	16	100	Y	120						N				323	
18:51	28	190	64		100	Y	120						Y					
18:55	29	190	64		100	Y	120						Y					

Figure 88 - Tests conducted on Thursday 5/23/2013

The line focus optic is estimated to increase the flux of the beam at its focus by a factor of 40, and this is reflected in the flux figures in Figure 88 and all subsequent list entries where the line focus is used. The factor of 40 is estimated by enlarging the x-axis of Figure 91 until the flux distribution is approximately circular. By that point, the x-axis is stretched by a factor of 40. There is an error associated with this estimate, an additional error associated with how well the test article is placed at the focus of the beam, and a further error introduced by flux variations within the ellipse shown in Figure 91. We do not attempt to quantify the errors here.

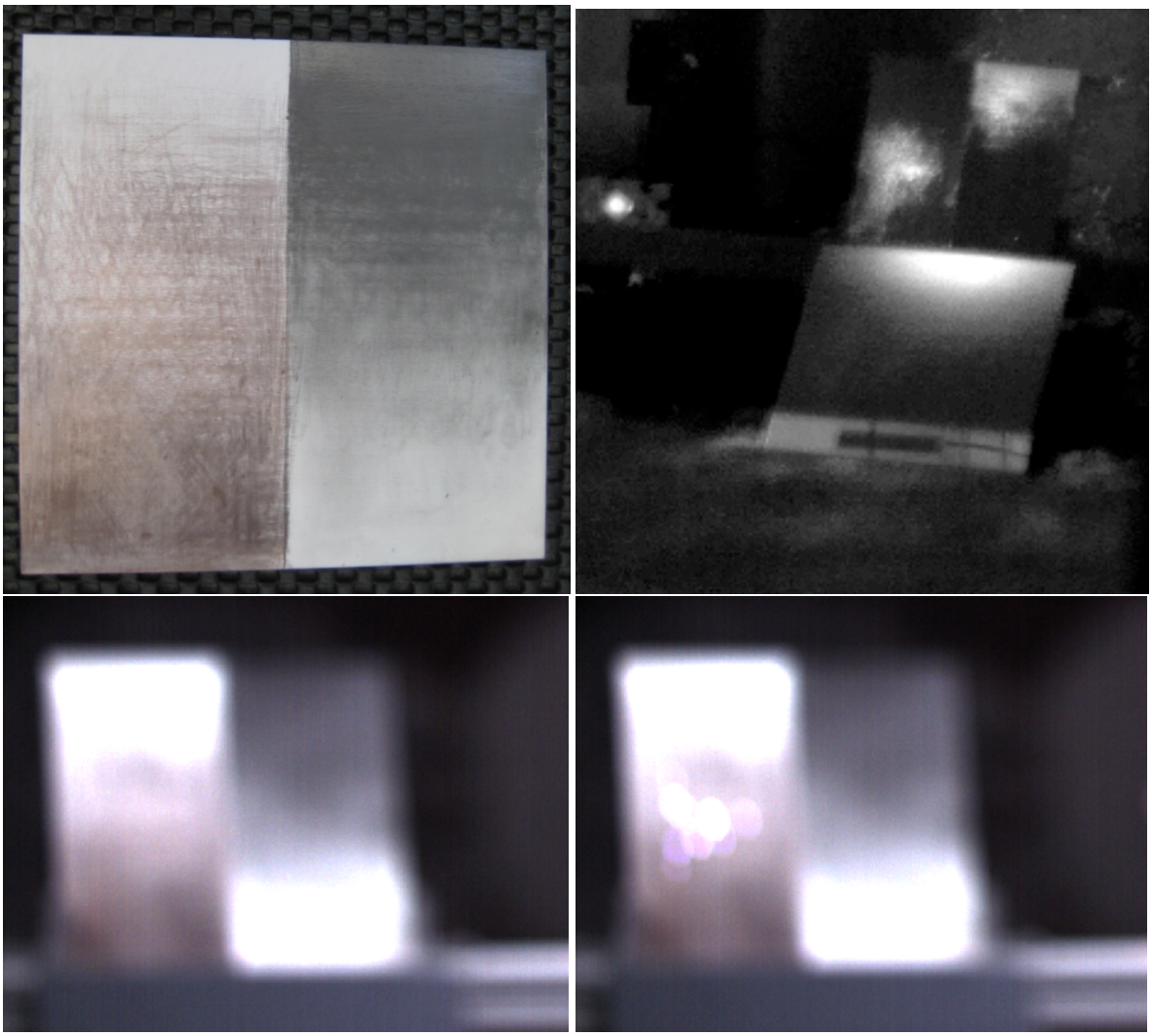

Figure 89 – Top left: An alumina plate is coated with graded thicknesses, copper on the left and graphite on the right applied by rubbing. One of us (Parkin) is seen making these coatings in Figure 73. Top right: LWIR image of run #6. The image reveals the thicknesses, and hence sheet resistances, at which the coatings absorb the most millimeter-waves. Bottom left: Visible camera image of the plate just prior to gyrotron pulse. There was insufficient time to focus this camera prior to initiating the procedure to seal the experimental section of the MTU and begin pulses. Bottom right: The visible camera image captures surface breakdown induced on the copper-covered side of the alumina plate but not the graphite side.

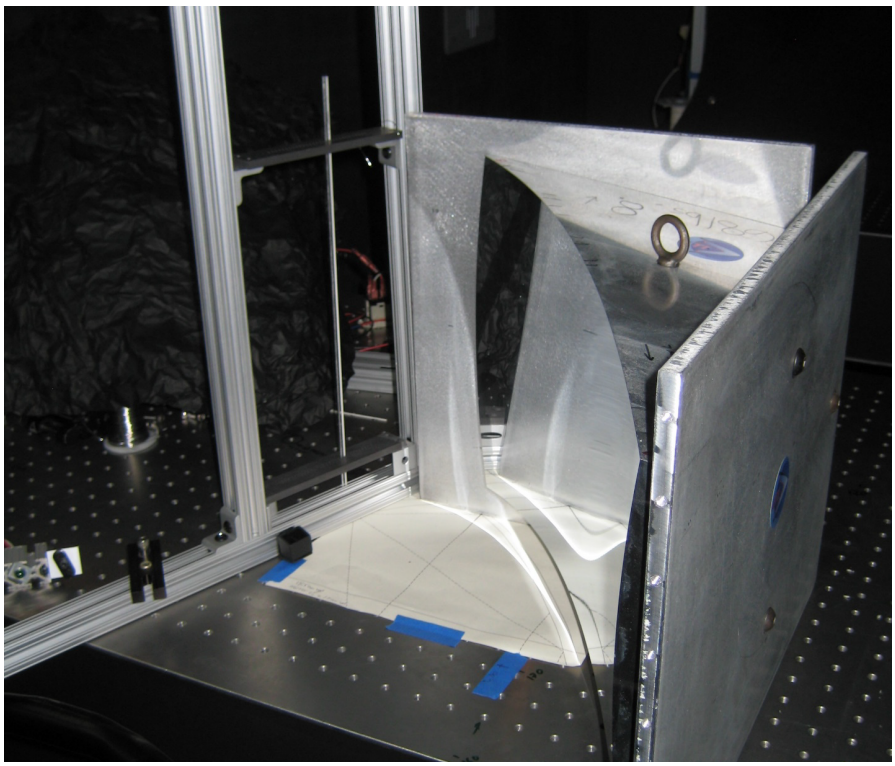

Figure 90 – The line focus optic provided by Myrabo/LTI. The focal line is 10 cm beyond the edge of the mirror. The mirror takes a 25-cm beam diameter.

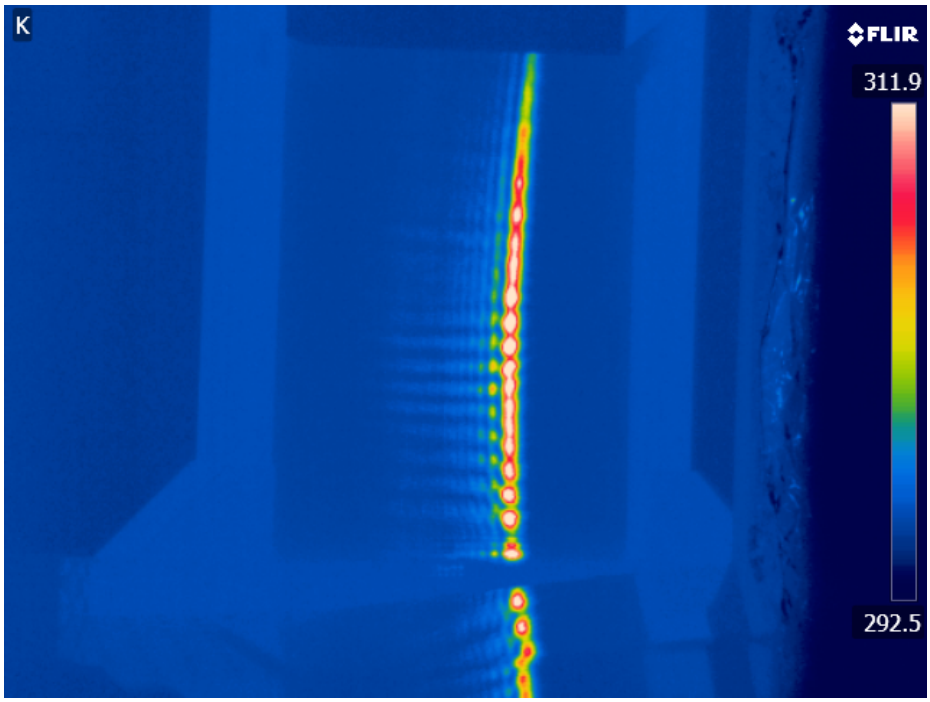

Figure 91 – A piece of paper placed in the jig is used to characterize the beam reflected from the Line focus optic provided by Myrabo/LTI and shown in Figure 90. Subsequently, we aligned tubes to the beam by overlaying this image (or later ones) with the live LWIR camera feed using the FLIR ResearchIR software.

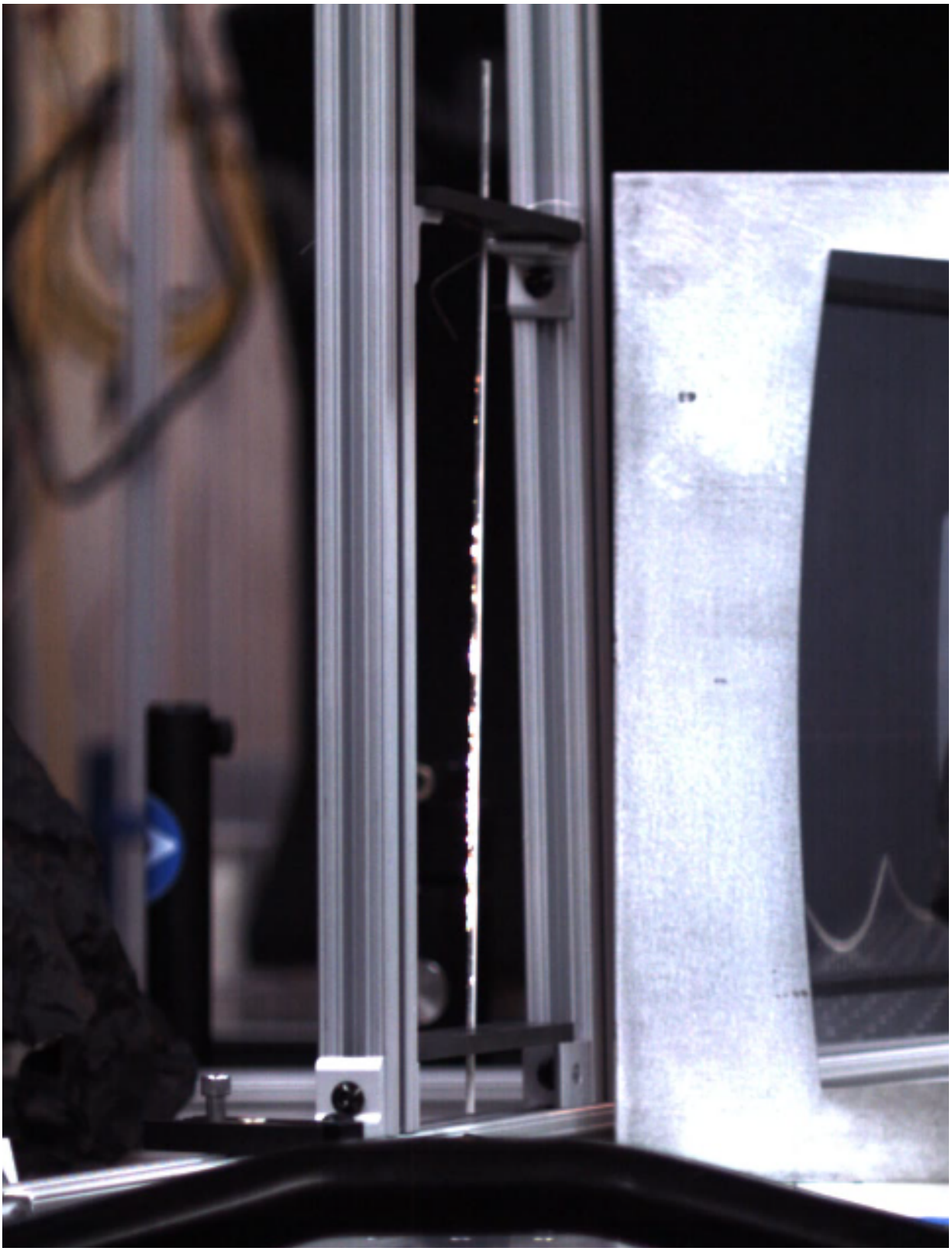

Figure 92 – The LTI line focus optic focuses high flux on an A.1.I tube (see Table 21 for specification), which displays a combination of plasmadynamic surface breakdown and tube heating. Source file: 23_05_2013___17_47_30.avi

5.1.2.1.5 Friday 5/24/2013. Millimeter-wave absorption by tubes and coatings.

Experimental parameters											Outcome				
Time	Run #	Position [cm]	Gyrotron voltage [kV]	Requested duration [ms]	Duty cycle [%]	Line focus used?	Peak flux at target [MW/m^2]	Fastcam rate [kFPS]	FLIR range [1/2/3]	Flow?	Full Pulse?	Actual duration [ms]	Fault?	Pop sound?	See FastCam data?	See HDCam data?	FLIR max temp [K]	Comments
Installed model D2a																		
2:00	1	185	68	5	100	Y	250											
	2	185	68	5.5	100	Y	250											
	3	185	68	6	100	Y	250						Y					
14:28	4	185	68	6	100	Y	250						N					
	5	185	68	7	100	Y	250											
14:32	6	185	68	8	100	Y	250											
	7	185	68	9	100	Y	250											
	8	185	68	10	100	Y	250											
14:37	9	185	68	14	100	Y	250											LM: puff of smoke off carbon foam absorber
14:38	10	185	68	20	100	Y	250											LM: puff of smoke off carbon foam absorber
14:40	11	185	68	25	100	Y	250											
Installed model D2b																		
15:15	12	160	68	25	100	Y	335											
15:18	13	160	68	30	100	Y	335	30					N					
15:26	14	160	68	35	100	Y	335						Y					LM: puff of smoke off carbon
15:25	15	160	68	35	100	Y	335						N				304	LM: puff of smoke off carbon
15:30	16	160	68	40	100	Y	335											LM: Fire on graphite absorber

Table 25 - Tests conducted on Friday 5/24/2013

The D2* series of tests focused on testing various external coatings that were either rubbed, painted or sprayed on:

- Yttria (Y_2O_3) spray, from Zypcoating
- Zirconia (ZrO_2) spray, from Zypcoating
- High-temperature enamel spray paint, from Rustoleum
- Oxititan, an antimicrobial coating composed of titanium dioxide nanoparticles
- Titanium(II) oxide (TiO) and copper(II) oxide (CuO), achieved by rubbing a bar of titanium or copper on the tube and heating it in air with a butane torch.
- Graphite rubbed on tube surface

For these coatings, a single type of tube is used: Alumina 99.98% 0.79 mm ID, 1.6 mm OD, 30 cm long. It was mounted in the test rig and used in combination with the line focus mirror. A carbon foam absorber was used to absorb stray millimeter waves around and beneath the mirror and to prevent reflections from the table. However, this absorber often outshone the targets, and in the final test of the day, it briefly burned before we extinguished it and abandoned the carbon absorber approach.

5.1.2.1.6 Tuesday 5/28/2013. Millimeter-wave absorption by tubes and coatings.

Experimental parameters										Outcome					
Time	Run #	Position [cm]	Gyrotron voltage [kV]	Requested duration [ms]	Duty cycle [%]	Line focus used?	Peak flux at target [MW/m^2]	Fastcam rate [kFPS]	FLIR range [1/2/3]	Flow?	Full Pulse?	Actual duration [ms]	Fault?	Pop sound?	See FastCam data?	See HDCam data?	FLIR max temp [K]	Comments
Installed model D2c: 4 + 3 tubes of alumina, put on two rows in Hx stand held by graphite jigs.																		
12:25	1	160	68		100	Y	335											
12:30	2	160	68		100	Y	335											
12:31	3	160	68		100	Y	335											
12:42	4	160	68		100	Y	335											
12:51	5	160	68		100	Y	335										303	reflected power increased over last 40ms
Break																		
13:25	6	160	68		100	Y	335						Y					pulse did not go through
14:00	7	160	68		100	Y	335						Y					
Break																		
14:51	8	160	68		100	Y	335						N					
15:03	9	160	68		100	Y	335						N				304	
15:07	10	160	68		100	Y	335											FLIR camera not ready
15:10	11	160	68		100	Y	335						Y					
15:12	12	160	68		100	Y	335						N				307	
Installed model D2d: 4 tubes with different coatings, in HX stand held by graphite jigs. Tube 1 = bare Alumina, 2 = Rubbed titanium oxidized with blowtorch, 3 = Oxititan solution painted on alumina, 4 = bare alumina. High flux susceptor experiments. Line of focus is																		
16:53	13	160	68		100	Y	335							Y				bottom tube got hot, breakdown sparks
16:57	14	160	68		100	Y	335							N			298	breakdown sparks
16:59	15	160	68		100	Y	335							N				breakdown sparks
17:03	16	160	68		100	Y	335						Y					TL: breakdown on tube + rising plasmoid
17:04	17	160	68		100	Y	335							Y				LM: breakdown. TL: same as 16
17:11	18	160	68		100	Y	335							Y			333	LM: great (?) breakdown
17:17	19	160	65		100	Y	211							N				LM: no breakdown
17:22	20	160	65		100	Y	211							N			373	
17:29	21	160	65		100	Y	211							Y			433	LM: small breakdown. TL: breakdown
17:57	22	160	64		100	Y	170							N			413	LM: no breakdown
18:00	23	160	64		100	Y	170	30						Y				LM: breakdown. TL: titanium tube broke
18:07	24	160	63		100	Y	129						N				363	
18:10	25	160	63		100	Y	129						N				453	
18:12	26	160	63		100	Y	129						Y					
18:14	27	160	63		100	Y	129										623	

Table 26 - Tests conducted on Tuesday 5/28/2013. Note that each "break", shown as a horizontal gray line, corresponds to a moment where the setup was disturbed in one way or other. For example, during the first break we installed some metal tape that caused faults on the following shots, so in the second break we adjusted it.

For model D2c, we used bare tubes of alumina arranged in two rows of three and four tubes respectively. The distance between tube centers was 0.75 times the outer tube diameter. The purpose of this setup was to confirm the transparency of the non-coated alumina tubes.

As expected, little temperature rise was seen even at the high incident fluxes used on this day. Model D2d provided our first conclusive tests of various tube coatings. Because of time pressure, we decided that instead of testing each tube individually and meticulously comparing each result, we would test a multitude of them in parallel and see which one stands out in each test.

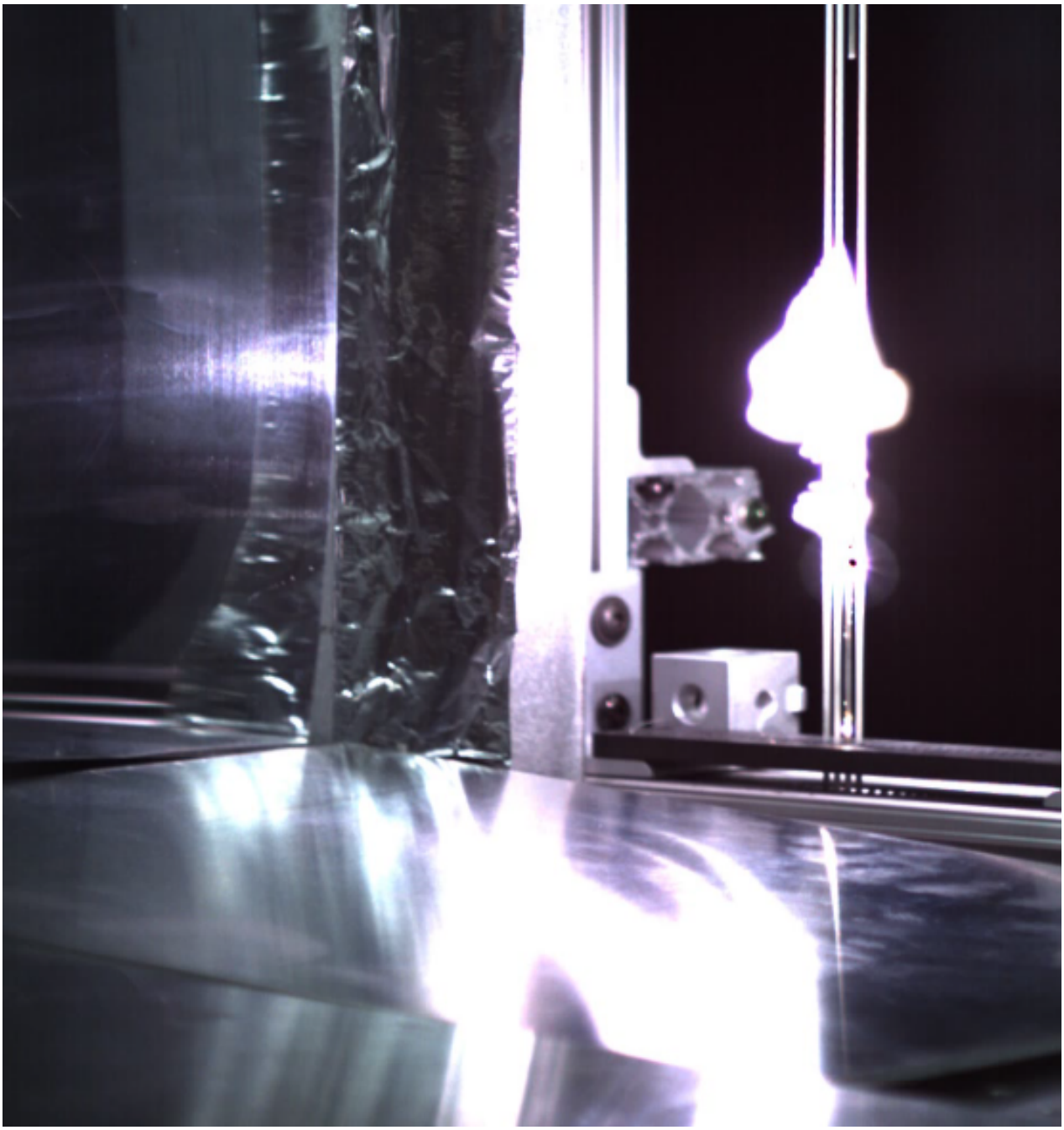

Figure 93 – In run #18, a plasmoid forms on the tube. The plasmoid rises due to buoyancy and grows while the millimeter-wave beam supports it. Source file: 28_05_2013___17_14_09.avi

Unfortunately, the tube coated with the oxidized titanium fell and broke before model D2c was assembled. We collected the two biggest pieces and put them where the tube was supposed to be (one taped to the top part of the stand, the other to the bottom). The bottom part of the tube created a spike in the middle of the beam, leading to the beautiful plasmoid shown in Figure 93, which made it very difficult to measure tube heating. A popping sound was heard each time a breakdown occurred, and after roughly half a dozen breakdowns, the bottom part of the tube broke as shown in Figure 94. The Oxititan coating barely absorbed (around 400 K maximum versus 310 K for the bare tubes for a shot duration of 0.8 seconds). The highest temperatures were on

the tube coated with oxidized titanium (~700 K maximum for a pulse of 0.8 seconds at the same spot). However, the temperature distribution on the latter was non-uniform and multiple sub-millimeter sized hot spots appeared and disappeared during the shot, probably due to localized surface breakdown.

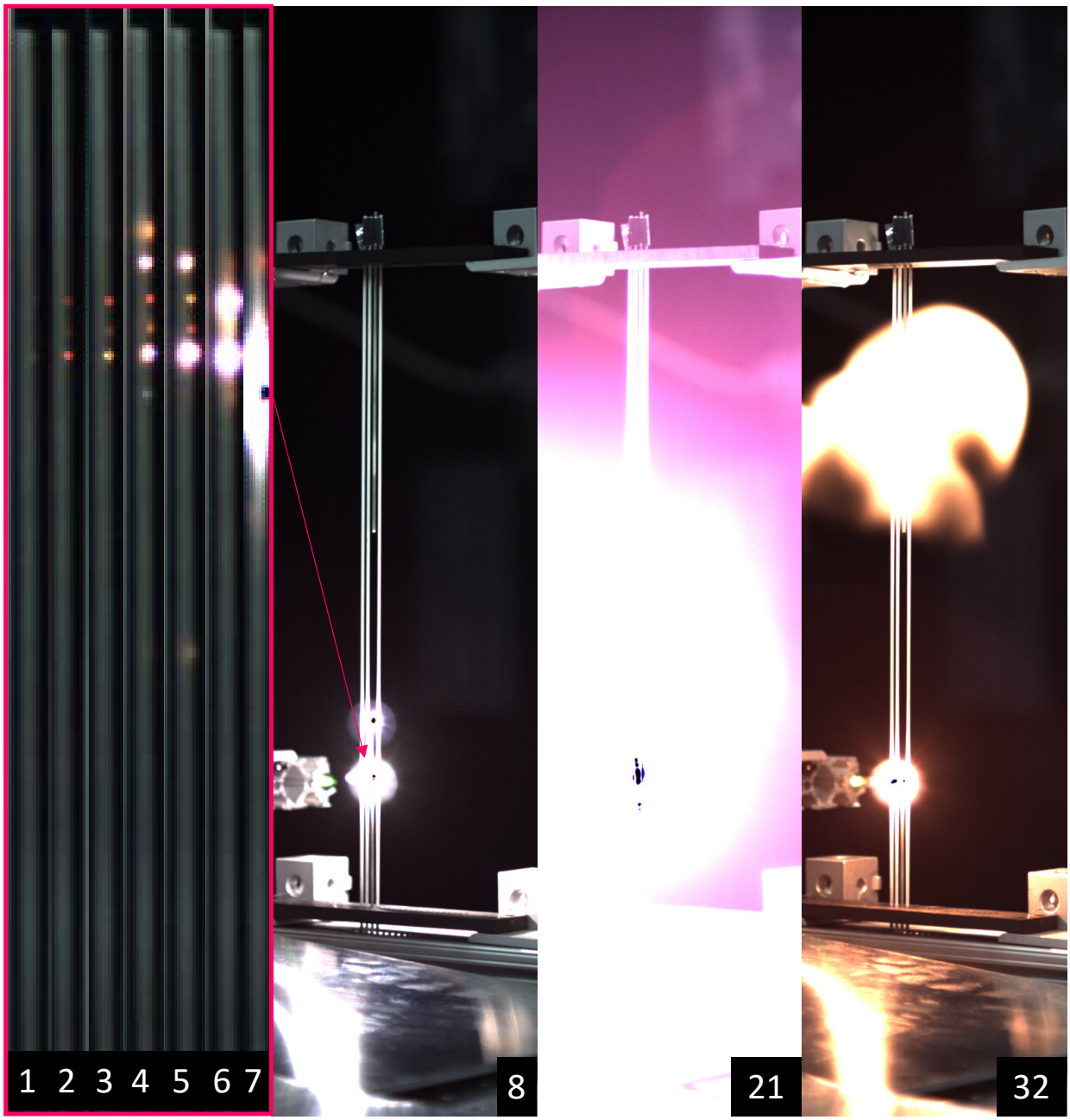

Figure 94 – Sequential frames (from left to right) of the surface breakdown and heating that occurs somewhat below the spike that is the source of the plasmoid in Figure 93. Frame numbers are given in the bottom right corner, and each frame is separated by 10 milliseconds. In frames 1-7 the region in which breakdown occurs is magnified. In frame 21 the breakdown has proceeded to its maximum brightness. By frame 32, the breakdown has been detected and the beam shut off, and the remnant plasmoid is rising under its own buoyancy. The top of the tube has been melted off at the site of surface breakdown, and the piece of tube above it is falling, just passing the green LED to the left. The site of melting is white hot and is the major source of light other than the remnant plasmoid. Source file: 28_05_2013___17_59_56.pptx

5.1.2.1.7 Wednesday 5/29/2013

Experimental parameters										Outcome					
Time	Run #	Position [cm]	Gyrotron voltage [kV]	Requested duration [ms]	Duty cycle [%]	Line focus used?	Peak flux at target [MW/m^2]	Fastcam rate [kFPS]	FLIR range [1/2/3] Flow?	Full Pulse?	Actual duration [ms]	Fault?	Pop sound?	See FastCam data?	See HDCam data?	FLIR max temp [K]	Comments
Installed model D2e. Same as D2d except: 1 = Al2O3, 2 = Soot, 3 = Zirconia, 4 = Yttria. High flux susceptor experiments.																	
10:42	1	160	63	5	100	Y	129	5								296	TL: temperature too low to read
10:43	2	160	63	100	100	Y	129	5								433	
10:47	3	160	63	200	100	Y	129	5								574	
10:50	4	160	63	400	100	Y	129					Y					LM: pulse did not go through
10:54	5	160	63	400	100	Y	129						Y			1114	LM: little smoke, plasma on tube. TL: plasma
11:17	6	160	63	600	100	Y	129						Y			1414	broke tube
11:25	7	160	63	700	100	Y	129					Y	N			1620	
Installed model D2f. 1 = Al2O3, 2 = Graphite, 3 = Copper rubbed and burnt with blowtorch (copper oxide), 4 = Sharpie. High flux susceptor experiments at distance of 160 cm from waveguide end.																	
17:03	8	160	63	5	100	Y	129	295					N			302	TL: tube might be slightly out of focus
17:05	9	160	63	20	100	Y	129	296					N			397	
17:07	10	160	63	100	100	Y	129	302				N	N			882	broke tube TL: tube broke at low temperature -> thermal shock. Temperature decay slowly afterward?
17:12	11	160	63	200	100	Y	129					Y					
17:15	12	160	63	200	100	Y	129									933	TL: remaining graphite tube from shot #10 fell right in another hole and exploded again
Installed model D2g. As before except 2 = Rustoleum.																	
17:40	13	160	63	5	100	Y	129					N				297	
17:41	14	160	63	20	100	Y	129					N				356	
17:41	15	160	63	100	100	Y	129					N				433	
17:50	16	160	63	200	100	Y	129					Y					TL:big plasmoid going up while dying
17:52	17	160	63	200	100	Y	129					N				497	
17:54	18	160	63	400	100	Y	129					N				626	
17:55	19	160	63	550	100	Y	129					N				694	
17:59	20	160	63	550	100	Y	129					Y					
18:00	21	160	63	550	100	Y	129					N				733	

Table 27 - Tests conducted on Wednesday 5/29/2013

Wednesday tests focused on the spray-on coated tubes of zirconia and yttria, next to a tube coated with soot and a bare one for reference (as observed by the visible and long-wave infrared cameras). While the yttria-coated tube did not show any significant temperature increase, the zirconia-coated one smoked during the short duration tests. After gradually increasing the millimeter-wave pulse length, some parts of the coating burst into plasma before braking the tube in three pieces, shown in Figure 95. Inspection of the coating after the event revealed a pattern of small burned pockets inside the coating where the tube broke off.

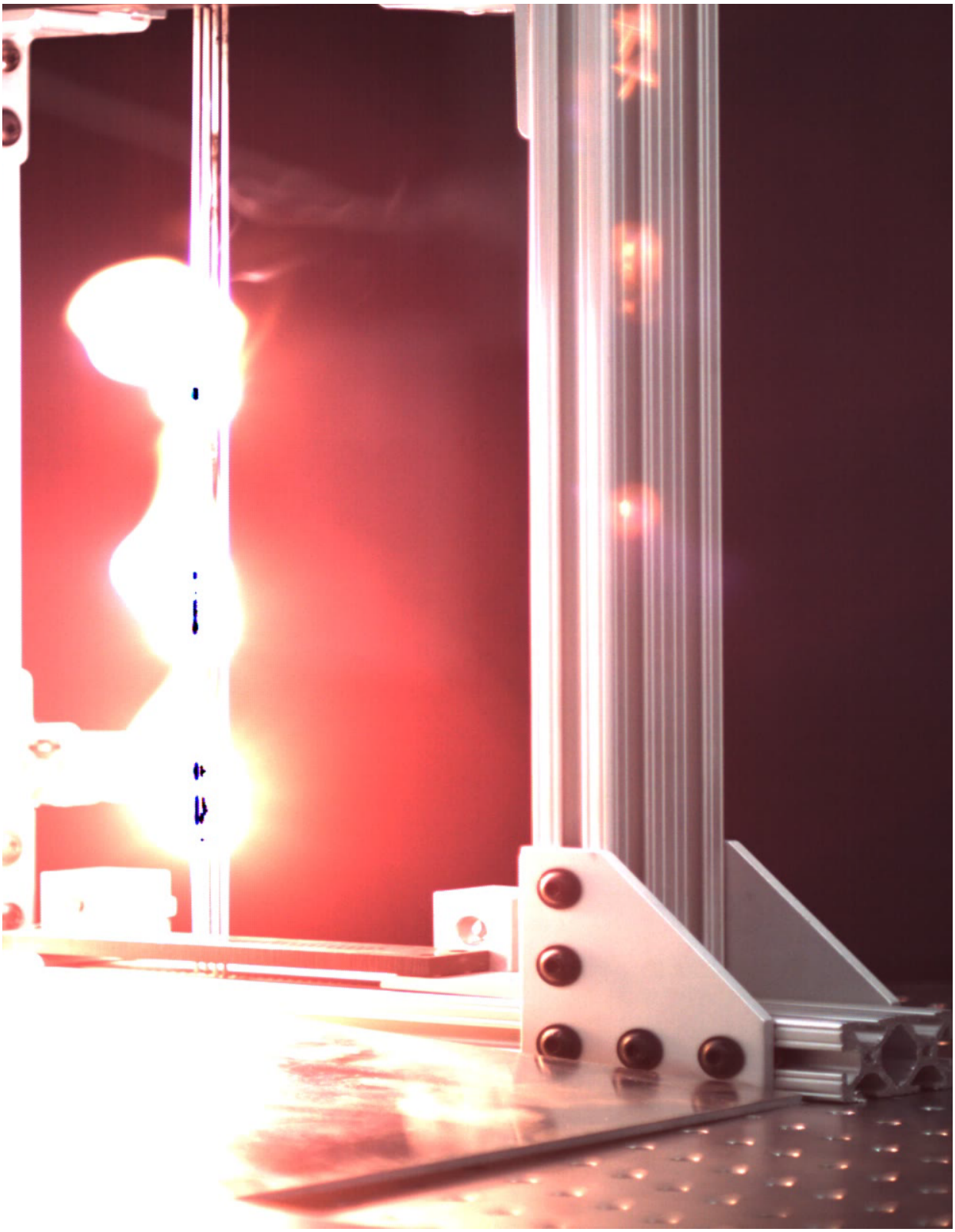

Figure 95 -— A zirconia-coated tube is broken by plasmoids during run #6. Source file: 29_05_2013___11_13_17.avi

5.1.2.1.8 Thursday 5/30/2013.

		Experimental parameters								Outcome					
Time	Run #	Position [cm]	Gyrotron voltage [kV]	Requested duration [ms]	Duty cycle [%]	Line focus used?	Peak flux at target [MW/m^2]	Fastcam rate [kFPS]	FLIR range [1/2/3]	Flow?	Full Pulse?	Actual duration [ms]	Fault?	Pop sound?	See FastCam data?	See HDCam data?	FLIR max temp [K]	Comments
Installed model E1 (TiO2 coated plates)																		
11:35	1																	POWER SENT TO DUMMY LOAD
11:39	2																	POWER SENT TO DUMMY LOAD
11:41	3																	POWER SENT TO DUMMY LOAD
11:42	4																	POWER SENT TO DUMMY LOAD
11:45	5																	Top/bottom plate peak temps [K]:
11:46	6	160	63	5	100	Y	129						N				302	298 / 302
11:47	7	160	63	10	100	Y	129						N				330	313/330
11:50	8	160	63	20	100	Y	129						N				343	313/343
11:51	9	160	63	40	100	Y	129						Y					
11:52	10	160	63	40	100	Y	129						N				433	378/433
11:54	11	160	63	80	100	Y	129						N				523	453/523
11:57	12	160	63	160	100	Y	129						N				673	523/673
11:59	13	160	63	320	100	Y	129						N				813	563/813
12:01	14	160	63	550	100	Y	129						N				923	573/923
12:05	15	160	63	550	100	Y	129						Y					fire alarm GA
13:20	16	160	65	5	100	Y	211						N				311	302/311
13:24	17	160	65	20	100	Y	211						N				433	363/433
13:26	18	160	65	20	100	Y	211						N				483	393/483
13:27	19	160	65	40	100	Y	211						N				623	473/623
13:29	20	160	65	80	100	Y	211						N				723	498/723
13:30	21	160	65	160	100	Y	211						N				973	623/973
13:35	22	160	65	250	100	Y	211						N				1073	693/1073
13:46	23	160	65	320	100	Y	211						N				1173	693/1173, TL: opened door after this test
14:12	24	160	68	5	100	Y	335						N				338	318/338
14:14	25	160	68	10	100	Y	335						N				498	373/498
14:15	26	160	68	20	100	Y	335						N				533	?/533
14:18	27	160	68	40	100	Y	335						N				773	523/773
14:24	28	160	68	80	100	Y	335						N				973	613/973
14:28	29	160	68	180	100	Y	335						N				1248	773/1248
14:40	30	160	73	5	100	Y	540											POWER SENT TO DUMMY LOAD
14:42	31	160	73	5	100	Y	540						Y	N			318	303/318
14:45	32	160	73	5	100	Y	540						Y				317	303/317
14:50	33	160	70	5	100	Y	417						Y				338	321/338

Table 28 - Tests conducted on model E1 on Thursday 5/30/2013

Experimental parameters											Outcome					
Time	Run #	Position [cm]	Gyrotron voltage [kV]	Requested duration [ms]	Duty cycle [%]	Line focus used?	Peak flux at target [MW/m^2]	Fastcam rate [kFPS]	FLIR range [1/2/3]	Flow?	Full Pulse?	Actual duration [ms]	Fault?	Pop sound?	See FastCam data?	See HDCam data?	FLIR max temp [K]	Comments
Installed model F (LTI Lightcraft model)																		
15:58	34	90	63	3.5	100	N	10											
16:02	35	90	65	3.5	100	N	17											
16:05	36	90	68	3.5	100	N	27											
16:06	37	90	69	3.5	100	N	30											
16:07	38	90	70	3.5	100	N	33											
16:09	39	90	71	3.5	100	N	37											
16:12	40	90	72	3.5	100	N	40											
16:14	41	90	73	3.5	100	N	43											
16:15	42	90	74	3.5	100	N	46											
16:16	43	90	75	3.3	100	N	50											
16:23	44	90	76	3.3	100	N	53						Y	Y				
16:23	45	90	76	3.3	100	N	53						Y	Y				
Installed model G																		
16:50	46		68	3.3	100								N	N				
16:51	47		70	3.3	100								N	N				
16:52	48		73	3.3	100								N	N				
16:50	49		74	3.3	100								N	N				
	50		3.5	3.3	100								N	N				LM: reflected power
Installed model H																		
17:26	51		68	3.3	100								N	N				
17:27	52		70	3.3	100								N	N				
17:28	53		73	3.3	100								N	N				
Installed model I (LTI Lightcraft model)																		
18:00	54	50	66	3.1	100	N	66						N					
18:04	55	50	68	3.1	100	N	88						N					
18:05	56	50	70	3.1	100	N	110						N					
18:08	57	50	71	3.1	100	N	121						N	Y				
18:10	58	50	72	3.1	100	N	131						N	Y				
18:12	59	50	73	3.1	100	N	142						N	Y				
18:15	60	50	74	3.1	100	N	153						N	Y				

Table 29 - Tests conducted on models F-I on Thursday 5/30/2013

On Thursday, the line of focus mirror was again used to test the absorption of coupons coated with various materials. We used coupons of the materials used on Wednesday's tubes in addition to titanium dioxide and "gray" alumina. The zirconia-coated aluminum coupon showed little absorption, and the yttria-coated one showed none. The best absorbers of the day were the family of coupons coated with titanium dioxide, with the thickest coatings absorbing the most, as seen in Figure 96.

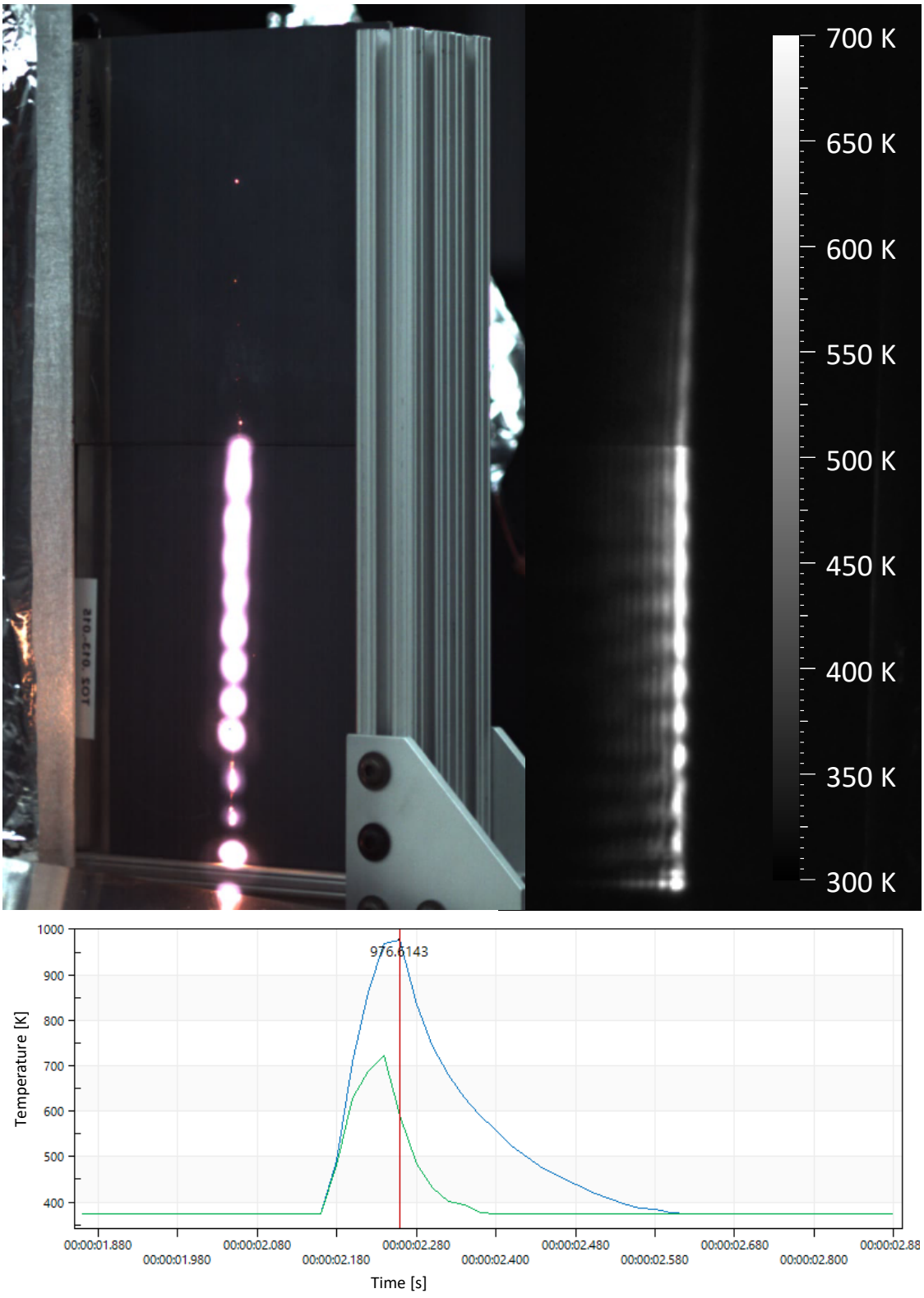

Figure 96 – Top Left: Frame from visible camera at peak brightness. Top Right: Frame from LWIR camera. Bottom: Temperature history as deduced from the LWIR camera reveals that the lower panel reaches a peak temperature of 975 K and the upper panel 720 K. The LWIR image shown on the right is at the time shown by the vertical red line. Source files: 30_05_2013___14_28_55.avi and 2013-05-30T141916782.fcf

5.1.2.1.9 Friday 5/31/2013.

Experimental parameters											Outcome				
Time	Run #	Position [cm]	Gyrotron voltage [kV]	Requested duration [ms]	Duty cycle [%]	Line focus used?	Peak flux at target [MW/m^2]	Fastcam rate [kFPS]	FLIR range [1/2/3]	Flow?	Full Pulse?	Actual duration [ms]	Fault?	Pop sound?	See FastCam data?	See HDCam data?	FLIR max temp [K]	Comments
Installed model D2h: Five graphite-coated tubes mounted in HX stand held by graphite jig. Line focus mirror used for high flux susceptor experiments at distance of 160 cm from waveguide end. 88(?) cm offset from line focus mirror.																		
11:24	1	160	63	3.3	100	Y	129						N				298	TL: temp distribution : tube 1= low; tube 2 =
11:25	2	160	63	5	100	Y	129						N				300	
11:27	3	160	63	10	100	Y	129						N				315	
11:30	4	160	63	20	100	Y	129						N				360	
11:32	5	160	63	30	100	Y	129						N				413	
11:33	6	160	63	40	100	Y	129						N				433S	Saturated temperature reading
11:35	7	160	63	40	100	Y	129						N				463	TL: increased range
11:36	8	160	63	50	100	Y	129						N				543	
11:39	9	160	63	55	100	Y	129						N				523	
11:41	10	160	63	60	100	Y	129						N				553	
11:47	11	160	63	70	100	Y	129						N				623	LM: 70 ms pulse. TL: one tube broke
		160		70	100								N				723	9.1 sec delay + second 70 ms pulse.
		160		40	100								N				473	LM: 3pulse, 5 sec requested delay
11:53	12	160	63	40	100	Y	129						N				493	17.4 sec delay actual
		160		40	100								N				533	12.4 sec delay actual
		160		50	100								N				500	TL: triple pulse
11:56	13	160	63	50	100	Y	129						N				570	10.7 sec delay actual
		160		50	100								N				620	9.9 sec delay actual
12:04	14	160	63	140	50	Y	64										670	
12:08	15	160	63	210	50	Y	64										850	
12:14	16	160	63	280	50	Y	64										845	TL: not getting higher, radiate heat ?
12:17	17	160	63	350	50	Y	64										815	
12:21	18	160	64	350	50												920	
						Y	85											TL: Uplanned shot, operator shot before ready-check, tubes (2?) broken. Only
		160			50												815	recorded end
12:30	19	160	64	700	50	Y	85										840	
		160		70													290	
12:39	20	160	63	70	100	Y	129										350	7.5 sec delay actual
		160		70													420	6.8 sec delay actual
		160		70													460	
Installed model D2I: 5 tubes with zirconia coating																		
14:36	21	160	63	5	100	Y	129										295	
						Y	129											TL: flux disposition: tube 1 = low; tube 2 = low; tube 3 = med; tube 4 = high; tube 5 =
14:41	22	160	63	20	100												296	med
14:44	23	160	63	70	100	Y	129										305	
14:47	24	160	63	140	100	Y	129										318	
14:51	25	160	63	200	100	Y	129										330	
14:56	26	160	63	400	100	Y	129										373	
15:01	27	160	63	600	100	Y	129										408	
15:03	28	160	63	700	100	Y	129										423	

Table 30 - Tests 1 of 2 conducted on Friday 5/31/2013

Experimental parameters											Outcome					
Time	Run #	Position [cm]	Gyrotron voltage [kV]	Requested duration [ms]	Duty cycle [%]	Line focus used?	Peak flux at target [MW/m^2]	Fastcam rate [kFPS]	FLIR range [1/2/3]	Flow?	Full Pulse?	Actual duration [ms]	Fault?	Pop sound?	See FastCam data?	See HDCam data?	FLIR max temp [K]	Comments
moved target closer to focus point																		
15:46	29	160	63	20	100	Y	129										/	shot to dummy load
15:48	30	160	63	20	100	Y	129										300	TL: tube 1 = low; tube 2 = low; tube 3 = med; tube 4 = high; tube 5 = low
	31	160	63	70	100	Y	129										305	
15:51	32	160	63	140	100	Y	129										320	
15:53	33	160	63	200	100	Y	129										328	
15:54	34	160	63	400	100	Y	129										368	
15:57	35	160	63	600	100	Y	129										418	
	36	160	63	700	100	Y	129										438	
		160		100													313	4 shots with ~5sec between them
16:05	37	160	63	100	100	Y	129										318	
		160		100													319	
		160		100													323	
moved target closer to focal point																		
16:32	38	160	63	70	100	Y	129										311	TL: tube 1 = low; tube 2 = med; tube 3 = high; tube 4 = high; tube 5 = low
16:33	39	160	63	140	100	Y	129										328	TL + LM: temperature are way lower than first shot on zirconia few day ago, should be the thickness of coating influence
16:34	40	160	63	200	100	Y	129										339	
	41	160	63	400	100	Y	129										394	
16:36	42	160	63	600	100	Y	129										433	
	43	160	63	600	100	Y	129										433	
	44	160	63	700	100	Y	129										463	
	45	160	64	350	100	Y	170										405	
Changed to hot surface ignitor, all shots when hot surface ignitore is ~1300K																		
	46	160	63	5	100		3							N				
	47	160	64	5	100		4							N				
	48	160	68	5	100		8							N				
	43	160	70	5	100		10							N				
Paper shot: 88 mm offset																		
18:25	(1)		63	3.3	100								N					
18:27	(2)		63	7	100								N					
18:28	(3)		63	10	100								N					
Paper shot: 44 mm offset																		
18:40	(4)		63	10	100								N					
Paper shot: 22 mm offset																		
18:50	(5)		63	7	100								N					

Table 31 - Tests 2 of 2 conducted on Friday 5/31/2013

The last day of the first campaign focused on confirming some of the preliminary findings and verifying the reproducibility of key results. This day also contained the first comprehensive investigation of graphite-coated tubes using the line of focus mirror. While the results showed that the graphite turned the tubes into an absorber, the high-heat fluxes and short pulse lengths made it difficult to obtain reliable readings from the LWIR camera.

We tried a system of multiple pulses with to “soft heat” the tubes. This approach was abandoned due to poor results. Instead, we decided to modulate the beam at a repetition rate of kHz and reduced duty cycle to allow a longer pulse duration while respecting the total energy limit of the gyrotron window. This approach was later used extensively in the second test campaign.

After an unplanned shot at full power destroyed two of the graphite tubes, freshly coated zirconia tubes were installed in the rig. These zirconia-coated tubes showed very low absorption compared to the earlier results, lending credence to an earlier theory that it was gas bubbles trapped inside the coating had generated plasmoids in earlier experiments.

The last test of Friday investigated how surface temperature modifies the millimeter-wave flux at which plasmadynamic breakdown occurs. As shown in Figure 97, hot surface ignitors were raised to a temperature of 1,300 K before being illuminated with increasing millimeter-wave fluxes. No breakdown was observed, and this experiment was de-prioritized as concern faded that the breakdown threshold might substantially limit the millimeter-wave flux that a heat exchanger can absorb. Ultimately, the experiment was incomplete because breakdown did not occur and a stability boundary was not established as a function of temperature and flux, but it is recommended for future work.

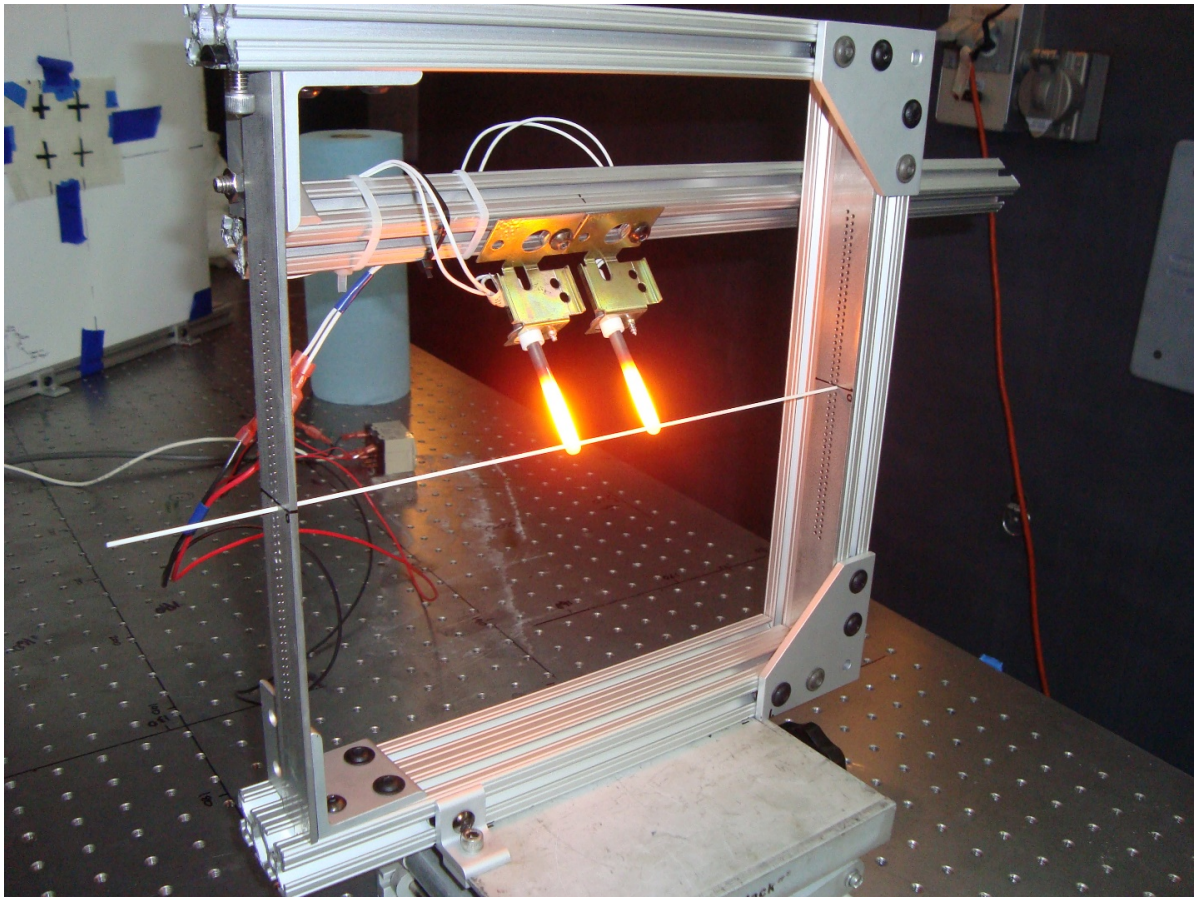

Figure 97 – Hot surface ignitors typically used in a home laundry dryer are instead used as part of an experiment to determine the plasmadynamic breakdown threshold as a function of surface temperature.

5.1.2.2 8/12/2013 - 8/16/2013 test campaign at 1 MW, 110 GHz static test facility

A key insight from the first test campaign was that a thin graphite or titanium dioxide layer is effective in absorbing millimeter-waves, but as described in §3.5.3.6.1, such a susceptor layer on the outside of a tube absorbs a theoretical maximum of 50% of the incident beam energy. Worse still, a thin graphite layer rapidly oxidizes once it reaches yellow heat. While investigating solutions to these problems shortly after the first test campaign, one of us (Parkin) came across a product called Aquadag which is a liquid suspension of graphite flakes in water and realized that it could be used to coat the inside of a heat exchanger tube with a graphite susceptor layer. Because it would be on the inside of the tube, the layer would not oxidize, the beam would be converted to heat directly adjacent to the flow, and the tube wall itself could be used as an anti-reflection coating to increase the absorption efficiency above 50%. Stratified layer simulations carried out at the time and reported in §3.5.3.6.2 predict that up to 90% absorption efficiency is possible.

Consequently, the objectives of second test campaign (which came only 3 months after the first) were to use graphite or titanium dioxide coatings to raise heat exchanger tubes to their melting point, and to compare measured absorption efficiencies and tube temperatures with those of the simulations. Tubes of both aluminum oxide and mullite with various dimensions were selected based on preliminary stratified layer calculations. As described earlier, the test campaign would take the shape of a tournament, where the previous best tube/coating pair would be matched against others with changing parameters. The 'winners' would then be assembled into a heat exchanger to realize the first ever millimeter-wave powered heat exchanger.

In this test campaign, the line focus optic was not used because the high fluxes were used to investigate plasmadynamic breakdown and absorbing materials, whereas much lower fluxes are used for thermal propulsion. To further reduce the incident flux, the beam was modulated at a kHz repetition rate with a selectable duty cycle.

5.1.2.2.1 Monday 8/12/2013

Monday morning was spent characterizing the beam using the 'paper shot' procedure described in §5.1.2.1.1. In the first test campaign, the beam had a high-quality Gaussian distribution with reflections observed only when the target was placed near the end of the optical table farthest from the waveguide horn. In this campaign, reflections from the table were more of a problem, leading us into an unsuccessful attempt to dampen them by using a layer of wet alumina felt as shown in Figure 98.

Once the beam characterization was complete, formal tests commenced with JIG-A, an array of alumina tubes as described in Table 21. The jig was placed 130 cm from the waveguide horn to achieve fluxes of between 1.5 and 4.9 MW/m^2. As expected, best results were obtained from the tubes with an Aquadag coating on the inside.

The day ended with a series of faults in the waveguide (accompanied by a clear popping sound), triggering an automatic shutdown of the pulse in progress. The culprit turned out to be a small piece of plastic tape that detached from the alignment laser onto the inside of the waveguide horn, creating a place favorable for plasmadynamic breakdown.

Experimental parameters										Outcome					
Time	Run #	Position [cm]	Gyrotron voltage [kV]	Requested duration [ms]	Duty cycle [%]	Line focus used?	Peak flux at target [MW/m^2]	Fastcam rate [kFPS]	FLIR range [1/2/3]	Flow?	Full Pulse?	Actual duration [ms]	Fault?	Pop sound?	See FastCam data?	See HDCam data?	FLIR max temp [K]	Comments
Paper shots to characterize beam																		
9:34	1	50	63	5	100		34		1	N	Y		N	N	N	N	305	
9:43	2	50	63	10	100		34		1	N	N		Y	N	N	N	303	
9:46	3	50	63	10	100		34		1	N	Y		N	N	N	N	337	
9:47	4	50	63	10	100		34		1	N	Y		N	N	N	N	332	a little slow compared to normal
10:12	5	100	63	10	100		8.3		1	N	Y		N	N			304	
10:14	6	100	63	20	100		8.3		1	N	N		Y	N			299	huge reflection
10:17	7	100	63	4	100		8.3		1	N	N		Y	N			299	diagnostic test
10:24	8	100	63	20	100		8.3		1	N	Y		N	N			323	
10:26	9	100	63	25	100		8.3		1	N	Y		N	N			333	
10:27	10	100	63	27	100		8.3		1	N	N		Y	N			308	
10:28	11	100	63	27	100		8.3		1	N	Y		N	N			333	
10:29	12	100	63	30	100		8.3		1	N	Y		N	N			338	
10:56	13	180	67	30	100		5.8		1	N	Y		N	N			321	stripes seen on IR (reflection from table?)
10:58	14	180	67	40	100		5.8		1	N	N		Y	Y			313	
11:02	15	180	65	30	100		4.2		1	N	Y		N	N			317	
11:04	16	180	65	40	100		4.2		1	N	N		Y	Y				
11:08	17	180	65	40	100		4.2		1	N	Y		N	N			325	
11:09	18	180	65	45	100		4.2		1	N	N		Y	N			320	
11:12	19	180	65	45	100		4.2		1	N	Y		N	N			328	
11:13	20	180	65	50	100		4.2		1	N	Y		N	N			334	
11:14	21	180	65	55	100		4.2		1	N	Y		N	N			335	
11:15	22	180	65	60	100		4.2		1	N	N	45	Y	N			328	
11:16	23	180	65	60	100		4.2		1	N	N	46	Y	N			329	
11:17	24	180	65	60	100		4.2		1	N	Y		N	N			337	
11:36	25	200	65	60	100		3.4		1	N	N	24	Y	N			312	
11:37	26	200	65	60	100		3.4		1	N	N	3	Y	N			300	
11:39	27	200	65	60	100		3.4		1	N	Y		N	N			333	
11:40	28	200	65	70	100		3.4		1	N	N	67	N	Y			337	
11:41	29	200	65	70	100		3.4		1	N	N	25	Y	N			312	
11:41	30	200	65	70	100		3.4		1	N	N	61	Y	Y			330	Big pop
11:43	31	200	65	70	100		3.4		1	N	N		Y	N				
11:44	32	200	65	70	100		3.4		1	N	N		Y	Y				
11:46	33	200	65	70	100		3.4		1	N	N		Y	Y				
11:47	34	200	64	70	100		2.7		1	N	N		Y	N			331	
11:49	35	200	63	70	100		2.1		1	N	Y		N	N			329	
11:50	36	200	63	80	100		2.1		1	N	Y		N	N			334	
11:51	37	200	63	90	100		2.1		1	N	N		Y	N				
11:52	38	200	63	90	100		2.1		1	N	N		Y	N				
11:53	39	200	63	90	100		2.1		1	N	Y		N	N			338	vert. and horiz. stripes. Due to aluminum frame?

Table 32 - Tests 1 of 2 conducted on Monday 8/12/2013

Experimental parameters											Outcome					
Time	Run #	Position [cm]	Gyrotron voltage [kV]	Requested duration [ms]	Duty cycle [%]	Line focus used?	Peak flux at target [MW/m^2]	Fastcam rate [kFPS]	FLIR range [1/2/3]	Flow?	Full Pulse?	Actual duration [ms]	Fault?	Pop sound?	See FastCam data?	See HDCam data?	FLIR max temp [K]	Comments
Attempted to reduce arcing by removing front horn. Kept same distance graduation.																		
12:22	40	200	63	90	100		2.1		1	N	N	50	Y	N			317	strong arc
12:25	41	200	63	90	100		2.1		1	N	Y		N	N			337	
12:26	42	200	63	90	100		2.1		1	N	Y		N	N			336	
12:47	43	220	63	90	100		1.7		1	N	Y		N	N			327	
12:48	44	220	63	100	100		1.7		1	N	Y		N	N			328	
12:51	45	220	64	90	100		2.2		1	N	Y		N	N			335	
12:52	46	220	64	100	100		2.2		1	N	Y		N	N			337	
12:53	47	220	64	110	100		2.2		1	N	Y		N	N			339	
Deployed damp alumina felt on table in attempt to reduce reflections																		
																		poor beam quality. Beam dump water
13:35	48	280	64	110	100		1.4		1	N	Y		N	N			333	boiling.
13:36	49	280	64	110	100		1.4		1	N	Y		N	N			333	
Removed alumina felt from table and titania beam dump. All else same.																		
13:56	50	280	64	110	100		1.4		1	N	Y		N	N			373	
13:57	51	280	64	110	100		1.4		1	N	Y		N	N			373	
Target back to 200 cm, beam raised so laser hit top right cross, aluminum adhesive put on side																		
14:35	52	200	63	90	100		2.1		1	N	Y		N	N			328	
14:36	53	200	63	100	100		2.1		1	N	Y		N	N			334	
14:37	54	200	63	110	100		2.1		1	N	Y		N	N			337	
Target moved to 130 cm, estimated 20 cm diameter at location																		
15:31	55	130	63	30	100		4.9		1	N	Y		N	N			316	
15:32	56	130	63	50	100		4.9		1	N	Y		N	N			330	
15:33	57	130	63	60	100		4.9		1	N	Y		N	N			336	
15:34	58	130	63	70	100		4.9		1	N	Y		N	N			343	
Installed Jig-A with coated tubes. Also did paper shots at 130 cm, but not recorded here.																		
16:53	59	130	63	5	100		4.9		1	N	Y		N	N			299	
17:05	60	130	63	50	50		2.4		1	N	Y		N	N			311	good modulation 50% see david photo
17:07	61	130	63	100	50		2.4		1	N	Y		N	N			328	
17:09	62	130	63	200	50		2.4		1	N	Y		N	N			368	
17:11	63	130	63	300	50		2.4		1	N	Y		N	N				FINISH TEST SERIES
17:21	64	130	63	300	30		1.5		1	N	N	280	Y	Y				might have heard something
17:25	65	130	63	300	30		1.5		1	N	Y		?	Y				sounds like a harmonica
17:28	66	130	63	400	50		2.4		2	N	N	123	Y	Y			348	humming sound
17:29	67	130	63	400	50		2.4		2	N	Y		N	Y			453	
17:31	68	130	63	500	50		2.4		2	N	N	78	Y	Y				
17:32	69	130	63	500	50		2.4		2	N	N		Y					
17:33	70	130	63	500	50		2.4		2	N	N	411	Y	Y			463	
17:34	71	130	63	500	50		2.4		2	N	N	411	Y	Y			473	
17:37	72	130	63	500	50		2.4		2	N	N	140	Y	Y			363	

Table 33 - Tests 2 of 2 conducted on Monday 8/12/2013

Figure 98 – Alumina felt is rolled out along the beamline and wetted to reduce beam interference effects caused by reflections from the table. David Murakami is seen adjusting a paper target used to image the beam. Source file: 2013-08-12 21.14.55.jpg

5.1.2.2.2 Tuesday 8/13/2013

Experimental parameters										Outcome					
Time	Run #	Position [cm]	Gyrotron voltage [kV]	Requested duration [ms]	Duty cycle [%]	Line focus used?	Peak flux at target [MW/m^2]	Fastcam rate [kFPS]	FLIR range [1/2/3]	Flow?	Full Pulse?	Actual duration [ms]	Fault?	Pop sound?	See FastCam data?	See HDCam data?	FLIR max temp [K]	Comments
Continued with Jig-A																		
9:44	1	130	63	100	50		2.4		1	N	Y		N	N			338	
9:46	2	130	63	500	50		2.4		1	N	N	173	Y	N			373	
9:47	3	130	63	500	50		2.4		1	N	Y		N	N				S denotes saturated reading
9:51	4	130	63	500	50		2.4		2	N	N	171	Y	N			373	
9:52	5	130	63	500	50		2.4		2	N	N	160	Y	N			363	
9:53	6	130	63	500	50		2.4		2	N	N	136	Y	N			353	
9:58	7	130	63	500	50		2.4		2	N	N	324	Y	N			433	FLIR data did not record correctly
10:00	8	130	63	500	50		2.4		2	N	Y		N	N		Y	498	tubes bent and lit up
10:02	9	130	63	600	50		2.4		2	N	Y		N	N		Y	533	
10:07	10	130	63	750	50		2.4		2	N	Y		N	N			573	
10:09	11	130	63	750	50		2.4		2	N	N	700	Y	N		Y	583	
10:15	12	130	63	50	90		4.4		1	N	Y		N	N			341	
10:16	13	130	63	100	90		4.4		2	N	Y		N	N			373	
10:17	14	130	63	200	90		4.4		2	N	Y		N	N		Y	433	
10:19	15	130	63	300	90		4.4		2	N	Y		N	N			513	
10:22	16	130	63	400	90		4.4		2	N	Y		N	N			573	
Installed JIG-B																		
11:53	17	130	63	50	50		2.4		1	N	Y		N	N			338	
11:55	18	130	63	100	50		2.4		1	N	Y		N	N			370	
11:56	19	130	63	200	50		2.4		2	N	Y		N	N			423	
11:57	20	130	63	300	50		2.4		2	N	Y		N	N			523	
12:00	21	130	63	400	50		2.4		2	N	N	15	Y	N			314	
12:01	22	130	63	400	50		2.4		2	N	Y		N	N			603	
12:02	23	130	63	500	50		2.4		2	N	Y		N	N			663	
12:04	24	130	63	600	50		2.4		2	N	Y		N	N			753	
12:06	25	130	63	750	50		2.4		2	N	N	21	Y	N			318	
12:08	26	130	63	750	50		2.4		2	N	N	31	Y	N			325	
12:09	27	130	63	50	50		2.4		2	N	N	0	Y					no pulse in trailer
12:13	28	130	63	50	50		2.4		2	N	N	46	Y	N			338	
12:15	29	130	63	50	50		2.4		2	N	Y		N				343	
12:16	30	130	63	750	50		2.4		2	N	N	600	Y	N			718	
12:16	31	130	63	750	50		2.4		2	N	N	450	Y	N			633	
12:21	32	130	63	750	50		2.4		2	N	N	0	Y					
12:22	33	130	63	750	50		2.4		2	N	N	320	Y	N			523	
12:24	34	130	63	750	50		2.4		2	N	N	125	Y	N			443	
12:28	35	130	63	50	90		4.4		1	N	Y		N	N			368	
12:29	36	130	63	100	90		4.4		2	N	Y		N	N			448	
12:30	37	130	63	200	90		4.4		2	N	Y		N	N			553	
12:32	38	130	63	300	90		4.4		2	N	N	251	Y	Y			573	weak pop, got voltage down
12:36	39	130	63	300	90		4.4		2	N	Y		N	N			693	
12:38	40	130	63	400	90		4.4		2	N	Y		N	N			813	
12:40	41	130	63	750	50		2.4		2	N	N	389	Y	N			573	voltage went down
12:44	42	130	63	750	50		2.4		2	N	Y		N	N			813	
12:46	43	130	63	750	50		2.4		2	N	Y		N	N			793	

Table 34 - Tests 1 of 2 conducted on Tuesday 8/13/2013

Experimental parameters										Outcome						
Time	Run #	Position [cm]	Gyrotron voltage [kV]	Requested duration [ms]	Duty cycle [%]	Line focus used?	Peak flux at target [MW/m^2]	Fastcam rate [kFPS]	FLIR range [1/2/3]	Flow?	Full Pulse?	Actual duration [ms]	Fault?	Pop sound?	See FastCam data?	See HDCam data?	FLIR max temp [K]	Comments
Installed paper target at 70 cm																		
12:24	44	70	63	10	100		17.1		1	N	Y		N	N			308	
12:25	45	70	63	20	100		17.1		1	N	Y		N	N			333	
12:26	46	70	63	25	100		17.1		1	N	Y		N	N			343	
Installed JIG C at 70 cm																		
15:04	47	70	63	50	30		5.1	5	1	N	Y		N	N			363	
15:05	48	70	63	100	30		5.1	5	2	N	Y		N	N			433	
15:07	49	70	63	200	30		5.1	5	2	N	Y		N	N			513	
15:11	50	70	63	400	30		5.1	5	2	N	Y		N	N			713	
15:13	51	70	63	600	30		5.1	5	2	N	Y		N	N			923	SATURATED
15:16	52	70	63	800	30		5.1	5	3	N	Y		N	N			973	
15:19	53	70	63	1000	30		5.1	5	3	N	Y		N	N	Y		1153	
15:24	54	70	63	1200	30		5.1	5	3	N	N	0	Y					no shot in MTU
15:25	55	70	63	1200	30		5.1	5	3	N	Y		N	N			1373	200ms were DC, then started to oscillate
15:35	56	70	63	1200	30		5.1	5	3	N	Y		N	N			1183	
15:47	57	70	63	700	30		5.1	5	3	N	Y		N				923	double shot, 10s between
?	58	70	63	700	30		5.1			N	Y		N				1023	
15:56	59	70	63	1400	30		5.1	5	3	N	Y		N				1323	
16:05	60	40	63	1900	30		16.0	5	3	N	Y		N	N			1573	
16:16	61	40	63	2100	30		16.0	5	3	N	N	2000	N	N			1573	operator limit of 2 sec lifted
16:20	62	40	63	2200	30		16.0	5	3	N	Y		N	N			1723	
16:28	63	40	63	2400	30		16.0	5	3	N	Y		N	N			1653	
16:34	64	40	63	2400	30		16.0	5	3	N	Y		N	N			1723	
16:40	65	40	63	2600	30		16.0	5	3	N	Y		N	N			1793	
16:45	66	40	63	3000	30		16.0	5	3	N	Y		N	N			1913	

Table 35 - Tests 2 of 2 conducted on Tuesday 8/13/2013

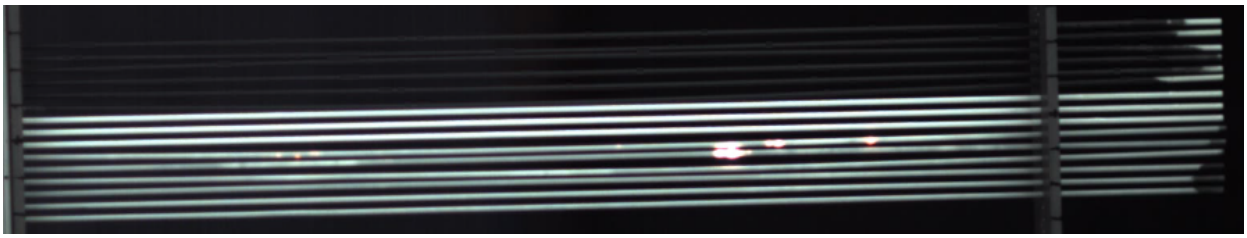

Figure 99 – As described by Table 21, Table 20, and Table 19, Jig-A is comprised of three titanium dioxide coated alumina tubes in the middle, and Aquadag-coated alumina tubes above and below these. The tubes above center are coated on the outside, whereas the tubes below center are coated on the inside. The internally coated Aquadag tubes below center appear to exhibit localized surface breakdown and begin to show promise as millimeter-wave absorbers at this stage. Source file: 13_08_2013___10_30_33.avi

The second day started by finishing the test series on JIG-A, confirming that inner coating of Aquadag gave better results than the outer coating. Throughout the day, alumina and mullite tubes of different dimensions were tested, while ramping up the pulse durations. Temperatures over 1,600 K were seen locally for the first time toward the end of the day. Some of these results may have been skewed by undried pockets of Aquadag liquid within some of the tubes. Later tubes were vacuum oven dried.

5.1.2.2.3 Wednesday 8/14/2013

Experimental parameters											Outcome						
Time	Run #	Position [cm]	Gyrotron voltage [kV]	Requested duration [ms]	Duty cycle [%]	Line focus used?	Peak flux at target [MW/m^2]	Fastcam rate [kFPS]	FLIR range [1/2/3]	Flow?	Full Pulse?	Actual duration [ms]	Fault?	Pop sound?	See FastCam data?	See HDCam data?	FLIR max temp [K]	Comments
Installed Jig-D																		
9:21	1	130	63	50	50		2.4	5	1	N	Y		N	N			343	mullite omega caot is the one that got hot, second is mullite omega 2, third is mullite (star of yesterday)
9:26	2	130	63	100	50		2.4	5	1	N	Y		N	N			383	could not hear countddown, missed shot
9:28	3	130	63	100	50		2.4	5	1	N	Y		N	N			383	mullite omega coat again
9:30	4	130	63	200	50		2.4	5	2	N	Y		N	N			458	
9:31	5	130	63	300	50		2.4	5	2	N	Y		N	N			553	
9:33	6	130	63	400	50		2.4	5	2	N	Y		N	N			658	
9:34	7	130	63	500	50		2.4	5	2	N	Y		N	N			733	
9:36	8	130	63	600	50		2.4	5	2	N	Y		N	N			823	
9:37	9	130	63	750	50		2.4	5	2	N	N	0	Y	N				no pulse in trailer
9:39	10	130	63	750	50		2.4	5	2	N	Y		N	N			923	thin tube coated is catching up on mullite
9:41	11	130	63	50	90		4.4	5	1	N	Y		N	N			388	
9:42	12	130	63	100	90		4.4	5	2	N	Y		N	N			453	
9:44	13	130	63	200	90		4.4	5	2	N	Y		N	N			613	
9:45	14	130	63	300	90		4.4	5	2	N	N	292	Y	Y		Y	743	loud pop. Sparkles on thin tubes then reflection of something bright on frame
9:56	15	130	63	300	90		4.4	5	2	N	N	77	Y	Y			433	faint pop, lost high voltage
10:06	16	130	63	300	90		4.4	5	2	N	N	157	Y	Y			538	pop louder than previous but weaker than first one, voltage down, miter bend fault
10:14	17	130	63	300	90		4.4	5	2	N	Y		N	N			783	
10:15	18	130	63	400	90		4.4	5	2	N	Y		N	N			923	saturated range
10:17	19	130	63	400	90		4.4	5	3	N	Y		N	N			883	
Installed Jig-E																		
12:00	20	70	63	50	30		5.1	10	1	N	Y		N	N			383	Top 2 = omega mullite, then 1thin then 2 mullite then thin
12:01	21	70	63	100	30		5.1	10	2	N	Y		N	N			443	
12:03	22	70	63	200	30		5.1	10	2	N	Y		N	N			603	
12:05	23	70	63	400	30		5.1	10	2	N	Y		N	N			893	
12:07	24	70	63	600	30		5.1	10	3	N	Y		N	N			1093	
12:08	25	70	63	800	30		5.1	10	3	N	Y		N	N			1363	
12:10	26	70	63	1000	30		5.1	10	3	N	Y		N	N			1493	
12:11	27	70	63	1200	30		5.1	10	3	N	Y		N	N			1723	
12:14	28	70	63	1400	30		5.1	10	3	N	Y		N	N			1773	
12:17	29	70	63	1800	30		5.1	10	3	N	Y		N	N			2073	both Omega Mullite tubes (not the one from yesterday) deformed permnanently

Table 36 - Tests 1 of 2 conducted on Wednesday 8/14/2013

Experimental parameters											Outcome					
Time	Run #	Position [cm]	Gyrotron voltage [kV]	Requested duration [ms]	Duty cycle [%]	Line focus used?	Peak flux at target [MW/m^2]	Fastcam rate [kFPS]	FLIR range [1/2/3]	Flow?	Full Pulse?	Actual duration [ms]	Fault?	Pop sound?	See FastCam data?	See HDCam data?	FLIR max temp [K]	Comments
Break																		
15:24	30	70	63	500	30		5.1	10	3	N	N		Y	N		N		signal from different gyrotron
15:27	31	70	63	500	30		5.1	10	3	N	N		Y	N				
15:30	32	70	63	500	30		5.1	10	3	N	Y		N	N			823	
15:31	34	70	63	1000	30		5.1	10	3	N	Y		N	N			1253	
15:33	35	70	63	1600	30		5.1	10	3	N	Y		N	N			1673	
15:37	36	70	63	1800	30		5.1	10	3	N	Y		N	N	Y		1673	
15:47	37	70	63	2000	30		5.1	10	3	N	Y		N	N	Y		1723	thin tube fell out of the jig
Break																		
16:17	38	70	63	2000	30		5.1	3	3	N	Y		N	N			1923	
16:19	39	70	63	2200	30		5.1	3	3	N	Y		N	N			1773	thin tube broke in 3 pieces, one still on the jig
16:27	40	70	63	2200	30		5.1	3	3	N	Y		N				1953	
16:32	41	70	63	2400	30		5.1	3	3	N	Y		N	N			1873	tubes sagged (lightly)
16:38	42	70	63	2700	30		5.1	3	3	N	Y		N	N			1873	

Table 37 - Tests 2 of 2 conducted on Wednesday 8/14/2013

By the end of Wednesday, it was clear that mullite tubes internally coated with Aquadag are the best absorbers. We reliably heated the tubes quasi-uniformly (at least, in a Gaussian pattern) and acquired high-quality video of the tubes deforming under rapid heating, reaching high temperature, and returning to their original shape. The mullite tubes from Omega absorbed slightly better than Coorstek, probably due to the higher content of glass (silicon dioxide), which is somewhat millimeter-wave absorbent but also less refractory than alumina.

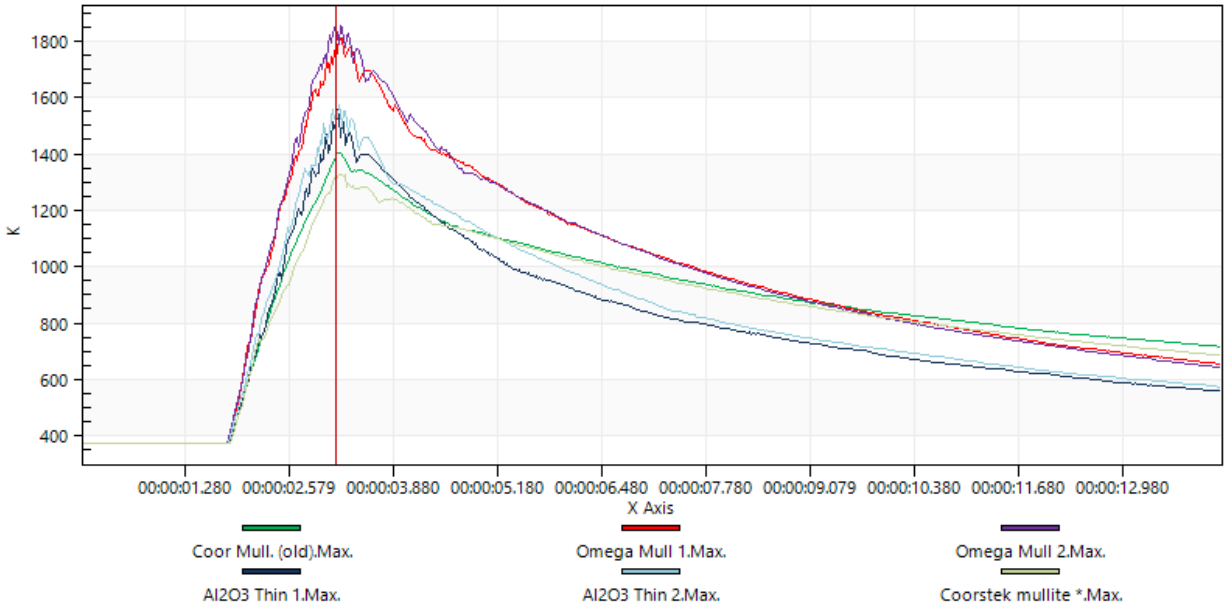

Figure 100 – Time history of peak temperatures of tubes seen in Figure 102. Source file: 2013-08-14T121721831.fcf

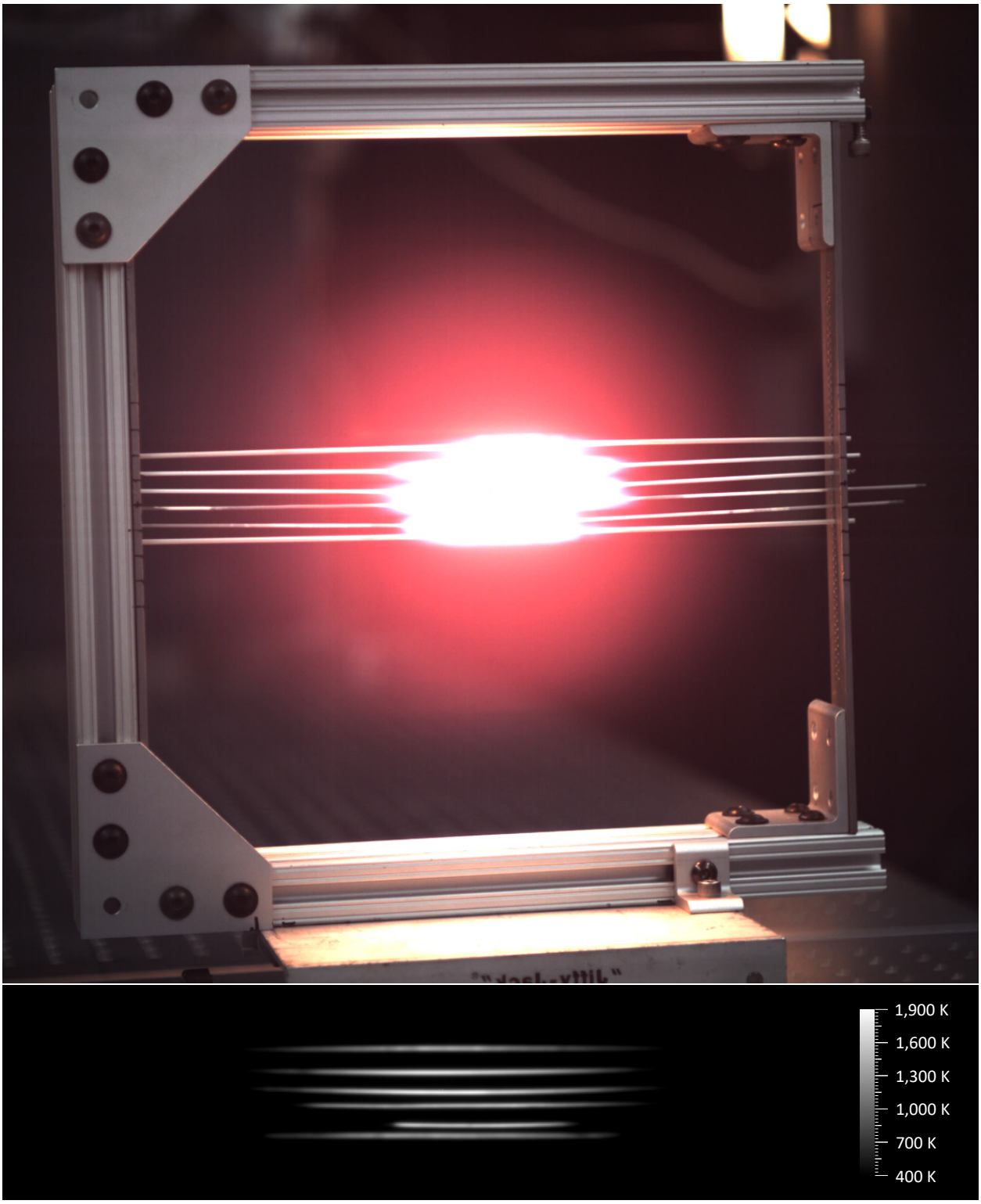

Figure 101 – Run #28: Top: Tubes reach very high temperature but do not permanently deform. Bottom: The LWIR video, processed into a thermal image using a mullite emissivity of 0.65, indicates that a peak temperature of 1,850 K is reached by the Omega mullite 2 tube at t=3.16 seconds. Source files: 14_08_2013___12_22_40.avi and 2013-08-14T121430472.fcf

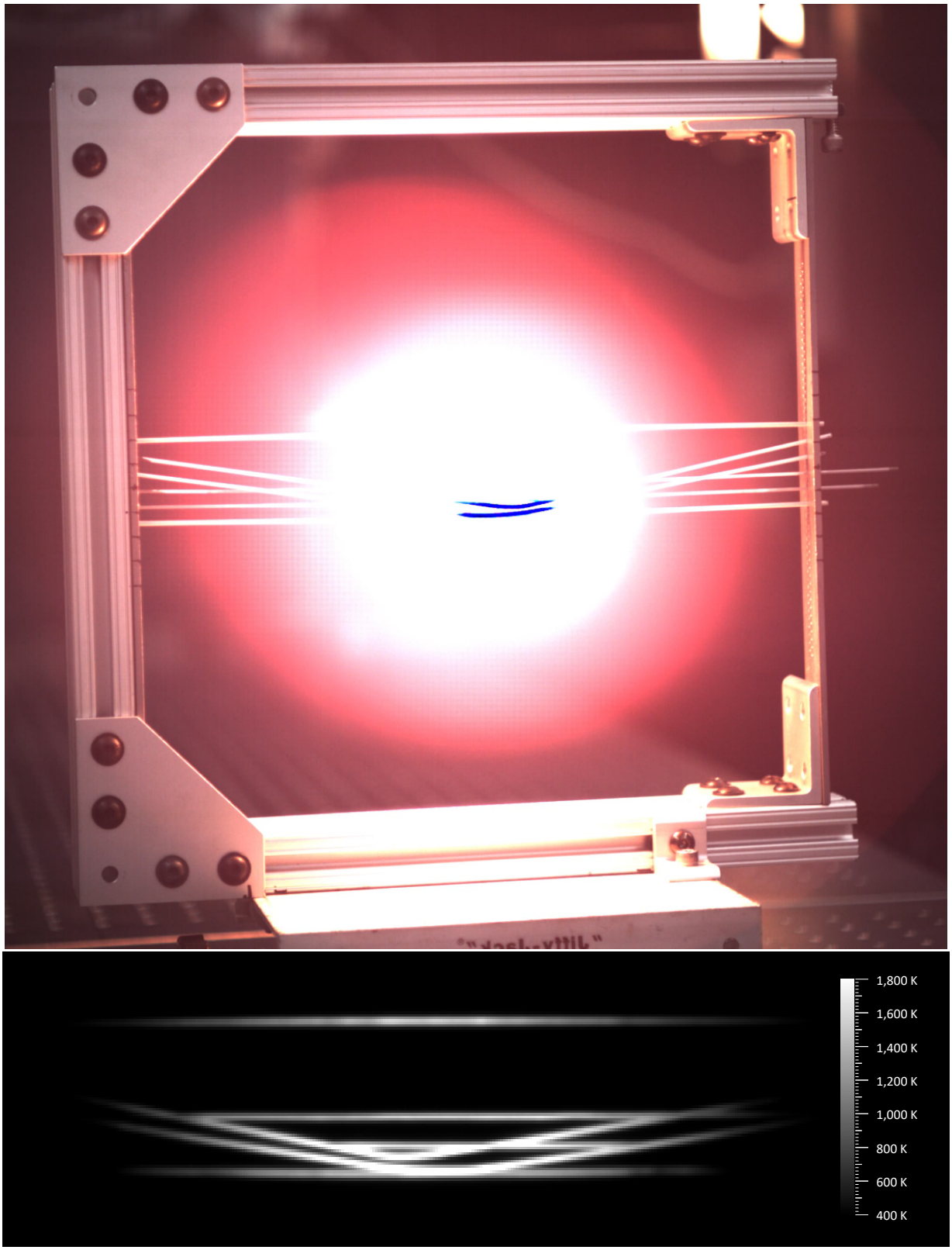

Figure 102 – Run #29: Top: The two D.1.I tubes melt in the center, being held only by their ends. Bottom: LWIR image of the melting tubes. As described in §3.5.3.5.2, the melting temperature of mullite is used to estimate an emissivity of 0.65. Source files: 14_08_2013___12_29_34.avi and 2013-08-14T121721831.fcf

5.1.2.2.4 Thursday 8/15/2013

Experimental parameters											Outcome					
Time	Run #	Position [cm]	Gyrotron voltage [kV]	Requested duration [ms]	Duty cycle [%]	Line focus used?	Peak flux at target [MW/m^2]	Fastcam rate [kFPS]	FLIR range [1/2/3]	Flow?	Full Pulse?	Actual duration [ms]	Fault?	Pop sound?	See FastCam data?	See HDCam data?	FLIR max temp [K]	Comments
Installed FLOW-1 experiment																		
10:00	1	130	63	5	50		2.4		1	N	Y		N	N		N		Lambot note to self: cold flow done at 9h50am (0.6ACFM read, 77psi, Nitrogen)
10:02	2	130	63	5	50		2.4		1	N	Y		N	N		N		2 big mullite tubes get hotter than rest
							2.4											no flow, best = big mullite, then Class A, then omega mullite (totally different from
10:03	3	130	63	50	50				1	N	Y		N	N		N	338	yesterday …)
10:08	4	130	63	50	50		2.4		1	Y	Y		N	N		N		second tube looks clogged
10:11	5	130	63	100	50		2.4		1	Y	Y		N	N		N		looking at next shot, same peak temeprature but cools faster
10:13	6	130	63	100	50		2.4		1	N	Y		N	N		N		
10:15	7	130	63	200	50		2.4		1	N	Y		N	N		N		S denotes saturated reading
10:18	8	130	63	200	50		2.4		2	N	Y		N	N		N		
10:19	9	130	63	200	50		2.4		2	Y	Y		N	N		N		
10:21	10	130	63	400	50		2.4		2	N	Y		N	N		N		
10:22	11	130	63	400	50		2.4		2	Y	Y		N	N		N		
10:24	12	130	63	600	50		2.4		2	N	Y		N	N		N		
10:25	13	130	63	600	50		2.4		2	Y	Y		N	N		N		
10:27	14	130	63	800	50		2.4		2	N	Y		N	N		N		
10:29	15	130	63	800	50		2.4		3	Y	Y		N	N		N		
10:32	16	130	63	1000	50		2.4		3	N	Y		N	N		N		
10:34	17	130	63	1000	50		2.4		3	Y	Y		N	N		N		
10:43	18	130	63	1250	50		2.4		3	N	Y		N	N				
10:46	19	130	63	1250	50		2.4		3	Y	N	0	Y	N		N		
10:50	20	130	63	1250	50		2.4		3	Y	Y		N	N				/!\ don't take in account the max
10:53	21	130	63	1500	50		2.4		3	N	Y		N	N				temperature, one tube is clogged -> that's
10:57	22	130	63	1500	50		2.4		3	Y	Y		N	N				the one that shows the max temperature
11:06	23	130	63	100	90		4.4		2	N	N		N	N				sent to dummy load
11:07	24	130	63	100	90		4.4		2	N	Y		N	N		N		
11:09	25	130	63	200	90		4.4		2	N	Y		N	N				
11:10	26	130	63	200	90		4.4		2	Y	N	190	Y	Y				lost high voiltage
11:26	27	130	63	400	90		4.4		2	?	N	160	Y	Y				lost high voltage
11:32	28	130	63	100	90		4.4		1	N	Y		N	N				trying to clear up the target
11:36	29	130	63	100	90		4.4		2	N	Y		N	N				
11:37	30	130	63	100	90		4.4		2	N	Y		N	N				
11:38	31	130	63	200	90		4.4		2	Y	Y		N	N				
11:40	32	130	63	400	90		4.4		2	N	N	329	Y	Y				voltage down
11:48	33	130	63	400	90		4.4		3	N	Y		N	N				
11:50	34	130	63	400	90		4.4		3	Y	Y		N	N			733	Lambot note to self: change max temp with
11:53	35	130	63	600	90		4.4		3	N	Y		N	N			898	the blue one (one not clogged)
11:56	36	130	63	600	90		4.4		3	Y	Y		N	N			848	
11:59	37	130	63	800	90		4.4		3	N	Y		N	N			1048	
12:02	38	130	63	800	90		4.4		3	Y	Y		N	N			933	
12:04	39	130	63	900	90		4.4		3	N	Y		N	N			1083	
12:08	40	130	63	900	90		4.4		3	Y	Y		N	N			1023	

Table 38 – Tests 1 of 2 conducted on Thursday 8/15/2013

Experimental parameters										Outcome					
Time	Run #	Position [cm]	Gyrotron voltage [kV]	Requested duration [ms]	Duty cycle [%]	Line focus used?	Peak flux at target [MW/m^2]	Fastcam rate [kFPS]	FLIR range [1/2/3]	Flow?	Full Pulse?	Actual duration [ms]	Fault?	Pop sound?	See FastCam data?	See HDCam data?	FLIR max temp [K]	Comments
FLOW-2 at 70 cm, replaced 2nd mullite tube from top. All tubes except very top blew black ink in cold flow test.																		
12:58	41	70	63	0	0		0.0		1	Y								
							5.1											THOSE SHOTS WERE AT 70% ON 30% OFF - >
13:02	42	70	63	50	30				1	N	Y		N	N				intensity on target
13:04	43	70	63	500	30		5.1		2	N	Y		N	N				top mullite tube broke early in pulse
FLOW-3: Replaced broken tube with new one, did one cold flow with no data to blow out the coating																		
13:46	44	70	63	250	30		5.1		2	Y	Y		N	N				
13:48	45	70	63	250	30		5.1		2	Y	Y		N	N			393	
13:49	46	70	63	250	30		5.1		2	N	Y		N	N			413	
13:50	47	70	63	500	30		5.1		2	Y	Y		N	N			533	
13:54	48	70	63	500	30		5.1		2	N	Y		N	N			623	
13:57	49	70	63	1000	30		5.1		3	Y	Y		N	N			613	
14:01	50	70	63	1000	30		5.1		3	N	Y		N	N			773	
14:03	51	70	63	1200	30		5.1		3	Y	Y		N	N			623	
14:06	52	70	63	1200	30		5.1		3	N	Y		N	N			873	
14:09	53	70	63	1200	30		5.1		3	Y	Y		N	N			633	got time wrong, repeated 1200
14:13	54	70	63	1600	30		5.1		3	Y	Y		N	N			723	top tube flew out of the jig
14:16	55	70	63	1600	30		5.1		3	N	Y		N	N			1183	
14:22	56	70	63	2000	30		5.1		3	Y	Y		N	N			973	
14:29	57	70	63	2000	30		5.1		3	N	Y		N	N			1473	
14:34	58	70	63	2500	30		5.1		3	Y	Y		N	N			1273	
							5.1											piece flew out, looks like the tube had flow
14:42	59	70	63	3000	30				3	Y	Y		N	N				but constrained
FLOW-4: Switched all tubes except mullite in pos. 4, thin tubes switched with regular alumina. One regular alumina added.																		
							5.1											missed HDCam data, one tube flew out of the
15:46	60	70	63	3000	30				3	Y	Y		N	N				jig
15:53	61	70	63	3000	30		5.1		3	Y	Y		N	N		Y		
16:00	62	70	63	3000	30		5.1		3	Y								
Switched to Bruccoleri H2O jig																		
17:13	63	70	63	10	30		5.1		1	Y	Y							
17:19	64	70	63	500	30		5.1		1	Y	Y						353	
17:21	65	70	63	1000	30		5.1		1	Y	Y						413	
17:23	66	70	63	1500	30		5.1		1	Y	Y							saturated range/ switching range
17:25	67	70	63	2000	30		5.1		1	Y	Y						513	
17:28	68	70	63	2500	30		5.1		1	Y	Y						573	
17:33	69	70	63	3000	30		5.1		1	Y	Y						623	
Switched to Myrabo H2O jig																		
19:23	70	185	63	10	30		0.7		1	N	Y							conditioning run, 006 nozzle loose
20:00	71	185	63	3000	30		0.7		1	Y	Y						373	006 nozzle loose
20:33	72	185	63	10	30		0.7		1	N	Y							conditioning run, 008 nozzle
20:41	73	185	63	3000	30		0.7		1	Y	Y						373	008 nozzle

Table 39 – Tests 2 of 2 conducted on Thursday 8/15/2013

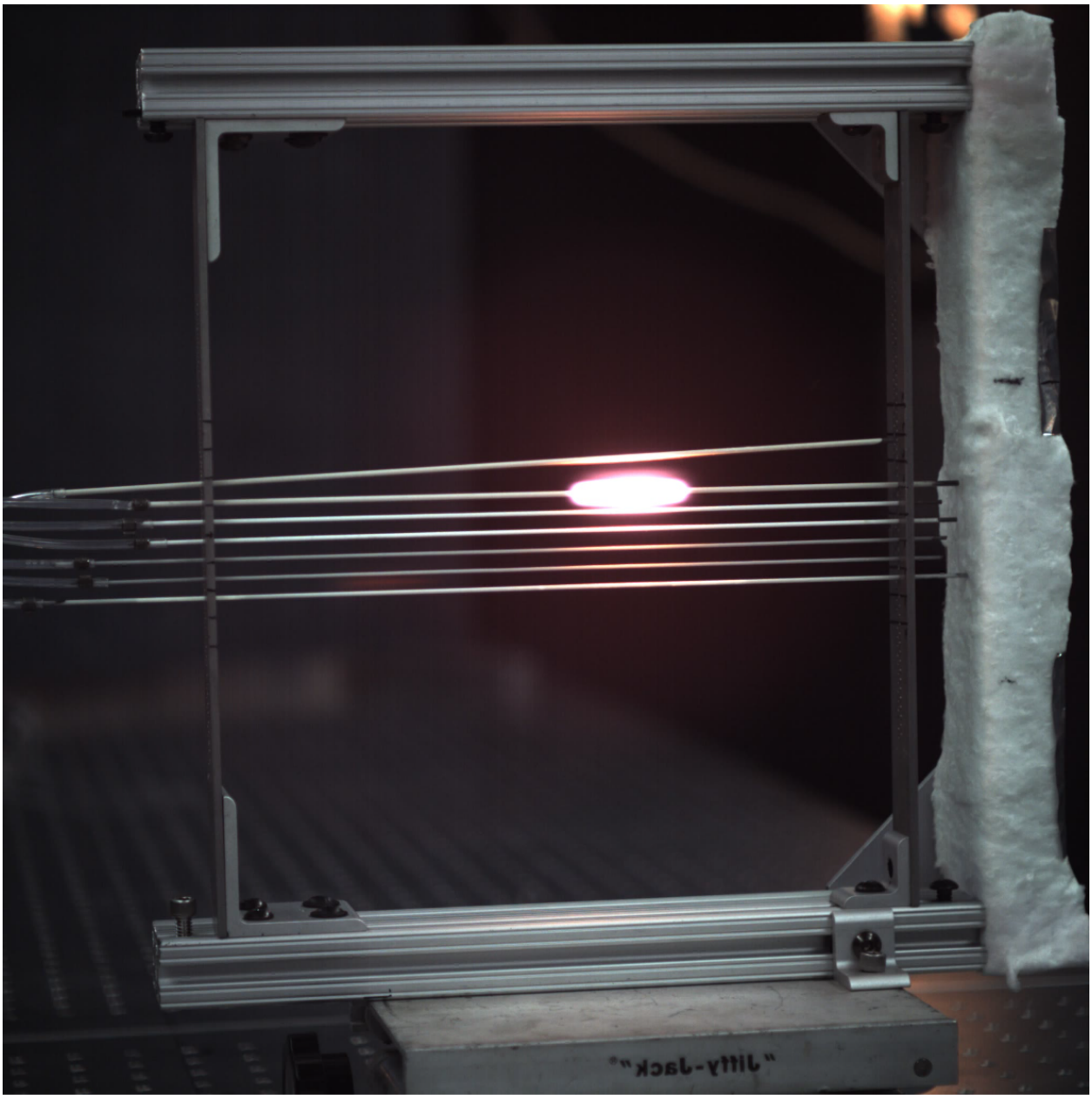

Figure 103 – 15 August 2:21 pm: A test with flowing gas is impeded by a tube whose flow is blocked, heating it disproportionately to the others. Source file: 15_08_2013___14_21_42.avi

Thursday's focus was to test tubes that were assembled in a rudimentary heat exchanger with flowing nitrogen at an inlet pressure of 5 bar (77 psi). Unfortunately, the tubes had to be coated the day before and did not have enough time to dry (the method of using a vacuum oven to rapidly dry the tubes came just after the campaign). The tubes therefore had to be conditioned by multiple pulses to dry them.

The end of the day and the following day experimented with direct propellant absorption using uncoated tubes of alumina and water as a propellant.

5.1.2.2.5 Friday 8/16/2013

Experimental parameters											Outcome						
Time	Run #	Position [cm]	Gyrotron voltage [kV]	Requested duration [ms]	Duty cycle [%]	Line focus used?	Peak flux at target [MW/m^2]	Fastcam rate [kFPS]	FLIR range [1/2/3]	Flow?	Full Pulse?	Actual duration [ms]	Fault?	Pop sound?	See FastCam data?	See HDCam data?	FLIR max temp [K]	Comments
Continued with Myrabo H20 Jig																		
9:36	1	185	63	3000	30	N	0.7		1	Y	Y		N	N	Y	Y	373	
Paper shots to characterize beam																		
11:26	2	170	63	5	100	Y	113.8		1	N	Y		N	N	N	N	300	installed line focus optic and aligned
11:28	3	170	63	10	100	Y	113.8		1	N	Y		N	N	N	N	318	
11:28	4	170	63	15	100	Y	113.8		1	N	Y		N	N	N	N	338	using this paper shot for 4 point calibration
Switched to Bruccoleri H2O jig																		
12:50	5	170	63	50	100	Y	113.8		1	N	Y		N	N	Y	Y		duty cycle requested was 30%, got 100%
12:53	6	170	63	50	30	Y	34.1		1	N	Y		N	N	Y	Y	308	
12:58	7	170	63	3000	30	Y	34.1		1	Y	Y		N	N	Y	Y	373	0.2 g/s 65 psi
13:03	8	170	63	3000	30	Y	34.1		1	Y	Y		N	N	Y	Y	373	0.2 g/s 65 psi
13:05	9	170	63	3000	30	Y	34.1		1	N	Y		N	N	Y	Y	373	
14:22	10	170	63	50	30	Y	34.1		1	N	Y		N	N	Y	Y	310	
14:27	11	170	63	3000	30	Y	34.1		1	Y	Y		N	N	Y	Y		mullite 1 khz hum 0.2 g/s 65 psi
14:32	12	170	63	3000	30	Y	34.1		1	Y	Y		N	N	Y	Y		mullite 1 khz hum 0.2 g/s 65 psi
14:38	13	170	63	3000	30	Y	34.1		1	Y	Y		N	N	Y	Y	1673	1 khz hum 0.2 g/s 65 psi
14:48	14	170	63	3000	30	Y	34.1		1	N	Y		N	N	Y	Y		mullite 1 khz hum
14:59	15	170	63	3000	30	Y	34.1		1	N	Y		N	N	Y	Y		mullite 1 khz hum
15:17	16	170	63	3000	30	Y	34.1		1	Y	Y		N	N	Y	Y	373	1 khz hum 0.2 g/s 65 psi.

Table 40 - Tests conducted on Friday 8/16/2013

Friday's tests continued experiments with direct propellant absorption using uncoated tubes of alumina and water as a propellant. While these tests showed some interesting results, a better-prepared approach should be taken in the future for investigating direct propellant absorption.

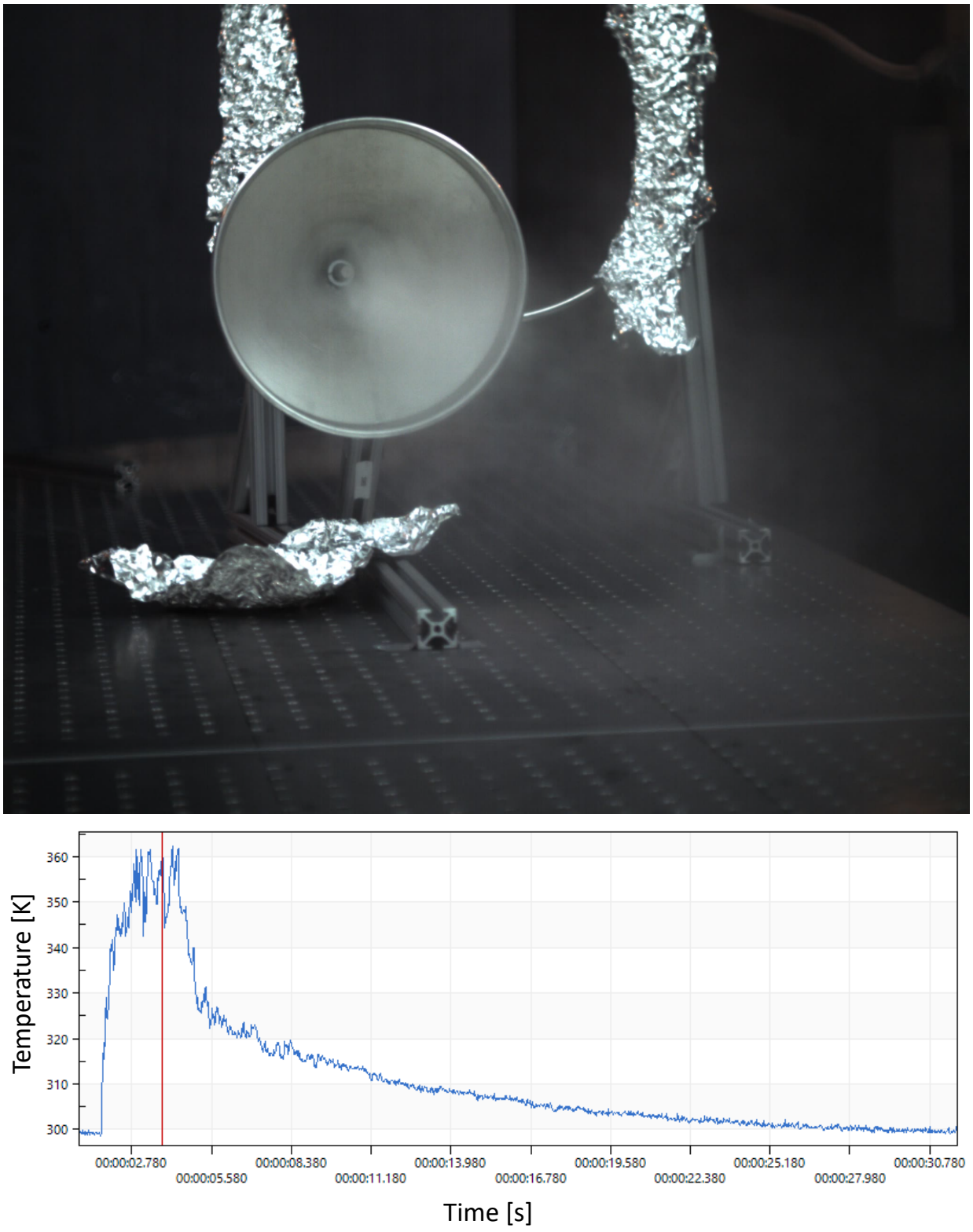

Figure 104 - 16 August 9:09 am: Top: 45 degree LTI conical reflector with approximately 0.5" alumina tube with high-pressure fogger nozzle as used for fire suppression. This experiment was led by Myrabo/LTI to understand how well a millimeter-wave beam is absorbed into atomized water droplets. Bottom: Peak temperature as measured by the LWIR camera. Source file: 16_08_2013___09_18_02.avi

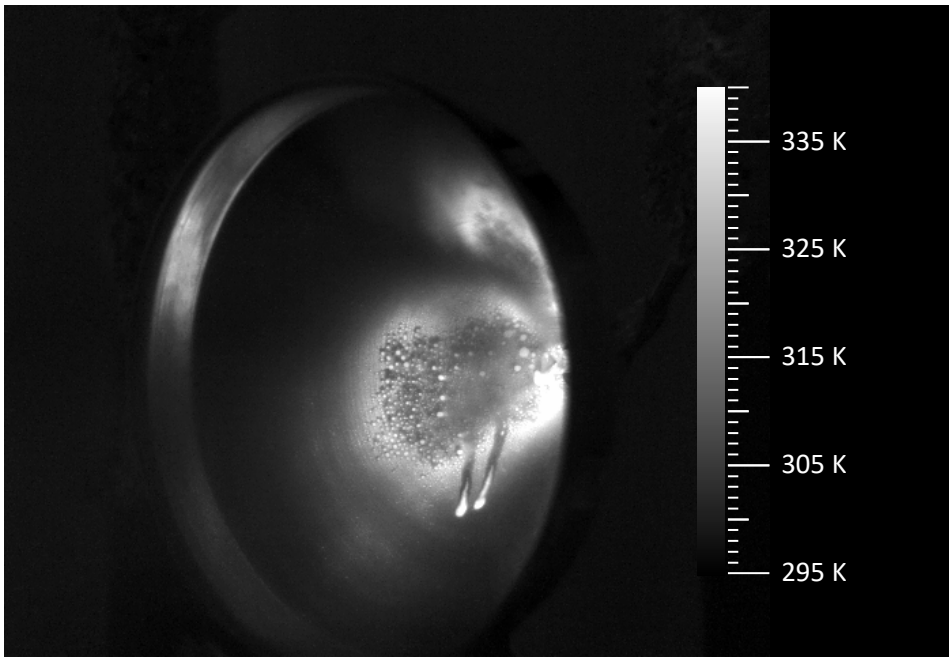

Figure 105 – 16 August 9:09 am: LWIR thermal image of the LTI conical reflector water absorption test. This camera frame is taken at the time indicated by the vertical red line at the bottom of Figure 104. The perspective on the conical reflector is different from that of Figure 104 because the LWIR camera is located on the opposite side of the waveguide. Source file: 2013-08-16T090913348.fcf

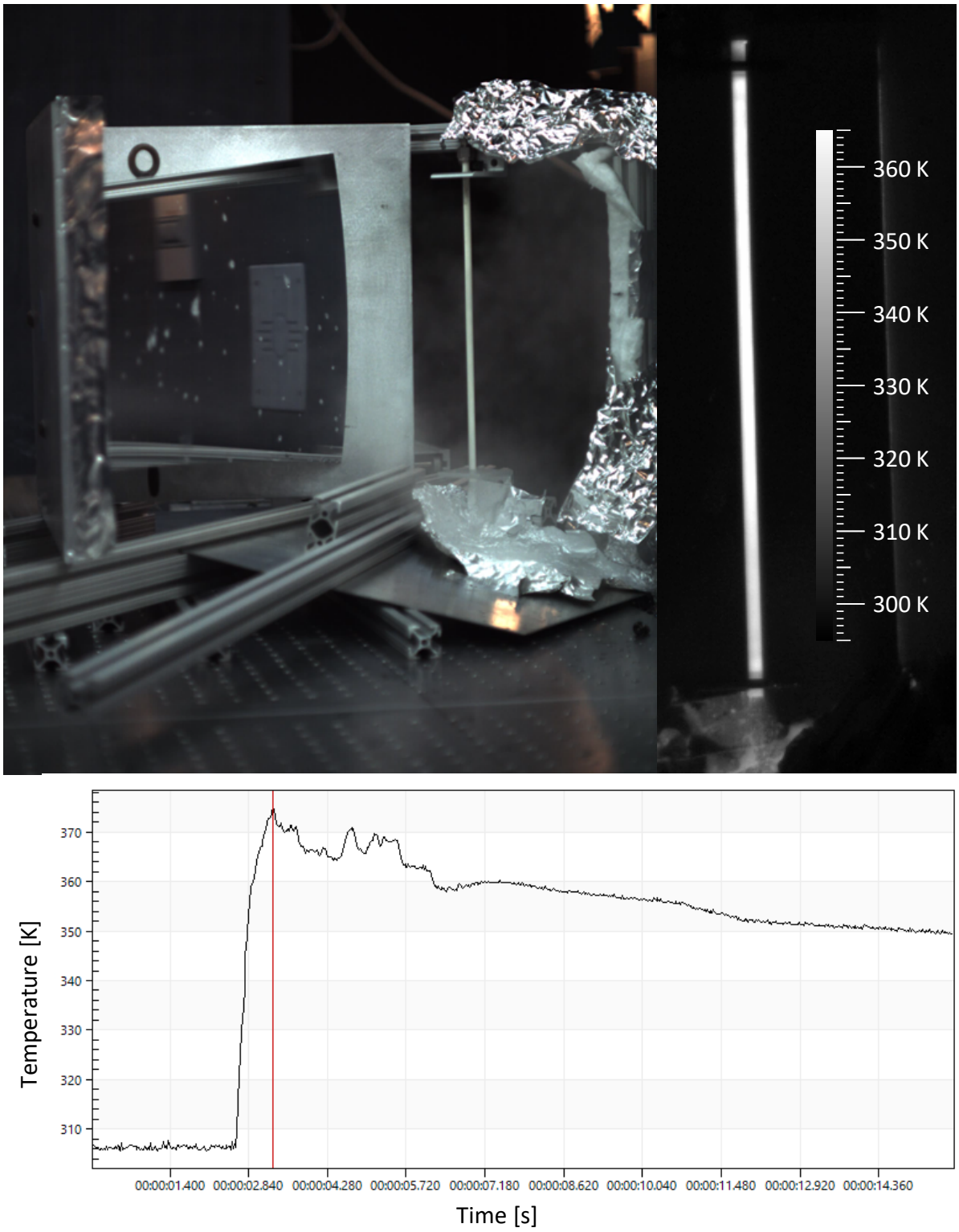

Figure 106 – The LTI line focus optic is used in a water propulsion experiment led by Alex Bruccoleri (Izentis). While heated by millimeter-waves, steam periodically chugs from the bottom of the tube. Source file: 16_08_2013___15_17_23.avi

5.2 Rocket

5.2.1 100 kW-class

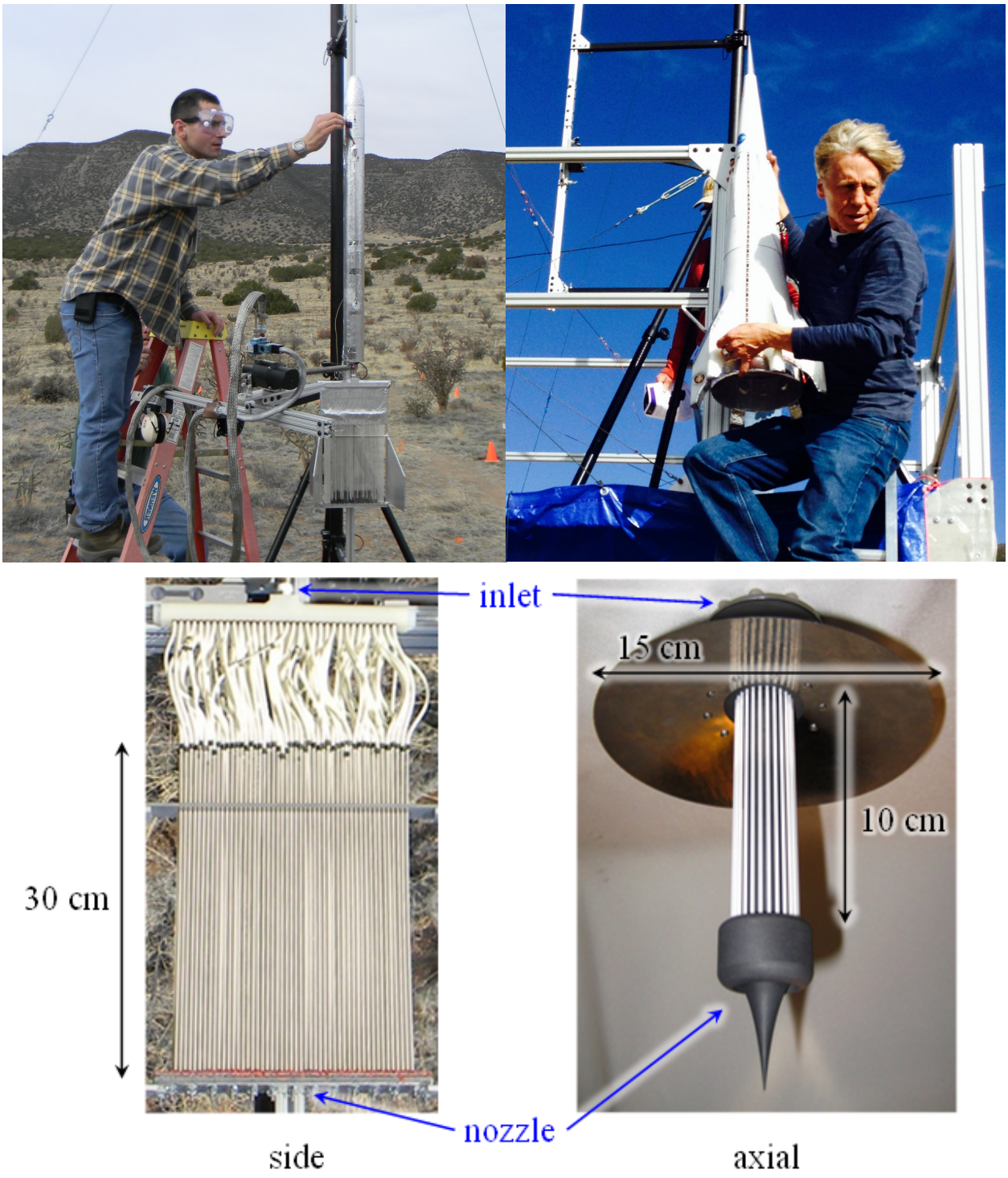

Figure 107 – The two types of 100 kW-class rockets developed for the MTLS project. The rocket on the left (being prepared by Alex Bruccoleri/Izentis in the image) is known as the side-illuminated rocket and on the right (being prepared by Leik Myrabo/LTI in the image) is known as the axial-illuminated rocket.

Two types of 100 kW-class rocket were developed for the MTLS project and are shown in Figure 107. The first is a simple small-scale analogy of Parkin's original concept, in which the beam is incident on the rocket from the side and absorbed onto a planar heat exchanger in the shape of a rectangle. This type of rocket is referred to hereafter as a side-illuminated rocket. The second is a new concept proposed by Myrabo/LTI (the Co-principal investigator of the MTLS project) in which the beam is aimed along the axis of the rocket and reflected by a parabolic mirror onto a cylindrical heat exchanger, as shown in the lower right corner of the figure. This type of rocket is referred to hereafter as an axial-illuminated rocket.

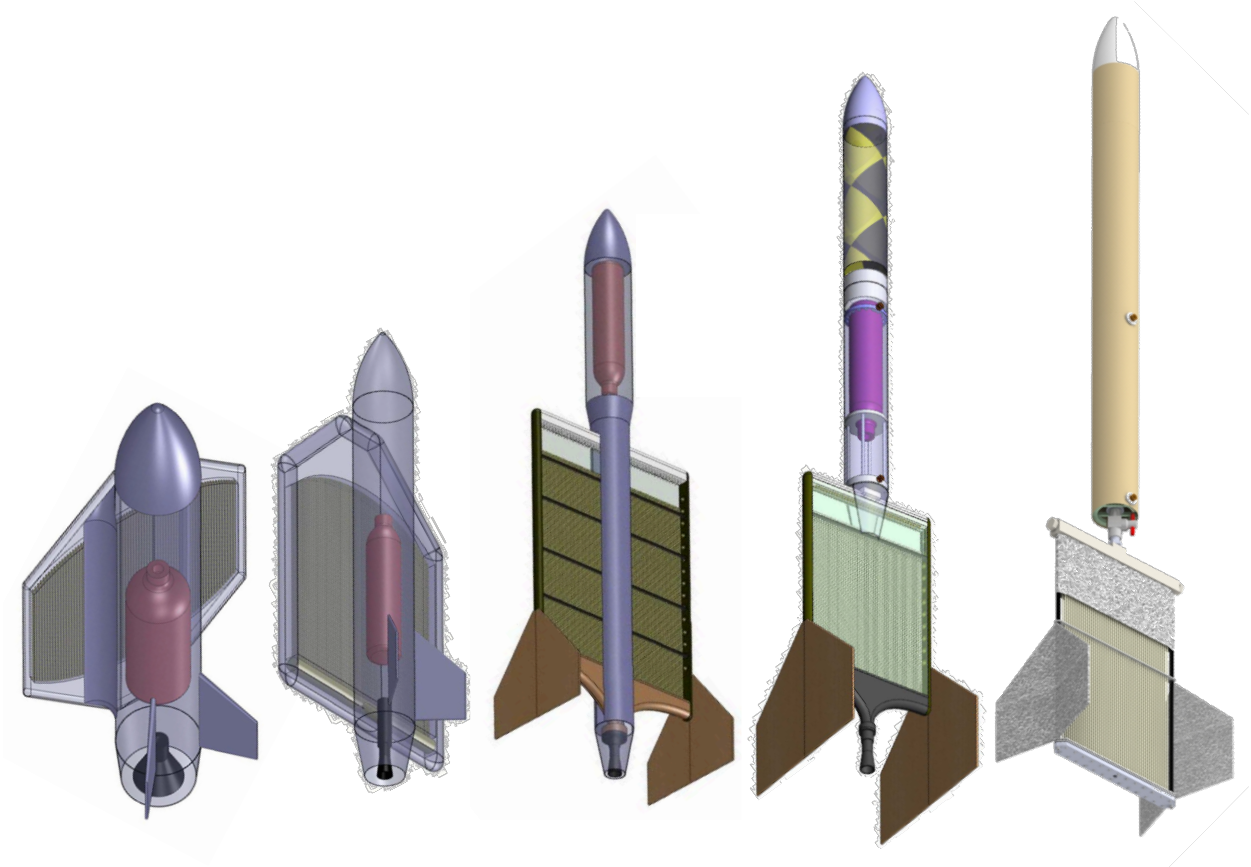

Figure 108 – Jim Eilers' axial-illuminated rocket concept evolution. From left to right: Version N1 (21 March 2013), version N2 (3 April 2013), version N3 (13 June 2013), version N6 (30 July 2013), as-flown version.

Following the scoping analysis presented in §3.1, Jim Eilers designed the first few iterations of the side-illuminated rocket starting in March 2013 as testing of the heat exchanger was underway at General Atomics. Further design, construction and support of the rocket test articles was transitioned to Alex Bruccoleri/Izentis (Bruccoleri, Eilers et al. 2015). Heat exchanger development was led by one of us (Lambot) and proceeded in parallel with the rocket development.

Similarly, Leik Myrabo/LTI began designing the axial-illuminated rocket in earnest during early 2013. The concept at that time is shown in Figure 109. Myrabo was assisted by Israel Salvador on CAD and Cesare Freppoli on heat exchanger analysis. The rocket aeroshell was based on the Sprint missile and the internals were arranged to reproduce the same moments of inertia.

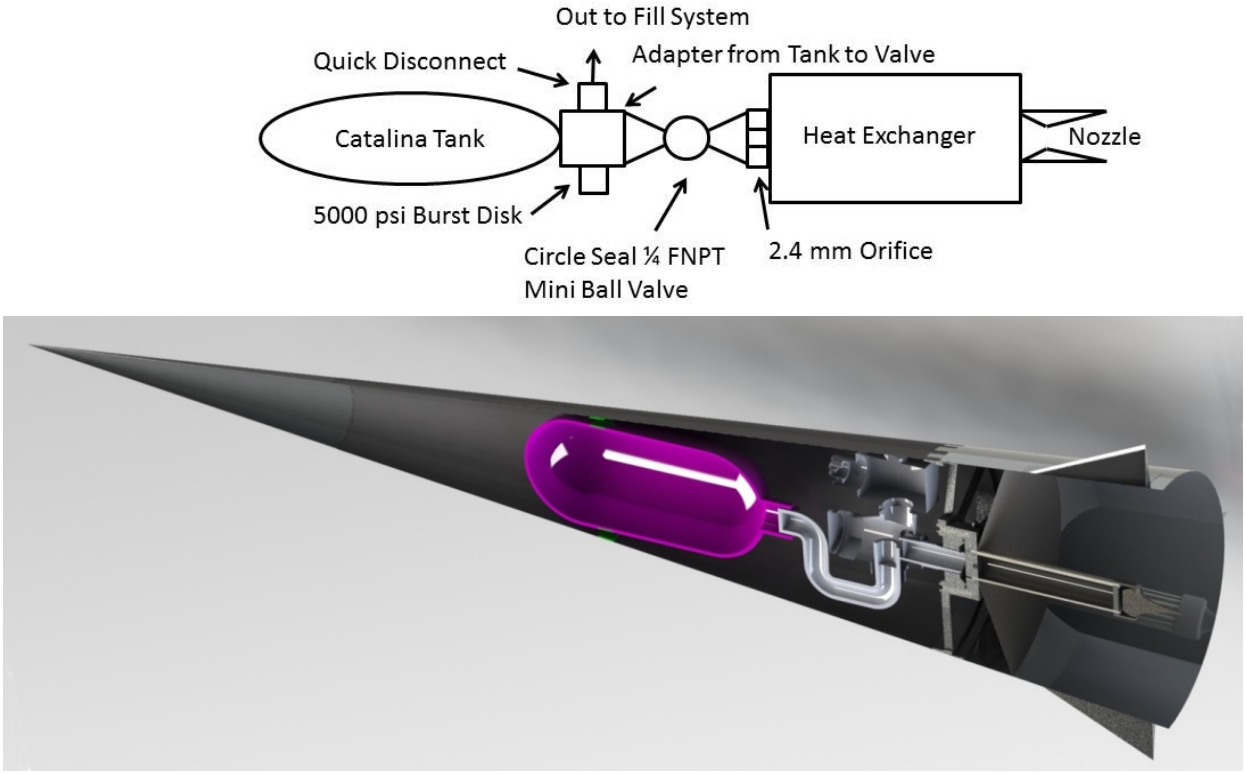

Figure 109 - From June 2013 MTLS Program Management Review – Myrabo/LTI conceptual design of axial-illuminated rocket based on Sprint missile geometry

Figure 110 - First engine assembly of the LTI axial-illuminated engine. Graphite core. Molybdenum reflector.

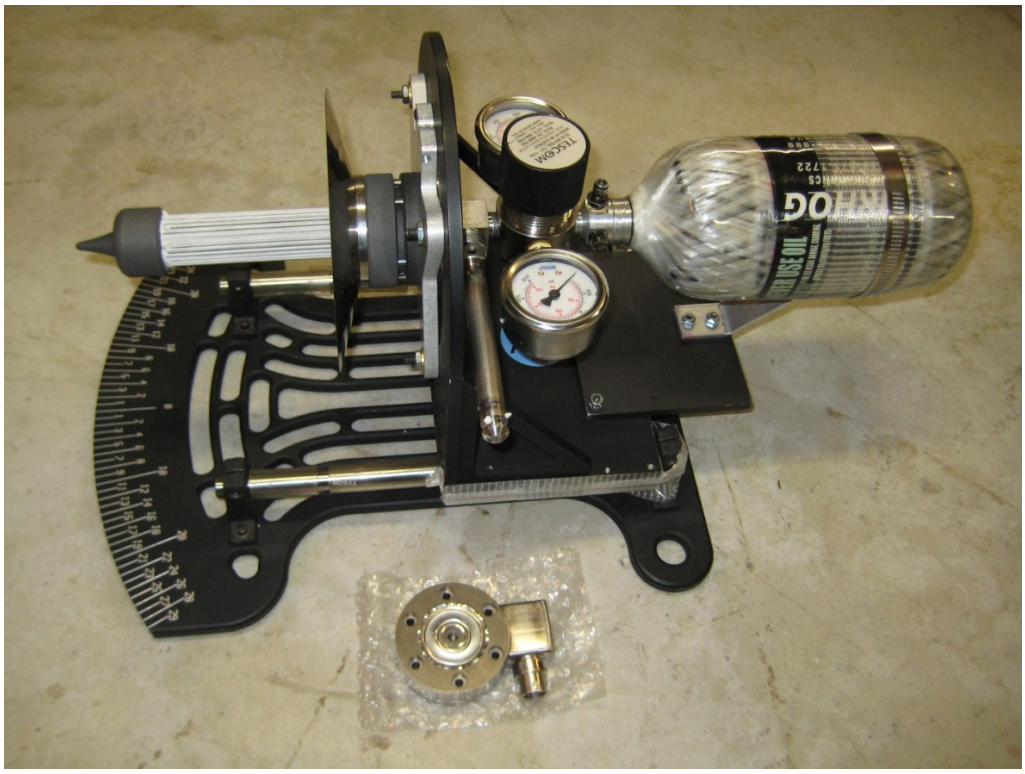

Figure 111 – LTI load cell thrust stand for the axial-illuminated rocket. The load cell is shown below. A Tescom regulator is used with the flight model. This was prepared for laboratory testing in the MTU but used at Kirtland.

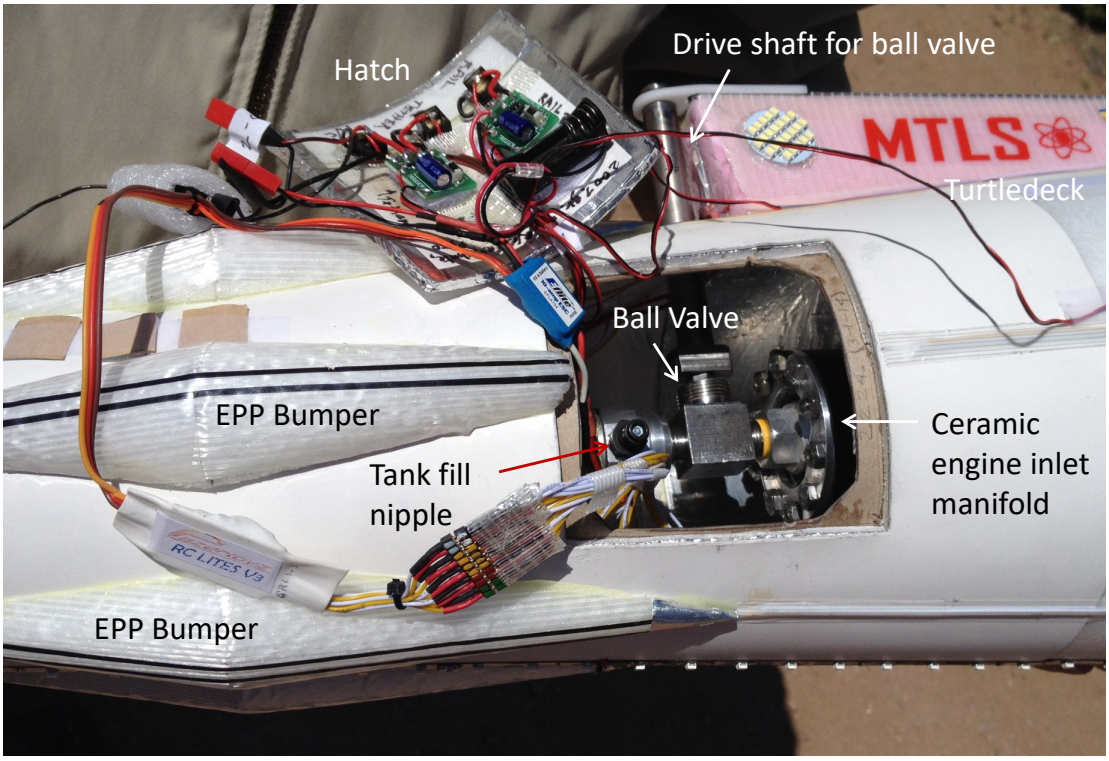

Figure 112 – A view of the LTI axial-illuminated rocket with open hatch showing key engine and electronic system components.

5.2.1.1 11/18/2013 - 11/26/2013 pre-testing at 100 kW, 95 GHz launch test facility

Date	Time	Run #	Distance [m]	Beam characteristics: Power level [%]	Peak intensity [kW/m^2]	power in 30 cm diameter [kW]	Shot duration [s]: pre heat [s]	delay	total	Temp. [K]: Max. (ε=0.95)	Mean (ε=0.95)	Comments
	Pre-test campaign with HX on boom arm											
	08:57	1	1.4	36	~1000				1 S			Range saturated, 3 tubes broken, smoke
	Changed target											
	09:48	2	1.4	18	~500	~20-25			0.25	450		
	09:54	3	1.4	18	~500	~20-25			0.5	680		bending?
Tuesday	09:57	4	1.4	18	~500	~20-25			0.75	820		bending
11/26/2013	10:05	5	1.4	18	~500	~20-25			1	1000		
	10:20	6	1.4	18	~500	~20-25			1.25	1150		
	10:25	7	1.4	18	~500	~20-25			1.5	1250		Tube [illegible] a bit
	Beam aimed down a little bit											
	10:34	8	1.4	18	~500	~20-25			1.76	1400		Vibration
	10:40	9	1.4	18	~500	~20-25			2	1520		

Table 41 - Tests conducted at the 100 kW, 95 GHz launch test facility between 11/18/2013 - 11/26/2013

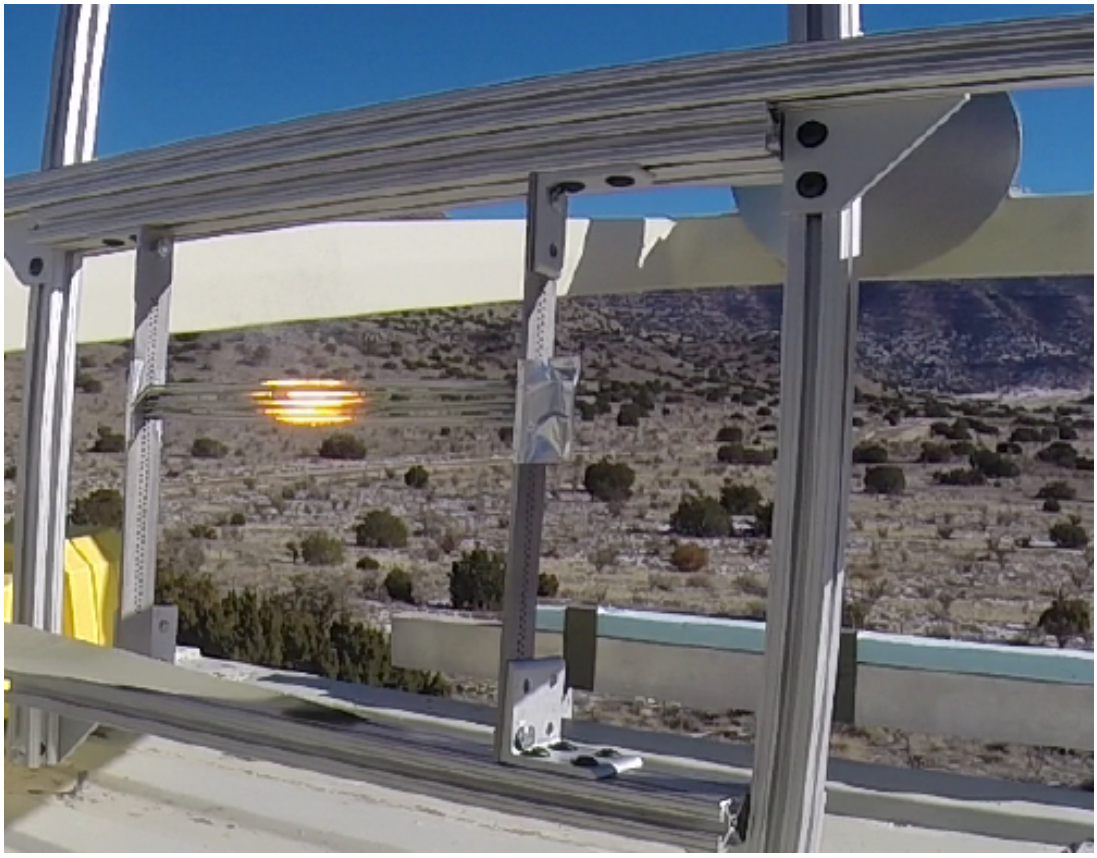

Figure 113 – 26 November 9:00 am: A first test verifies that the 95 GHz beam can raise the heat exchanger tubes to white hot temperature as was achieved three months earlier at the 1 MW, 110 GHz static test facility at General Atomics in San Diego. For this test only, a small mirror diverts the beam from the millimeter-wave source directly onto the heat exchanger tubes. After this test, the beam director structure shown in Figure 78 was built and used. Source file: GOPR0053.MP4

5.2.1.2 12/2/2013 - 12/18/2013 test campaign at 100 kW, 95 GHz launch test facility

Date	Time	Run #	Distance [m]	Beam characteristics: Power level [%]	Beam characteristics: Peak intensity [kW/m^2]	Beam characteristics: power in 30 cm diameter [kW]	Shot duration [s]: pre heat [s]	Shot duration [s]: delay	Shot duration [s]: total	Temp. [K]: Max. (ε=0.95)	Temp. [K]: Mean (ε=0.95)	Comments
Thursday	Rocket propellant tank fill procedure and pressurization tests											
12/5/2012	09:29	1										GOPR0094.MP4, HDV_0486.MP4
Friday	COLD-LAUNCH-1: First beamless launch. Testing aeroshell performance and parachute deployment.											
12/6/2013	12:54	1										Success. Rocket worked first time.
Tuesday	COLD-STATIC-1: First beamless static test of propulsive flowpath with heat exchanger (1/16" orifice)											
12/17/2013	15:22	1										Jet blew up dirt. Invert next time.
	COLD-STATIC-2: Beamless static test propulsive flowpath with heat exchanger (1/16" orifice)											
Wednesday	**09:00**	**1**										2013-12-18T085850069.fcf
12/18/2013	COLD-STATIC-3: Beamless static test propulsive flowpath after heat exchanger integration (1/8" orifice)											
	03:19	2										2013-12-18T143202937.fcf

Table 42 - Tests conducted at the 100 kW, 95 GHz launch test facility between 12/2/2013 - 12/18/2013

Figure 114 – 6 December 12:54 pm: This ideal windless sunny day followed a snowstorm the previous day. A montage of overlaid frames shows the first launch of the side-illuminated rocket without the beam. Because there was no beam and we did not wish to risk breaking a heat exchanger as the rocket landed, we used a straight pipe and a nozzle to mimic the estimated thrust/weight of the rocket at liftoff. This successful first launch demonstrated the correct function of the launch rail, that the rocket can clear the rail without needing beam power, and that the Pyrodex charge deploys the parachute at apogee. Alex Bruccoleri/Izentis is holding the rocket in the center of the montage. Source files: GOPR0097.mp4 and GOPR0099.mp4

Figure 115 - 18 December 3:19 pm: Second test of flow through 1/8" orifice and heat exchanger without beam. The first test, conducted the previous day, was oriented with the nozzle toward the ground, which generated dirt and dust. Note the flow actuation system in which an actuator opens the flow valve between the tank and heat exchanger to initialize propellant flow. Source file: DSCN2028.JPG

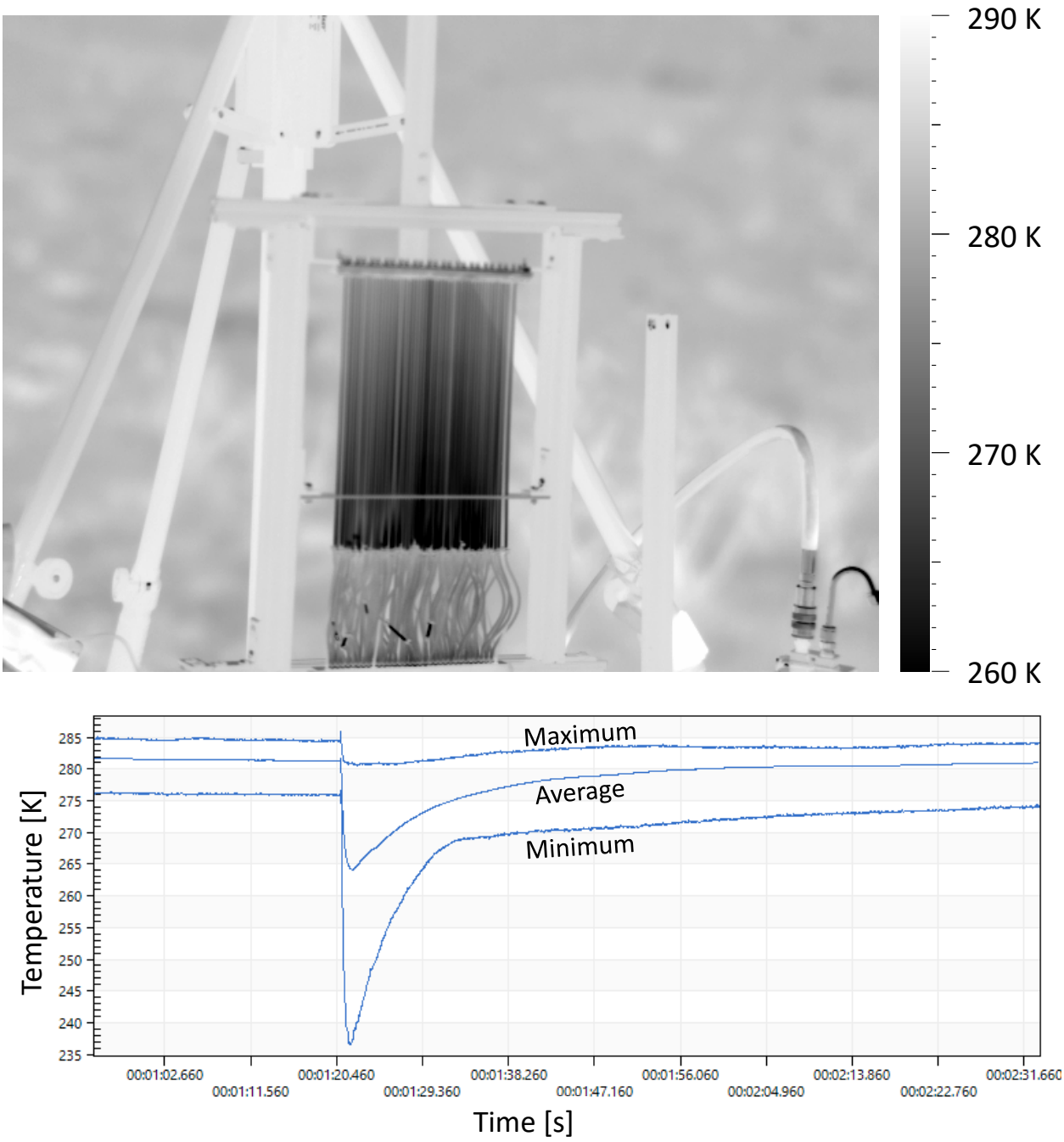

Figure 116 – 18 December 3:19 pm: Second test of flow through 1/8" orifice and heat exchanger without beam. The LWIR image shows that the central tubes are coldest due to a higher mass flow rate, in turn generated by a greater pressure difference along the central tubes than the outer ones. Notice that the second tube from the right is clogged or leaking, hence appears white in contrast to the other tubes. The polyurethane inlet tubes have a thermal conductivity that is two orders of magnitude lower than mullite, so they appear warmer. Source file: 2013-12-18T143202937.fcf

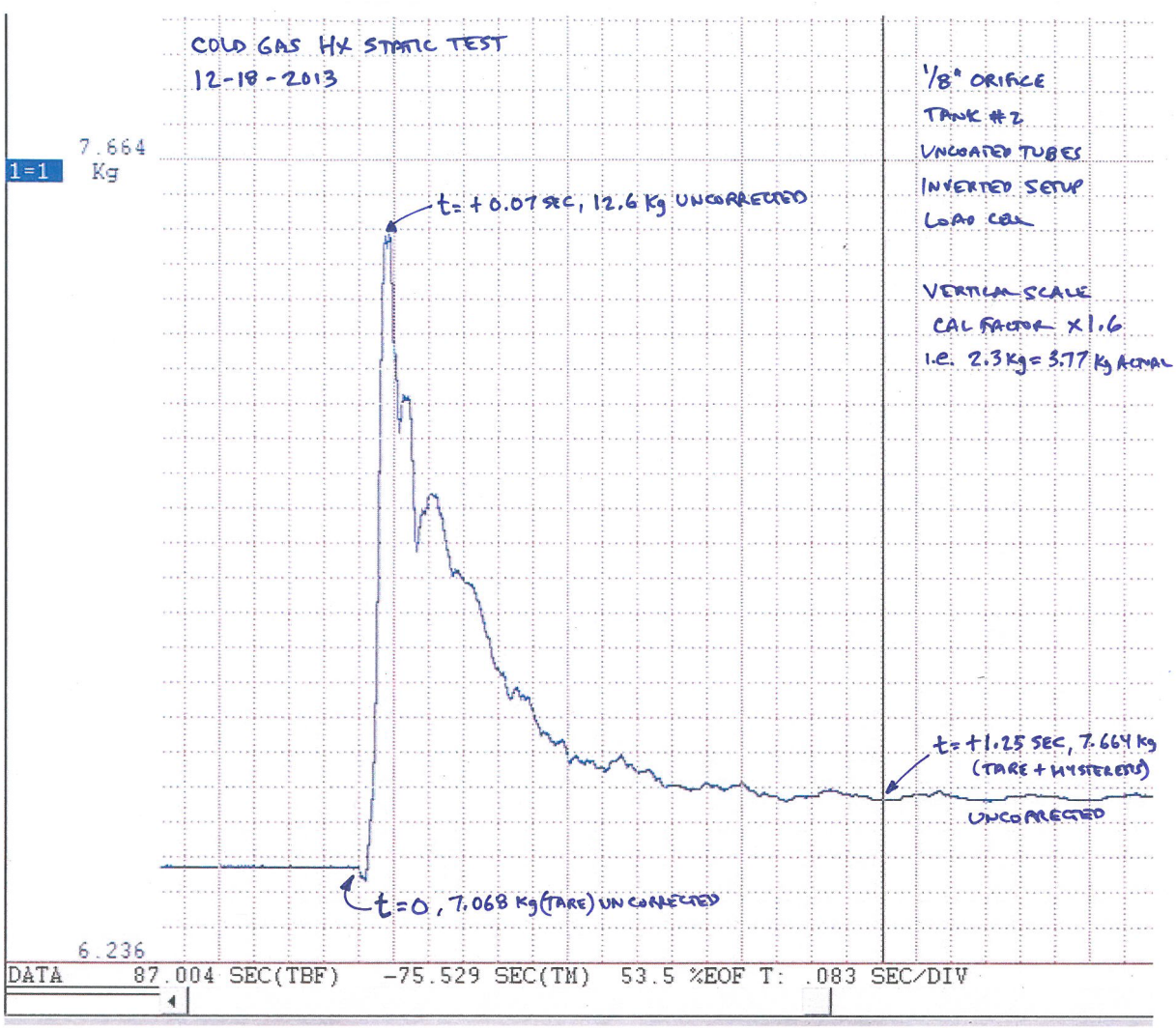

Figure 117 – 18 December: Load cell trace of thrust generated by static test without beam.

The method of measurement of thrust used to produce Figure 117 turned out to be unreliable for two reasons:

1. There was a strong hysteresis in the thrust measured vs time due to the way the setup was constructed (the contact between load cell and rocket). The construction was later improved.
2. The amplifier furnished with the load cell had an inexplicable drift that was important enough to invalidate a 10-second measurement test. To remedy the problem, the load cell was plugged directly into an appropriate National Instruments Module and future measurements were taken using the corresponding LabVIEW software.

5.2.1.3 1/12/2014 - 1/31/2014 test campaign at 100 kW, 95 GHz launch test facility

Date	Time	Run #	Distance [m]	Beam characteristics: Power level [%]	Beam characteristics: Peak intensity [kW/m^2]	Beam characteristics: power in 30 cm diameter [kW]	Shot duration [s]: pre heat [s]	Shot duration [s]: delay	Shot duration [s]: total	Temp. [K]: Max. (ε=0.95)	Temp. [K]: Mean (ε=0.95)	Comments
	Rocket component HPM test board. Beam 14 cm diameter half max horizontal, 18 cm vertical											
	13:57	1	29	100	450				2			Fin smoke
	Fin removed											
	14:04	2	29	100	450				2			Round shape becoming warmer
	14:09	3	29	100	450				2			Fishing line ok
	14:15	4	29	100	450				2			Carbon tube gets warm
	14:19	5	29	100	450				2			Red wire got warm
	14:22	6	29	100	450				2			
Friday 1/24/2014	14:29	7	29	100	450				3			
	Changed board to LED											
	14:55	8	29	100	450				3			2 LEDs blew, 3rd OK but lost plastic case
	Changed to Catalina tank											
	15:06	9	29	100	450				3			
	Changed to paper tube hot rocket tubing											
	15:14	10	29	100	450				3			
	Changed to tubes configuration											
	15:21	11	29	100	450				3			All tubes heated
	15:26	12	29	100	450				6			Tubes melted pretty bad
	15:29	13	29	100	450				10			Reached 950 K
	HOT-STATIC-1: Test installation plus beam alignment											
Tuesday 1/28/2014	13:28	7	63	100	280	15	0	3	5	530	400	2 tubes broke as soon as pressure turned on. Filename: 28T32838358
	HOT-STATIC-2: Replaced 2 inlet tubes, broke ceramic tubes further so does not blow hot gas on inlet + does not oscill											
	15:33	8	63	100	280	15	5	0	10	708	461	28_01_2014___15_33_56
	HOT-STATIC-3											
Wednesday 1/29/2014	15:47	1	30	100	933	35 (23 in 20 cm)	0	0	0.15			aiming shot, dT = 70K
	15:52	2	30	100	933	35 (23 in 20cm)	0	0.75	5	1707	900	[is it same HX as before?]

Table 43 - Tests conducted at the 100 kW, 95 GHz launch test facility between 1/12/2014 - 1/31/2014

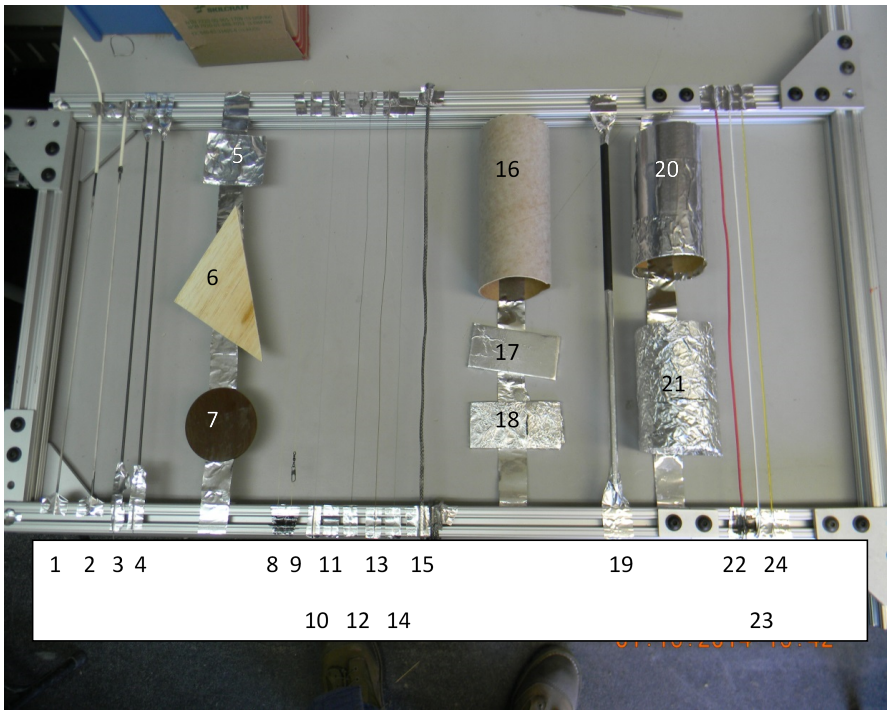

1. Heat exchanger tube with polyurethane flex tube
2. Heat exchanger tube with polyurethane flex tube and clamp
3. Silicone Carbide tube
4. Silicone Carbide tube
5. 3M 3380 Linered foil tape
6. Balsa with fiberglass coating, no cover
7. Vespel
8. Kevlar thread, size 23, (TEX 21), natural
9. Kevlar thread, size 23, (TEX 21), natural, with swivel
10. Rio Products trout tapered leader, heavy end, 7.5 ft, 5 lb
11. Rio Products trout tapered leader, thin end, 7.5 ft, 5 lb
12. Power Pro microfilament braid, 15 lb test
13. Rio Products, power flex wire bite, 0.016" dia, 20 lb test
14. Kevlar fly tying thread, spring green
15. Spectra rope on tower
16. Bare cardboard rocket tube
17. Balsa with fiberglass coating, covered with aluminum tape, one layer
18. Balsa with fiberglass coating, covered with aluminum foil, one layer left side, two layers right side.
19. Carbon Exacta #90529A Arrow top bare, bottom one layer aluminum tape
20. Cardboard rocket tube with one layer aluminum tape
21. Cardboard rocket tube with one layer aluminum foil top, two layers on bottom
22. 18 AWG red wire
23. 24 AWG white wire
24. 30 AWG yellow wire

Figure 118 – 24 January: Burn testing of various rocket components. Figure compiled by Greg Paulson.

Figure 119 - 24 January 1:57 pm: Burn testing of various rocket components. If the experiment were to be repeated, we recommend choosing a camera angle so that the sky is the background. The sky in this image is at 240 K whereas the hills are at 275 K. The bright line in the middle of the plywood triangle and Vespel disk is due to the metallic tape behind them reflecting the beam and intensifying the heating in that area. Source file: GOPR0112.MP4

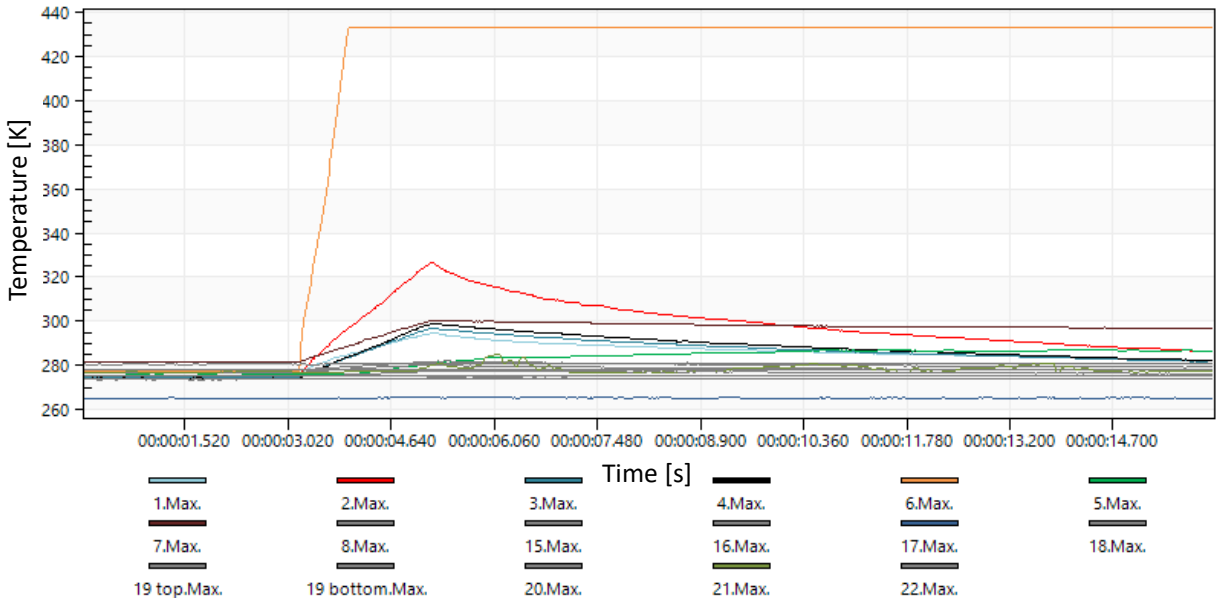

Figure 120 – 24 January 1:57 pm: Temperature history of various rocket components under high-power millimeter-wave illumination. Some items that were not visible against the background are not included. Those showing minimal heat are plotted in gray so that the other traces stand out. Both green traces are anomalous. The beam was not large enough to illuminate the whole board so we aimed 4-5 shots at different parts of the board. The traces shown here are for a beam aimed to the top left. Source file:

Figure 121 - 28 January 10:46 am: Setup of the first static heat exchanger test with beam. Source file: 28_01_2014___10_46_59.avi

Following the setup shown in Figure 121, the first and second static tests of the heat exchanger with beam and flow were carried out that afternoon at a distance of 63 meters from the beam director and achieved peak temperatures of <1,000 K. The next day, the heat exchanger was moved to 30 meters, increasing the power level from 15 kW to ~35 kW in a 30-cm diameter bucket (0.94 MW/m^2 intensity). The third static test with beam and flow was one of the most successful tests we carried out, with one of the best heat exchangers that we constructed. The beam was exactly centered, and the heat exchanger glowed brightly (Figure 122, Figure 124) with a peak temperature above 2,000 K (Figure 123). The tubes on the left were chosen for their low sheet resistance and those on the right for their high sheet resistance. The test established that lower was better, but either performed well enough.

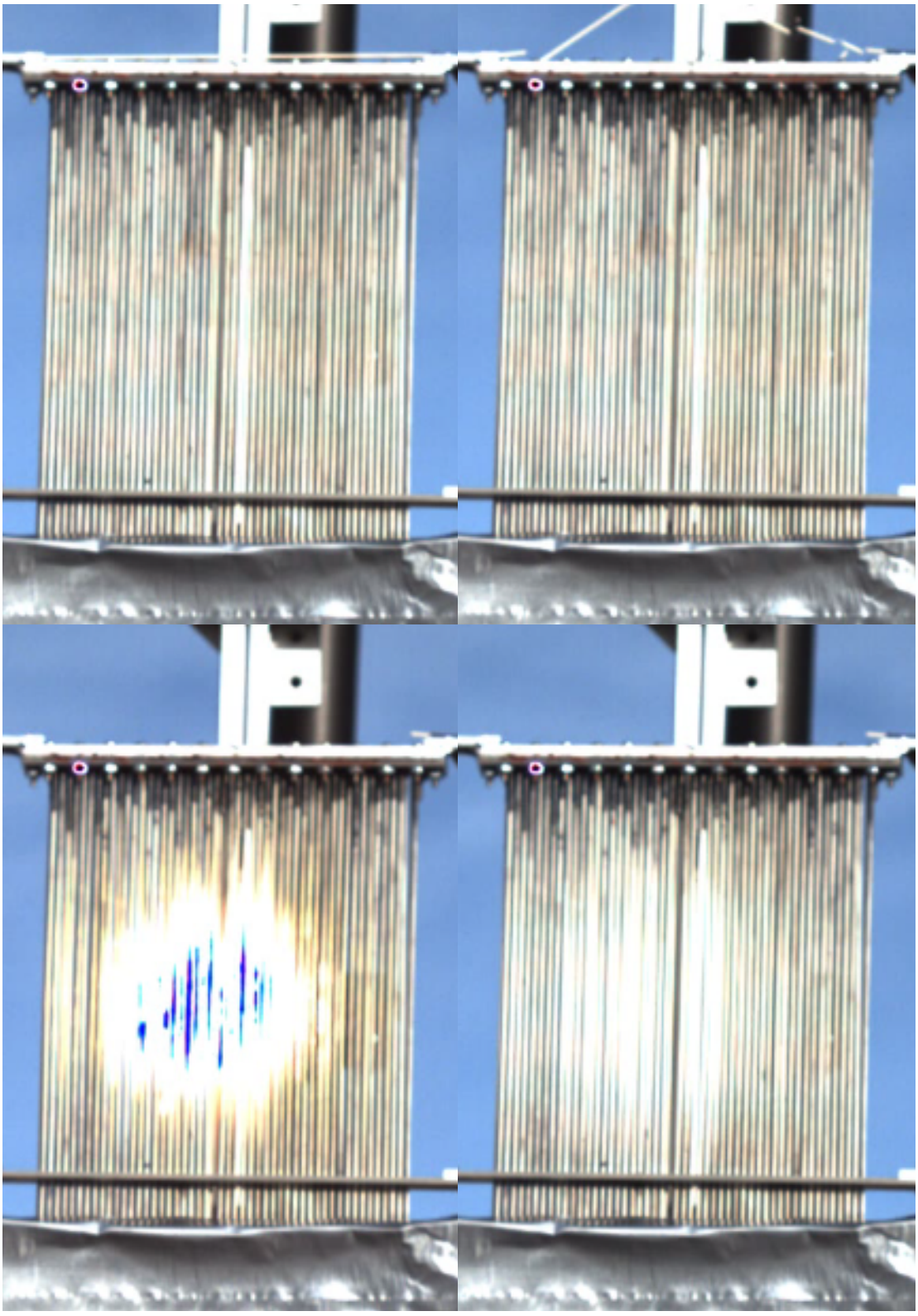

Figure 122 - 29 January 3:52 pm: 3rd static test of the heat exchanger with beam and flow. A tube is placed horizontally over the nozzle at the top of the heat exchanger (top left image) and fractures to indicate that flow has been initiated (top right image). Source file: 29_01_2014___15_52_56.avi

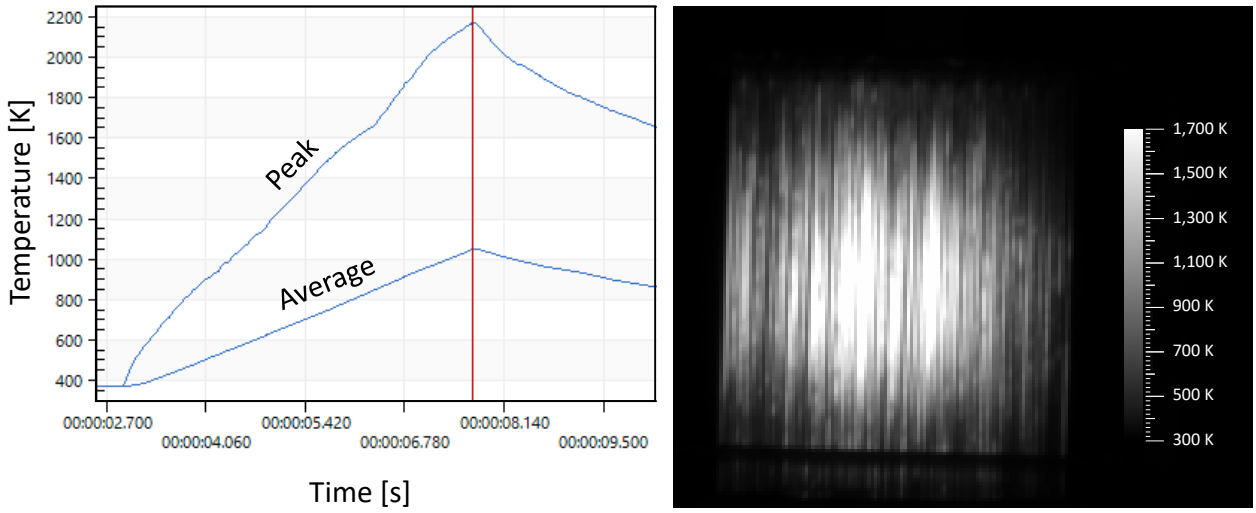

Figure 123 - 29 January 3:52 pm: 3rd static test of the heat exchanger with beam and flow. Left: Time series of temperature, peaking at above 2,000 K. Right: Temperature distribution of heat exchanger at t=7.74 sec, just prior to beam off. An emissivity of 0.65 is assumed. Source file: 2014-01-29T155244930.fcf

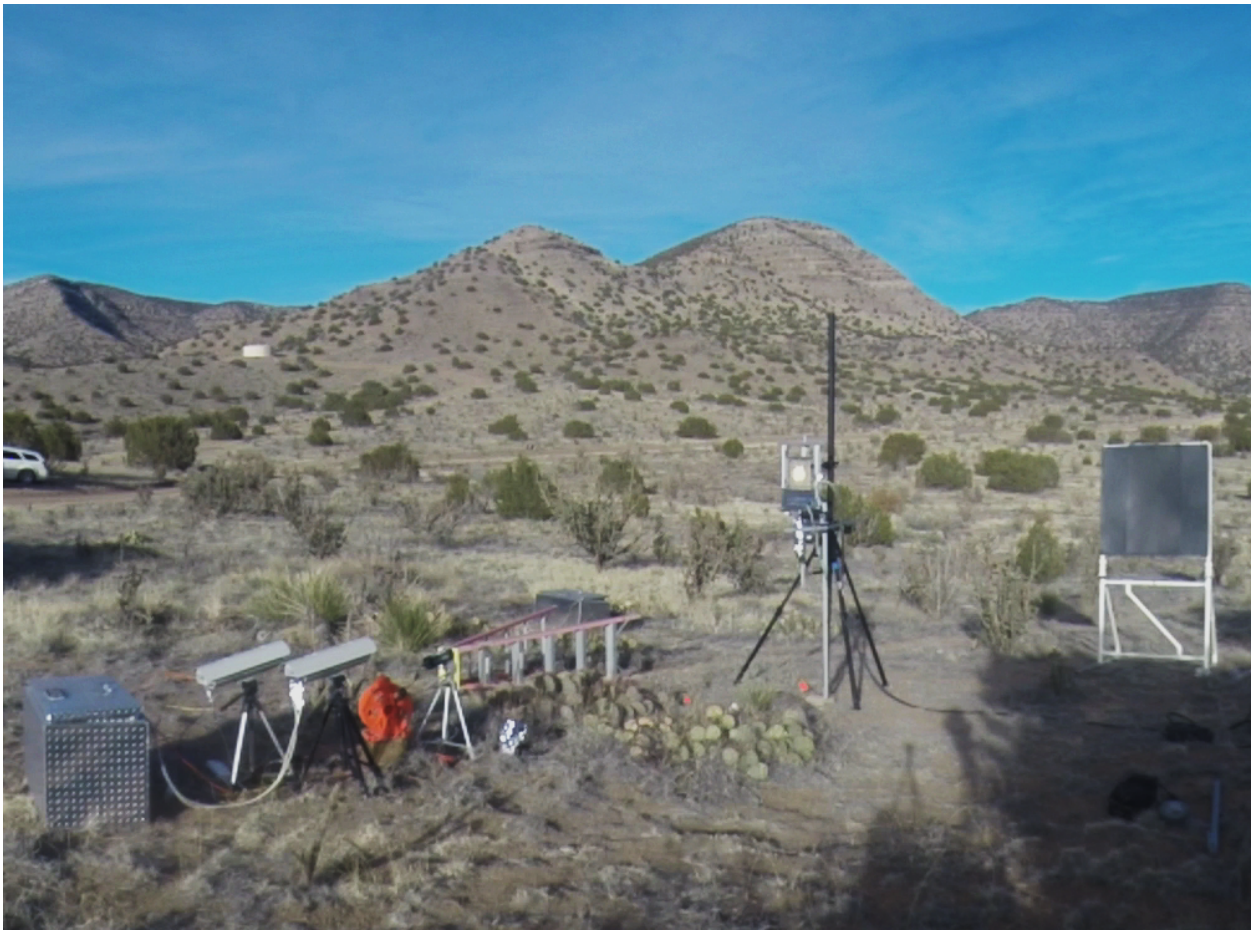

Figure 124 - 29 January 3:52 pm: 3rd static test of the heat exchanger with beam and flow. The heat exchanger visibly glows white hot despite strong illumination from the sun and is recorded in visible and LWIR wavelengths by the cameras on the left. Source file: GOPR0176.MP4

Assuming an emissivity of 0.65, the peak temperature in Figure 123 is 2,172 K. This presents an apparent impossibility, as the melting temperature of mullite is 2,110 K. Even if the melting temperature is not this value, the emissivity itself is deduced from a test shown in Figure 102 of §5.1.2.2.3 in which two tubes of the same type as those used here melt in the center. Thus, regardless of the value of the melting temperature, the radiance measured in the relevant pixels of the LWIR camera is higher in this case, indicating that the tube(s) in those pixels should be melting.

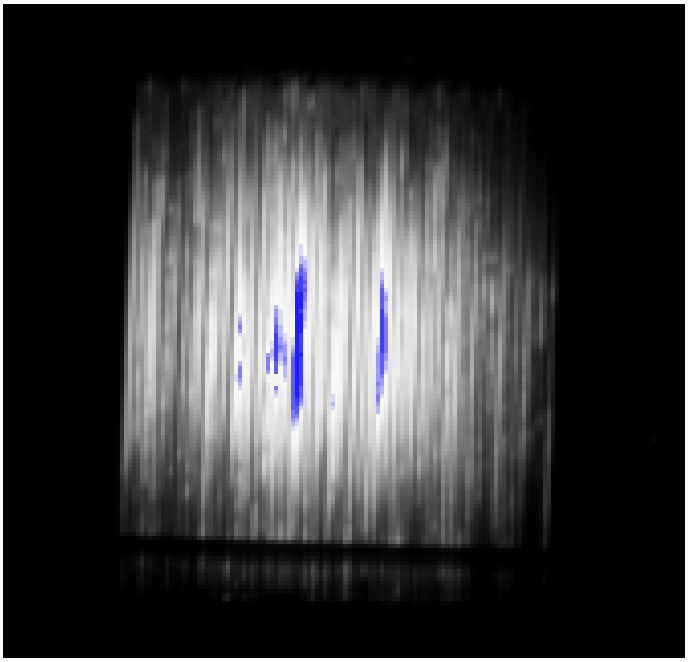

Figure 125 - 29 January 3:52 pm: Third static test of the heat exchanger with beam and flow. Temperature distribution of heat exchanger at t=7.74 sec, just prior to beam off. Temperatures above 1,900 K are colored in blue. Source file: 2014-01-29T155244930.fcf

Figure 125 is similar to Figure 123 except that it shows the very hottest tubes at temperatures above 1,900 K as blue. These correspond to the most luminous tubes in the visible spectrum in Figure 122. In this figure, the brightest tubes are also colored blue because they are saturating the image sensor in the camera despite bright daylight conditions. The hottest tube on the left of the LWIR image in Figure 125 corresponds to the hottest tube in the visible spectrum image.

The temperature of the heat exchanger prior to the experiment is measured by the LWIR camera as ~300 K, hence the reflected sunlight from the heat exchanger is not a significant source of experimental error. Another difference between this arrangement and the MTU arrangement is that the tubes are oriented vertically in this case, as opposed to horizontally in the MTU. Hence, a melting tube may not obviously bend. However, our experience in melting many tubes in the 2.45 GHz resonator experiments of 2005-2006 is that melting tubes first attain the consistency of bubble gum and blow bubbles if under internal pressure. Bubbles would have left holes in the heat exchanger (there were none). Another possibility is that a surface plasma formed and contributed to the radiance. Despite this, we think it most likely that the decreased separation between the tubes increased the effective emissivity as reflections were introduced and the arrangement tended toward a blackbody cavity. This effect would need to be quantified in future work to make LWIR temperature measurements to within about 100 K of the true value.

5.2.1.4 2/17/2014 - 2/28/2014 test campaign at 100 kW, 95 GHz launch test facility

Date	Time	Run #	Distance [m]	Beam characteristics: Power level [%]	Peak intensity [kW/m^2]	power in 30 cm diameter [kW]	Shot duration [s]: pre heat [s]	delay	total	Temp. [K]: Max. (ε=0.95)	Mean (ε=0.95)	Comments
Tuesday 2/18/2014	COLD-LAUNCH-2 beamless launch primarily to test LED tracking system											
Wednesday 2/19/2014	COLD-LAUNCH-3 beamless launch											
	10:05											Cold gas launch misfire
	11:16											Cold gas launch, parachute failure
Thursday 2/20/2014	HOT-STATIC-4											
	14:06	6	50	100	572	26.9	4	0	8	1150	660	Tubes on left are slightly different to those on right. 2 tubes broke, middle one, one snapped at crimp.
	HOT-STATIC-5: Fix the HX, cut off 2 tubes and put aluminum plate to prevent broken tube to break shielding											
	15:06	7	50	25	143	6.725			0.25			Adjustment shot. Ok dead on
	15:16	8	50	100	572	26.9	4	0	8	1375	868	Flow transports heat upward and smooths the temperature distribution. Puff of smoke.
Monday 2/24/2014	COLD-LAUNCH-AXIAL-1: First launch of axial-engaged rocket without beam											
	16:36	1										Cleared rail. Parachute did not deploy
Tuesday 2/25/2014	COLD-LAUNCH-4											
		4										Tangled parachute
	HOT-LAUNCH-1: First side-engaged launch with beam											
		5	40	100	710	33			0.25			adjustment shot
	15:01	6	40	100	710	33			?			Reached top of rail and fell back
Wednesday 2/26/2014	COLD-STATIC-4: (1/16" orifice)											
												4 tubes rerouted, not very middle,
	10:33	0	40									Thrust equivalent to ~4.8 kg
	Beam polarization tests											
	11:+	1	40	50	355	16.5			0.25			graphene = second group(?)
		2	40	50	355	16.5			0.25			
		3	40	100	710	33			1			
	Changed orientation											
		4	40	50	355	16.5			0.25			
	Added aluminum tape to cover reflections											
		5	40	50	355	16.5			0.25			
		6	40									NO SHOT
		7	40	100	710	33			1			
	Switch to HOT-STATIC-6 static test (1/16" orifice)											
												Epoxy from Bruccoleri is creating hot
	13:59	8	40	50	355	16.5			0.25			spot slightly left
	14:04	9	40	50	355	16.5			0.25			Beam alignment improved
	14:08	10	40	100	710	33	3 s or 1000 K		6			Small flame from epoxy
	Switch to COLD-STATIC-5 test of 3/32" orifice											
	15:15+	11	40									
	Switch to HOT-STATIC-7 (3/32" orifice)											
	15:50+	12	40	50	355	16.5			0.25			too high
		13	40	50	355	16.5			0.25			right on
		14	40	50	355	16.5	3 s or 1000 K		6			

Table 44 - Tests conducted at the 100 kW, 95 GHz launch test facility between 2/17/2014 - 2/28/2014, 1 of 2

Date	Time	Run #	Distance [m]	Beam characteristics: Power level [%]	Peak intensity [kW/m^2]	power in 30 cm diameter [kW]	Shot duration [s]: pre heat [s]	delay	total	Temp. [K]: Max. (ε=0.95)	Mean (ε=0.95)	Comments
	Switch to HOT-LAUNCH-2 (3/32" orifice)											
	8:46	2	40	50	355	16.5			0.25			saw nothing
	9:06	3	40	50	355	16.5			0.25			saw nothing
	9:08	4	40	50	355	16.5			0.25			too much right
	9:09	5	40	50	355	16.5			0.25			OK
	Readjustment											
	10:13	13	40	100	710	33	3 s or 1000 K		6			2014-02-28T101026644, GOPR0228.MP4
	Switch to HOT-LAUNCH-3 (1/8" orifice)											
	11:21	14	40	50	355	16.5			0.25			Calibration shots
	11:23	15	40	50	355	16.5			0.25			
Friday 2/28/2014	11:28	16	40	50	355	16.5			0.25			Beam center but tubes on the left are hot. Uniformity of absorption is poor.
	11:30	17	40	50	355	16.5			0.25			
	11:31	18	40	50	355	16.5			0.25			
	Put crumpled foil on left fin											
	11:38	19	40	50	355	16.5			0.25			
	Put crumpled foil on both fins. Tape put on side of tube to cover hot spot											
	12:43	22	40	100	710	33	3 s or 1000 K		7			2014-02-28T124424658, 28_02_2014___14_11_36.avi
	Switch to HOT-LAUNCH-AXIAL-1: ZIA-2-10A first launch with beam											
	15:59	23	1.4 mm orifice. 0.3 mm nozzle gap. N2 propellant at 4.5 ksi. graphite inlet manifold (2014-02-28T155814817.fcf)									Survived first hot run; hung up on rail;
	HOT-LAUNCH-AXIAL-2: ZIA-2-10A launch test with beam											
	16:36	24	1.4 mm orifice. 0.3 mm nozzle gap. N2 propellant at 4.5 ksi. hung up on rail; graphite inlet manifold. (28_02_2014___16_36_18.avi)									Failed on 2nd run when valve opened;

Table 45 - Tests conducted at the 100 kW, 95 GHz launch test facility between 2/17/2014 - 2/28/2014, 2 of 2

Figure 126 – 18 February 1 pm: Alex Bruccoleri (Izentis) arms a rocket for launch without the beam. Source file: 18_02_2014___15_41_48.avi

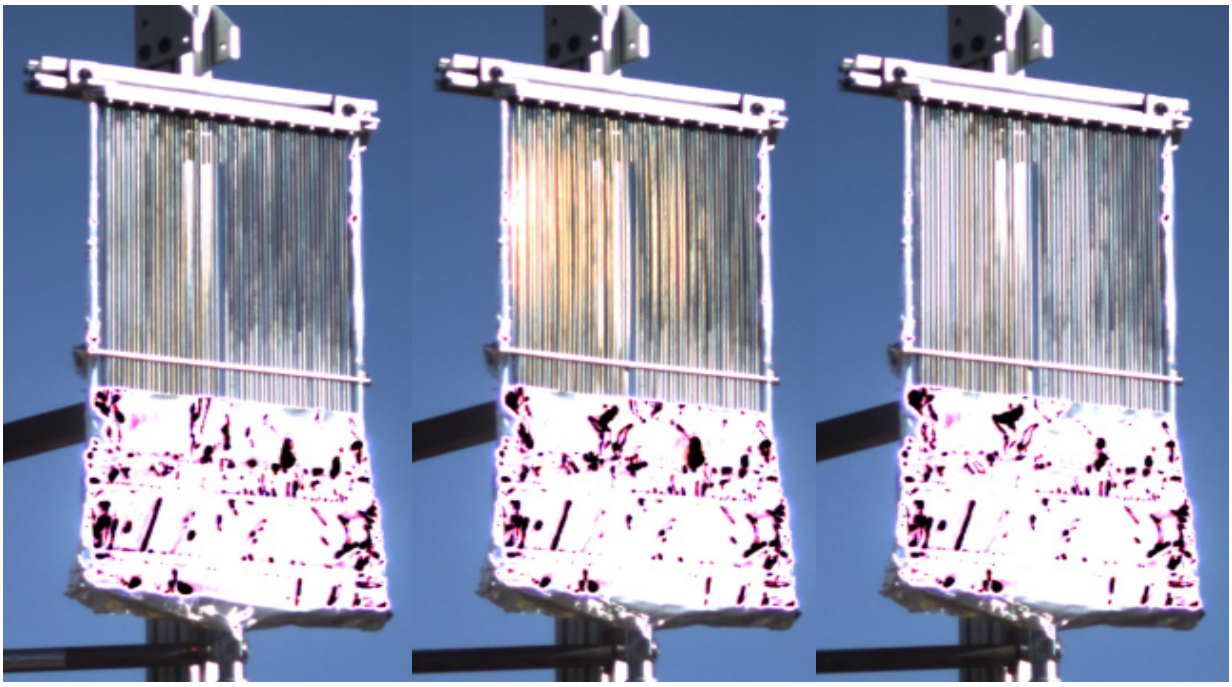

Figure 127 - Run #2 on 20 February 3:22 pm: A left to right sequence showing before, during and after a static test with flow and beam. Source file: 20_02_2014___15_22_39.avi

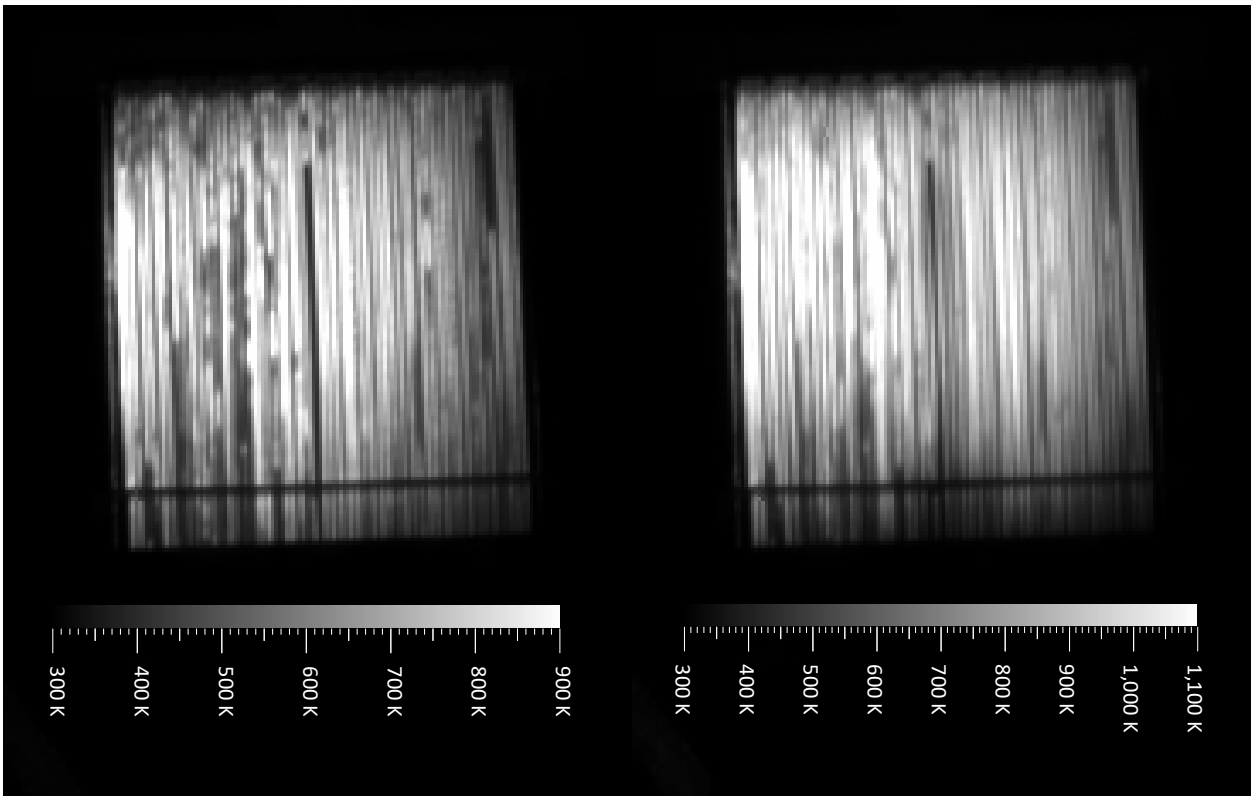

Figure 128 - Run #2 on 20 February 3:22 pm: Static test with flow and beam. At a range of 50 meters, 26 kW radiates into a 30-cm diameter bucket centered on the heat exchanger, achieving a peak incident intensity of 57 W/cm^2. LWIR footage is shown on the bottom left at t=13.08 sec, just prior to flow on, and on the bottom right at t=17.20 sec, just prior to beam off. Source file: 2014-02-20T152221544.fcf

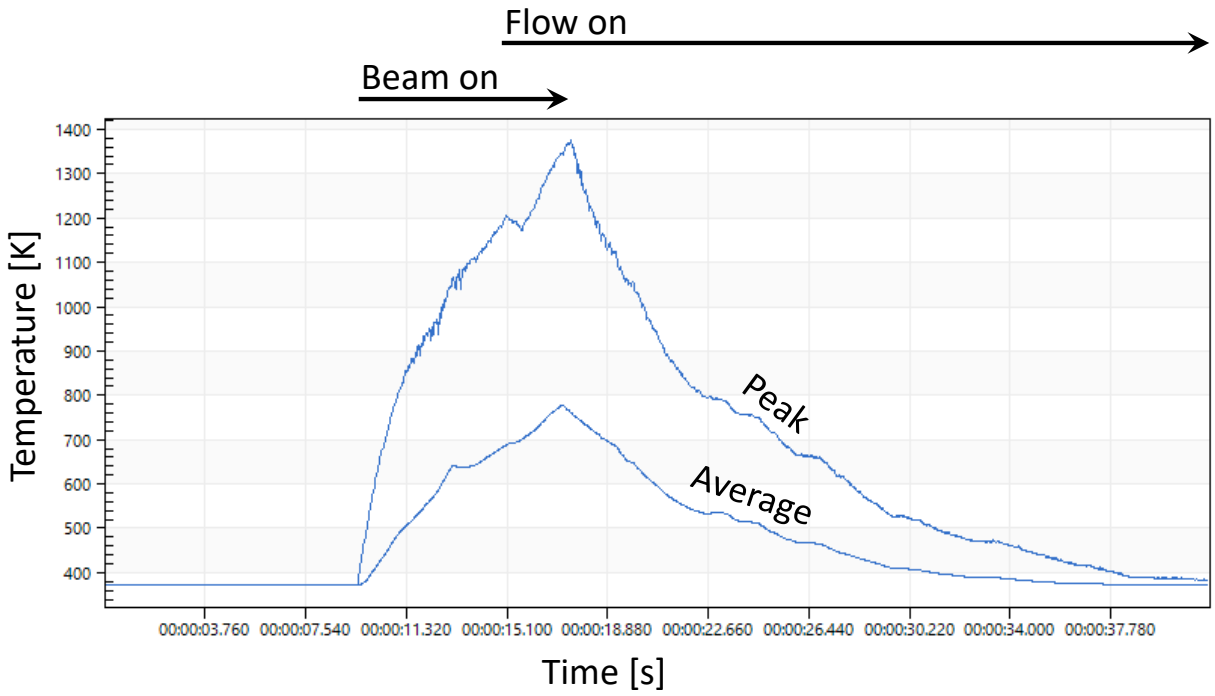

Figure 129 – Run #2 on 20 February 3:22 pm: Static test with flow and beam. The flow is initiated as the peak heat exchanger temperature rises past 1,000 K. Source file: 2014-02-20T152221544.fcf

Figure 130 – 24 February 6:44 am: The LTI Zia-1 axial-illuminated rocket mounted on the launch rail. Source file: IMG_0865.JPG

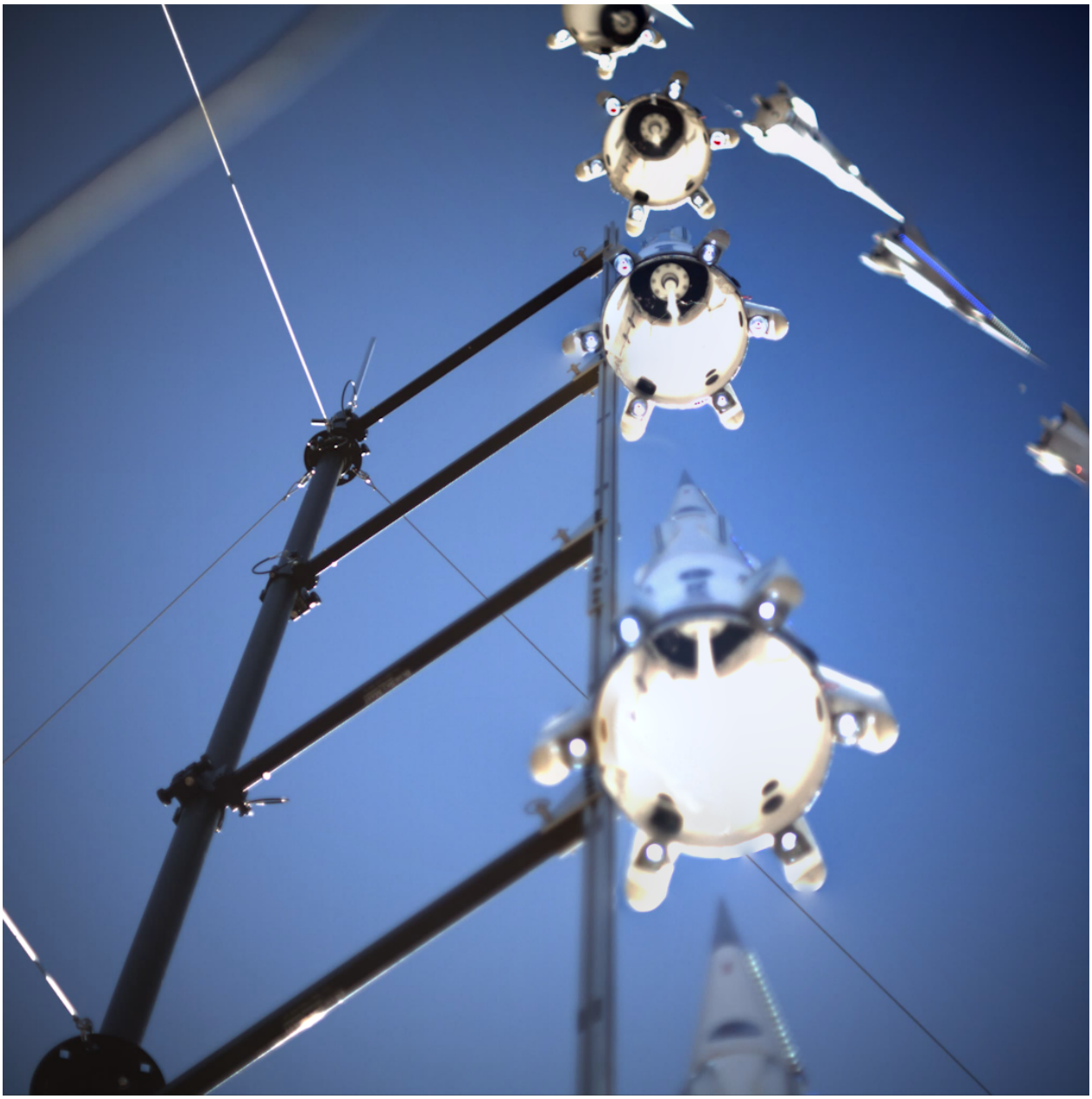

Figure 131 – 24 February 4:36 pm: The first launch of the LTI axial-illuminated rocket without beam. The montage shows the argon plume and tracking lights of the rocket. All such launches used argon as a propellant to maximize thrust. The rocket turned sharply after departing the launch rail. A later LTI swing test affirmed that the rocket was stable regardless of a moment change due to the missing heat exchanger, thus LTI concluded that the crosswind was strong. The parachute failed to deploy in this test, which is one reason why such tests are conducted prior to risking a heat exchanger. Source file: 24_02_2014___16_36_18.avi

Figure 132 - 25 February 11:17 am: A rocket launches without the beam to test the tracking of the green LEDs (visible in the image) and the ability to use this signal to drive the pan-tilt unit of the beam director. As the rocket ascends the launch rail, its fins hit the mechanism that opens the rocket flow valve and is damaged. Thereafter, the parachute deploys but is caught in the tether. The purpose of the tether is to pull the parachute deployment pin if the rocket rises past its altitude ceiling. Source file: GOPR0216.MP4

Figure 133 – 25 February 3:01 pm, run #6: The first launch of a millimeter-wave beam powered rocket. The heat exchanger begins to glow prior to liftoff, however the rocket does not clear the rail and the heat exchanger is destroyed when the rocket hits an obstacle as it falls back down the rail. Source file: 25_02_2014___15_01_21.avi (also seen in GOPR0218.mp4)

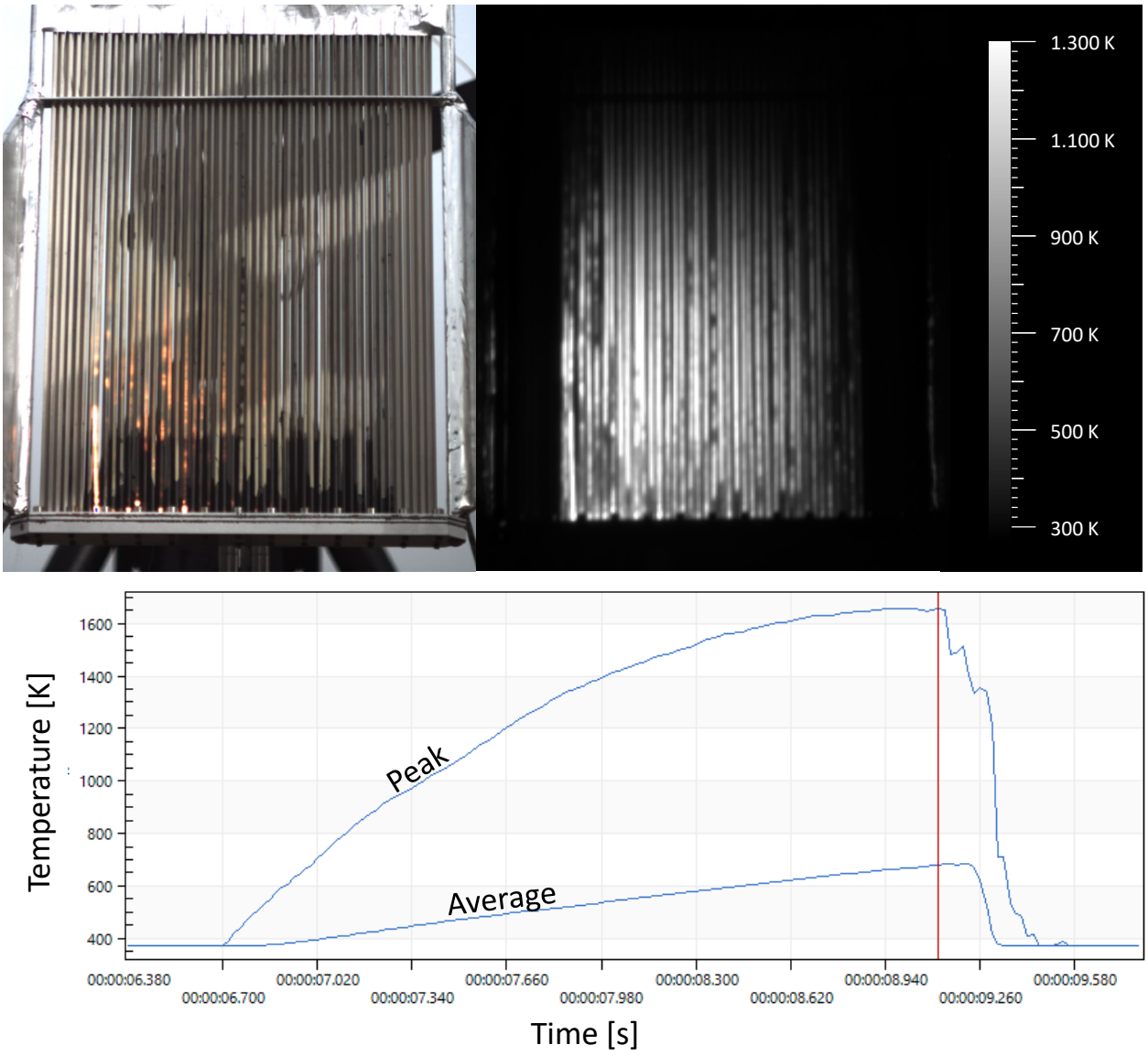

Figure 134 – 25 February 3:01 pm, run #6: The first launch of a millimeter-wave beam powered rocket. Top left: Frame just prior to flow initiation. Top right: Frame from LWIR dataset just prior to flow initiation. Bottom: Temperature time history from the LWIR dataset. An emissivity of 0.65 is assumed for the tubes, yielding a peak temperature of 1,650 K. The images are taken at the time indicated by the vertical red line in the temperature time history. Source files: 25_02_2014___15_01_21.avi and 2014-02-25T150105944.fcf

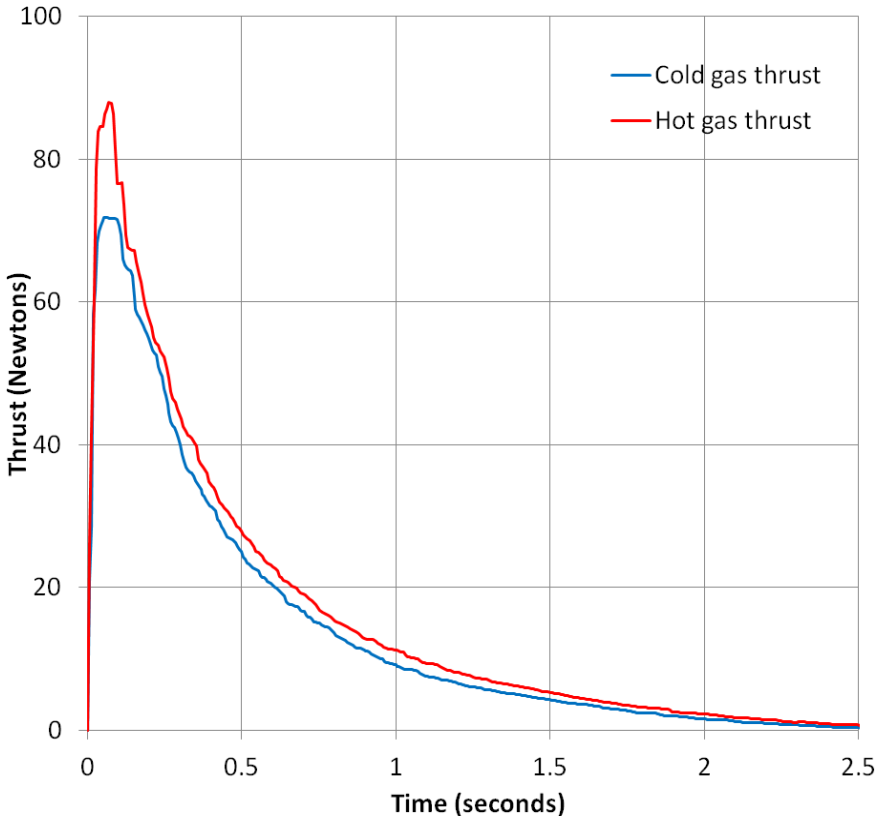

Figure 135 – 26 February: Calibrated load cell measurements showing static thrust vs time for the heat exchanger with and without the beam turned on.

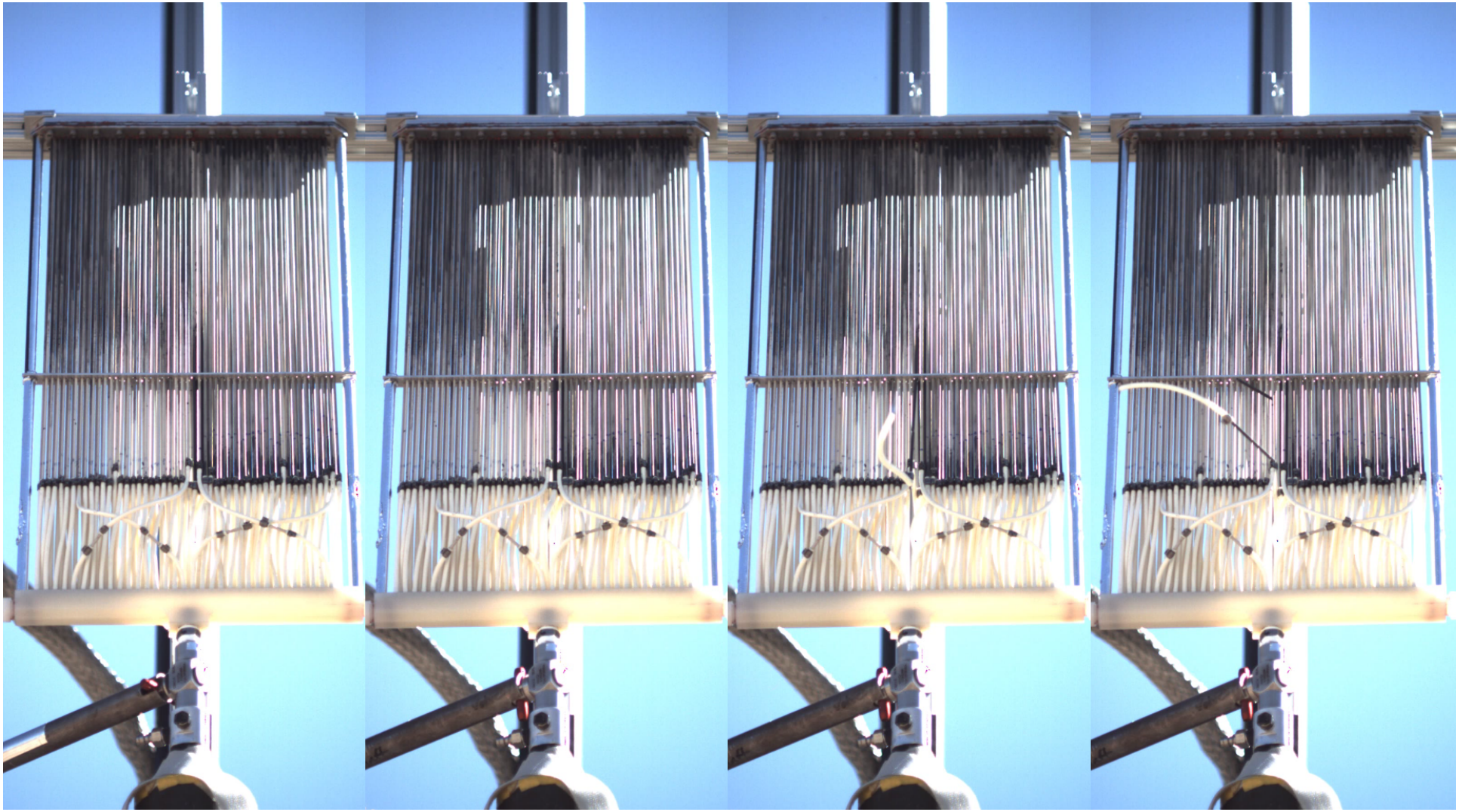

Figure 136 – 26 February 10:34 am: A left to right sequence of images from a static test without beam using a 1/16" orifice. A tube is blown out shortly after the flow valve is opened. The first frame (left) is prior to valve opening. The next is just after the valve is opened, as seen from the valve position in the images. The next frame shows a flexible inlet tube that is blown out, and the final frame shows that the inertia snaps the attached Omegatite 200 tube and both depart to the left. Source file: 26_02_2014___10_34_49.avi

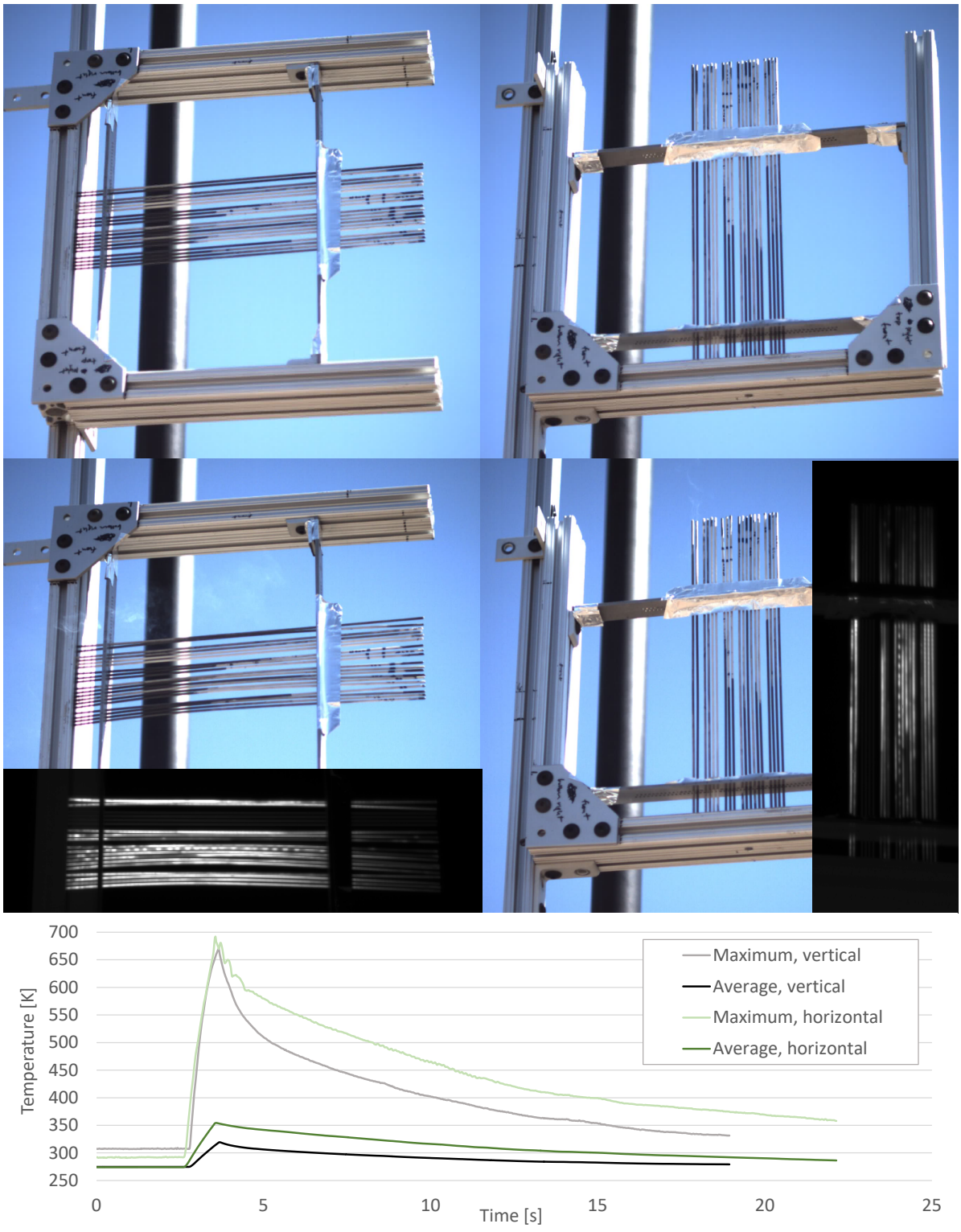

Figure 137 – 26 February 11:20 am: Polarization effect tests. Pictures on the top are before the beam is turned on and pictures on the bottom are during maximum temperature due to the beam. Horizontal deformation is more apparent due to angle of camera. Vertical deflection is inferred from the change of sun shadowing at the top of the tubes. Infrared images are shown in their corresponding frames at a temperature scale of 200-600 K. The graph at the bottom shows LWIR temperatures. Source files: 26_02_2014___11_23_36.avi and 26_02_2014___11_51_50.avi

Based on Figure 137, the effect of heat exchanger orientation on absorption is inconclusive. The average values shown in the bottom graph indicate better performance with horizontal tubes, but the average is derived from the pixels in a box drawn within the FLIR ResearchIR software, and the size of this box may not be the same due to differences in perspective caused by different camera angles between the two cases. Additionally, the beam is not necessarily well aligned in both cases.

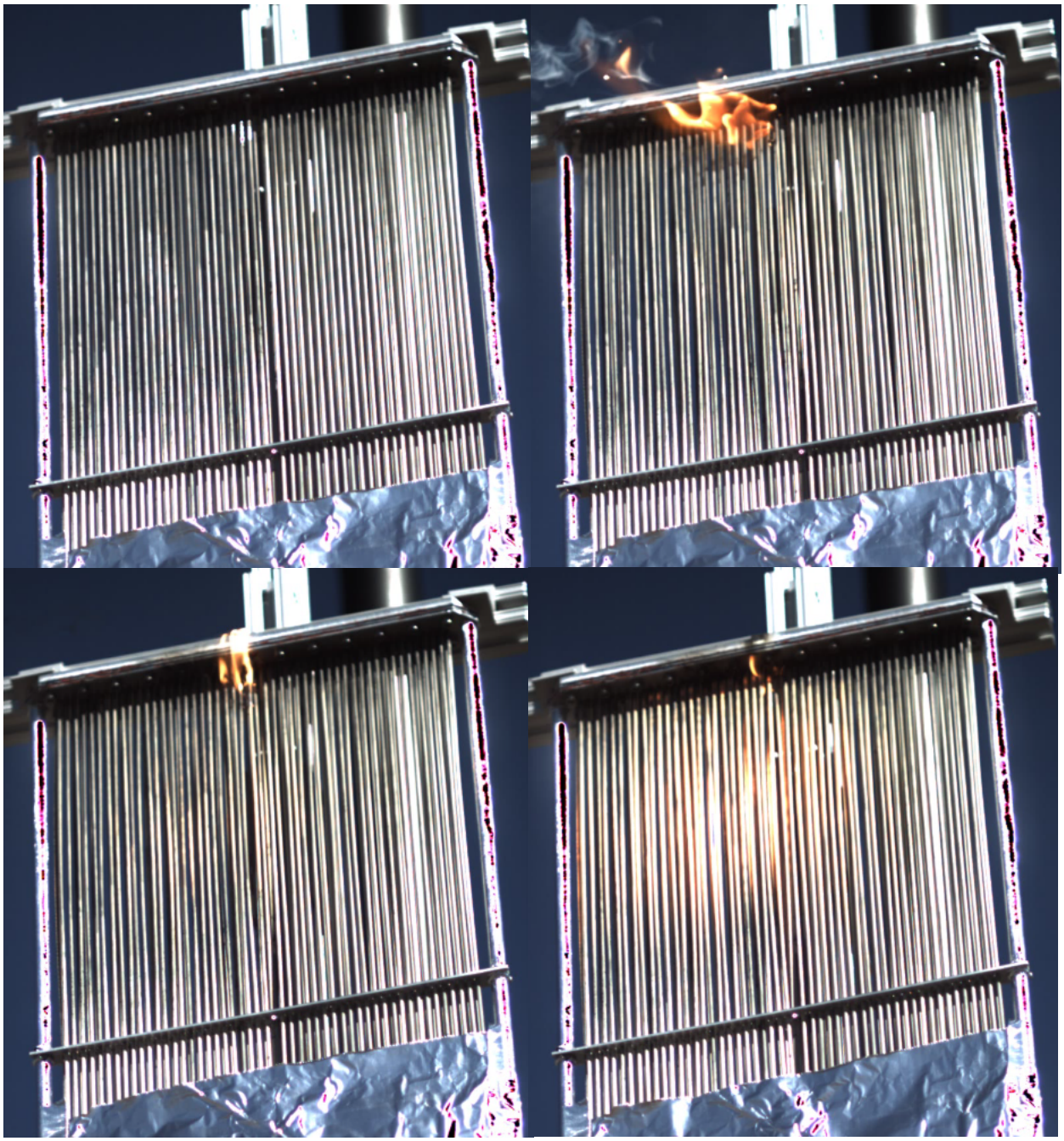

Figure 138 – 26 February 2:08 pm, run #8: Test with flow (1/16" orifice) and beam at a range of 40 meters and power of 33 kW in a 30-cm diameter bucket. Flame erupts from some residual epoxy used to plug a leak where an earlier tube was broken, but the remaining tubes are unaffected. The heat exchanger achieves good uniformity and high temperature, though the contrast in these images is poor due to the bright sunlight. Frame exposure time is reduced to compensate, which is why the sky appears dark. Source file: 26_02_2014___14_08_15.avi

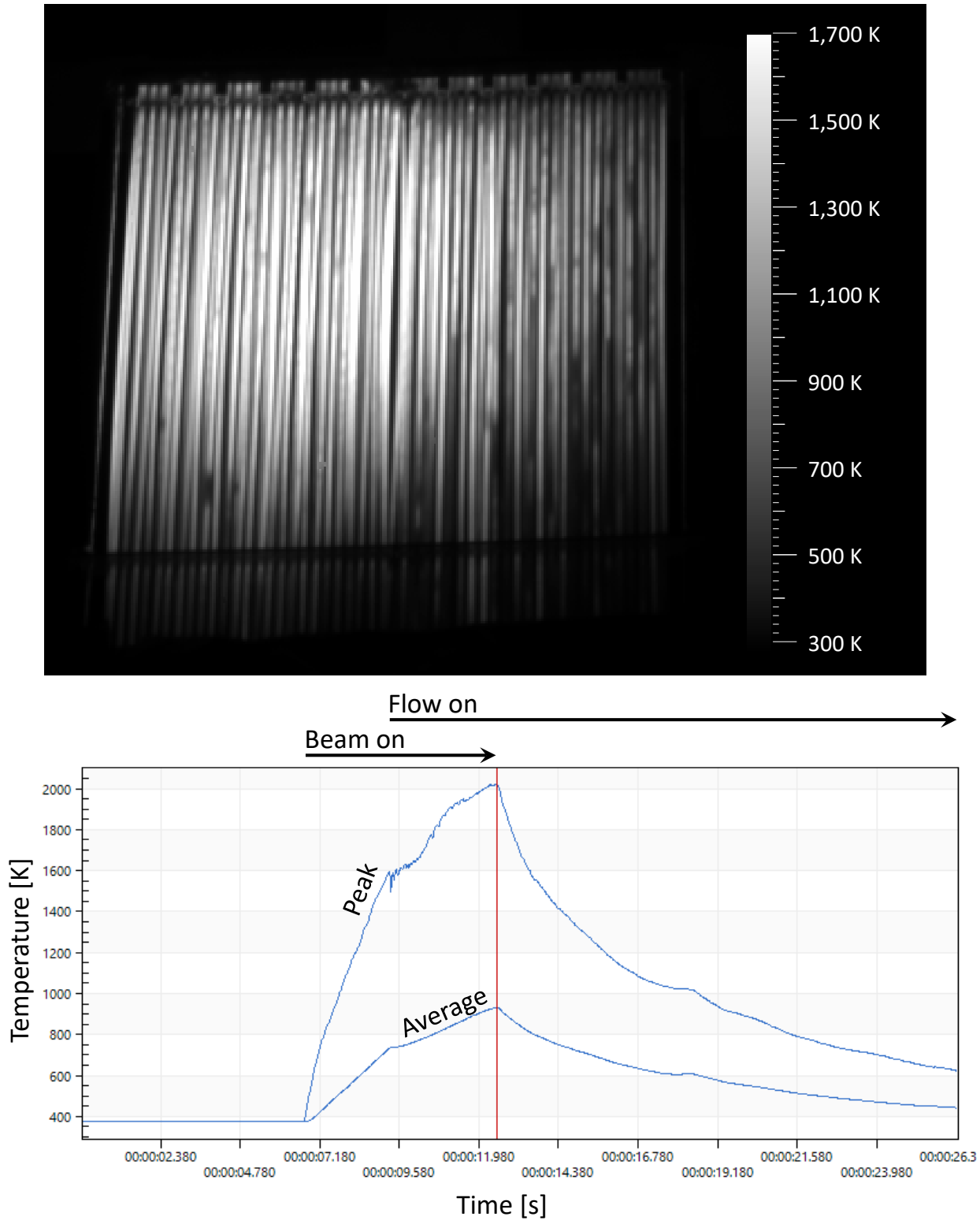

Figure 139 - 26 February 2:08 pm, run #8: Test with flow (1/16" orifice) and beam at a range of 40 meters and power of 33 kW in a 30-cm diameter bucket. An emissivity of 0.65 is assumed for the tubes, yielding a peak temperature of 2,000 K. The upper thermal image is taken at the time indicated by the vertical red line in the temperature time history. Source file: 2014-02-26T140806099.fcf

Figure 140 – 26 February 2:08 pm, run #8: Test with flow (1/16" orifice) and beam at a range of 40 meters and power of 33 kW in a 30-cm diameter bucket. The heat exchanger reaches peak brightness as seen from the back. Source file: GOPR0226.MP4

Figure 141 – 26 February 4:07 pm, run #14: Static test with flow (3/32" orifice) and beam. No epoxy fire in this test and the beam is better aligned. However, in the video, vibrations from the valve action reveal that several tubes on the far right of the heat exchanger are no longer attached to the outlet manifold. Source file: 26_02_2014___16_07_44.avi

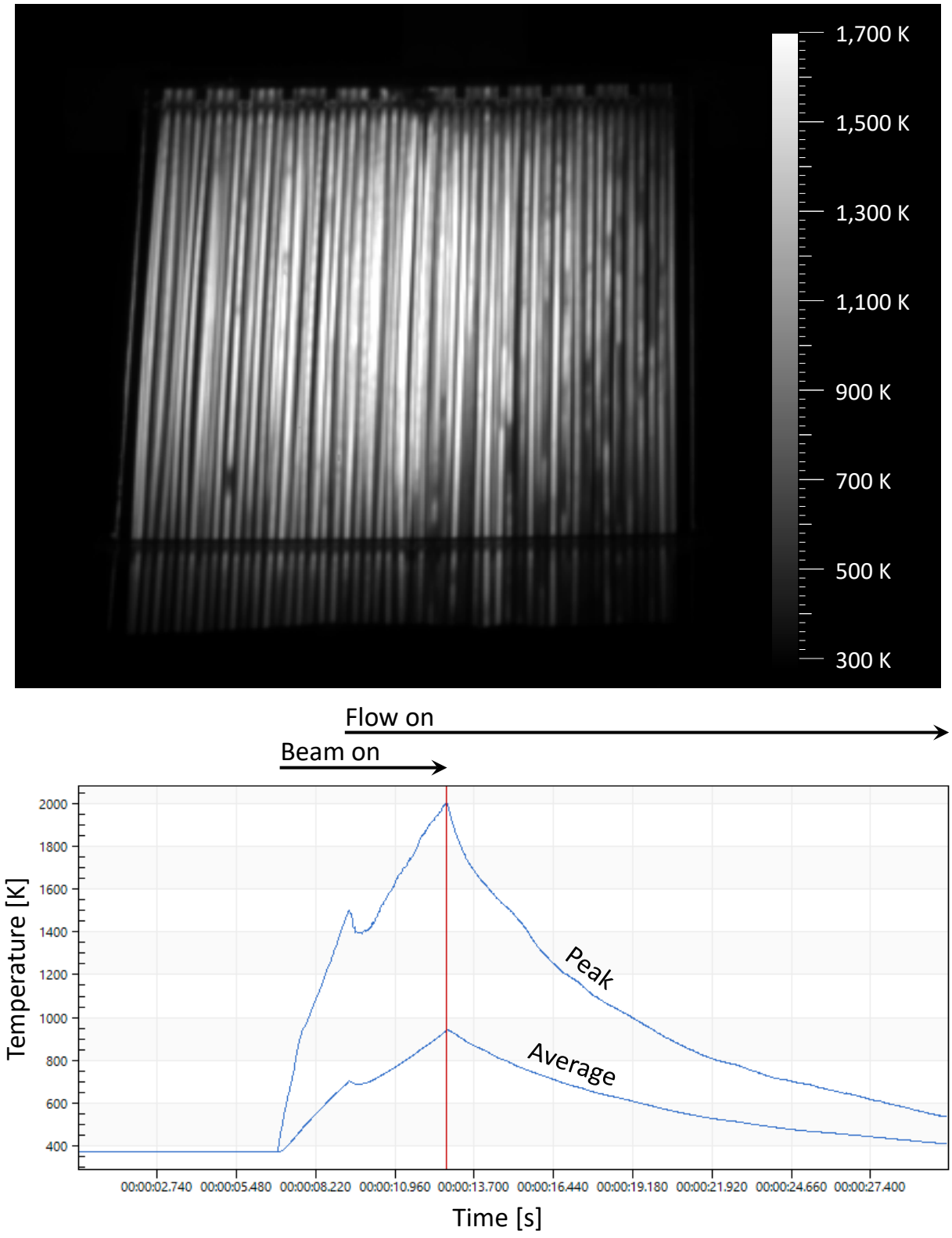

Figure 142 - 26 February 4:07 pm, run #14: Static test with flow (3/32" orifice) and beam. Thermal image of static hot gas test from dataset. An emissivity of 0.65 is used for the tubes, yielding a peak temperature of 2,000 K. The image is at the time indicated by the vertical red line in the temperature time history. Source file: 2014-02-26T160720695.fcf

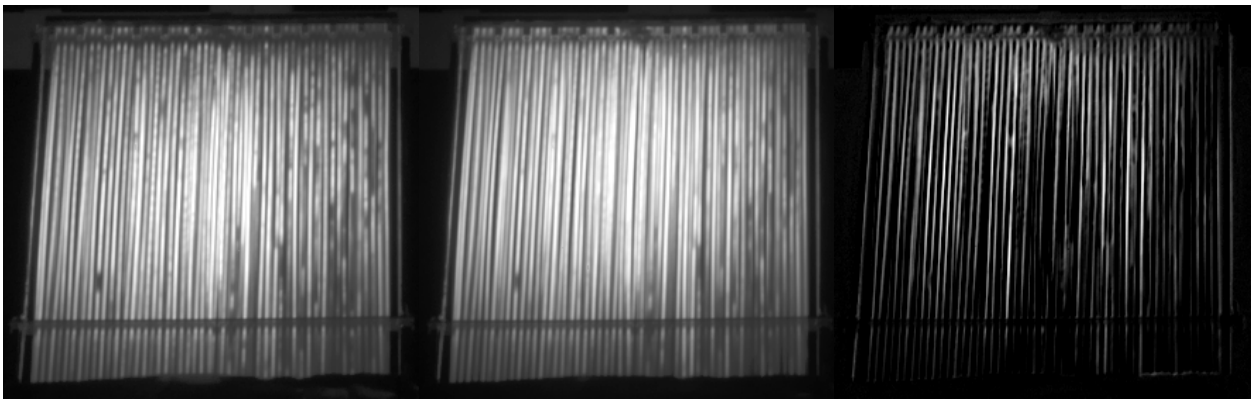

frame prior to flow on (t = 9.32 s) | frame prior to beam off (t = 12.76 s) | subtraction

Figure 143 – 26 February 4:07 pm, run #14: Static test with flow (3/32" orifice) and beam. Change in relative temperature distribution in the heat exchanger caused by energy transport via fluid flow. This change in the distribution is visible in the video but harder to show between static frames. To do this, the frame just prior to turning the flow on is subtracted from the frame just prior to turning the beam off, in which the flow has had time to affect the temperature distribution. The two are frames histogram equalized to isolate the just the effect of the flow, and not the additional heating between the two frames. Source file: 2014-02-26T160720695.fcf

The subtraction shown in Figure 143 shows that the fluid, entering the heat exchanger from the bottom and pushing upwards, is also transporting tube heat from bottom to top. This behavior was experimentally observed in earlier work (Parkin 2006c) and is used as a quick confirmation of the effectiveness of the convective heat transfer from the tubes into the working fluid. In this case, the convective heat transfer is not very effective; otherwise, the hottest area in the image would be the top ends of the tubes, and not toward the center.

Surprisingly poor heat transfer is already identified in the earlier static thrust measurements. The next step is to compare these experimental results with the prediction of the heat exchanger model given in §3.5.3.1 to diagnose the source of this poor performance. This work is not peculiar to gyrotron heating and can be carried out at much lower cost using the hot jet static test facility described in §4.4.

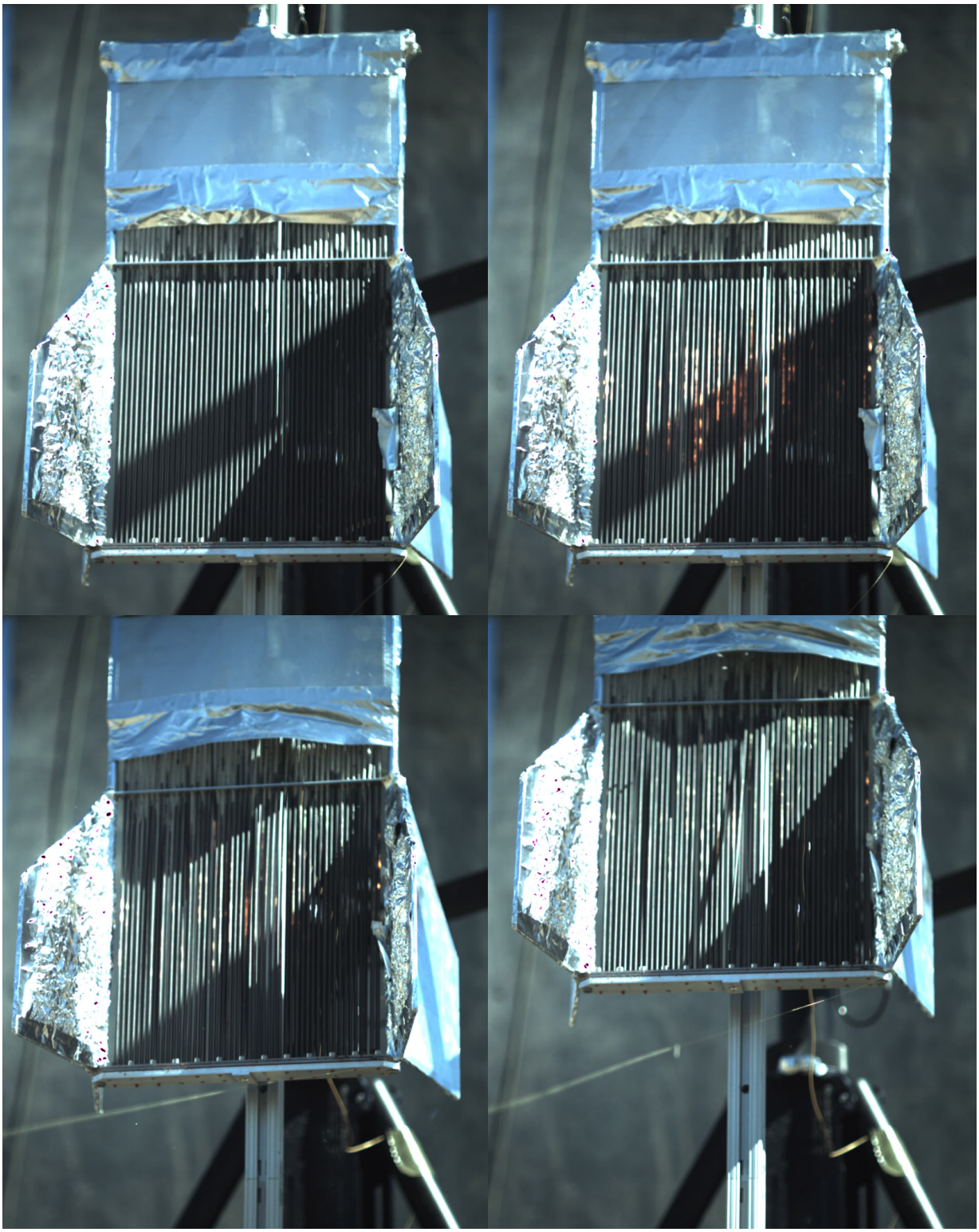

Figure 144 – 28 February 12:48 pm, run #22: Third Launch with beam. The beam pre-heats the heat exchanger (top two frames), then the propellant flow starts and the rocket accelerates (bottom two frames). However, the foil is a clue that tubes have ruptured, and close examination of the video shows this. The larger 1/8" orifice provides insufficient impulse for the rocket to clear the launch rail, so it falls back to the starting position (not shown). Source file: 28_02_2014___14_11_36.avi

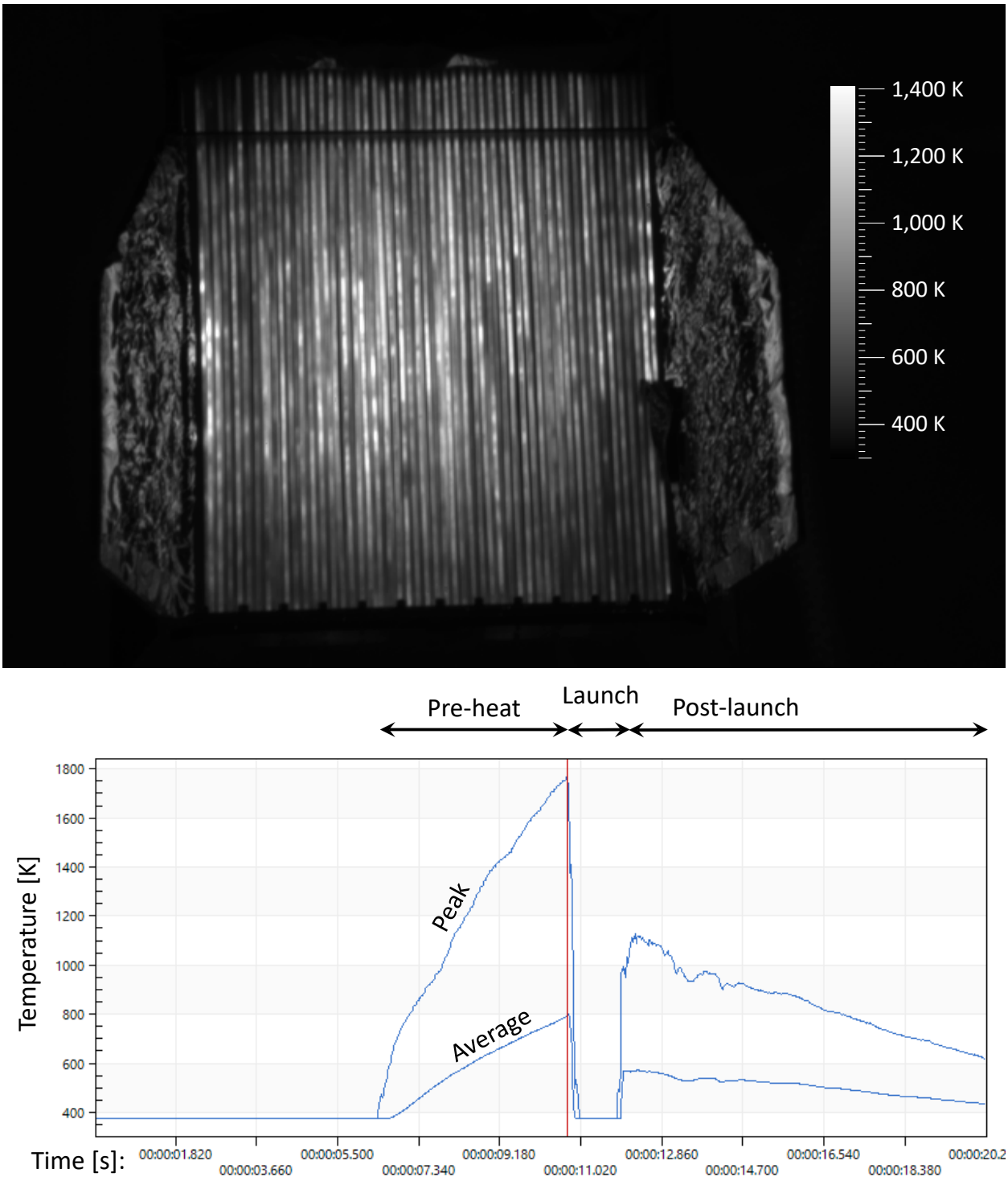

Figure 145 – 28 February 12:48 pm, run #22: Third Launch with beam. Based on LWIR data, the temperature peaks at 1,773 K immediately prior to launch, assuming a tube emissivity of 0.65. The peak temperature is mostly driven by hotspots and for the most part, the tubes are below 1,000 K. This image illustrates the problem of achieving a uniform coating for hastily prepared tubes. These tubes were graphite-coated on the interior and exterior, and it was expected that high-temperature operation would burn off the exterior coating very quickly during use. It turns out this was the final opportunity to launch the axial-illuminated rocket.. Source file: 2014-02-28T124424658.fcf

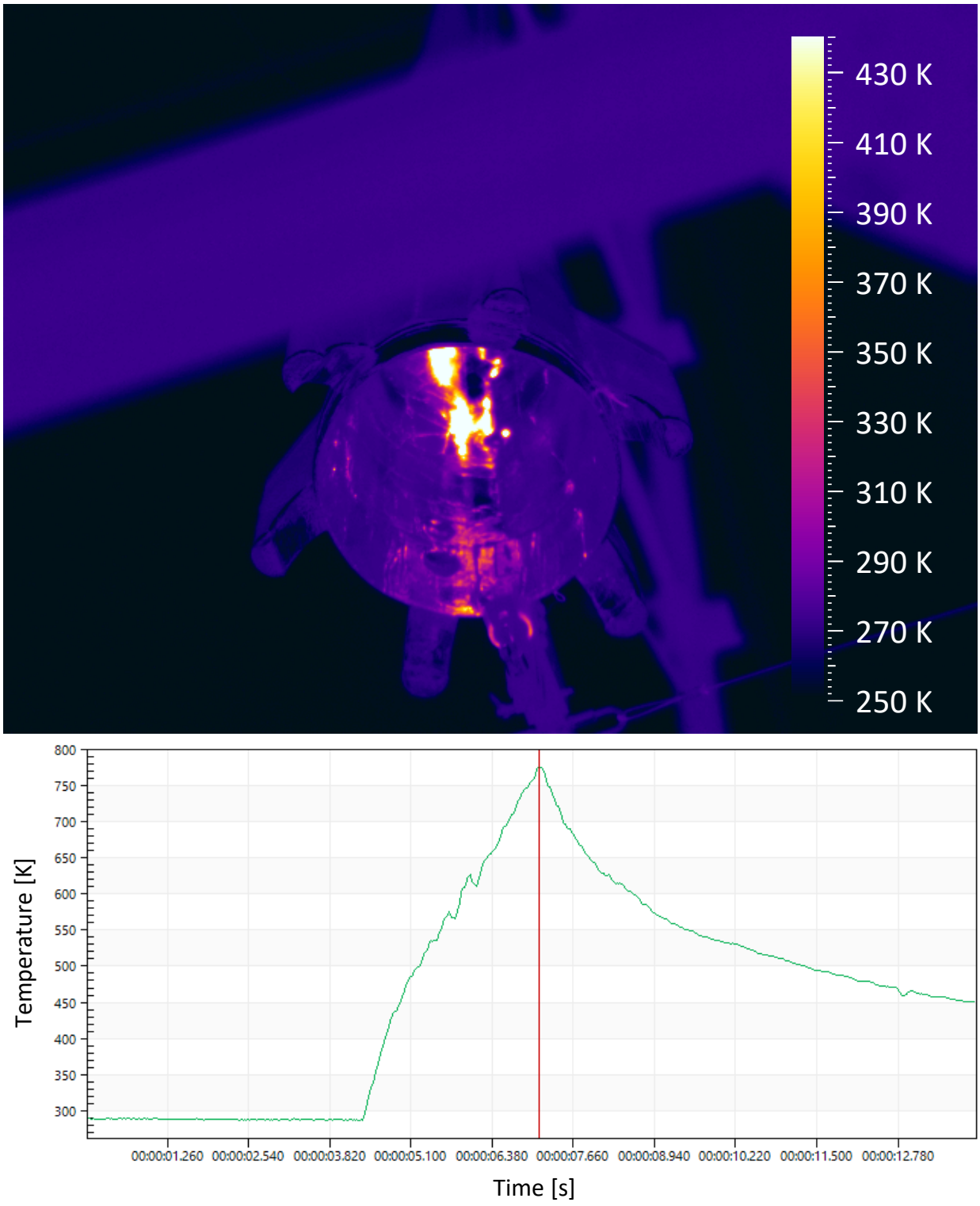

Figure 146 – 28 February 3:58 pm: Launch test of the LTI axial-engaged rocket with beam. The rocket became caught on the launch rail and did not enter the field of view of the visible camera; however, the LWIR camera acquired a temperature history from the reflection of the heat exchanger. Peak temperature is 775 K assuming a tube emissivity of 0.95 as above, or 904 K assuming an emissivity of 0.65. Source file: 2014-02-28T155814817.fcf

Figure 147 - 28 February 3:58 pm: Launch test of the LTI axial-engaged rocket with beam. The LTI Zia-2 rocket is caught on the launch rail, but reflected yellow and orange light from the engine proves that it has reached relatively high temperature. Source file: ZIA2-1.mp4

5.2.1.5 3/24/2014 - 3/28/2014 test campaign at 100 kW, 95 GHz launch test facility

Date	Time	Run #	Distance [m]	Beam characteristics: Power level [%]	Beam characteristics: Peak intensity [kW/m^2]	Beam characteristics: power in 30 cm diameter [kW]	Shot duration [s]: pre heat [s]	Shot duration [s]: delay	Shot duration [s]: total	Temp. [K]: Max. (ε=0.95)	Temp. [K]: Mean (ε=0.95)	Comments
Tuesday 3/25/2014	HOT-LAUNCH-AXIAL-3: ZIA-2-6A launch test with beam											
		1										1.4 mm orifice. 0.6 mm nozzle gap. N_2 propellant at 4.5 ksi. Survived 3-sec. run hot; hung up on rail; graphite inlet manifold
Thursday 3/27/2014	COLD-LAUNCH-AXIAL-2: Launch test without beam											
		1										Successful cold gas launch, clears rail, parachute deploys
Friday 3/28/2014	HOT-LAUNCH-AXIAL-4: ZIA-2-7A launch test with beam											
		1										2 mm orifice. 0.6 mm nozzle gap. N_2 propellant at 4.5 ksi. Failed on valve actuation; hung up on rail; Ti inlet manifold; valve leaking
	HOT-LAUNCH-AXIAL-5: ZIA-2-8A launch test with beam											
		2										1.95 mm orifice. 0.6 mm nozzle gap. N_2 propellant at 4.5 ksi. Failed on valve actuation; hung up on rail; graphite inlet manifold; valve leaking

Table 46 - Tests conducted at the 100 kW, 95 GHz launch test facility between 3/24/2014 - 3/28/2014

Figure 148 - 25 March: Blended video frames showing a successful launch without beam, but with parachute deployment. Source file: gopro234.mp4

Figure 149 – 27 March: Another successful launch without beam shows the launch site arrangement from the point of view of a camera mounted on-board the LTI axial-illuminated rocket as it ascends the launch rail, just after rail departure. A problem at this time was the rocket becoming caught on the launch rail. Source file: "3-27 Onboard.mov"

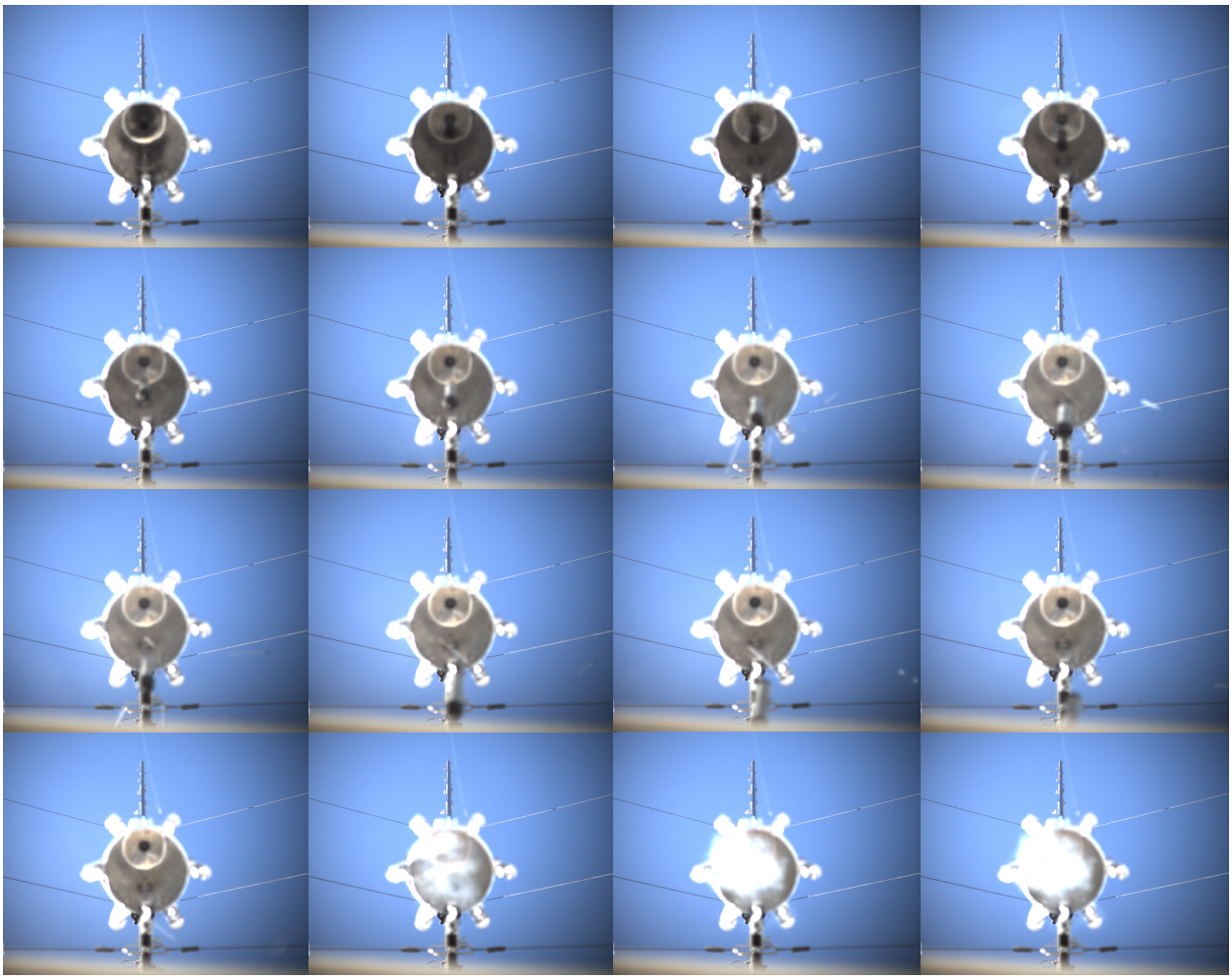

Figure 150 - 28 March 9:46 am: In the final test, the inlet manifold structurally fails, ejecting the heat exchanger and nozzle from the LTI Zia-2 rocket. The rocket is again caught on the launch rail. Source file: 28_03_2014___09_10_18.avi

This test campaign involved the LTI Zia-2 vehicle only owing to difficulty with the pan-tilt unit, which for the time being prevented the beam from following the side-illuminated rocket as it launched. All Zia-2 engines were identical – employing the same fifty 1/16" OD alumina tubes (Aquadag coated interior), in two concentric rings of 25 tubes each.

6 Concluding remarks

We have conducted research in microwave thermal propulsion as part of the space exploration access technologies (SEAT) research program, a cooperation between Carnegie Mellon University and NASA Ames Research Center. The SEAT program commenced on the 19th of February 2009 and concluded on the 30th of September 2015. The DARPA/NASA Millimeter-wave Thermal Launch System (MTLS) project subsumed the SEAT program from May 2012 to March 2014 and one of us (Parkin) served as its principal investigator and chief engineer. The MTLS project had no final report of its own, so we have included the MTLS work in this report and incorporate its conclusions here.

In the six years from 2009 until 2015 there has been significant progress in millimeter-wave thermal rocketry (a subset of microwave thermal rocketry), most of which has been made under the auspices of the SEAT and MTLS programs documented here. We were the first to demonstrate a millimeter-wave absorbent refractory heat exchanger. We integrated this into the propulsion system of a small rocket to produce the first millimeter-wave thermal rocket. Simultaneously, we developed the first high-power cooperative target millimeter-wave beam director, and we trained it upon the rocket to produce the first millimeter-wave thermal rocket launch (albeit to <100 meters altitude and with only partial success before funding ran out).

We were also the first to develop an inference engine for the purpose of rocket design. Our successful synthesis of artificial intelligence with rocket science resulted in a system model that uses 22,000 variables to describe the millimeter-wave thermal rocket, its flow path, ascent trajectory and beam director. However, Version 3.0 of the system model is unfinished: We need to add methane as a propellant and to include its decomposition to hydrogen and carbon within the heat exchanger. Its predictions need to be compared with experiments, and then we can use the resulting capability to upgrade the existing LH_2 launch system point design to an optimized CH_4 launch system point design, which is expected to have substantially better economic performance. As we continue to develop the system model, the number of variables and its computational complexity will continue to grow as it becomes a more faithful representation of the eventual launch system.

	At conclusion of this project	**Attainable with straightforward refinement**	**50 kg rocket point design**
Maximum operating pressure [bar]	10	15-30	45
Maximum wall temperature [K] (at pressure)	1,400	1,700	1,900
Specific Impulse [sec] (propellant-dependent)	35 (argon, sea level)	100 (argon, sea level) 600 (vacuum H_2) 400 (vacuum CH_4)	725 (vacuum H_2)
Run time [sec]	5-8	300	300
Average incident flux [MW/m^2]	2	5-10	6
Areal density [kg/m^2]	5	1-3	1.4
Areal cost [k$/m^2]	15	5	10

Table 47 - Heat exchanger figures of merit

What we have learned from simulating, building and launching a sub-scale millimeter-wave rocket is that it is indeed possible to build a millimeter-wave heat exchanger whose figures of merit are

comparable with those needed for orbital launch, as summarized in Table 47 above. Because these were the first heat exchangers, there are many untried materials and techniques. Therefore, straightforward refinement of the heat exchanger should be tried to bridge the performance gap to the 50-kg point design. If a particular figure of merit proves difficult to attain, the point design is by no means absolute and can be re-converged to accommodate. For example, lower than expected flux performance can be mitigated by moving to a larger heat exchanger, thus reducing beam director size.

MTLS was a crash project, with all the advantages and disadvantages that a crash project entails. We crossed many significant milestones in a short time and laid to rest technical uncertainties with high confidence in comparison to simulations. Specifically, the areal density of the heat exchanger proved to be low enough for orbital applications, surface plasmadynamic breakdown proved not to threaten the feasibility, and thermal shock and thermally-induced deformations proved not to threaten the feasibility.

MTLS was an existence proof that we could make rapid experimental progress at lower cost than incremental research and paper studies. However, we adapted tools, techniques, and plans accumulated during our prior decade of research to accomplish crash objectives: Our first discussion with General Atomics about using the DIII-D gyrotrons for millimeter-wave thermal propulsion research was in August 2002. Our first discussion with AFRL about using their gyrotrons for millimeter-wave thermal propulsion research was in August 2004. We leveraged our experience with ceramic tubes from the first demonstration of a microwave thermal thruster in 2005, and we used our susceptor idea from 2003 to absorb millimeter-waves into the heat exchanger. In addition, the plan to launch a small-scale argon-propelled rocket with a 100 kW gyrotron beam was adapted from our 2008 plan to launch a small-scale butane-propelled rocket using a 10-kW floodlight beam. All this being said, without a crash program it could have taken a second decade before we were able to conduct experiments using the gyrotron sources at General Atomics and AFRL.

MTLS omitted much of the detailed experimentation and modeling that we would have undertaken in traditional incremental academic research (e.g., the original SEAT program). These omissions were evident from the poor uniformity of absorption over the heat exchanger and the poor heat transfer, which led to disappointing thrust and specific impulse performance that is unrepresentative of what is possible using the millimeter-wave thermal approach. With several more months of refinement, we feel that these problems could have been overcome. In addition, for the beam director we were constrained in our choice of pan-tilt unit by the cost and lead-time; an order had to be placed before a detailed conceptual design of the beam director could be made. It was a risk we would not have taken in regular research. It turned out that the weight of the turning flat combined with the initial transient as the rocket is released exceeds the control authority of the pan-tilt unit. Given several more months, we would have crafted a lighter turning flat, better shielded it from wind, and refined the control system to re-acquire the rocket shortly after the launch transient. Some people may interpret these outcomes as a failure of the millimeter-wave thermal propulsion concept. They are not. Given the constraints in time and resources, we broke new ground and provided a path toward a millimeter-wave powered rocket. Our first crude rocket needs to be refined to realize the predicted performance.

MTLS had simulation and modeling needs that exceeded the capacity of our two-person core research team. MTLS required rocket point designs, detailed heat exchanger models including compressible propellants and non-uniform illumination effects, a beam director conceptual design, stratified layer

models, temperature-dependent material models, and numerous other related calculations. We met some of these needs using the pre-existing Version 2.0 of the system model, and our solutions to other problems were built directly into Version 3.0 of the system model as it was being written. Though these models proved their worth, they were unready to function as design tools in a crash project. This was particularly felt in the case of the quasi-1D channel flow model, which was used to predict the heat transfer performance of the heat exchanger. We modified this model and its code to use a Helmholtz equation of state representing compressible and cryogenic propellants; however, we had to press the code into service before adequate debugging. A long-term core research team of four to six people would probably have been sufficient to support the MTLS project. A research group is needed more than a development team because, unlike projects in more mature fields, this work currently takes place in an unstructured context. Specifically, key equations and models are in the process of derivation, simulation tools are unwritten, set-piece experiments and procedures are not yet established, few engineers are trained with the relevant body of knowledge, there are no established authorities, and no textbooks to turn to. It is our hope that the present report is of some help in the latter regard.

In the course of the SEAT program, we found no technical issues that call into question the feasibility of the millimeter-wave rocket concept. For each aspect of the launch system, there are several different technological approaches, and the greatest risk is that a chosen approach turns out to be unacceptably expensive or performs poorly relative to the alternatives, causing us to switch to an alternate technology for an element of the system. Key technical risks are associated with the heat exchanger, the propellant tank(s), beam combining, and the secondary and tertiary optics of the beam director. Nearly all key technological aspects of the rocket and beam director can be demonstrated at small scale and relatively low cost. Heat transfer within the heat exchanger can be refined using the 100-kW hot jet static test facility prior to more expensive gyrotron testing. Absorption performance of the heat exchanger can be tested with the reflectometer test facility prior to more expensive gyrotron testing. Spectral beam combining can be demonstrated using milliwatt-class millimeter-wave sources and a regular mill to produce the diffraction gratings. Using tunable sources, it is possible to deduce the efficiency with which dozens or hundreds of millimeter-wave sources can be spectrally combined.

Testing the beam director optical train at small scale is somewhat harder. Our preferred technical approach is to use a spherical reflector that is the size and optical type of the Arecibo telescope but built using conventional low-cost rigid steel frame construction so that it has high surface accuracy and hence high aperture efficiency at millimeter wavelengths. To reduce risk, the Chinese Five-hundred-meter Aperture Spherical Telescope (FAST) produced a panel of the primary reflector first, and then assembled a sub-scale dish from these panels. We feel that the same steps are appropriate for a millimeter-wave beam director.

Upgrading the primary reflector panels from basic metal to an active metasurface enables the beam to be steered electrically instead of steered by physically moving the secondary reflector and tertiary optics across a focal surface. Consequently, we would like to see reflectarray research work toward an active metasurface that can a take a 95 GHz or 170 GHz millimeter-wave beam of >1 kW/m^2 peak intensity and reflect it through an angular range of better than -70° to +70° off-normal with >50% efficiency over a bandwidth of 5 GHz. It should be the size (1 m^2), cost (<$1,000/$m^2$) and power consumption of a plasma TV (<100 W/m^2). We would arrange 50,000 of these units into a fixed 250-meter diameter spherical sector of relatively flat profile close to the ground. Using this, we would build a beam director capable

of projecting a high-power millimeter-wave spot onto the underside of a rocket throughout its ascent to space.

Correspondingly, millimeter-wave thermal launchers will benefit from certain developments in millimeter-wave sources: Decreases in $/Watt for gyro amplifiers at 95 GHz or 170 GHz. For gyrotron oscillators at 170 GHz, decreases in $/Watt, smaller more stable bandwidth for improved spectral beam combining, or a successful implementation of phase locking.

To put the present state of development into context, directed energy rockets are analogous in many ways to Goddard's liquid propellant rockets circa 1930. Although we will not be re-inventing rockets, we do have to develop the beam directors and the heat exchanger-based propulsion subsystems that power them. It makes sense to retire technical risks at small scale, and to develop a pipeline from the laboratory, to static testing, to small-scale launches, to ever-higher altitudes until we reach orbit. Is there any other reasonable way to structure a millimeter-wave thermal rocket program?

Our most important conclusion is that if the ground infrastructure for millimeter-wave rockets costs less than $22/Watt, then it makes economic sense for the United States Government to transition from traditional chemical rockets to millimeter-wave thermal rockets. Current beam director cost estimates are $0.1-1/Watt for the heaviest launchers, or one to two orders of magnitude lower. This is already low enough to recommend a changeover from chemical to millimeter-wave thermal rockets. Given the current economically significant United States government expenditure of $169M per week on space launch, the price of inaction is great indeed.

7 Acknowledgements

We are indebted to the pioneers of directed energy and propulsion on whose work we build. We would like to thank Pete Worden, whose steadfast financial support over the past six years has made all this possible. We would also like to thank Paul Eremenko and Chris Schulz for initiating the DARPA-NASA MTLS project, Julie Mikula and Donna Dickey for making it a reality, and Leik Myrabo for energetically serving alongside one of us (Parkin) as MTLS co-principal investigator.

Finally, we would like to thank our colleagues at NASA and Carnegie Mellon University, and the teams we have worked with over the course of the past six years, particularly the MTLS team - your work achieved in two years what otherwise could have taken a decade more.

Millimeter-Wave Thermal Launch System (MTLS) Teams

DARPA	**NASA**	**United States Air Force Research Laboratory**	**Carnegie Mellon University**
Paul Eremenko	Bala Balakrishnan	Anthony Baros	Hillary Nicholson
Chris Schulz	Jim Eilers	David Hardy	Hector Rastrullo
Jess Sponable	Doug Fraser	Brad Hoff	Steven Rosenberg
Centra	Dan Leiser	Eddie Klepacki	**Lightcraft Technologies**
Donna Dickey	Creon Levit	Brian Long	Cesare Frepoli
Timmie Thompson	Julie Mikula	Scott Maethner	Van Jacobi
Schafer Associates	Richard Morrison	Katrina Schweiker	John Likakis
Mike Walter	David Murakami	Mike Zmuda	Leik N. Myrabo
HELSTF	Steve Ord	**Leidos**	Israel I. Salvador
Jeff Radtke	Greg Paulson	Jim Duffey	**Izentis**
Steve Squires	**DOE/General Atomics**	William Shaefer	Alex Bruccoleri
Mike Thurston	Mark Foster	Jim Staggs	
	Yuri Gorolev		
	Arnie Kellman		
	John Lohr		

8 References

Acheson, E. G. (1907). "Deflocculated graphite." Journal of the Franklin Institute **164**(5): 375-385.

Agarwal, G. S., et al. (2004). "Coherence properties of sunlight." Optics letters **29**(5): 459-461.

AIAA (2006). AIAA Standard - Mass Properties Control for Space Systems (S-120-2006), S-120-2006e.

Altschuler, D. R. (2002). The National Astronomy and Ionosphere Center's (NAIC) Arecibo Observatory in Puerto Rico. Single-Dish Radio Astronomy: Techniques and Applications.

Andronov, A. A., et al. (1978). The gyrotron-High-power source of millimetre and submillimetre waves.

Arbit, H. A., et al. (1970). "Investigation of the Lithium-Fluorine-Hydrogen Tripropellant Svstem." J. Spacecraft **7**(10).

Auerkari, P. (1996). Mechanical and physical properties of engineering alumina ceramics, Technical Research Centre of Finland Finland.

Bakunin, V., et al. (2014). "Frequency and phase stabilization of a multimode gyrotron with megawatt power by an external signal." Technical Physics Letters **40**(5): 382-385.

Benford, J. and R. Dickinson (1995a). Space Propulsion and Power Beaming Using Millimeter Systems. Intense Microwave Pulses III. Also published in Space Energy and Transportation, 1, p. 211.

Benford, J., et al. (2007). High power microwaves, Inst of Physics Pub Inc.

Benford, J. N. and R. Dickinson (1995b). Space propulsion and power beaming using millimeter systems. SPIE's 1995 International Symposium on Optical Science, Engineering, and Instrumentation, International Society for Optics and Photonics.

Berry, D., et al. (1963). "The reflectarray antenna." Antennas and Propagation, IEEE Transactions on **11**(6): 645-651.

Boren, H. E. and H. G. Campbell (1970). Learning-Curve Tables, RAND Corporation.

Bruccoleri, A. R. and L. Daniel (2009). Analysis of Propellant Density Influence on Microwave Thermal Rocket Vehicle Mass. 45th AIAA/ASME/SAE/ASEE Joint Propulsion Conference & Exhibit.

Bruccoleri, A. R., et al. (2015). Development and Short-Range Testing of a 100 kW Side-Illuminated Millimeter-Wave Thermal Rocket. NASA/TM—2015–218756.

Bruccoleri, A. R., et al. (2007). "Axial temperature behavior of a heat exchanger tube for microwave thermal rockets." Journal of Propulsion and Power **23**(4): 889-894.

Burrows, M. and L. Ricardi (1967). "Aperture feed for a spherical reflector." Antennas and Propagation, IEEE Transactions on **15**(2): 227-230.

Cornella, B., et al. (2010). "Thrust Augmentation of Solid Rocket Motors Using Beamed Microwave Energy." Journal of Propulsion and Power **26**(5): 1016-1024.

Drachenberg, D. (2011). Ultra High Density Spectral Beam Combining by Thermal Tuning of Volume Bragg Gratings in Photo-thermo-refractive Glass, University of Central Florida Orlando, Florida.

Duval, D. J., et al. (2008). Mullite. Ceramic and Glass Materials, Springer**:** 27-39.

Frank, M., et al. (2003). "Particle migration in pressure-driven flow of a Brownian suspension." Journal of Fluid Mechanics **493**: 363-378.

Fukunari, M. (2012). Analytical Study of Reed Valve Air-breathing System for Microwave Rocket, University of Tokyo.

Futron (2003). NASA ASCENT Study Final Report.

GAO (2013). Space: Defense and Civilian Agencies Request Significant Funding for Launch-Related Activities. GAO-13-802R.

George, P. and R. Beach (2012). Beamed-Energy Propulsion (BEP) Study. NASA/TM—2012-217014.

Gimelshein, N. E., et al. (2009). Thrust Augmentation in Solid Rocket Motors Using Beamed Microwave Energy, Defense Technical Information Center.

Ginzburg, N., et al. (2015). "Time-domain self-consistent theory of frequency-locking regimes in gyrotrons with low-Q resonators." Physics of Plasmas (1994-present) **22**(3): 033101.

Goldsmith, P. (2001). "Resetting the Arecibo Primary Reflector Surface." The Arecibo Observatory Newsletter **32**: 1-4.

Goldsmith, P. F., et al. (1998). Quasioptical systems: Gaussian beam quasioptical propagation and applications, IEEE press New York.

Goodson, C. C. (1997). Simulation of Microwave Heating of Mullite Rods. Department of Mechanical Engineering, Virginia Polytechnic Institute and State University. Master of Science.

Goubau, G. (1970). "Microwave power transmission from an orbiting solar power station(Microwave power transmission from orbiting solar power station to earth, discussing design optimization problems)." Journal of Microwave Power **5**: 223-231.

Goubau, G. and F. Schwering (1968). "3.5 Free Space Beam Transmission." Microwave Power Engineering: Generation, transmission, rectification **1**: 241.

Halmann, M., et al. (2014). "Vacuum carbothermic reduction of alumina." Mineral Processing and Extractive Metallurgy Review **35**(2): 126-135.

Ho, W. W. (1984). "Millimeter wave dielectric property measurement of gyrotron window materials." ORNL/SUB/83-51926/1 (April 1984) and ORNL/SUB/83-51926/2 (April 1985).

Holzrichter, M. (2012). An application of the constraint programming to the design and operation of synthetic aperture radars. High Performance Extreme Computing (HPEC), 2012 IEEE Conference on, IEEE.

Huang, J. and J. Encinar (2008). Reflectarray Antennas, by Institute of Electrical and Electronics Engineers, John Wiley & Sons.

Hum, S. V. and J. Perruisseau-Carrier (2014). "Reconfigurable reflectarrays and array lenses for dynamic antenna beam control: A review." Antennas and Propagation, IEEE Transactions on **62**(1): 183-198.

Jacobsen, R. T., et al. (1997). Thermodynamic properties of cryogenic fluids, Springer.

Kakaç, S., et al. (1987). Handbook of Single-Phase Convective Heat Transfer, Wiley-Interscience.

Kakinuma, K., et al. (2015). Two-Stage-to-Orbit Transporting System Combining Microwave Rocket and Microwave Thermal Rocket for Small Satellite Launch. Joint Conference of 30th International Symposium on Space Technology and Science 34th International Electric Propulsion Conference and 6th Nano-satellite Symposium. Hyogo-Kobe, Japan.

Kantrowitz, A. (1972). "Propulsion to orbit by ground-based lasers." Astronautics and Aeronautics **10**(74-76).

Kare, J. T. (1992). Development of Laser-Driven Heat Exchanger Rocket for Ground-to-Orbit Launch. Washington, DC International Astronautical Federation Congress.

Kare, J. T. and K. L. G. Parkin (2005). A Comparison of Laser and Microwave Approaches to CW Beamed Energy Launch. Fourth International Symposium on Beamed Energy Propulsion, Nara, Japan, AIP.

Katz, J. D. (1992). "Microwave sintering of ceramics." Annual Review of Materials Science **22**(1): 153-170.

King, R. E. (2013). Research on Bird-Detecting Radar. DOT/FAA/TC-13/3.

Kupiszewski, A. (1979). "The Gyrotron: A High-Frequency Microwave Amplifier." The Deep Space Network Progress Report 42 **52**: 8.

Kurita, S. (2014). Development of a Ti-Taper Reed Valve for Microwave Rocket and Effect on Its Thrust Performance, University of Tokyo.

Lamb, J. W. (1996). "Miscellaneous data on materials for millimetre and submillimetre optics." International journal of infrared and millimeter waves **17**(12): 1997-2034.

Lambot, T., et al. (2014a). Development and Testing of a Refractory Millimeter-Wave Absorbent Heat Exchanger. International High Power Laser Ablation and Beamed Energy Propulsion (HPLA/BEP) Symposium, Santa Fe, New Mexico.

Lambot, T., et al. (2014b). Development and Testing of a Refractory Millimeter-Wave Absorbent Heat Exchanger. 20th Advanced Space Propulsion Workshop, Ohio Aerospace Institute, Cleveland, Ohio.

Lemmon, E. W., et al. (2002). NIST reference fluid thermodynamic and transport properties–REFPROP, Version.

Liu, Y. and J. Tan (2013). "Frequency Dependent Model of Sheet Resistance and Effect Analysis on Shielding Effectiveness of Transparent Conductive Mesh Coatings." Progress In Electromagnetics Research **140**: 353-368.

Marshall, W. and V. Beukelaers (2011). PhoneSat: a smartphone-based spacecraft bus. 62nd International Astronautical Congress.

Mason, J. (2010). Microwave Beam-Satellites Intersections, NASA Ames Research Center.

McBride, B. and S. Gordon (2004). "Chemical equilibrium program CEA2." NASA Glenn Research Center, Cleveland, OH.

Minin, I. V. and O. V. Minin (2004). Diffractional optics of millimetre waves, CRC Press.

Minovich, M. A. (1972). The laser rocket – A rocket engine design concept for achieving a high exhaust thrust with high I_{SP}, Jet Propulsion Laboratory of the California Institute of Technology. JPL TM 393-92.

Moy, G., et al. (2000). A compliant tactile display for teletaction. Robotics and Automation, 2000. Proceedings. ICRA'00. IEEE International Conference on, IEEE.

Myrabo, L. N. and J. Benford (1994). "Propulsion of Small Launch Vehicles Using High Power Millimeter Waves." SPIE 2154: 198.

NASA (1994). "Commercial Space Transportation Study." from http://www.hq.nasa.gov/webaccess/CommSpaceTrans/.

Oda, Y. (2008). Application of Atmospheric Millimeter Wave Plasma to Rocket Propulsion, University of Tokyo. Ph.D.

Oda, Y., et al. (2003). An observation of plasma inside of microwave boosted thruster. Second International Symposium on Beamed Energy Propulsion, Sendai, Japan, Conf. Proc. AIP.

Parkin, K. L. G. (2006a). A microwave-thermal thruster for high-volume low-cost launch of microsatellites. Final report to DARPA/AFRL HOT EAGLE program.

Parkin, K. L. G. (2006b). Microwave heat-exchange thruster and method of operating the same. USPTO, California Institute of Technology.

Parkin, K. L. G. (2006c). The Microwave Thermal Thruster and its Application to the Launch Problem. Department of Aeronautics (GALCIT). Pasadena, CA, California Institute of Technology.

Parkin, K. L. G. (2008). Microwave Thermal Rockets—A Progress Report. BEAMED ENERGY PROPULSION: Fifth International Symposium on Beamed Energy Propulsion, AIP Publishing.

Parkin, K. L. G. and F. E. C. Culick (2003). Feasibility and Performance of the Microwave Thermal Rocket Launcher. Proc. ISBEP2, Sendai, Japan, AIP.

Parkin, K. L. G., et al. (2002). A Microwave-Thermal Thruster for Ultra Low-Cost Launch of Microsatellites, Jet Propulsion Center, California Institute of Technology.

Parkin, K. L. G., et al. (2003). The Microwave Thermal Thruster Concept. Proc. ISBEP2, Sendai, Japan, AIP.

Parkin, K. L. G., et al. (2014a). Overview of the Millimeter-Wave Thermal Launch System (MTLS) Project. International High Power Laser Ablation and Beamed Energy Propulsion (HPLA/BEP) Symposium, Santa Fe, New Mexico.

Parkin, K. L. G., et al. (2014b). Overview of the Millimeter-Wave Thermal Launch System (MTLS) Project. The 20th Advanced Space Propulsion Workshop, Ohio Aerospace Institute, Cleveland, Ohio.

Parkin, K. L. G. and L. Webster (2012). Millimeter-wave Thermal Launch System (MTLS) Reference Design Report (ERC 6019), NASA.

Penn, S. J., et al. (1997). "Effect of porosity and grain size on the microwave dielectric properties of sintered alumina." Journal of the American Ceramic Society **80**(7): 1885-1888.

Pfeiffer, C. and A. Grbic (2013). "Metamaterial Huygens' surfaces: tailoring wave fronts with reflectionless sheets." Physical review letters **110**(19): 197401.

Prahlad, H., et al. (2005). Programmable surface deformation: thickness-mode electroactive polymer actuators and their applications. Smart Structures and Materials, International Society for Optics and Photonics.

Ruttle, D. and M. Fitzsimmons (1993). Development of miniature 35 lbf fast response bipropellant divert thruster. 29th Joint Propulsion Conference and Exhibit, American Institute of Aeronautics and Astronautics.

Rzesnicki, T., et al. (2010). "2.2-MW record power of the 170-GHz European preprototype coaxial-cavity gyrotron for ITER." Plasma Science, IEEE Transactions on **38**(6): 1141-1149.

Saito, S. (2013). Performance Evaluation of Reed Valve Air-Breathing System for Microwave Rocket, University of Tokyo.

Shibata, T. (2008). Structural analysis of a microwave supported detonation wave, University of Tokyo.

Shimada, Y. (2010). A New Theory of a Microwave Supported Detonation, University of Tokyo.

Shiraishi, Y. (2009). Propeller length and beam condition dependence of the microwave rocket propulsion performance, University of Tokyo.

Sloop, J. L. (1978). "Liquid Hydrogen as a Propulsion Fuel, 1945-1959. NASA SP-4404." NASA Special Publication **4404**.

Starodubova, E., et al. (2015). "Injection locking of a two-mode electron oscillator with close frequencies." Physics of Plasmas (1994-present) **22**(3): 033108.

Tsiolkovsky, K. E. (1924). Spaceship, 1924, in Izbrannye Trudy, Compiled by Vorob'ev, B.N., Sokol'skii, V.N., General Editor Acad. Blagonravov, Izdatel'stvo Akademii Nauk SSSR, Moscow, Russia, 1962, 222 (in Russian). Edited Machine Translation prepared by Translation Division, Foreign Technology Division, WP-AFB, Ohio, on May 5th, 1966, 307.

United States. FedBizOpps: Federal business opportunities. Washington, D. C. G. S. A. (2014). Collaborative Opportunities for Research, Development, and Demonstration at Sandia's National Solar Thermal Test Facility (NSTTF).

Velazquez, R., et al. (2005). Miniature shape memory alloy actuator for tactile binary information display. Robotics and Automation, 2005. ICRA 2005. Proceedings of the 2005 IEEE International Conference on, IEEE.

Vidal-Verdú, F. and R. Navas-González (2003). Thermopneumatic actuator for tactile displays. 18th Conference on Design of Circuits and Integrated Systems, DCIS, Citeseer.

Viswanathan, V., et al. (2013). "National Assessment of Energy Storage for Grid Balancing and Arbitrage. Phase II. Volume 2: Cost and Performance Characterization." US Department of Energy.

von Hoerner, S. (1975). "Radio telescopes for millimeter wavelength." Astronomy and Astrophysics **41**: 301-306.

Wiese, J. L. (2001). Strength of metal-to-ceramic brazed joints. Department of Materials Science and Engineering, Massachusetts Institute of Technology. Master of Science**:** 210.

Wilkening, D. A. (2003). "Airborne boost-phase ballistic missile defense." Science & Global Security: The Technical Basis for Arms Control, Disarmament, and Nonproliferation Initiatives **12**(1-2).

Willinski, M. I. (1959). "Beamed electromagnetic power as a propulsion energy source." Amer. Rocket Soc. J. **29**(8): 601-603.

Willinski, M. I. (1966). "Microwave powered ferry vehicles." Spaceflight **8**: 217-225.

Wright, T. P. (1936). "Learning curve." Journal of the Aeronautical Sciences **3**(1): 122-128.

Yamaguchi, T. (2010). Application of microwave beam control technology to a Microwave Rocket.

Young, D. A. and J. R. Olds (2005). "Responsive access small cargo affordable launch (RASCAL) independent performance evaluation." Proceedings of AIAA/CIRA 13th International Space Planes and Hypersonics Systems and Technolo. San Jose, California: AIAA **3241**.

Yu, N. and F. Capasso (2014). "Flat optics with designer metasurfaces." Nature materials **13**(2): 139-150.

REPORT DOCUMENTATION PAGE

Form Approved
OMB No. 0704-0188

1. REPORT DATE *(DD-MM-YYYY)*	2. REPORT TYPE	3. DATES COVERED *(From - To)*
12-15-2015	**Final report**	**Feb 2009 – Sep 2015**

4. TITLE AND SUBTITLE

Microwave Thermal Propulsion
Final Report

5a. CONTRACT NUMBER

5b. GRANT NUMBER
NNX09AF52A

5c. PROGRAM ELEMENT NUMBER

6. AUTHOR(S)

Parkin, Kevin L.G.
Lambot, Thomas

5d. PROJECT NUMBER

5e. TASK NUMBER

5f. WORK UNIT NUMBER

7. PERFORMING ORGANIZATION NAME(S) AND ADDRESS(ES)

Carnegie Mellon University
5000 Forbes Ave.
Pittsburgh, PA 15213-3815

8. PERFORMING ORGANIZATION REPORT NUMBER

SEAT-MTP-FINAL-B

9. SPONSORING / MONITORING AGENCY NAME(S) AND ADDRESS(ES)

NASA Ames Research Center
Moffett Field, CA 94035-1000

10. SPONSOR/MONITOR'S ACRONYM(S)

NASA

11. SPONSOR/MONITOR'S REPORT NUMBER(S)

12. DISTRIBUTION / AVAILABILITY STATEMENT

DISTRIBUTION STATEMENT A. Approved for public release; distribution is unlimited.

13. SUPPLEMENTARY NOTES

14. ABSTRACT

We have conducted research in microwave thermal propulsion as part of the space exploration access technologies (SEAT) research program, a cooperative agreement (NNX09AF52A) between NASA and Carnegie Mellon University. The SEAT program commenced on the 19th of February 2009 and concluded on the 30th of September 2015. The DARPA/NASA Millimeter-wave Thermal Launch System (MTLS) project subsumed the SEAT program from May 2012 to March 2014 and one of us (Parkin) served as its principal investigator and chief engineer. The MTLS project had no final report of its own, so we have included the MTLS work in this report and incorporate its conclusions here.

In the six years from 2009 until 2015 there has been significant progress in millimeter-wave thermal rocketry (a subset of microwave thermal rocketry), most of which has been made under the auspices of the SEAT and MTLS programs.

This final report is intended for multiple audiences. For researchers, we present techniques that we have developed to simplify and quantify the performance of thermal rockets and their constituent technologies. For program managers, we detail the facilities that we have built and the outcomes of experiments that were conducted using them. We also include incomplete and unfruitful lines of research. For decision-makers, we introduce the millimeter-wave thermal rocket in historical context. Considering the economic significance of space launch, we present a brief but significant cost-benefit analysis, for the first time showing that there is a compelling economic case for replacing conventional rockets with millimeter-wave thermal rockets.

15. SUBJECT TERMS
Microwave thermal propulsion, millimeter-wave thermal launch system

16. SECURITY CLASSIFICATION OF:			17. LIMITATION OF ABSTRACT	18. NUMBER OF PAGES	19a. NAME OF RESPONSIBLE PERSON
a. REPORT	b. ABSTRACT	c. THIS PAGE			19b. TELEPHONE NUMBER *(include area code)*
Unclassified	**Unclassified**	**Unclassified**	**Unclassified Unlimited**	**215**	